2007

# NMR investigations of biological and synthetic phosphate-based nanocomposites

Aditya Rawal
*Iowa State University*

# NMR investigations of biological and synthetic phosphate-based nanocomposites

by

**Aditya Rawal**

A dissertation submitted to the graduate faculty

in partial fulfillment of the requirements for the degree of

DOCTOR OF PHILOSOPHY

Major: Chemistry

Program of Study Committee:
Klaus Schmidt-Rohr, Major Professor
Mei Hong
Jacob Petrich
Yan Zhao
Surya Mallapragada

Iowa State University

Ames, Iowa

2007

*na choraharyam na cha rajaharyam na bhratrubhajyam na cha bharakari l*

*vyaye krte vardhata eva nityam vidya dhanam sarvadhana pradhanam ll*

Not stolen by thieves or seized by kings,

Not dividable among siblings or burdensome to carry,

As it is spent, ever does it grow,

The wealth of knowledge is the foremost among all wealth.

# TABLE OF CONTENTS

# ACKNOWLEDGMENTS

The process of obtaining or attempting to obtain a doctorate in any field is necessarily a rigorous one. With proper guidance, the hopeful candidate will, over the course time evolve and mature in thought and attitude. Certainly, depending upon one's chosen discipline, there is an enhanced awareness regarding one's self and surrounding. We begin to view the universe or at the very least a relevant portion thereof in a new light, probably because the old one blew a fuse. In this regard, I would like to thank Prof. Klaus Schmidt-Rohr under whose guidance the work in this dissertation was conducted, for switching on the new light. I would also like to thanks Prof. Mei Hong for her support in performing various experiments and a variety of collaborations with the groups of Prof. Surya Mallapragada, Prof. Akinc and others, which has contributed significantly towards this dissertation and expanding my knowledge of materials science.

The hostility of Iowa winters could only be survived by the warmth and company of friends and colleagues. Bosa, Abhi, Rajee, Tim, Yanyan, Sarah, Xiaowen and others made the experience a memorable one.

Deepest respects are due to my parents and grandparents who have watched over my welfare. Especially my long suffering mother whose threats of cutting of my dietary rations motivated me to try and find my place in the world.

# ABSTRACT

The study of complex organic, inorganic and composite systems is greatly facilitated by solid state nuclear magnetic resonance (NMR) spectroscopy. This is especially true for materials lacking crystalline long-range order or having low atomic mass contrast, such as amorphous organic materials, which renders other methods such as x-ray diffraction (XRD) and transmission electron microscopy (TEM) incapable of comprehensive characterization. In this dissertation, a variety of one- and two-dimensional (2D) solid-state NMR measurements are applied to investigate the composition and nanometer-scale structure of a variety of organic-inorganic hybrid systems as well as complex inorganic phases. Bone, which is a natural nanocomposite of an inorganic apatitic phosphate and the organic protein collagen, has been studied by $^{1}$H single-resonance, $^{1}$H-$^{31}$P and $^{1}$H-$^{13}$C double-resonance, as well as $^{1}$H-$^{13}$C-$^{31}$P triple-resonance experiments. Analysis of $^{31}$P dephasing by heteronuclear recoupling with dephasing by strong homonuclear interactions of protons (HARDSHIP) has provided information about the size of the apatite nanocrystals. The concentrations of various moieties in the composite, such as the $OH^-$, $CO_3^{2-}$, $HPO_4^{2-}$, $H_2O$-$PO_4^{3-}$, and Na in the inorganic apatite, were determined by quantitative spectroscopy via spectral selection of specific chemical moieties. X{$^{1}$H} HARDSHIP NMR was used to prove their incorporation into the apatite nanocrystals. $^{31}$P chemical shift anisotropy (CSA) dephasing experiments as well as $^{1}$H{$^{31}$P} rotational echo double resonance (REDOR) experiments have identified and quantified the hydrogen and phosphate species located at the surface and the interior of the apatite crystal. Strongly bound $H_2O$, as well as a layer of viscous water, is present at the organic-inorganic interface, as proven by $^{1}$H spin-diffusion detected via $^{13}$C and $^{31}$P nuclei. Investigation of the proximity of organic moieties to the apatite surface via $^{13}$C{$^{31}$P} heteronuclear recoupling experiments provide a structural insight of the organic–inorganic interface.

Biomimetic synthetic organic-inorganic phosphate hybrid materials have been investigated. $^{31}$P NMR spectroscopy has enabled identification and quantification of the different types of phosphates in these materials, and the formation of nanocomposites is proven by wideline separation (WISE) NMR with spin diffusion. A bone-replacement material, Si/Zn-doped β-tricalcium phosphate (TCP), has also been investigated. Spectral selection techniques based on J-modulation and double-quantum filtering have enabled elucidation of the spectrally overlapping silicate Q species. $^{29}$Si{$^{31}$P} REDOR proves that while the silicate is indeed incorporated into the TCP matrix, it is significantly aggregated into ~7 nm diameter domains. Further, a new class of hybrid systems based on polyamide 6 and phosphate glass was studied, where HARDSHIP has confirmed the formation of nanocomposites of the phosphate glass dispersed in the polyamide matrix. $^{1}$H-$^{31}$P heteronuclear correlation (HetCor) NMR indicated phosphate-polyamide interactions and alterations of the phosphate glass surface by the polyamide matrix. $^{13}$C NMR has also shown that the phosphate glass promotes the crystalline γ-phase of the polyamide.

# CHAPTER 1
# GENERAL INTRODUCTION

## 1.1 Bone

Bone is a nano-composite of a biomineralized calcium phosphate (bioapatite) and the fibrous triple helical collagen protein. It has evolved as a stiff skeletal framework to meet the structural needs of mechanically supporting vertebrates such as mammals, birds, reptiles, and fish. It is unique in that essentially one motif has the versatility in supporting a vast diversity of organisms from mice to elephants. Bone's remarkable strength-to-weight ratio and its marvelous ability for self-repair is of extensive medical and materials science interest. The structural morphology, composition and formation and the mechanical properties of bone have been investigated for nearly a century[1].

The composition of bone has been difficult to determine accurately. Even though a variety of techniques such as wet chemistry, infrared vibration spectroscopy (IR) and more recent nuclear magnetic resonance spectroscopy (NMR) methods have been used, the question of its composition has remained contentious. In particular, questions relating to the calcium deficiency, carbonate content, and presence of hydroxyl ions in the bone mineral have sparked much debate. The aspect of bone morphology has also been subject to similar misconceptions. The shape of the bioapatite nanocrystals was first investigated in the 1940's with the advent of electron microscopy[2]. Improved microscopy[3] methods, investigations by small angle x-ray scattering (SAXS)[4] and atomic force microscopy[5] have produced conflicting results regarding nanoparticle size and shape. Similarly a variety of models have been proposed for the interface between the bioapatite and collagen [6]. Thus, there is a need to establish a coherent and unambiguous picture from the myriad opinions, about the nature of the bone nanocomposite.

**1.2 Biological and biomimetic materials and solid state NMR**

As the awareness about the complex structures present in nature increases, synthetic material chemists are looking towards biological systems for inspiration to develop new materials and facile processes to meet the demand for environmentally benign yet high performance materials. There are a variety of organisms in nature that deposit a variety of minerals in diverse ways[7]. There is a practical interest in investigating and understanding this biomineralization (for example osteogenesis: the formation of bone mineral and bones), as well as the structure and composition of the biomineral[8] and one of the most powerful methods for investigating these issues is nuclear magnetic resonance.

NMR has proved to be a versatile tool to investigate structure and dynamics in a variety of systems. It is provides the selectivity and sensitivity to elucidate structural detail from the atomic scale to a range of tens of nanometers, that is over two orders of magnitude in length scale. It is also an excellent probe of molecular dynamics and order and can investigate a variety of physical states from crystalline to amorphous, solids and liquids. These properties make it a powerful method for studying a diverse range of biological issues such as molecular and supermolecular structure, protein dynamics and binding interactions, in addition to questions about composition and surface structure, in conditions that are very close to the native states. In conjunction with other methods such as scattering and electron microscopy, NMR can provide a comprehensive understanding of these complex naturally occurring materials.

Solid-state NMR is a promising method for investigating nanocomposites, where an inorganic phase is dispersed in an organic matrix, with the particles of the inorganic phase having dimensions of tens of nanometers or less. This is the morphology of many

biomaterials (for example bone, nacre and diatom cell walls). Because of the high surface-to-volume ratio of nanocomposites, NMR can study the interaction of the two phases in the composite, which is what determines the overall properties of the material. Being a quantitative method, the integrated areas of the peaks in an NMR spectrum represent the actual fractions of various components and thus can be used for nondestructive compositional analysis as well.

As NMR can give a unique insight into biological materials, similarly it can be used to great benefit for investigating the structure of biomimetic materials and also resorbable bone replacement materials. Indeed, a variety of nanocomposites where the dispersed phase is amorphous (for XRD) or has poor contrast (for electron microscopy) are best investigated by solid state NMR.

### 1.3 **Structure of the Dissertation**

The primary focus of this dissertation is to give a comprehensive composition of bioapatite, determining its size and shape, investigating its surface structure, and elucidating the interfacial region between the bioapatite and collagen. Further, three related projects involving biomimetic and synthetic nanocomposites will also be presented.

1. Characterizing biomimetic composites: Solid state NMR is used to guide synthesis of biomimetic nanocomposites, as relatively simple experiments can be use to monitor the formation of a nanocomposite under various conditions.
2. Elucidating the dispersion of silicate in a tricalcium phosphate (TCP) matrix: The location of silicate, which is doped into a TCP matrix to optimize its solubility as a bone replacement material, is elucidated by solid state NMR.
3. Characterizing polyamide-6/phosphate glass composites: The nanoscale dispersion of a low-Tg phosphate glass in a polyamide-6 matrix has been

investigated, and the effects of the glass on the polyamide crystallization have been documented.

Chapter 2 gives a literature survey of the current understanding of bone nanostructure. Chapter 3 presents a novel solid state NMR method for determination of the size of nanoparticles dispersed in an organic matrix, which is applied to bone. Chapter 4 details the surface composition of the bioapatite particles and then Chapter 5 presents a comprehensive compositional analysis of the bioapatite. In Chapter 6, we investigate the inhomogeneity of the $OH^-$ ions in the bioapatite and Chapter 7 deals with the assignment of the collagen $^{13}C$ NMR signals. In Chapter 8, we investigate the nature of water in bone and propose a model for the collagen-bioapatite interface. Chapter 9 is about characterizing synthetic biomimetic composite materials, and Chapter 10 discusses the distribution of silicate in tricalcium phosphate, a potential bone-replacement material. Chapter 11 details the polyamide-6/phosphate glass nanocomposite structure as elucidated by multinuclear NMR experiments and finally, Chapter 12 is a short note on the influence of phosphate glass on the crystal structure of polyamide-6.

(1) Hendricks, S. B.; Hill, W. L. Science 1942, 96, 255-257.

(2) Wolpers, C. Grenzgebiete Med 1949, 2, 527.

(3) Johansen, E.; Parks, H. F. J Biophy Biochem Cyt 1960, 7, 743-745.

(4) Fratzl, P.; Groschner, M.; Vogl, G.; Plenk, H., Jr.; Eschberger, J.; Fratzl-Zelman, N.; Koller, K.; Klaushofer, K. J Bone Miner Res 1992, 7, 329-334.

(5) Tong, W.; Glimcher, M. J.; Katz, J. L.; Kuhn, L.; Eppell, S. J. Calci Tiss Int 2003, 72, 592-598.

(6) Jaeger, C.; Groom, N. S.; Bowe, E. A.; Horner, A.; Davies, M. E.; Murray, R. C.; Duer, M. J. Chem Mater 2005, 17, 3059-3061.

(7) Crick, R. E.; Editor. Origin, Evolution, and Modern Aspects of Biomineralization in Plants and Animals Plenum Press: New York, 1989.

(8) Aizenberg, J.; McKittrick, J. M.; Orme, C. A. Biological and Biomimetic Materials-Properties to Function. : San Francisco, 2002.

# CHAPTER 2.
# BONE, A BIOLOGICAL NANOCOMPOSITE

## 2.1 Introduction

A structure for mechanical support and enabling motion is needed by vertebrates. It is provided by the skeletal structure which is made up of bone material. Bone is a complex composite material made up primarily of a fibrous protein called collagen and a calcium phosphate mineral that resembles hydroxyapatite (called bioapatite). Bone also contains water which is extremely important for its mechanical properties. The process of bone formation is known as osteogenesis[1]. The first step is laying down the extracellular organic matrix (collagen) which is done by specialized cells known as osteoblasts. These cells then begin the process of mineralizing this collagen scaffolding and embed themselves into tiny lacunae in the mineralized matrix at which point they are called osteocytes. The cell processes are carried out via minute canals (canalicule) which permit the circulation of tissue fluids. To meet the requirements of growth as well as mechanical function, bone undergoes a continual and dynamic modeling process where by the old mineral is resorbed by cells called osteoclasts at a low pH $\approx$ 4 and redeposited by osteoblasts.

From the basic building blocks of collagen and bioapatite up to the macroscpic functional structure, there are many levels of hierarchy[2]. The basic precursor is the collagen I protein also known as protocollagen. Three strands of protocollagen combine to form the triple helical type I collagen[3]. The collagen molecules self assemble to form collagen fibrils that are then mineralized by the osteoblasts. In mature bone, the mineralized collagen fibrils arrange in layers (lamellae) to form lamellar bone. Bundles of lamellar bone jointly form the Haversian system which forms the macroscopic bone. The bone organ is hollow and filled with bone marrow. The ends of the bone have a different structure, where they are less dense

and more spongy. This is known as trabecular bone and its primary structural function is to act as a shock absorber. The ends of the bone are covered by a layer of soft and flexible tissue known as cartilage, which lubricates the motion of the joints, i.e. between the surfaces of two bones.

From the perspective of materials science, the answers to the following questions about bone are of interest:

1. What is the composition of the bioapatite?
2. What is the surface composition of the bioapatite particles?
3. What is the shape and size of the bioapatite nanoparticles?
4. How is the bioapatite distributed in the collagen matrix?
5. How does the collagen interact and bond with the bioapatite and which collagen residues are involved?
6. What does the bioapatite-collagen interface look like?
7. What role does water play?

**2.2 Composition of the bone mineral**

The structure and composition of the inorganic constituent of bone has been a subject of active discussion for over 150 years. Although the major ionic constituents of the bone mineral have been identified, the literature values quantifying them are a composite of fractional compositions from different specimens and different methods. While it is know that variety of factors for instance alteration of minerals in the diet can induce variations[4] in (the) composition, a reliable comprehensive compositional analysis has not been achieved. What is required is the study of a single uniform sample, by methods that are mutually compatible and do not alter the composition by unduly harsh processes.

### 2.2.1 Calcium and phosphate ions

The fact that bone mineral is some form of calcium phosphate has been known for a couple of centuries. In the past a variety of compositions have been proposed for example: $Ca_5H_2(PO_4)_4$, Brezelius (1845); $Ca_{10}(PO_4)_6CO_3$, Gassman (1937); $(Ca,-C)_{8\text{-}9+}[(P,C)O_4]_6$ $Ca(OH)_2$, Gruner, McConnel and Armstrong (1937); $Ca_{10}(PO_4)_6(OH)_2$, hydroxyapatite, Klement (1938) which is still widely considered a good approximation; a neutral compound containing carbonate, Logan (1938). The variety is highlighted by the fact that in the formula of Gruner et al., carbon is presented not only as a hypothetical $[CO_4]^{-4}$ group but also as $C^{+4}$ ions replacing $Ca^{2+}$ ions. Of course, these early methods relied on wet chemistry quantification methods that are subject to a variety of interpretations, but certainly they indicated that the bone mineral was primarily a compound of calcium and phosphorus. A variety of early accurate measurements[5-8] indicated minor substitutions of calcium by sodium and magnesium. The wet chemistry methods, however, could not be certain if there was a single phase or several phases; for example one of the formulations was of two distinct phases of $Ca_9(PO_4)_6(H_2O)_2$ and $CaCO_3$[9]. The question of the carbonate will be discussed later. Suffice it to say that the x-ray diffraction patterns indicated only a single phase, structurally similar to fluorapatite ($Ca_{10}(PO_4)_6F_2$), without any indication of the calcium carbonate, even by the sensitive birefringence tests[9].

The calcium to phosphorus ratio was determined by a variety of wet chemistry and ashing method and the Ca:P molar ratios were in the 1.67 range[9,10]. However, the fact that upon heating to 600 $^oC$, bone forms pyrophosphate, while heating to higher temperatures (800 $^oC$) produces $\beta$-$Ca_3PO_4$ indicates a calcium deficient system with the Ca:P ratio more in the 1.5 region[11]. The use of infrared (IR) vibration spectroscopy permitted a means of measurement whereby the mineral was not significantly altered by the process. The $\nu_1$ and $\nu_3$ $PO_4^{3-}$ contours in the 900-1200 $cm^{-1}$ range are assigned to apatitic phosphate and acid

phosphate ($HPO_4^{2-}$) environments[12]. Aditionally the $HPO_4^{2-}$ content and crystallinity has also been estimated from the $\nu_4$ $PO_4^{3-}$ spectral region (500-650 $cm^{-1}$) where a broad band centered between 530 and 540 $cm^{-1}$ is assigned to $HPO_4^{2-}$. In an IR study done on a wide variety of samples, it was concluded that the percentage of $HPO_4^{2-}$ decreased from ca. 40% to 25% of the total bone phosphate as the bone matured[13]. It should be noted however that the different IR frequencies are coupled and as a result very much broadened and overlapped. Determination of the contribution of the different components relies heavily on simulating the overlapping contours by curve fitting methods.

NMR spectroscopy is another method to identify the $PO_4^{3-}$ and $HPO_4^{2-}$ groups. Although both groups have the same chemical shift, $HPO_4^{2-}$ has a larger chemical shift anisotropy (CSA)[14]. Earlier NMR methods relied on combining lineshapes of hydroxyapatite, brushite, and type B carbonatoapatite to simulate the $^{31}P$ NMR lineshape of bone mineral[15] and concluded that approximately 5-10 % of the phosphates in bone were $HPO_4^{2-}$. However this was based on the assumption that the bone mineral consists of hydroxyapatite and brushite mineral phases. It is clear that this analysis is dependent on the crystallinity of the material and that a nanocrystalline phosphate with a protonated surface would have a very different lineshape that simply than that of the bulk crystalline model samples. In a more recent work[16], it was attempted to elucidate the $HPO_4^{2-}$ fraction by studying the $^1H$-$^{31}P$ cross polarization (CP) kinetics and fitting them to a composite of CP kinetics of hydroxyapatite, brushite and type B carbonatoapatite. However noting that the $T_2$ and $T_{1r}$ of the bone sample is markedly different from the synthetic model analogues, it was admitted that this method suffered from severe limitations. Attempts were made to identify $HPO_4^{2-}$ via $^1H$ detected $^1H$-$^{31}P$ NMR[14,17]. However on comparing the observed spectra with that of brushite, the characteristic $HPO_4^{2-}$ resonance at 10.6 ppm was not identified. There reasons for this being that the proton evolution was not under a homonuclear decoupling field and in cases where

single pulse $^{1}H$ NMR is used, the large water and collagen proton signal from the bone overwhelmed the smaller $HPO_4^{2-}$ resonance. It should be noted that a broad and low resonance at the expected chemical shifts can be observed in work done mentioned earlier[17], but it was directly overlapped by a spinning sideband from the $OH^-$ resonance and ignored.

### 2.2.2 Hydroxyl ions in the bone mineral

The presence of $OH^-$ ions in bone mineral has been the subject of a long debate. While the concentration of hydroxyl ion was determined as being 50% of that expected for hydroxyapatite by Vataserry et al.[18] on the basis of a Karl Fischer titration, it was later thought that this might actually be tightly bound water that is misrecognized[19] as hydroxyl groups. Attempts to detect the $OH^-$ moiety by IR[20-24] in a variety of bone and calcium deficient synthetic apatites, and initial attempts by NMR[25] found no clear indication of the hydroxide peak in their spectra, especially when contrasted with the very clear and unambiguous signal from hydroxyapatite. It was only in recent work by Cho et al.[17] using two dimensional $^{1}H$-$^{31}P$ correlation NMR that the $OH^-$ peak was identified. This was achieved because the $^{1}H$ resonances were indirectly detected via $^{31}P$ thereby selecting only those protons closely associated with the phosphate groups and reducing the spectral overlap from the collagen protons. The $OH^-$ concentration was estimated to be ca. 20% of the stoichiometric value.

### 2.2.3 Carbonate ions in the bone mineral

The presence of carbonate in bone has been detected since early on[10]. It is thought to be important in providing the necessary solubility to bioapatite crystals for continual resorption and deposition and also interferes with crystal growth because it leads to change in lattice dimensions and increased disorder[26]. However both its concentration and location in the bone mineral have been subject to a wide variety of opinions. $CO_3^{2-}$ can substitute for

$OH^-$ and $PO_4^{3-}$ in the apatite crystal and these are known as type A and type B carbonatoapatites[27]. The carbonate in bone measured by wet chemistry methods indicated that carbonate was about 3-5 % by weight of the bone minera[9,28]. Another way to determine carbonate content was by comparing the radial distribution function calculated from X-ray diffraction data of bone mineral and hydroxyapatite with varying amount of substituted carbonate[11]. This method too seemed to indicate that the carbonate was ca 3.5% by weight. Infrared spectroscopy technique to estimate carbonate percentage primarily depend on comparing carbonate absorption (1415 $cm^{-1}$) band to the phosphate absorption band (575 $cm^{-1}$)[29] and these methods give carbonate percentages of ca. 5%[26]. However the most important domain of the $CO_3^{2-}$ vibration frequencies (1400-1500 $cm^{-1}$) is obscured by the protein absorption bands in bone.

The location and the environment of the carbonate has also been a subject on debate and a variety of work has been done in this regard. Solid state $^{13}C$ MAS NMR was used to study carbonates in various locations in apatites[30]. The $CO_3^{2-}$ ions replacing $PO_4^{3-}$ or $OH^-$ give distinct chemical shifts. The carbonate was studied in enamel tissue which has a small organic content which overlaps the carbonate chemical shift regime. The primary species observed was the type B carbonatoapatite ($CO_3^2$ replacing $PO_4^{3-}$). A peak belonging to type A carbonatoapatite ($CO_3^{2-}$ replacing $OH^-$) was also observed but not confidently resolved from the noise. Additionally cross polarization was used to acquire the signal, which does not yield quantitative results. Infrared investigations on bone were carried out by studying the $CO_3^{2-}$ $\nu_2$ band (878-871 $cm^{-1}$) which was deconvoluted into three frequencies. The frequencies at 878 $cm^{-1}$ and 871 $cm^{-1}$ were assigned to type A and type B carbonatoapatites, respectively[31]. A shoulder at 866 $cm^{-1}$ was assigned to surface-adsorbed carbonate as its intensity decreases during bone maturation or in fast partial dissolution experiments in EDTA as compared to the 878 $cm^{-1}$ and 871 $cm^{-1}$ bands. Comparison of the ratios of the three bands

were done in enamel samples and indicated that the ratio of the type B carbonate to type A carbonate is ca. 1.1 and the ratio of surface carbonate to type B carbonate is ca. 0.4[32].

The limitation with the work done regarding the bone mineral carbonate is as follows.

1. There is no direct evidence that the carbonate is located in the apatitic phase. X-ray diffraction and circular dichroism would not work for nanoparticles of poorly formed calcium carbonate. Under the same conditions of poorly formed crystals, IR cannot distinguish between the carbonate in an apatite and in calcium carbonate (bands at 1430 $cm^{-1}$, 1795 $cm^{-1}$, 876 $cm^{-1}$)

2. The wet chemistry methods have inherent limitations in detecting the carbonate. This is because the bone matter has first to be deproteinated, a process which has been shown to affect the mineral even when mild methods are used[31].

3. The IR methods heavily rely on deconvoluting severely overlapping bands. Often the bands are very broad and with additional disorder-induced frequencies, which make the analysis difficult.

The primary deductions regarding bone composition, have been made by spectroscopic work done on enamel where larger crystal sizes and very reduced organic matrix help make the spectra more tractable. However, the composition of the bioapatite in bone and enamel are not the same; for instance, the hydroxide concentration in enamel is ~ 3 times larger than in bone.

**2.2 Shape and size of bone mineral**

The first indication of the nanoscale morphology of bone was seen in 1948 when Wolpers[33] using electron microscopy observed needle-shaped crystals, 3 to 6 nm wide and 40 to 100 nm long. There has been controversy over the shape and size of the bioapatite crystals

ever since. Robinson et al.[34] indicated hexagonal platelets with average dimensions of 50 nm by 25 nm and 10 nm thick. Schwarz et al.[35] concluded that the particles were spindle shaped. A variety of work using electron microscopy done up to 1957, led Spekman et al.[36] to indicate that the bioapatite crystallites were rod shaped about 5 nm thick and 60 to 70 nm long, with occasional lengths of 120 nm being observed. In 1957 studies by Finean *et al.*[37] using low angle x-ray scattering indicated that the scattering units were 20 nm by 40 nm in size but they did not indicated if these were platelets or rods. Fernandez-Moran *et al.*[38] noticed that while x-ray studies gave particle sizes of 4 to 7.5 nm wide and 20 nm long, the electron microscope studies were indicating particles of a variety of shapes and sizes. Their electron microscopy studies on a variety of samples indicated needle shaped particles of 4 nm diameter and 20 nm in length in dense areas of the samples while in thinner areas of the samples, flakes of 2 to 5 nm thickness and 30 to 50 nm in diameter were observed. Johansen *et al.*[39] saw plates ca. 3 nm x 20 nm x 100 nm in dimension when they looked at disaggrated crystals via transmission electron microscopy (TEM). Arsenault et al.[40] used a combination of TEM and x-ray diffraction to determine shape and size of the bioapatite crystals in calcified cartilage and cortical bone. Looking at ultramicrotomed sections of bone with TEM they saw rod shaped particles 4- to 5 nm wide and 30 to 80 nm long.

The line widths of x-ray powder diffraction peaks can also be used to calculate the particle size by the measuring the effect of finite size on the diffraction peak widths by applying the Scherrer equation:

$$d = \frac{K\lambda \ radian}{B_{1/2} \cos\theta}$$

where K is a constant, chosen as 0.9, λ is the x-ray wavelength, θ the diffraction angle, $B_{1/2}$ the full width at half maximum of the diffraction peaks and d is the dimension perpendicular the diffraction plane. Applying this equation to the 002 and 130 reflections, they obtained dimensions of ca. 6 nm x 6 nm x 17 nm. The discrepancy between SAXS and TEM

illustrates two points. The first is that although TEM is a direct measurement method, it cannot differentiate between individual crystals and crystal aggregates and in cases of aggregation there is spatial overprojection that contributes to seeing large crystal lengths and widths. Secondly for small crystals there is overlapping of the diffraction peaks and there are also thought to be effects from crystal stress and strain that give rise to peak broadening. Danilchenko *et al.*[40] attempted to separate the effects of lattice strain and finite size on the diffraction profile. Their method requires two peaks corresponding to different diffraction orders from the same plane that are not overlapped by any other peak. In the case of bone this is only observed for the plane perpendicular the c-axis, it the 002 and 004 peaks. They obtained lengths of ca. 18 nm for the long crystal axis. However there are no peaks in the other two dimensions that are suitable for this analysis. This method also requires assumption of the nature of total broadening effects β, i.e. whether it is Cauchy where $\beta^2 = \beta_{strain}^2 + \beta_{size}^2$ or Gaussian where $\beta = \beta_{strain} + \beta_{size}$. More importantly it is difficult to conceive of lattice strain in crystals that are only a few unit cells in dimension and have a very large surface area that can relax any residual strain in the crystal.

Fratzl *et al.*[41-44] carried out small angle x-ray scattering (SAXS) on a wide variety of bone samples to characterize the size, shape, and ordering of the bioapatite crystallites. In case of a system with low density of scattering particles, at low values of the scattering angle θ, defined within the parameter q, where

$$q = \frac{4\pi}{\lambda} \sin(\frac{\theta}{2})$$

the scattered intensity I(q) is dependent on the size and shape of the scattering particles. Thus for a variety of different shapes the following “rules” can be applied.

Spheres: $I(q) \approx q^{0}$

Long rods: $I(q) \approx q^{-1}$

Plates: $I(q) \approx q^{-2}$

Applying these rules to a variety of bones, Fratzl at al. concluded that the shape some bone mineral (eg. mouse femur) is cylindrical or needle-like while others (eg. turkey tendon) are plate like. However Schmidt-Rohr[45] has shown that these "rules" need to be applied with care especially when there is a high density of the scattering particles, such as in native bone. When the density of the scattering particles exceeds 25 volume % of the matrix, particle-particle correlation effects tend to make the rules invalid. For example, he showed that a densely packed system of "boards" (particles intermediate between plates and long rods) can give a 1/q dependence, especially at the smaller values of q. Fratzl et al. also applied an analytical treatment to determine the average crystal size T, of the bone nanocrystals. T, in case of long rods or "needles" would be their diameter. In case of plate it would be twice the thickness. For a given volume V and surface area S,

$$2T = \frac{4V}{S}$$

The spherically averaged scattering intensity I (q) can be defined as

$$I(q) = I_0 T^3 F(qT)(1+G(q))$$

Where F is a form factor characteristic for the shape of the mineral crystal and G(q) is the interference function between the centers of the crystals. For sharp interfaces the "Porod law" applies, for larger values of q, where the constant P is given by

$$P = (\frac{4\pi}{T})\int q^2 I(q)dq$$

with the approximation that $I(q) \approx P/q^4$, the value of T was determined assuming no interference (i.e. G(q) = 0) and suitable form factor ($F(q) \approx q^{-1}$ or $q^{-2}$ )for needles and plates. T values of 3.7 nm for turkey tendon and 3.1 nm, 3.4 nm, and 3.9 nm for mouse, rat and dog femur respectively, were reported[44]. However, Schmidt-Rohr[45] also pointed out that a treatment in terms of form and structure factors poses difficulties in densely packed systems (volume fraction of ca. 25% or higher in case of cylindrical scatterers). Indeed, the correlation peak that would be present at $q = 2\pi/T$ as per the treatment of Fratzl et al. is conspicuous by its absence[42]. The attempt to explain the absence of the correlation peak[41] results in a system with much lower apatite volume fraction[45] than in native bone.

The most recent attempts to directly visualize bioapatite crystallites was by Tong *et al.*[46] by atomic force microscopy (AFM). Isolated crystallites of bovine femurs that were observed on mica surfaces gave a mean thickness of 0.68 nm (this is for 98 % of the particles that had a thickness of 2 nm or less), 10 nm width and 15 nm length. The thickness is seemingly unphysical as it describes a dimension smaller that the unit cell. This is not consistent with the observed XRD of the bioapatite which would have the 212 diffraction peak exceptionally broadened which is not the case. Indeed it seems very unlikely that a crystal would grow several nanometers in two directions but essentially have no crystal growth in the third dimension. It is of interest to note that the process to obtain isolated crystallites is quite harsh (repeated boiling with hydrazine followed by plasma ashing). Although tests on model calcium phosphates under similar de-proteinating conditions showed no loss of mineral, it must be remembered that solubility is a size dependent quantity especially in the nanometer regime. It is quite likely that the harsh processing conditions stripped away the surface and indeed a significant portion of the crystallites. This also lends credence to our earlier claims about inaccurate determination of mineral composition via IR spectroscopy methods because the bone was often deproteinated by similarly harsh methods

to simplify the spectra. Thus in spite of a long history of investigation there is a need for a clear understanding of the crystal size and shape of the bone mineral.

**2.4 Distribution of bioapatite**

What is the arrangement of the bioapatite crystallites and the fibrillar collagen protein? Several models have been put forth primarily from TEM studies and later from SAXS investigations. From high voltage TEM analysis, Landis et al. proposed that the bioapatite crystals are primarily located in the staggered gaps formed during the self assembly of collagen fibrils[47]. However this is an unreasonable model as this does not account for the fact that the bioapatite makes up 40 % volume of the composite. Glimcher et al. also proposed that the basic structure of the collagen –bioapatite composite was of needle shaped crystals tens of nanometers long and ca. 2 nm crystals wide, located in the holes or gaps inside the collagen fibril[48] while Katz et al. suggested that at least 20-30% of the crystals were located either between the triple helical molecules or more likely outside the fibrils[49,50]. Weiner *et al.* based on TEM studies on individual mineralized collagen fibril from turkey leg tendon and asserted that plate shaped crystals (average size 50 nm x 25 nm) are arranged within the fibers in parallel layers with the interlayer distance of 4-5 nm. Looking at mouse femur bone which is simple due to a lack of the Haversian systems, they suggested a highly organized structure where the bioapatite crystals are uniformly distributed within the fibril and the fibrils themselves are arranged to be at an offset angle to one another and also rotated about their axis to give isotropic properties. The main limitation of this model is that in such an ordered system, one would see a correlation peak in the SAXS data at a q value of $4\pi/d$, where d is the interlayer distance, and this peak is absent.

Fratzl et al. interpreted the crystallite shape to be cylindrical in certain bones (e.g. dog femur) and based on the absence of a correlation peak proposed an arrangement with the

crystals being parallel along the c-axis but having no periodic spacing to explain the absence of a correlation peak[41]. However this model also has the drawback that it cannot account for the 40 % volume of the bioapatite. Indeed Schmidt-Rohr has shown that packing cylindrical rods at a 40 % volume fraction will enforce a correlation among the rods and produce a correlation peak in the SAXS intensity[45].

**2.5 Interaction between the bioapatite and collagen**

To form a strong composite material, there must be appropriate interaction between the components of the nanocomposite. Too weak an interaction and the composite will have little strength, while an excessively strong interaction would make it brittle. For example, it is known that change in the structure of type 1 collagen caused by a mutation in the COL1A1 or COL1A2 gene leads to types II, III and IV of *osteogenesis imperfecta* (brittle bone disease). It is thought that the altered structure causes a change in both the structure of the collagen fibril and the interaction between the collagen and the bioapatite. Therefore, understanding the nature of the interaction between collagen and bioapatite is important. Furthermore, it has been noted that a solution having the same concentration of mineral ions as natural body fluids has virtually no tendency to precipitate any mineral, which suggests the role of collagen in promoting mineralization. The interaction between the bioapatite and the collagen was initially inferred from Langmuir-Blodgett monolayer film experiments, where a film of alkyl chains terminated by COOH or $NH_2$ was immersed in simulated body fluid. Apatite particles were shown to form only on the COOH terminated films and not on the $NH_2$ terminated films[51]. This indicates that the COOH groups promoted the crystallization of apatite (in the deprotonated $COO^-$ state), acting as a binding site for $Ca^{2+}$ ions which would then serve to nucleate the apatite crystal. Based on this study, it was proposed that glutamic and aspartic amino acid residues, which have side chain structures of $CH_2CH_2COOH$ and $CH_2COOH$, respectively, were responsible for nucleating the apatite

crystals in bone. Jaeger *et al.*[52] investigated the collagen−apatite interface by solid state NMR measurements using the $^{13}C\{^{31}P\}$ rotational echo double resonance (REDOR)[53] method. They concluded that the carbon from the $COO^-$ group of the glutamate residue is at a distance of 0.24 nm from the surface phosphorus. Then however they claim the glutamate to be from a non-collagenous protein because the protein contains very little glutamate. Additionally they cite the non observance of concomitant dephasing of proline and hydroxyproline residues at 60 and 71 ppm in support of this hypothesis. We have noted however that their experiments were not run at optimal conditions, for instance 12.5 kHz MAS was used, which necessitates more recoupling pulses and the pulses were not compensated for pulse imperfections. Furthermore, their distance evaluation was based on a spin−pair approximation, which does not hold true as many $^{31}P$ dephase the $^{13}C$. This leads us to predict that the distance between the surface phosphate and the glutamate $COO^-$ is greater than proposed, and would also explain the relatively limited dephasing of the other residues. A comprehensive understanding of the interaction between the bioapatite and the collagen in bone is still lacking.

**2.6 Types of water in bone**

Water is an important structural component of bone. Indeed Currey[54] presents mineralized bone tissue as a ternary system of water, organic and mineral components. The mechanical response of bone is altered by the change in its hydration state, for example dry bone is much more brittle that wet bone[55], dry tendon is brittle but wet tendon is stretchy. Dehydrating the bone by a graded series of ethanol baths or replacing the water in bones with solvents of varying polarity had significant effects on the mechanical properties of bone[56]. To understand the role of water in bone, one must recognize that water exists in several different environments in bone.

*2.6.1. Unbound water.*

This is simply free bulk water of the body fluid surrounding bone. It maintains appropriate pH and ionic concentrations for the processes of mineralization and continual remodeling of bone to occur, and carries the various nutrients necessary for the osteoblast and osterclast cells that inhabit bone tissue.

*2.6.2 Structurally bound water in the collagen.*

A significant quantity of water present in bone functions to hydrate the collagen itself. Ramachandran et al. suggested that the water molecule might serve as a possible hydrogen bonding linkage between a set of NH and CO groups holding neighboring chains in the triple helix together by secondary valence linkages occurring regularly at intervals of about 3 Å along the length of the protofibril[57]. It is thus thought to assist in the self−assembly of the collagen triple helix. A variety of measurements[58-62] indicate that the structure of water in the collagen is very different from bulk water, by the fact that it has restricted mobility and asymmetric orientation. Studies have also shown that the hydroxyproline (Hyp) plays a critical role in stabilizing the triple helix via hydrogen bonding[63]. But it is clear from fiber diffraction data that the Hyp hydroxyl group cannot form direct hydrogen bonds with peptide CO groups in the same chain, neighboring chain or the chains of a neighboring molecule. This also contributed to the idea that the Hyp stabilized the molecule via intramolecular water bridges.

*2.6.3 Water layer on the bioapatite surface.*

Wilson et al.[64] applied a 2D Lee-Goldberg CP scheme to detect the apatite protons on

bone samples that had been dried for varying amounts of time. As a function of the CP time, the $^{1}H$ intensity at the water frequency was an oscillatory function overlaying an exponential. The exponential behavior was attributed to the disordered water and the oscillatory behavior to ordered water. As the oscillatory behavior was seen only at a certain level of hydration, they proposed a model where at full hydration there was bulk water and an ordered layer at bioapatite surface. Upon dehydration, the bulk water is first removed, giving only the oscillatory behavior from ordered water layer. Further dehydration irreversibly depletes the ordered water layer and the signal again becomes exponential a function of the CP time. However this model does not consider the fact that the bioapatite surface has significantly protonated phosphates ($HPO_4^{2-}$) which cross polarized to the $^{31}P$ nuclei in the bioapatite and that the mobile water molecules have a short $T_{1\rho}$ and would not give much signal beyond 1 ms of CP. They also do not consider the fact that nanocystalline apatite surfaces hold on to water strongly. Indeed, our measurements show that even after very significant drying, a layer of mobile water is present. Sukhodub et al.[65] investigated the hydration of collagen and mineralized collagen by piezogravimetry and IR and Raman spectroscopy. They saw that mineralized collagen had reduced water absorption. Additionally, the shifts and reduction in IR intensities as a function of hydration were less in mineralized collagen than in the unmineralized collagen. On this basis they proposed two kinds of water, one that surrounds the collagen and an other in the gap regions between the collagen molecules. Mineralization reduces water absorption because there bioapatite fills the gap region. This is a fundamentally wrong assertion because at 40 vol. % the bioapatite must certainly cover the collagen surface as well and not be located only in the gap regions. Our experiments have shown several other types of water especially between the bioapatite and collagen.

*2.6.4. Water within the bioapatite*.

It has been have suggested that octacalcium phosphate (OCP, $Ca_8H_2(PO_4)_6.5H_2O$) might form a smooth epitaxic interface with hydroxyapatite and is proposed to be the initial precipitate that transforms into an apatite by hydrolysis, and acts as a template for the epitaxic overgrowth of hydroxyapatite[66]. As such, the waters of crystallization that are associated with the OCP layer would be present in the crystal. Additionally Wilson et al.[67] by looking at $^1$H NMR of deproteinated bone samples heated to various temperatures noted that some of the water did not come off even at temperatures of 225 $^o$C. They concluded that this must be from structural water in the bioapatite crystal and proposed that the water is in two distinct locations created by substitutions and defects in the crystal lattice and stabilize the vocal structure by forming hydrogen bonding bridges between surrounding ions. However the following points must be considered. Posner et al.[68] measured the strong interaction between the bioapatite and water and pointed out that the heat of adsorption of water on bone mineral is 23 kcal/mol at the minimal coverage (one water layer) but does not approach the heat of vaporization of water (11 kcal/mol) until two monolayers are adsorbed. Secondly, the bioapatite has a much larger surface area (due to its nanocrystalline size) than the carbonatoapatite used as a model compound in the study. The large bone mineral surface is extremely hygroscopic for the first two layers of water and could easily have adsorbed moisture from the atmosphere during transfer to the rotor. Indeed we have observed that hydroxyapatite even when packed in NMR rotors and kept in a desiccator, over time does show an increase in the adsorbed water.

**2.7 Conclusions**

A clearer understanding of many aspects of the structure of bone on the 10 nm scale , even though they have been studied for many years is still needed. These insights can be

expected to have a significant impact in a variety of fields, from human health and nutrition to bioengineering and materials science.

The many opinions regarding the composition or size of the bioapatite crystals, the collagen−bioapatite interface and the interaction between the organic moieties and the inorganic apatite need to be investigated in a comprehensive study that addressess the misconceptions prevalent in the literature.

**References**


1. Kierszenbaum, A. L. Histology and cell biology : an introduction to pathology Mosby Elsevier: Philadelphia, PA, 2007.
2. Rho, J. Y.; Kuhn-Spearing, L.; Zioupos, P. *Med Eng Phys* 1998, 20, 92-102.
3. Ramachandran, G. N. *Int J Peptide Protein Res* 1988, 31, 1-16.
4. Sobel, A. E.; Rockenmacher, M.; Kramer, B. *Journal of Biological Chemistry* 1945, 159, 159-171.
5. Logan, M. A. *J Biol Chem* 1935, 110, 375-389.
6. Burns, C. M.; Henderson, N. *Biochem J* 1936, 30, 1207-1214.
7. Marek, J.; Wellmann, O.; Urbanek, L. *Z Physiol Chem.* 1935, 234, 165-175.
8. Klement, R. *Naturwissenschaften* 1938, 26, 145-152.
9. Hendricks, S. B.; Hill, W. L. *PNAS* 1950, 36, 731-737.
10. Hendricks, S. B.; Hill, W. L. *Science* 1942, 96, 255-257.
11. Betts, F.; Blumenthal, N. C.; Posner, A. S. *J Crystal Growth* 1981, 53, 63-73.
12. Paschalis, E. P.; DiCarlo, E.; Betts, F.; Sherman, P.; Mendelsohn, R.; Boskey, A. L. *Calc Tiss Int* 1996, 59, 480-487.

13. Miller, L. M.; Vairavamurthy, V.; Chance, M. R.; Mendelsohn, R.; Paschalis, E. P.; Betts, F.; Boskey, A. L. *Biochim et Biophys Acta* 2001, 1527, 11-19.

14. Kolodziejski, W. *Top Curr Chem* 2005, 246, 235-270.

15. Roufosse, A. H.; Aue, W. P.; Roberts, J. E.; Glimcher, M. J.; Griffin, R. G. *Biochemistry* 1984, 23, 6115-6120.

16. Kaflak-Hachulska, A.; Samoson, A.; Kolodziejski, W. *Calc Tiss Int* 2003, 73, 476-486.

17. Cho, G.; Wu, Y.; Ackerman, J. L. *Science* 2003, 300, 1123-1127.

18. Vatassery, G. T.; Armstrong, W. D.; Singer, L. *Calc Tiss Res* 1970, 5, 183-188.

19. Biltz, R. M.; Pellegrino, E. D. *Calc Tiss Res* 1971, 7, 259-263.

20. Pasteris Jill, D.; Wopenka, B.; Freeman John, J.; Rogers, K.; Valsami-Jones, E.; van der Houwen Jacqueline, A. M.; Silva Matthew, J. *Biomaterials* 2004, 25, 229-238.

21. Berry, E. E. *J Inorg Nucl Chem* 1967, 29, 1585-1590.

22. Termine, J. D.; Eanes, E. D.; Greenfield, D. J.; Nylen, M. U.; Harper, R. A. *Calc Tiss Res* 1973, 12, 73-90.

23. Termine, J. D.; Lundy, D. R. *Calc Tiss Res* 1973, 13, 73-82.

24. Blumenthal, N. C.; Posner, A. S. *Calc Tiss Res* 1973, 13, 235-243.

25. Rey, C.; Miquel, J. L.; Facchini, L.; Legrand, A. P.; Glimcher, M. J. *Bone* 1995, 16, 583-586.

26. Ou-Yang, H.; Paschalis, E. P.; Mayo, W. E.; Boskey, A. L.; Mendelsohn, R. *J Bone Miner Res*, 16, 893-900.

27. Labarthe, J. C.; Bonel, G.; Montel, G. *Comptes Rendus des Seances de l'Academie des Sciences, Serie C: Sciences Chimiques* 1971, 273, 349-351.

28. Armstrong, W. D.; Singer, L. *Clin Orthop Relat Res* 1965, 38, 179-190.

29. Featherstone, J. D. B.; S.Pearson; LeGeros, R. Z. *Caries Research* 1984, 18, 63-66.

30. Beshah, K.; Rey, C.; Glimcher, M. J.; Schimizu, M.; Griffin, R. G. *J Solid State Chem* 1990, 84, 71-81.

31. Rey, C.; Collins, B.; Goehl, T.; Dickson, I. R.; Glimcher, M. J. *Calcified Tiss Int* 1989, 45, 157-164.

32. Rey, C.; Renugopalakrishnan, V.; Shimizu, M.; Collins, B.; Glimcher, M. J. *Calcified Tiss Int* 1991, 49, 259-268.

33. Wolpers, C. *Grenzgebiete Med.* 1949, 2, 527.

34. Robinson, R. A. *J. Bone & Joint Surg.* 1952, 34A, 389-435,476.

35. Schwarz, W.; Pahlke, G. *Z Zellforsch Mikrosk Anat* 1953, 38, 475-487.

36. Speckman, T. W.; Norris, W. P. *Science* 1957, 126, 753.

37. Finean, J. B.; Engstrom, A. *Biochim Biophys Acta* 1957, 23, 202.

38. Fernandez-Moran, H.; Engstrom, A. *Biochim Biophys Acta* 1957, 23, 260-264.

39. Johansen, E.; Parks, H. F. *J. Biophy. Biochem. Cyt.* 1960, 7, 743-745.

40. Danilchenko, S. N.; Kukharenko, O. G.; Moseke, C.; Protsenko, I. Y.; Sukhodub, L. F.; Sulkio-Cleff, B. *Crystal Research and Technology* 2002, 37, 1234-1240.

41. Fratzl, P.; Fratzl-Zelman, N.; Klaushofer, K.; Vogl, G.; Koller, K. *Calcif Tissue Int* 1991, 48, 407-413.

42. Fratzl, P.; Groschner, M.; Vogl, G.; Plenk, H., Jr.; Eschberger, J.; Fratzl-Zelman, N.; Koller, K.; Klaushofer, K. *J Bone Miner Res* 1992, 7, 329-334.

43. Fratzl, P.; Paris, O.; Klaushofer, K.; Landis, W. J. *Journal of Clinical Investigation* 1996, 97, 396-402.

44. Fratzl, P.; Schreiber, S.; Klaushofer, K. *Connect Tissue Res* 1996, 34, 247-254.

45. Schmidt-Rohr, K. *J Appl Crystallogr* 2007, 40, 16-25.

46. Tong, W.; Glimcher, M. J.; Katz, J. L.; Kuhn, L.; Eppell, S. J. *Calci. Tiss. Int.* 2003, 72, 592-598.

47. Landis, W. J.; Hodgens, K. J.; Arena, J.; Song, M. J.; McEwen, B. F. *Microsc Res Tech* 1996, 33, 192-202. .

48. Glimcher, M. J. *Philos T R Soc B* 1984, 304, 479-508.

49. Katz, E. P.; Li, S.-T. *J Mol Biol* 1973, 80, 1-15.

50. Lees, S.; Prostak, K. *Connect Tissue Res* 18, 41-54.

51. Sato, K.; Kumagai, Y.; Tanaka, J. *J Biomed Mater Res* 2000, 50, 16-20.

52. Jaeger, C.; Groom, N. S.; Bowe, E. A.; Horner, A.; Davies, M. E.; Murray, R. C.; Duer, M. J. *Chem. Mater.* 2005, 17, 3059-3061.

53. Gullion, T.; Schaefer, J. *J. Magn. Reson.* 1989, 81, 196-200.

54. Currey, J. The Mechanical Adaptations of Bone; Princeton University Press: Princeton, NJ, 1984.

55. Sedlin, E. D.; Hirsch, C. *Acta Orthop Scand* 1966, 37, 29-48.

56. Bembey, A. K.; Bushby, A. J.; Boyde, A.; Ferguson, V. L.; Oyen, M. L. *J Mater Res* 2006, 21, 1962-1968.

57. Ramachandran, G. N.; Chandrasekharan, R. *Biopolymers* 1968, 6, 1649-1658.

58. Berendsen, H. J. C.; Migchelsen, C. *Ann NY Acad Sci* 1965, 125, 365-379.

59. Grigera, J. R.; Berendsen, H. J. C. *Biopolymers* 1979, 18, 47-57.

60. Nomura, S.; Hiltner, A.; Lando, J. B.; Baer, E. *Biopolymers* 1977, 16, 231-246.

61. Cusack, S.; Lees, S. *Biopolymers* 1984, 23, 337-351.

62. Peto, S.; Gillis, P.; Henri, V. P. *Biophys J* 1990, 57, 71-84.

63. Bella, J.; Brodsky, B.; Berman, H. M. *Structure* 1995, 3, 893-906.

64. Wilson, E. E.; Awonusi, A.; Morris, M. D.; Kohn, D. H.; Tecklenburg, M. M. J.; Beck, L. W. *J Bone Min Res* 2005, 20, 625-634.

65. Sukhodub, L. F.; Moseke, C.; Sukhodub, L. B.; Sulkio-Cleff, B.; Maleev, V. Y.; Semenov, M. A.; Bereznyak, E. G.; Bolbukh, T. V. *J Mol Struct* 2004, 704, 53-58.

66. Fernandez, M. E.; Zorrilla-Cangas, C.; Garcia-Garcia, R.; Ascencio, J. A.; Reyes-Gasga, J. *Acta Crystallogr A* 2003, B59, 175-181.

67. Wilson, E. E.; Awonusi, A.; Morris, M. D.; Kohn, D. H.; Tecklenburg, M. M. J.; Beck, L. W. *Biophys J* 2006, 90, 3722-3731.

68. Posner, A. S. *J Biomed Mater Res* 1985, 19, 241-250.

# CHAPTER 3.
# DETERMINING THE THICKNESS OF THE BIOAPATITE NANOPARTICLES IN BONE

*Includes excerpts from:* Schmidt-Rohr, K. Rawal, A. Fang X-W. "A new NMR method for determining the particle thickness in nanocomposites, using $T_{2,H}$-selective X{$^1$H} recoupling", *Journal of Chemical Physics* **2007**, 126, 504701-504716

## ABSTRACT

A new nuclear magnetic resonance (NMR) approach for characterizing the thickness of bioapatite nanocrystals in bone is presented. The particle thickness is probed using the strongly distance-dependent dipolar couplings between the abundant protons in the organic phase and $^{31}$P nuclei in the biopatite phase. This approach requires pulse sequences with heteronuclear dephasing only by the polymer or surface protons that experience strong homonuclear interactions, but not by dispersed OH in the inorganic phase, which have long transverse relaxation times $T_{2,H}$. This goal is achieved by HeteronucleAr Recoupling with Dephasing by Strong Homonuclear Interactions of Protons (HARDSHIP). The pulse sequence alternates heteronuclear recoupling for ~0.15 ms with periods of homonuclear dipolar dephasing that are flanked by canceling 90$^o$ pulses. The heteronuclear evolution of the long-$T_{2,H}$ protons is refocused within two recoupling periods, so that $^1$H spin diffusion cannot significantly dephase these coherences. For the short-$T_{2,H}$ protons of a relatively immobile organic matrix, the heteronuclear dephasing rate depends simply on the heteronuclear second moment. The thickness of apatite nanocrystals in bovine and avian cortical bones was determined by this method. Additionally, wide angle x-ray- diffraction patterns of the bioapatite particles were simulated. Based on the measurements, a revised model of the mineralized collagen fibril is presented.

### 3.1 Introduction

The load-bearing material of bone consists of bioapatite nanocrystals in a collagen matrix. Electron microscopy and scattering methods can provide information on the spacings of the bioapatite particles and on some of their dimensions. However, electron microscopy is unable to differentiate between individual nanocrystals and particles that have aggregated, resulting in a wide variation of results for the particle sizes. For probing spatial variations in nanoparticle composition, the interfacial structure, and other features on the 1-nm scale, however, solid-state nuclear magnetic resonance (NMR) holds the most promise.

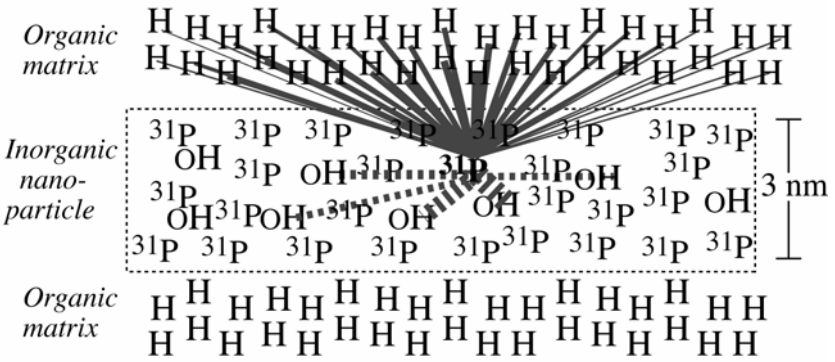


**FIG. 1.** Principle of thickness measurement of inorganic particles in organic-inorganic nanocomposites based on $^{1}$H-X dipolar couplings. The dephasing of X-nuclei ($^{31}$P in this picture) in the inorganic particles by $^{1}$H in the organic matrix depends strongly on their distance from the interface with the organic matrix. X{$^{1}$H} HARDSHIP NMR eliminates dephasing by protons in the inorganic phase (dashed lines); thus, fast dephasing proves a large fraction of X nuclei near the interface, i.e. thin particles (< 2 nm), while slow but observable dephasing on a 10-ms time scale indicates greater particle thickness (up to ~ 10 nm for phosphates).

In this chapter we discuss a new NMR approach for probing the thickness of the bioapatite nanoparticles and the distances of their component ions or atoms from the organic-inorganic interface. It takes advantage of the strongly distant-dependent dipolar couplings (~ $1/r_{HX}^{3}$) between the abundant protons in the organic phase and NMR-active X-nuclei ($^{31}$P, $^{29}$Si, $^{13}$C, $^{27}$Al, $^{23}$Na, etc.) in the inorganic phase, as shown schematically in Fig. 1. Under standard magic-angle spinning (MAS) conditions, these interactions can be recoupled by X{$^{1}$H} rotational-echo double resonance (REDOR) NMR [1] or its continuous-wave

alternatives, [2] all of which use radio-frequency irradiation to interfere with the time averaging of the dipolar couplings by magic angle spinning.[3] However, such recoupling alone is usually not sufficient for nanoparticles thickness measurements, since interfering couplings to OH and $H_2O$ protons inside the inorganic particles are often dominant.

Therefore, we have developed a pulse sequence that refocuses the undesirable couplings within the inorganic phase while retaining heteronuclear dephasing by the organic-matrix protons. X{$^1$H} HeteronucleAr Recoupling with Dephasing by Strong Homonuclear Interactions of Protons (HARDSHIP) NMR relies on the difference in the $T_{2,H}$ relaxation times of the dilute, long-$T_{2,H}$ inorganic protons and the short-$T_{2,H}$ organic-matrix protons. The pulse sequence alternates X{$^1$H} REDOR heteronuclear recoupling with periods of homonuclear dipolar dephasing that are flanked by canceling $90^o$ pulses, as indicated in Fig. 2. The heteronuclear evolution of the long-$T_{2,H}$ protons is refocused after two recoupling periods; this is confirmed experimentally in hydroxyapatite, a calcium phosphate containing $OH^-$ ions, and hectorite clay, a layered silicate with inner OH groups. For the short-$T_{2,H}$ protons in the matrix, the heteronuclear-dephasing rate in the HARDSHIP experiment depends simply on the heteronuclear second moment, but not on the homonuclear interactions,[4] even though no homonuclear decoupling is applied. The detailed simulation procedure has been described elsewhere[4] and its accuracy tested by experiments on ~1-nm thick silicate sheets in clay-polymer nanocomposites, on ~4-nm diameter nanodiamond with protonated surfaces, and on bioapatite nanocrystals in bone.[4] The pulse sequence is designed such that in the end it produces simple exponential heteronuclear dephasing without effects of homonuclear interactions. Since the HARDSHIP experiment does not require homonuclear multiple-pulse decoupling, it is relatively simple to set up and run.

## 3.2 Experimental

### *3.2.1 Samples.*

Hectorite clay, SHCa-1, was obtained from the Source Clay Minerals Repository. Five gram of clay was dispersed in 200 ml of de-ionized water, using mechanical stirring and then ultrasonication for 5 min. A pair of disc shaped Nd-Fe-B permanent magnets was used to extract the magnetic impurities from the suspension. [5] The supernatant was decanted off, dried in an oven, heated to 570 K for 2 days to remove residual water, and finally mechanically powdered. Before the NMR experiments, the clay was heated at 470 K for a week.

Polymer-hectorite nanocomposites were prepared using 90 and 10 mass % of poly(vinylalcohol) (PVOH) and hectorite clay, respectively. First, the clay was dispersed in water by ultrasonication, then PVOH was added the mixture ultrasonicated. Pulses of 20 s on and 20 s off were used until PVOH was completely dissolved. Low heat was applied during ultrasonication to swell the polymer until a viscous gel was obtained. After ultrasonication, the gel was dried in a vacuum oven at 310 K for several days.

Standard hydroxyapatite, $Ca_{10}(PO_4)_6(OH)_2$, was purchased from NIST and kept in a desiccator before use to prevent absorption of water. Avian and bovine bone were extracted from the mid sections of femur bones from a mature hen and a 4 year old cow. The surface was cleaned with a scalpel to remove muscle tissue and then washed with a solution of methanol and chloroform to remove lipids. The bone was ground to a powder and lyophilized to remove any traces of solvent and water.

*3.2.2 NMR parameters.*

The NMR experiments were performed using a Bruker DSX400 spectrometer at 400 MHz for $^{1}H$, 162 MHz for $^{31}P$, 100 MHz for $^{13}C$, and 79 MHz for $^{29}Si$. A Bruker 2.5-mm double-resonance magic-angle spinning (MAS) probe head was used for the 13-kHz MAS experiments, while the 6.5-kHz MAS experiments were performed with larger 7-mm sample rotors in a different Bruker double-resonance probe head. The $90^{o}$ pulse lengths were approximately 4 μs in the 7-mm probe head, and 2.8 μs in the 2.5-mm probe head. The samples filled the coil approximately from end to end. All experiments were performed with direct-polarization (DP) for equal excitation of all X-nuclei regardless of their distance from the nearest protons. Recycle delays were 60 s for the clay silicate, 20 s for nanodiamond (which contains unpaired electrons that drive $T_{1,C}$ relaxation on the < 1 s time scale), and 300 s for the phosphates (where $^{31}P$ spin diffusion homogenizes the magnetization over ~ 1 nm on a 10-s scale). Proton decoupling during detection was applied with two-pulse phase modulation (TPPM).[6]

*3.2.3 Special HARDSHIP set-up.*

It is advisable to characterize the protons in the nanocomposite before running HARDSHIP experiments. Most importantly, one should measure the $^{1}H$ spectrum of the inorganic phase and then set its main proton peak on resonance during the HARDSHIP experiment, since the $^{1}H$ $180^{o}$ pulses intended to refocus off-resonance transverse I-coherence work sufficiently well only in strictly center-packed samples. Such center-packing is certainly feasible for phosphates, due to the strong $^{31}P$ signal intensity. In performing the $^{1}H$ spectroscopy, $T_{2,H}$ filtering of the $^{1}H$ signal may be useful to eliminate the usually

dominant matrix-proton signal and selectively observe the inorganic protons. In phosphates, $^{1}H\{^{31}P\}$ REDOR can also be used to this purpose.

HARDSHIP usually works best at intermediate spinning frequencies (6 – 13 kHz). On the one hand, faster spinning favorably lengthens the $T_{2,H}$ relaxation time of the inorganic protons. On the other hand, at higher spinning frequencies dephasing of matrix protons during $2t_r$ may be incomplete. It may be useful to measure the $^{1}H$ dephasing of the various protons, in simple spin-echo and delayed-acquisition experiments, before choosing the optimum spinning frequency and homonuclear dephasing time. The $^{1}H$ 180° pulse length should be confirmed on the nanocomposite of interest in double-resonance set-up, using the null-condition of the cross polarized intensity.

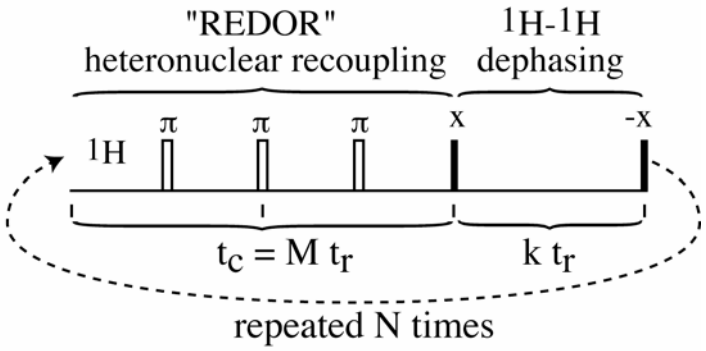


**FIG. 2.** Basic cycle of the proton pulses in the HARDSHIP pulse sequence. Heteronuclear recoupling by one 180° (π) pulse every half rotation period ($t_r/2$), as in REDOR,[5] alternates with dephasing of transverse $^{1}H$ (I-spin) coherence flanked by 90° pulses (filled rectangles) of opposite phases. Heteronuclear recoupling for M = 2 rotation periods is shown; M = 1, i.e. with a single 180° (π) pulse at $t_r/2$, is also commonly used in HARDSHIP experiments.

### 3.3 Theory of HARDSHIP

The basic building block of the HARDSHIP pulse sequence is shown in Fig. 2. It combines recoupling of heteronuclear interactions by 180° $^{1}H$ pulses, as in REDOR, with 90°

$^1$H pulses that first generate transverse $^1$H coherences and later restore long $T_{2,H}$-components to the z-direction. As will be discussed in more details below, these 90$^o$ pulses serve two purposes: (i) They terminate REDOR before $^1$H-$^1$H coupling effects (long-range spin diffusion, see below) become significant; this greatly simplifies the analysis and simulation of HARDSHIP curves. (ii) They dephase short-$T_{2,H}$ $^1$H coherences of the organic matrix while retaining the long-$T_{2,H}$ coherences so that the next REDOR period refocuses them. The treatment of the multi-spin system and the different evolution of long- and short-$T_{2,H}$ proton coherences are discussed in the following.

### *3.3.1 Heteronuclear Recoupling and Homonuclear Couplings*

While the HARDSHIP experiment is not particularly difficult to set up and run, the multi-spin system to analyze is rather complex at first sight. Heteronuclear couplings, with a Hamiltonian $H_{IS}$, act simultaneously with strong homonuclear interactions of protons, $H_{II}$.[7] All dipolar couplings are time-dependent due to magic-angle spinning. However, a number of specific experimental observations have been made that indicate under what conditions the spin system is tractable:

(i) Strong homonuclear $^1$H-$^1$H couplings do not prevent refocusing of very weak heteronuclear couplings into rotational echoes by sufficiently fast MAS.

(ii) In contrast, strong $^1$H-$^1$H homonuclear couplings do prevent refocusing of strong heteronuclear couplings by MAS; it is well known that in the absence of $^1$H irradiation, no rotational echoes are observed for $^{13}$C-H groups.

(iii) Even strong $^1$H-$^1$H homonuclear couplings do not truncate weak heteronuclear couplings to zero, and they do not prevent recoupling of weak heteronuclear couplings by 180$^o$ pulses on $^1$H.[8]

*3.3.1.1 I-S Recoupling by I-pulses.*

For an I-S REDOR-type experiment without I-I decoupling, heteronuclear recoupling is achieved by applying an I-spin $180^o$ pulse every $t_r/2$. Since the I-I couplings are unaffected by the $180^o$ pulse, its effect can be treated simply as a sign change of heteronuclear Hamiltonian, $H_{IS}(t')$, every half rotation period. The evolution of a X-H (SI) spin pair under the REDOR pulse sequence can then be written. Here a X-nucleus coupled only to an isolated $^1H$ in the inorganic crystal will exhibit this behavior. After the first half of the selection period (the "excitation" period $t_c = Mt_r$), the heteronuclear dipolar interaction has converted the X-spin (S) magnetization into two-spin coherence [1,9]

$$\rho(Mt_r) = S_x \cos(2M\Phi) + 2\, S_y\, I_z \sin(2M\Phi) \qquad (1)$$

Let us first consider a regular REDOR sequence for reference. With one $180^o$ pulse every half rotation period, heteronuclear dipolar evolution continues and yields

$$\rho(2Mt_r) = S_x \cos(4M\Phi) + 2\, S_y\, I_z \sin(4M\Phi) \qquad (2)$$

However with one $180^o$ pulse less at time $Mt_r$ (or two canceling $90^o$ pulses in the case of HARDSHIP), the sign of the second term in Eq. (1) is inverted, and

$$\rho_r(Mt_r) = S_x \cos(2M\Phi) - 2\, S_y\, I_z \sin(2M\Phi) \qquad (3)$$

reconverts to form an echo

$$\rho_r(2Mt_r) = S_x\, (\cos^2(2M\Phi) + \sin^2(2M\Phi)) = S_x \qquad (4)$$

i.e. the full signal is recovered by this refocusing of the recoupling. This effect will be used to remove heteronuclear dephasing by long-$T_{2,H}$ protons in the HARDSHIP experiment, see Eq.(9) below.

*3.3.1.2 Homonuclear effects: Spin diffusion.*

We now need to consider one S spin coupled to K I-spins $I_1...I_M$, which are also coupled by strong I-I interactions. Given the multi-spin nature of the problem, any simple treatment will have to be approximate and has been covered in detail in[4]. The evolution is evaluated in time steps of duration $t_c$, which usually equals $Mt_r$ and the heteronuclear and homonuclear couplings are treated sequentially.

Extending the REDOR calculation from the case of the spin pair, Eq. (1) by the successive application of the K commuting SI-spin propagators of the recoupled heteronuclear interaction produces

$$\rho(Mt_r) = S_x \Pi_n \cos(2M\Phi_n) + 2\, S_y \Sigma_n I_{z,n} \sin(2M\Phi_n) \Pi_{k\neq n} \cos(2M\Phi_k)$$
$$- 4\, S_x \Sigma_{n,m} I_{z,n} I_{z,m} \sin(\Phi_n) \sin(2M\Phi_m) \Pi_{k\neq n,m} \cos(2M\Phi_k)$$
$$- 8\, S_y \Sigma_{n,m,j} I_{z,n} I_{z,m} I_{z,j} \sin(2M\Phi_n) \sin(2M\Phi_m)$$
$$\sin(2M\Phi_j) \Pi_{k\neq n,m,j} \cos(2M\Phi_k) + ... \qquad (5)$$

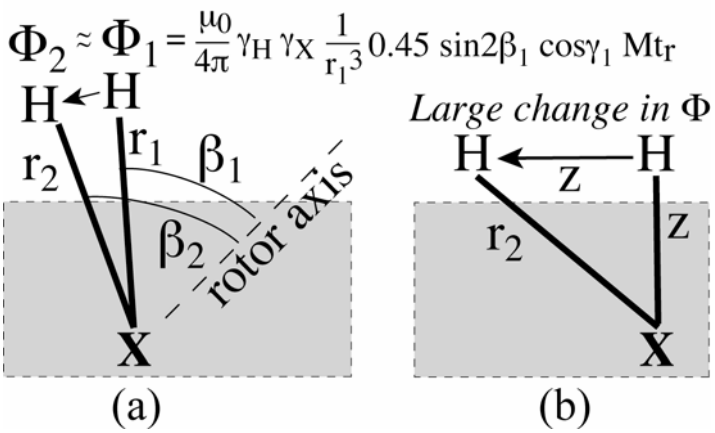


**FIG. 3.** Schematic representation of spin diffusion between nearby matrix protons coupled to a distant X-nucleus in the inorganic phase. (a) When the two X-H vectors are similar in length $r_n$ and orientation ($\beta_n$, $\gamma_n$), then the X-$H_n$ couplings and the corresponding phases $\Phi_n$ do not differ much. (b) A significant change in the heteronuclear phase $\Phi_n$ and resulting interference with heteronuclear recoupling occurs after $^1$H spin diffusion to protons at distances approximately equal to the heteronuclear distance z in question.

The evolution of $I_{zn}$ can be best understood by considering the evolution of $I_z$ magnetization under strong homonuclear couplings $H_{II}(t')$, it is well established that spin exchange, or spin diffusion,[9,10] occurs under these conditions, with $\Sigma_n I_{z,n}$ being a conserved quantity since $[H_{II}, \Sigma_n I_{z,n}] = 0$. [9] After a certain spin-diffusion time $t_{SD}$, the change in the coefficients of the heteronuclear coherences results in a significant change in the heteronuclear dephasing behavior. In the HARDSHIP experiment, we avoid this effect by choosing $t_c < t_{SD}$.

*3.3.1.3 The spin diffusion time $t_{SD}$.*

Not every spin exchange from $I_{zn}$ to $I_{zm}$ changes the heteronuclear dephasing. What is required is a significant change in the phase Φ, i.e. in the heteronuclear dipolar couplings of S to $I^{(n)}$ versus S to $I^{(m)}$. This can be seen in a calculation for a model three-spin system of an S-spin coupled to two I-spins, see Fig. 3(a). It has been determined that for $\Phi_1 \approx \Phi_2$ even

complete spin exchange does not change the density operator in a REDOR period of the HARDSHIP experiment significantly and the effect that defines $t_{SD}$ has not occurred. Only if $\Phi_1$ and $\Phi_2$ are sufficiently different will the dephasing be affected. These considerations show that $t_{SD}$ is the time within which $^1$H spin diffusion transfers the $I_z$-coherence to protons with significantly different heteronuclear coupling strengths. The change can arise from the orientation- or distance-dependent parts of the heteronuclear coupling. The I-I spin diffusion distance required to achieve this significant change is comparable to the S-I distance $r_{IS}$. This is indicated in Fig. 3(b). With the spin diffusion coefficient D, which is ~ 0.3 nm$^2$/ms on sub-nm length scales for rigid solids,[11] we can write

$$4\,D\,t_{SD} = r^2_{IS} \quad \text{or} \quad t_{SD} = r^2_{IS} / (4D) \tag{6}$$

For an S-spin at a depth of $r^2_{IS}$ = 1 nm, Eq. (6) gives $t_{SD}$ = 0.8 ms. This is an approximation, but fortunately the exact value does not affect depth measurements in the HARDSHIP experiment, which only requires $t_{SD} > t_c$. In contrast, $t_{SD}$ would be needed for simulations of REDOR data (acquired with a standard REDOR recoupling sequence without 90$^o$ pulses), which is a serious disadvantage relative to HARDSHIP.

*3.3.1.4 Avoiding $^1$H homonuclear effects during heteronuclear recoupling.*

The discussion in the preceding sections showed that homonuclear effects during the heteronuclear recoupling arise relatively slowly. They can be prevented from becoming significant by ending the recoupling period before effects of $^1$H spin diffusion becomes strong; surface sites, for which spin diffusion effects develop fast, are dephased quickly anyway. Therefore, in the HARDSHIP sequence the heteronuclear evolution is terminated by a 90$^o$ pulse at a time $t_c = M\,t_r < t_{SD}$, see Fig. 4. Good results are achieved with $t_c = M\,t_r$ =

0.16 ms. In this way, there is no need for homonuclear decoupling. Note also that even significant spin diffusion among the organic-matrix protons would not result in any artifacts; it would only reduce the efficiency of the heteronuclear dephasing slightly.

The $90^o$ pulse makes the $I_{zn}$ coherence transverse. Under the strong homonuclear couplings, the resulting $I_{xn}$ or $I_{yn}$ terms of protons in the organic matrix dephase quickly, i.e. they behave very differently from $I_{zn}$ coherences. Therefore, there is no contradiction in neglecting homonuclear effects during the heteronuclear recoupling but invoking them for homonuclear dipolar dephasing after a $90^o$ pulse.

### *3.3.2 Refocusing of Long-$T_{2,H}$ $^1H$ Coherences*

#### *3.3.2.1 Transverse $^1H$ evolution: Refocusing vs. dephasing.*

It is one of the most important features of the HARDSHIP pulse sequence that dephasing of the X-nuclei by the nearby dilute, long-$T_{2,H}$ protons in the inorganic phase is refocused. One complete double-cycle of the HARDSHIP pulse sequence with homonuclear dipolar dephasing is shown in Fig. 4. For simplicity, only one rotation period of heteronuclear recoupling is presented in each subcycle, i.e. $t_c = M\, t_r$ with $M = 1$. Figure 4(a) shows the effect of the sequence on protons with long $T_{2,H}$, Fig. 4(b) the effect on short-$T_{2,H}$ protons. The long-$T_{2,H}$ protons effectively see only one $180^o$ pulse in the middle of each rotation period, which results in refocusing of the heteronuclear coupling at the end of two periods $t_c = t_r$ of heteronuclear recoupling. During these short times, $^1H$ spin diffusion can never develop significant effects.

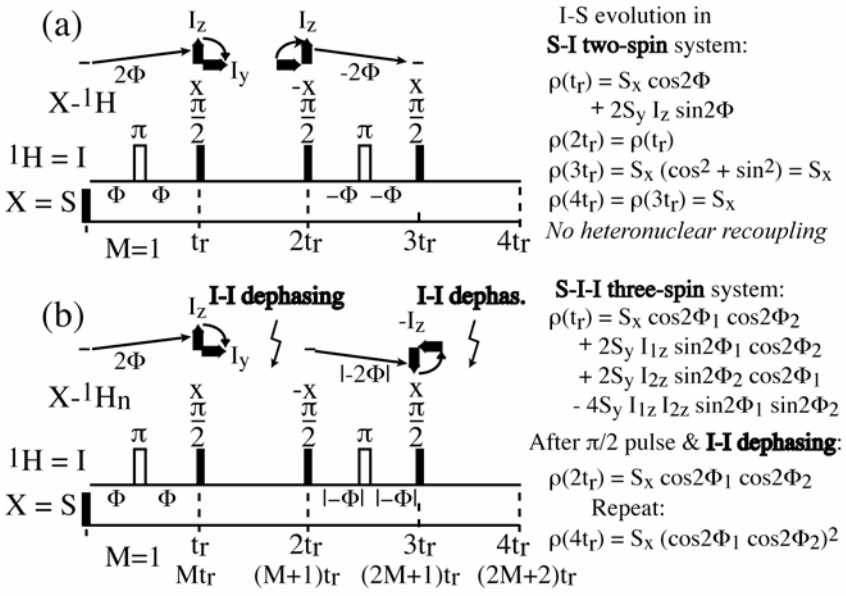


**FIG. 4.** Effects of the basic double-cycle of the HARDSHIP pulse sequence on (a) protons with long $T_{2,H}$ that are on resonance and (b) protons with short $T_{2,H}$. The corresponding I-spin ($^1$H) parts of the coherences are indicated pictorially above the pulses. The density operators at various times are given on the right for the simplest examples of these spin systems. The duration of the heteronuclear recoupling periods, which is $t_c = M\, t_r$ in general, is shown as $t_c = t_r$ (M = 1). The figure shows N = 2 heteronuclear dephasing periods.

For a quantitative analysis, we consider the state of a heteronuclear two-spin system with weak homonuclear couplings. After $t_c = M\, t_r$ of heteronuclear recoupling, the spin state is given by Eq.(1). The first proton 90$^o$ pulse converts this into

$$\rho(Mt_r) = S_x \cos(2M\Phi) + 2\, S_y\, I_y \sin(2M\Phi) \qquad (7)$$

This state is unaffected by the heteronuclear coupling, since $[S_z\, I_z,\, S_y\, I_y] = 0$. If we set the long-$T_{2,H}$ proton signal on resonance, we will only have homonuclear dephasing, which will be minor due to MAS spinning out most of the weak homonuclear couplings. We denote the homonuclear dephasing factor by $r = \exp(-t_r/T_{2,H})$. After the second 90$^o$ pulse, the spin state is

$$\rho((M+1)t_r) = S_x \cos(2M\Phi) + r\ 2\ S_y\ I_z \sin(2M\Phi) \qquad (8)$$

Due to the lack of an inversion ($180^o$) pulse before the start of the next recoupling period, the phase acquired in the second recoupling period is of the opposite sign as in the first rotation period ($-\Phi$ vs. $\Phi$). A calculation analogous to that for Eqs.(3) and (4) shows that the observable magnetization at the end of the second recoupling period is refocused into an echo,

$$\rho((2M+1)t_r) = S_x\ (\cos^2(2M\Phi) + r \sin^2(2M\Phi)) \qquad (9)$$

There is no I-coherence during the following homonuclear dephasing period, so it does not produce an additional factor r. With $T_{2,H}$ = 3 ms and $Mt_r$ = 0.14 ms, we have r = 0.95. With an effective heteronuclear coupling constant of 0.45/2 · 1 kHz (scaled by the REDOR factor of $\sqrt{2}/\pi = 0.45$,[1] and an average orientational factor of 1/2), we have $2M\Phi = 2\pi \cdot 0.23$ kHz $\cdot$ 0.14 ms $= 2\pi \cdot 0.032$ (corresponding to $12^o$). This gives $\cos^2 2M\Phi + r \sin^2 2M\Phi = 0.998$. After N cycles of heteronuclear recoupling, each of duration $Mt_r$, i.e. after N/2 double-cycles, the dephasing factor is

$$(\cos^2 2M\Phi + r \sin^2 2M\Phi)^{N/2} \qquad (10)$$

which for N = 78 (10 ms) is $0.998^{39} = 0.92$. This estimate agrees well with the limited dephasing observed in pure hectorite clay (see below). In the faster-spinning version of HARDSHIP with chemical-shift refocusing by a $^1$H $180^o$ pulse, slower relaxation with $T_{2,H} \approx 6$ ms yields r = 0.977, and the undesirable dephasing factor is $\cos^2 2M\Phi + r \sin^2 2M\Phi = 0.999$, which after 10 ms gives $0.999^{39} = 0.96$, in agreement with experimental data on hydroxyapatite shown below.

The analogous behavior occurs for each of many isolated protons coupled to many S-spins, as long as the $^{1}H$-$^{1}H$ (I-I) couplings are eliminated by MAS. The cancellation of the dipolar phase indicated in Fig. 4(a) applies to each of the simultaneously acting heteronuclear couplings and ensures complete refocusing.

*3.3.2.2 Different versions of the HARDSHIP pulse sequence.*

Figure 5 displays several different versions of the HARDSHIP pulse sequence, for different spinning frequencies. Cross polarization (CP) from $^{1}H$ or direct polarization (DP) by a $90^{o}$ X-pulse can be used to generate the X-spin signal. In all the experiments shown below, DP was used, in order to ensure equal excitation of all X-spins. All sequences feature a $180^{o}$ pulse on the X-spins after a full number of rotation periods, which refocuses isotropic-chemical-shift dephasing. On the $^{1}H$ channel, heteronuclear recoupling alternates with homonuclear dephasing of transverse coherence.

At low spinning frequencies < 3.3 kHz, $T_{2,H}$ of the dispersed protons is relatively short, in particular compared to the long rotation periods. Therefore, the homonuclear dephasing period must be kept short. As shown in Fig. 5(a), a ~25-μs homonuclear dephasing period can be incorporated into the $t_r$ > 300 μs heteronuclear dephasing period, since it accounts for only < 9% of the rotation period. This is less than the fractional duration of composite $180^{o}$ pulses in REDOR or HARDSHIP at fast spinning frequencies (>13 kHz). Due to the shortness of the homonuclear dephasing period, this version is quite broadband (tolerant of a spread of $^{1}H$ frequencies); however, dephasing by a large $^{1}H$ CSA (which can reach 10 kHz for X-OH protons in a 9.4 T field [12]) might be a problem.

Intermediate spinning frequencies of 3.3 – 10 kHz are attractive since they provide good sensitivity due to the large sample volume in 7-mm rotors (compared to smaller rotors for faster MAS) and reduced spinning side bands (compared to slower spinning). The corresponding HARDSHIP sequence for a single long-$T_{2,H}$ proton peak, which would be placed on resonance, is shown in Fig. 5(b). During the homonuclear dephasing period, chemical-shift filtering, i.e. a $\cos(\Delta\omega\, t_r)$ modulation of the I-coherence of protons off-resonance by $\Delta\omega$, also occurs. Sometimes, this can be useful to prevent the coherence of mobile matrix protons from being refocused, but generally, it limits the number of long-$T_{2,H}$ proton resonances that can be prevented from dephasing the X-nuclei. In favorable cases, the spinning speed can be chosen such that two resonances, one at $\Delta\omega = 0$ and one at $\Delta\omega = 2\pi\, \nu_r$, are unaffected.

At higher spinning frequencies > 10 kHz, $T_{2,H}$ becomes longer and $t_r$ shorter, which is desirable when the dipolar couplings between $^1$H in the inorganic particle are relatively strong and consequently their $T_{2,H}$ is quite short. As indicated in Fig. 5(c), every other homonuclear dephasing period can be longer, typically 2 $t_r$ in duration, because at that time the $^1$H coherence of the long-$T_{2,H}$ protons has been fully reconverted into X-magnetization.

At these higher spinning frequencies, a recoupling period of $t_c = 1\ t_r$ is not long enough to produce significant heteronuclear dephasing. The heteronuclear dephasing period is easily extended by applying one 180$^o$ pulse every half rotation period as in REDOR, see Fig. 5(c). Typically, $t_c = 2\ t_r \approx 0.15$ ms provides good results.

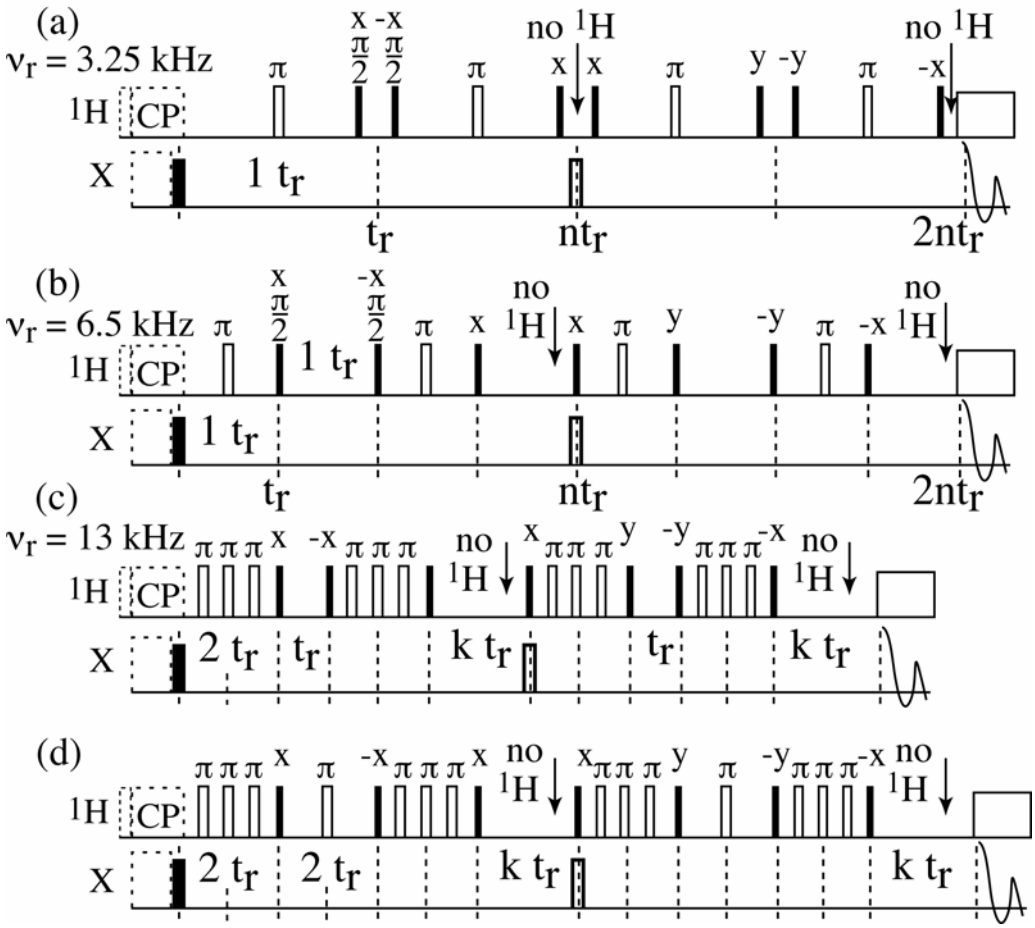


**FIG. 5.** Four versions of the HARDSHIP sequence for different spinning frequencies. (a) Slow-spinning version (1 – 3.3 kHz). The heteronuclear recoupling and a short homonuclear dipolar-dephasing period are incorporated into one rotation period. (b) Standard version for intermediate spinning speeds (3.3-10 kHz). One rotation period with a $^1$H recoupling pulse in its center for heteronuclear dephasing alternates with one rotation period for homonuclear dephasing. (c) Version for relatively fast spinning (10-16 kHz). This is desirable when the $^1$H-$^1$H couplings in the inorganic particles are relatively strong, since faster spinning increases the relaxation time $T_{2,H}$ and shortens the $^1$H dephasing period of duration $t_r$ in the pulse sequence. The heteronuclear recoupling period is kept significant by extending it to M = 2 rotation periods, with one 180$^o$ $^1$H pulse per $t_r$/2. (d) Version for relatively fast spinning and a spread of $^1$H frequencies in the inorganic phase (including a short $T_{2,H}^*$). Compared to c), every odd-numbered homonuclear dephasing period is extended to two rotation periods with a 180$^o$ pulse at its center, which refocuses dephasing by $^1$H isotropic-shift dispersion. Except for these refocusing 180$^o$ pulses, all pulses in (a-d) are composite as shown in Fig. 6. In all the sequences, the $^1$H 90$^o$ pulse immediately after a period labeled "no $^1$H", where no $^1$H coherence exists, is optional. The $S_0$ reference intensity is obtained by strong $^1$H decoupling during the full time where the X-spin magnetization is transverse.

The sequence in Fig. 5(c) is most advantageous for nanoparticles with a single $^{1}H$ resonance associated with a relatively short $T_{2,H} \approx T_{2,H}^{*}$ (the star denotes the relaxation time without a refocusing pulse) which needs to be placed on resonance. However, if the line is inhomogeneously broadened (short $T_{2,H}^{*} << T_{2,H}$) or if there are several different types of $^{1}H$ in the nanoparticle, it is desirable to refocus the chemical-shift/off-resonance evolution of the transverse $^{1}H$ coherence by a $180^{o}$ pulse applied after 1 $t_r$, see Fig. 5(d). At $\nu_r > 10$ kHz, i.e. at $t_r < 100$ μs, the rotation period is short enough, and $T_{2,H}$ usually long enough, to allow for the additional time needed for the refocusing. In fact, the duration of the hetero- and homonuclear dephasing periods is the same as with the sequence of Fig. 5(b) at half the spinning frequency, while the $T_{2,H}$ at higher-speed MAS is longer and $T_{2,H}^{*}$ dephasing has been refocused.

Which of the sequences in Fig. 5 should be chosen will depend on the $T_{2,H}$ and $T_{2,H}^{*}$ of the protons in the inorganic phase, as well as on the required sensitivity. While $^{31}P$ gives excellent signal even in very small rotors that enable fast spinning and strong pulses, unlabeled silicates and carbonates need larger rotors, even with signal enhancement by refocused detection. [13] In practice, the choice of spinning frequency may of course also depend on the type of probe head available.

*3.3.2.3 Composite pulses and phase sequence.*

For reducing the sensitivity of the HARDSHIP pulse sequence to $B_1$ inhomogeneity, it uses not only composite $180^{o}$ pulses,[14] see Fig. 6(a), during heteronuclear recoupling,[15] but also composite $90^{o}$ pulses for minimizing the residual z-component of the I-spin coherence after the pulse, see Fig. 6(a, b). Note, however, that the $^{1}H$ $180^{o}$ pulse refocusing the $^{1}H$ isotropic chemical shift in Fig. 5(d) is not composite, since the coherence to be refocused is

transverse. The phase sequence in this case is shown in Fig. 6(c) and illustrated in Fig. 6(d). Like the phase sequence of the two composite 90° pulses shown in Fig. 6(a, b), the phase sequence in Fig. 6(c, d) achieves perfect refocusing of $^1$H coherence on resonance, regardless of pulse length. In the simulations of HARDSHIP curves, the theoretical recoupling time is reduced from $Mt_r$ by half the duration of the composite pulses (typically 10%); in other words, a scaling factor of ~ 0.9 is applied to the heteronuclear couplings.

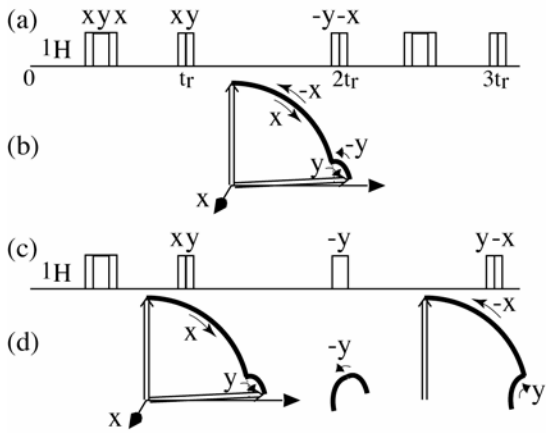


**FIG. 6.** Schematic representation of the effects of composite pulses, which reduce the sensitivity to pulse-strength errors, when applied to on-resonance $^1$H coherence during the HARDSHIP experiment. (a) Cycle of the simplest HARDSHIP pulse sequence with composite 180° (ref. [14]) and 90° pulses indicated. (b) Rotations of initial $I_z$ coherence, as produced by a composite 90° pulse that minimizes the residual $I_z$-component (inner pulse phases and arrows), and by the complementary composite pulse that restores the on-resonance coherence with long $T_{2,H}$ exactly to $I_z$ (outer pulse phases and arrows). (c) Composite-pulse phase sequence in the pulse scheme of Fig. 5(d). (d) Corresponding rotations, which return on-resonance coherence to $I_z$ regardless of pulse length.

*3.3.2.4 Reference signal $S_0$.*

The reference signal $S_0$ is measured with TPPM [6] $^1$H decoupling for the time $N(M+k)t_r$, so that it only reflects intrinsic $T_2$ relaxation of the X-spin. For obtaining reliable $S/S_0$ data, sufficiently strong decoupling of $^1$H during $S_0$ measurements is important, in particularly at higher spinning frequencies where spinning may interfere detectably with

decoupling even if the decoupling field $B_1$ is strong enough that $\omega_1 = \gamma B_1$ is three times larger than $\omega_r$. For NIST hydroxyapatite, at $\omega_r = 2\pi$ 13 kHz and after $2\tau = 10$ ms we observed an additional intensity loss in $S_0$ of about 10% with $\gamma B_1 = 2\pi$ 60 kHz compared to $2\pi$ 86 kHz.

### *3.3.3 Simulation of HARDSHIP Curves*

In the preceding sections, we showed that (i) homonuclear effects during one or two REDOR cycles ($t_c \approx 0.15$ ms) are negligible even for short-$T_{2,H}$ protons in the organic matrix and (ii) the dephasing by long-$T_{2,H}$ protons is refocused by the HARDSHIP sequence. In the following, we will discuss the cumulative dephasing of nanoparticle X-magnetization by the short-$T_{2,H}$ matrix protons after many cycles of the HARDSHIP pulse sequence, and how to simulate it for various nanoparticle geometries.

#### *3.3.3.1 Exponential dephasing under HARDSHIP.*

The effects of a cycle of the HARDSHIP pulse sequence on short-$T_{2,H}$ protons in the organic matrix are indicated in Fig. 4(b). The $90^o$ pulses on the proton channel at $t_c = M\, t_r$ ($M = 1$ is shown in the figure) make the $I_{zn}$ coherences in Eq. (5) transverse, and during the following dipolar dephasing the homonuclear couplings destroy these terms effectively, i.e. $T_{2,H}$ is short. At the end of the homonuclear dipolar dephasing period, we thus have only the pure $S_x$ term,

$$\rho(t_c) = S_x \Pi_n \cos(2M\Phi_n) \qquad (11)$$

Here and in the following, the time of interest is only the sum of the heteronuclear dephasing times, $NMt_r$, while the duration of the homonuclear dephasing periods is

irrelevant. Therefore, the homonuclear dephasing time will not be counted as contributing to the time t. After N heteronuclear dephasing periods, the density operator is

$$\rho(t = NMt_r) = S_x \{\Pi_n \cos(2M\Phi_n)\}^N \quad (12)$$

This represents exponential dephasing, as seen when we use $t = NMt_r$ and $c = \exp(\ln(c))$ to rewrite Eq. (37) as

$$\rho(t) = S_x \exp(\ln\{\Pi_n \cos(2M\Phi_n)\}\ t/t_c\ ) = S_x \exp(-Wt) \quad (13)$$

with

$$W = -\ln\{\Pi_n \cos(2M\Phi_n)\}/t_c \geq 0 \quad (14)$$

The rate of Eq. (39) can be understood more easily if we use some approximations. Since $t_c = Mt_r$ is short, we have $2M\Phi_n = \omega_n t_c << 1$ for all sites except for the surface layers, and we can approximate the density operator of Eq.(12) by

$$\rho(t) \approx S_x \Pi_n (1- (\omega_n t_c)^2/2)^N \approx S_x \Pi_n \exp(- N(\omega_n t_c)^2/2)$$

It can be shown that under the action of the HARDSHIP sequence, the dephasing can be approximated as

$$\rho(t) \approx S_x \exp(- N(\Sigma_n (\omega_n t_c)^2/2)) = S_x \exp(- 1/2\ \Sigma_n\ \omega_n^2\ t_c\ t) \quad (15)$$

where the HARDSHIP dephasing rate is

$$W = t_c\ 1/2\ \Sigma_n\ \omega_n^2 = M_2\ \ Mt_r/2 \quad (16)$$

with the second moment $M_2 = \Sigma_n \omega_n^2$ of the H-X dipolar couplings. Thus, the dephasing rate depends only on the second moment of the heteronuclear couplings and linearly on the length of the individual recoupling period $t_c = Mt_r$.

For the surface layer, $\omega_n t_c << 1$ often does not hold and the approximations made in Eq. (15) are not valid. However, the surface dephasing is fast anyway, so within the shortest dephasing time the signal is strongly attenuated even using the incorrect approximation.

*3.3.3.2 Simulation for nanoparticles.*

In contrast to REDOR, the HARDSHIP dephasing curves are dependent on the spinning speed if the number M of recoupled rotation periods is fixed, but in such a simple way that an $\omega_r$-independent master curve could still be used. This has been confirmed in HARDSHIP experiments of nanodiamond[4] where the detailed method for the determination of the second moment is described. For quantitative fits, the observed dephasing can be simulated by superposition of the dephasing curves for X-nuclei at the various depths, see Fig. 7. For each depth, we calculate the dephasing curves for various crystallite orientations relative to the rotor axis. For convenience, these calculations are performed in a crystal-fixed frame, see Fig. 7(b). The z-axis is chosen perpendicular to the crystal surface. For sheets, the orientation of the rotor axis is varied relative to the sheet normal, which is the z-axis, for rods, relative to the rod axis, which is the y-axis (so that the z-axis is still along to the local surface normal). The rotor axis is specified by polar coordinates $(\theta,0)$ relative to this symmetry axis; different azimuthal angles give the same second moment due to the summation over all the organic-matrix protons in the planar sheet or around the rod axis. The $B_0$ field makes the magic angle of $54.7^o$ with the rotor axis, in a plane with the reference axis (z- or y-axis) and is rotated around the rotor axis by the angle $\gamma_0$.

The dephasing curves (not the second moments) for different relative orientations $\theta$ of crystallite surface normal and rotor axis, and with the $B_0$ field ($\gamma_0$), are averaged for a given depth from the interface with the organic matrix, and then the curves S(t;z) for different depths z are averaged. Figures 7(c, d) show examples of the dephasing at various depths and the total dephasing calculated numerically for phosphate platelets and nanospheres, respectively. In Fig. 7(c), the calculated intensities after HARDSHIP dephasing are represented by filled symbols. The lines through the data points are empirical biexponential or single-exponential fits

$$S(t;z) = f_{fast}(z)\exp(-t/\tau_{fast}(z)) + (1-f_{fast}(z))\exp(-t/\tau_{slow}(z)) \qquad (50)$$

with the depth-dependent time constants and relative weight shown in Fig. 7(e) (stars, marked "3-nm thickness"). These parameters are plotted, as a function of depth z from the nearest protons, for sheets of 1, 2, 3, and 4 nm thickness. The slow decay times, $\tau_{slow}$, are shown by open, the fast decay times, $\tau_{fast}$, by the corresponding filled symbols. The dashed line slightly above the data corresponds to $\tau \sim z^3$. The deviations of the data from this curve at the largest depths are due to dephasing by the second surface of the sheet, the deviations on the other, near-surface end of the curve due to dominance of the strong couplings to the nearest protons (for a spin pair, $M_2 \sim 1/z^6$). The depth dependence of the fraction of the fast decay time, $f_{fast}$, is shown in the inset in Fig. 7(e). The fit parameters shown in Fig. 7(f) are for spherical nanoparticles of the indicated diameters; they give fits of similar quality as those shown in Fig. 7(c), for dephasing times < 10 ms.

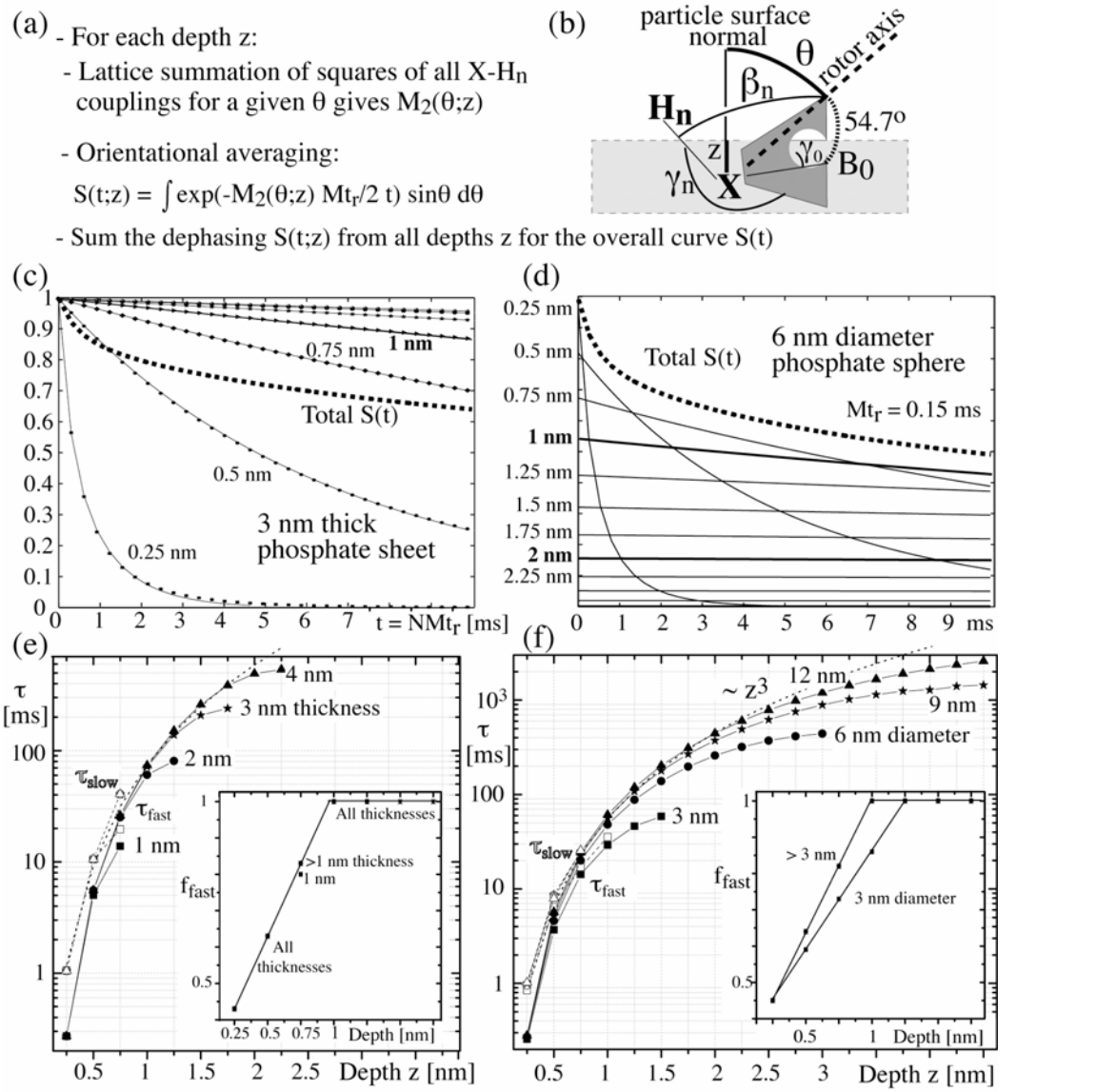


**FIG. 7.** (a) Outline of the simulation procedure for obtaining HARDSHIP $S/S_0$ curves. (b) Angles relevant in the calculation of the heteronuclear-coupling frequencies and powder averaging (see also the text). The nanoparticle is shaded light gray, the plane containing the rotor axis and the $B_0$ field darker gray. (c, d) Signal intensity as a function of dephasing time $N \cdot M \cdot t_r$ for (c) laterally wide 3-nm thick phosphate platelets and (d) 6-nm diameter spherical phosphate nanoparticles, assuming N recoupling periods of $Mt_r = 1/(6.5\ \text{kHz})$. Curves S(t;z) for various depths z, in steps of 0.25 nm, from the interface (z = minimum $^1$H-$^{31}$P distance) are shown, as well as the overall dephasing curve (dashed line). The proton density in the matrix was $1/(0.27\ \text{nm})^3$. (e) Parameters for biexponential fits of the data in c) and of similar data for phosphate sheets of 1, 2, and 4 nm thickness. Decay constants $\tau_{slow}$ (open symbols) and $\tau_{fast}$ (filled symbols), on a logarithmic scale, and the weighting factor $f_{fast}$ (see inset) are plotted as a function of depth z. For $z \geq 1$ nm, the decay is single-exponential on the 10-ms time scale. The dashed line is a curve $\tau \sim z^3$. (f) Same as e) for spherical phosphate nanoparticles of 3, 6, 9, and 12 nm diameter. These parameters can be used to produce HARDSHIP fits without explicit orientational averaging. Fit parameters courtesy of Xiaowen Fang.

The parameters shown in Fig. 7(e, f) make it possible to produce HARDSHIP dephasing curves in a simple manner, without requiring the complex scanning of orientations and atomic positions discussed above. When required, scaling of the dephasing rate (the inverse of $\tau$) for nuclei of different $\gamma_X$ according to Eq.(45) is straightforward. Changes in proton density can also be made based on Eq.(45), which shows that the dephasing rate is proportional to the proton number density $1/a^3$.

**3.4 Results and discussion**

*3.4.1 Overview.*

In order to demonstrate the HARDSHIP method, we have acquired HARDSHIP and REDOR dephasing curves of dry layered silicate (clay) and a polymer-clay nanocomposite where the thickness of the clay platelets is known and hydroxyapatite. It is then applied to the bioapatite-collagen nanocomposites in avian and bovine bone. Most experiments were performed at spinning frequencies of 6.5, 8 or 13 kHz, with $Mt_r$ = 1/6.5 kHz = 0.15 ms.

Fast REDOR dephasing in the pure inorganic materials (clay and hydroxyapatite) confirms that couplings to protons in the inorganic phase interfere with measurement of the relatively weak particle-matrix X-H couplings of interest. To demonstrate that HARDSHIP works, we have to prove that these interfering couplings in the pure inorganic materials are refocused, while dephasing of nanoparticle X-magnetization by protons in the organic matrix is significant.

For particle-size determination by HARDSHIP, quantitative fits of the dephasing by the matrix protons are required. We will use the data from the clay-polymer nanocomposite to demonstrate that the analysis presented above provides a good description of the

HARDSHIP dephasing behavior. Finally the HARSDHIP measurements are coupled with WAXD to determine the size and shape of the bioapatite nanoparticles and to present a picture of the mineralized fibril.

*3.4 2 $^{29}Si\{^{1}H\}$ HARDSHIP dephasing of a layered silicate and a clay-polymer composite.*

Clay-polymer nanocomposites consist of ~1-nm thick silicate platelets dispersed in a polymer matrix, see Fig. 8(a, b). Due to improvements in some mechanical and barrier properties, they have found large volume applications, for instance in car bumpers.[16] The structure of the crystalline silicate platelets is relatively well known, so this is a good model system for testing the HARDSHIP experiment.

The pure clay silicate contains inner OH groups as a regular part of the lattice, see Fig. 8(a). The distance of a given proton to each of its six nearest neighbors is 0.42 nm, corresponding to six 2.4-kHz couplings (in the strong-coupling limit), or a second moment of ~6 kHz. At 6.5 kHz MAS, the transverse relaxation time $T_{2,H}$ of these protons is 3 ms.[13] The $^{1}H$-$^{29}Si$ distance is 0.29 nm, corresponding to a 1-kHz coupling.[13] The multiple $^{1}H$-$^{29}Si$ couplings result in fast initial $^{29}Si\{^{1}H\}$ REDOR dephasing, see Fig. 8(c). (Note that ref. [13] showed the simpler $^{1}H\{^{29}Si\}$ REDOR dephasing). Water in the van der Waals gap between silicate platelets would lead to undesirable heteronuclear dephasing. In order to avoid this, the sample had been dried at 470 K for two weeks. Nevertheless, a bound-water peak with an area of 50% relative to the OH signal was observed. Still, the $^{29}Si\{^{1}H\}$ HARDSHIP dephasing is quite minor, see Fig. 8(c).

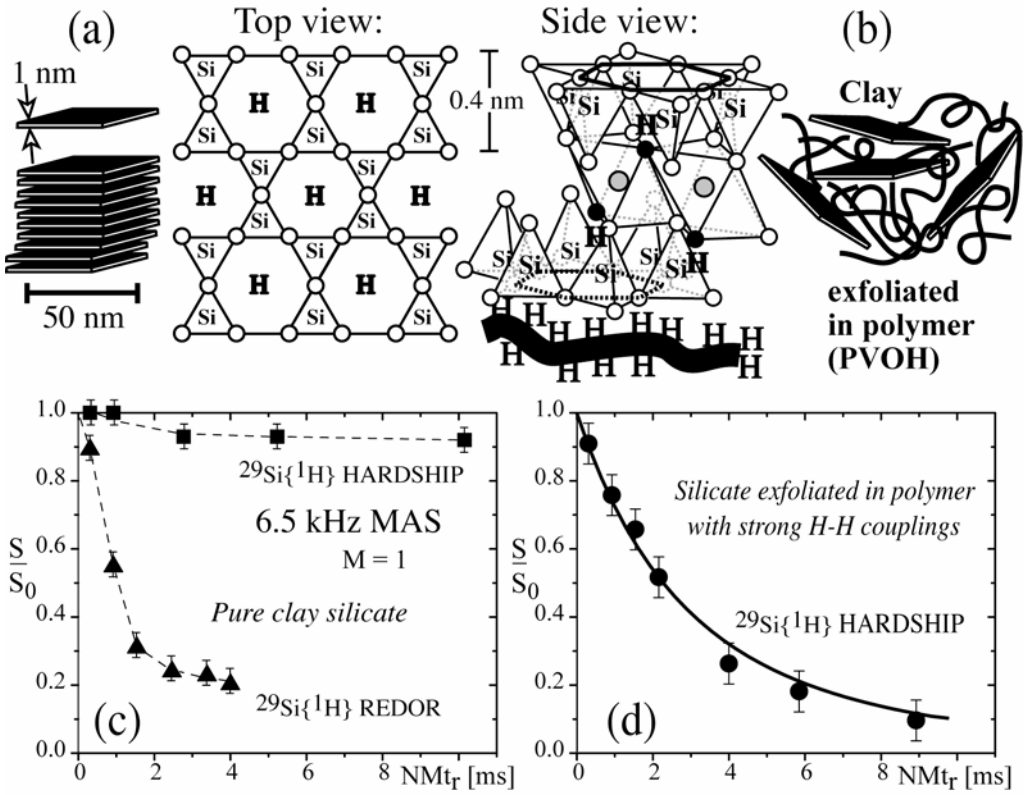


**FIG. 8.** $^{29}Si\{^{1}H\}$ dephasing in hectorite clay. (a) Schematic representations of the structure of pure hectorite clay. Oxygen atoms are indicated by open circles, except in OH groups (filled circles). The lines connecting oxygen atoms are not chemical bonds. Silicon and hydrogen atoms are denoted by Si and H, respectively. The closest Si-H distance is 0.28 nm. (b) Schematic of hectorite clay exfoliated in a hydrophilic polymer. (c) $^{29}Si\{^{1}H\}$ HARDSHIP data (squares) and $^{29}Si\{^{1}H\}$ REDOR data (triangles) of pure hectorite clay. (d) $^{29}Si\{^{1}H\}$ HARDSHIP data of hectorite clay dispersed in poly(vinyl alcohol) (circles), with a fit curve based on the structural parameters shown in b) (see the text for details). All data were acquired at 6.5-kHz MAS after direct polarization ($^{29}Si$ 90°-pulse excitation) with 60-s recycle delays and refocused detection for signal enhancement.[13] The $T_{2,H}$ relaxation time of the OH protons is ~ 3 ms in pure hectorite clay, and ~ 1.5 ms in the presence of polymer.[13] The pulse sequence shown in Fig. 5(b) was used.

The successful refocusing of the heteronuclear couplings in pure hectorite clay enables measurements of polymer-silicate $^{1}H$-$^{29}Si$ interactions in polymer-clay composites by HARDSHIP. The $^{29}Si\{^{1}H\}$ HARDHSHIP data of 5 wt% (~2.5% vol%) hectorite clay exfoliated in poly(vinyl alcohol), are shown in Fig. 8(d). Due to the 40-fold dilution, the $^{29}Si$ signal of this sample is quite weak; for signal enhancement, refocused $^{29}Si$ detection [13] was used.

The HARDSHIP dephasing in this system is relatively straightforward to simulate. As shown in Fig. 8(a), the 1-nm thick silicate platelet contains just two equivalent silicon layers, which are separated by 0.65 nm. Both are at the same distance from the nearest surface. Thus, this system consists effectively of a single silicon layer, which provides a good test of the shape of the HARDSHIP dephasing curve for a single layer; the simulation nevertheless considered both layers realistically, or equivalently the effect of polymer above and below the platelet on a given silicon layer. The signal dephases approximately exponentially, but not exactly, due to orientational averaging: different orientations of the plate relative to the rotor axis and $B_0$ field result in slightly different $^{1}H$-$^{29}Si$ second moments. In the fitting, the only distance that is somewhat uncertain is that between the silicon layer and the nearest polymer protons. Based on the 1.0-nm repeat distance in pure dry hectorite clay (which includes the van der Waals gap), and assuming an average distance of 0.11-nm between the center of the van der Waals gap and the polymer protons, we used a minimum $^{1}H$-$^{29}Si$ distance of 0.28 nm. A proton number density of $1/(0.27\ nm)^3$ in the poly(vinyl alcohol) matrix was used in the simulation that produced the fit curve in Fig. 8(d).

### *3.4.3 $^{31}P\{^{1}H\}$ HARDSHIP dephasing of hydroxyapatite.*

Ideal hydroxyapatite, $Ca_{10}(PO_4)_6(OH)_2$, contains two OH protons per unit cell of volume 0.6 $nm^3$.[17] These OH protons are arranged on lines parallel to the c-axis of the crystal structure.[18] Though the closest H-H distance within a line is quite small, between 0.32 and 0.25 nm, the resulting dipolar couplings of all spins on a given line form an inhomogeneous Hamiltonian and are refocused even by slow MAS.[9,19] Only the relatively weak couplings between protons on different lines need to be eliminated by sufficiently fast MAS. In the hexagonal crystal structure, a given line of protons has six nearest neighbors at a distance of 0.94 nm.[18]

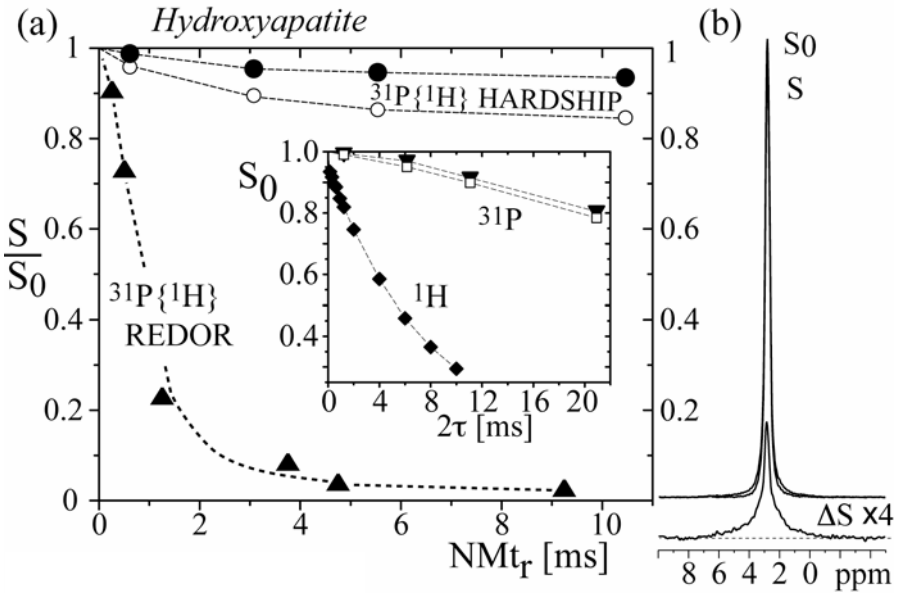


**FIG. 10.** $^{31}P\{^{1}H\}$ dephasing in apatites (calcium phosphates). (a) $^{31}P\{^{1}H\}$ HARDSHIP (filled circles: peak height; open circles: peak area) and REDOR (triangles) dephasing of pure NIST hydroxyapatite. Recycle delay: 600 s; spinning frequency: 13 kHz, except for the REDOR data (8 kHz). The HARDSHIP pulse sequence of Fig. 5(d) was used with M = 2 and k = 2. The inset shows the $^{31}P$ $T_2$ decay under 86-kHz $^{1}H$ decoupling (filled inverted triangles: peak height; open squares: peak area), and the $T_{2,H}$ decay of the hydroxide protons (filled diamonds), again at 13 kHz MAS. The dashed lines are guides to the eye. (b) $S_0$, S, and scaled-up ΔS spectra of NIST hydroxyapatite obtained in $^{31}P\{^{1}H\}$ HARDSHIP with $NMt_r$ = 10.5 ms. Preferential dephasing of a broad component is clearly seen.

For each $^{31}P$, the nearest OH proton is at a 0.4-nm distance. As a result, REDOR dephasing is quite fast, see Fig. 10(a), and prevents hydroxyapatite crystal thickness measurements by REDOR in nanocomposites. $^{31}P\{^{1}H\}$ HARDSHIP successfully refocuses the dephasing by the OH protons, as evidenced by the slow decay of the peak height (filled circles in Fig. 10(a)). The peak area decreases more quickly (open circles), due to the dephasing of a broad base of the signal, see Fig. 10(b), that must be associated with protonated or hydrogen-bonded phosphates, most likely at crystallite surfaces; we have indeed observed such protonated phosphate sites in $^{1}H\{^{31}P\}$ REDOR NMR of this sample.

*3.4.4 $^{31}P\{^{1}H\}$ HARDSHIP dephasing of bone bioapatite.*

Bone is a nanocomposite consisting of a collagen matrix and apatite nanocrystals. Having demonstrated that the dephasing by OH protons in hydroxyapatite can be successfully refocused by $^{31}P\{^{1}H\}$ HARDSHIP, we can use the new technique to probe the thickness of the apatite nanocrystals in bone. In fact, the undesirable dephasing effects of OH protons in $^{31}P\{^{1}H\}$ HARDSHIP NMR of bioapatite will be even smaller than in ideal hydroxyapatite, since the OH concentration in bone bioapatite is reduced by at least a factor of 5 compared to ideal hydroxyapatite.[20]

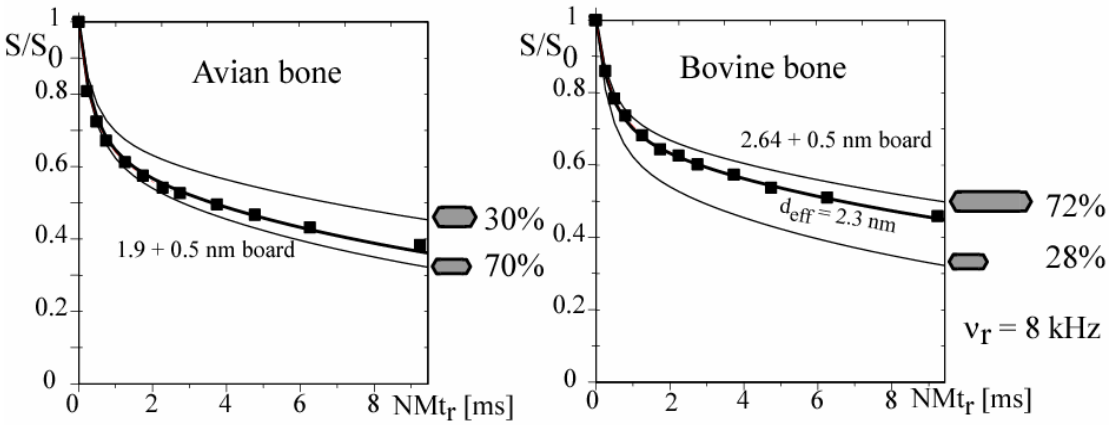


**FIG 11.** $^{31}P\{^{1}H\}$ HARDSHIP dephasing of bioapatite in native avian and bovine bone(matrix: collagen) indicated by filled black squares. Recycle delay: 300 s; spinning frequency: 8 kHz. The full curve shown was simulated assuming a 1.9-nm thick and 2.64-nm thick (P-to-P) platelet for the avian and bovine bones. Dephasing curves for 3 and 4 unit cell thick platelets are included along with their percentage contribution to the full curve.

The $^{31}P\{^{1}H\}$ HARDSHIP data of avian and bovine femur bone displayed in Fig. 11 show significant dephasing. The simulation curves were obtained assuming wide platelets of 1.9 or 2.64 nm P-to-P thickness, with a 0.38-nm phosphate layer spacing. The actual platelet thicknesses would be ~2.5 and 3.2 nm, respectively, i.e. ~ 0.6 nm larger than the P-to-P thickness, since P is surrounded by oxygen and therefore never directly at the surface; we estimate the average distance between P closest to the surface and the center of the gap

between phosphate and collagen to be 0.3 nm, slightly larger than a P-O-H two-bond internuclear distance. A proton number density of $1/(0.29\ \text{nm})^3$ in the collagen matrix was used in the simulation. The model of platelets of equal thickness is only an approximation to the true situation. If one considers that the thickness of the nanocrystals is in integer number of unit cells, then one has to assume a distribution of thicknesses. In Fig. 10 (c) we show that for the avian bone the data is fit by a 70:30 ratio of 3 and 4 unit cell thick crystals respectively while for bovine bone the ratio is 28:72. Over all the reduced dephasing of the bovine bone as compared to the avian bone indicates larger crystal size for the bovine bone.

*3.4.5 Size of the bioapatite by WAXD.*

It is possible to calculate the scattered x-ray intensity of nanocrystals of a given size and shape .[21] The intensity spherically averaged in reciprocal space is described by the Debye formula[22] :

$$I_N(b) = \sum_{n,m\neq n}^{N} f_n f_m \frac{\sin(2\pi b r_{nm})}{2\pi b r_{nm}} \qquad (17)$$

where $b=1/d = 2\sin\theta/\lambda$ , $\lambda$ is the wavelength and $2\theta$ is the scattering angle NOTE: IN CHAPTER 2, THE SCATTERING ANGLE WAS JUST $\theta$. The sum runs over all the pair distances $r_{nm}$ of the atoms $n$, $m$ with scattering amplitudes $f_n$, $f_m$ in a nanocrystal consisting of N atoms. The experimental and calculated scattering intensities for the avian and bovine bone are shown in Figure 12. Nanocrystal sizes of 2.4 nm x 6 nm x 12 nm for avian bone and 3.2 nm x 10 nm x 16 nm for the bovine bone gave the best fits to the experimental data. The thicknesses obtained via this method agree well with the thicknesses determined by

HARDSHIP. In particular, the sharper peaks in the x-ray diffraction of bovine bone show directly that the bovine bone has the larger crystallite dimensions, in agreement with NMR.

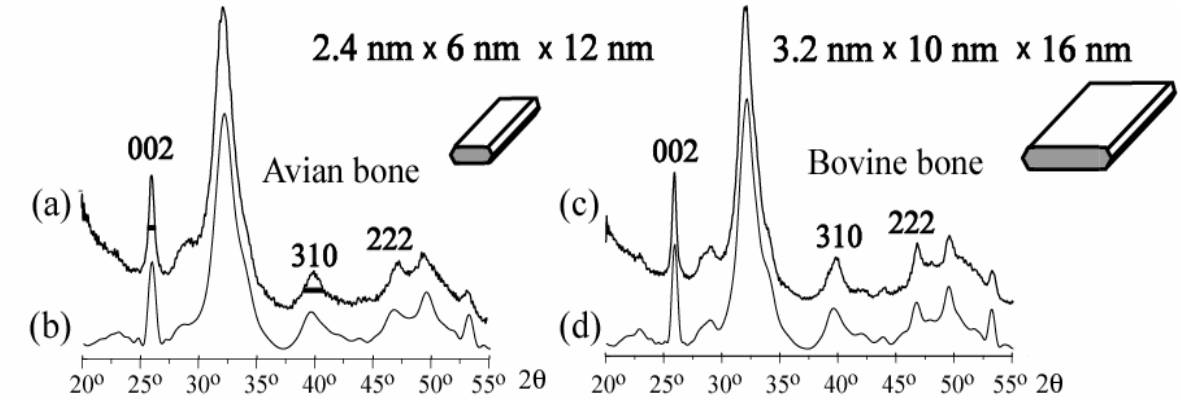


**FIG 11.** WAXD powder patterns of avian and bovine bone. (a) and (c) are the experimental powder diffraction peaks while (b) and (d) are simulated using the Debye formula. The width of the 002 reflection is indicative of the long axis of the crystallite while 222 reflection and 310 reflections are indicative of the width and thickness of the crystallites. The dimensions of crystallite used for simulating the peaks and the relative size of the crystallites are shown.

### 3.5 Conclusions

X{$^1$H} HARDSHIP NMR enables the measurement of the thickness (more specifically, the surface-to-volume ratio) of inorganic nanoparticles in an organic matrix and thus opens new possibilities for NMR studies of nanocomposites. Protons in the organic matrix dephase X-nuclei in the nanoparticles, while effects of dispersed, long-$T_{2,H}$ protons in the nanoparticles are minimal, as demonstrated on model silicates and phosphates. If spectroscopically resolved sites are located at a specific depth from the organic-inorganic interface, that depth can be determined. HARDSHIP dephasing is slower than standard REDOR, but significantly simpler to analyze in these multi-spin systems. Thus, even for nanocomposites without protons in the inorganic phase, HARDSHIP may be preferable to

REDOR for obtaining quantitative thicknesses. The theoretical treatment in terms of interaction representations and relatively slow I-spin diffusion enables simulations of the dephasing curves even in the absence of homonuclear decoupling.

While the theoretical treatment of the multispin system may appear daunting, a relatively simple result, namely exponential dephasing that depends only on the heteronuclear second moment, is obtained. Calculation of the simulation curves does not require quantum mechanics but only spatial averaging of dipolar couplings. Set-up of the experiment is not significantly more difficult than for REDOR.

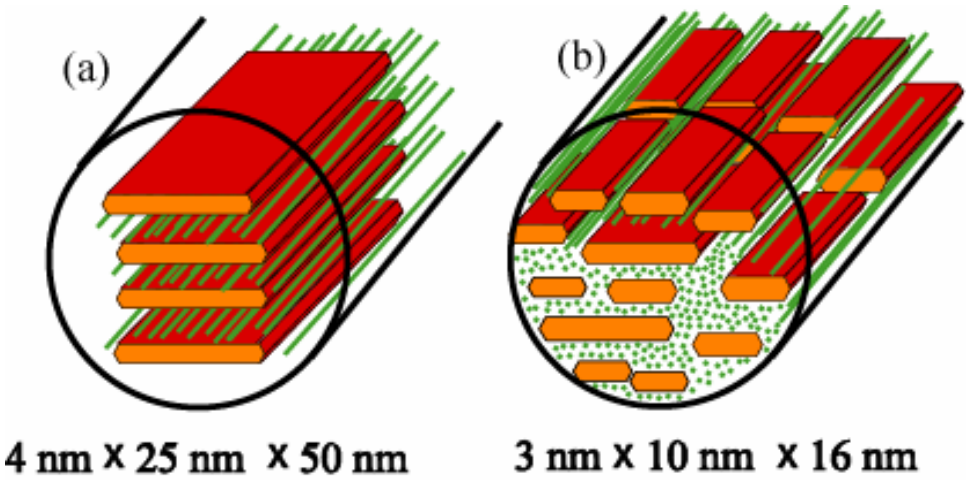


**FIG 12.** A sketch of a mineralized collagen fibril, where the straight lines represent the collagen molecules and the "boards" represent the bioapatite nanaparticles. The average sizes of the nanoparticles in each case are indicated. (a) represents the generally accepted structure of the mineralized collagen fibril while (b) represents the revised structure.

We have applied the HARDSHIP sequence to determine the size of bioapatite particles in avian and bovine cortical bone. In the prevalent literature[23], the size of the bioapatite nanocrystals is generally regarded as ~ 4 nm x 25 nm x 50 nm. Accordingly, a schematic of a mineralized nanocrystal would look like Figure 12 a. However, the combination of NMR and WAXD proves that the nanocrystals are significantly smaller than

previously thought. On that basis, we propose a revised schematic of the mineralized fibril with smaller crystals of a range of thicknesses and widths as shown in Figure 12 (b). The smaller size of the crystallites implies that the surface interaction between the bioapatite crystallites and the collagen, which is crucial to the strength of the composite, is nearly 1.5 times greater than previously thought. This structural insight gives us a better understanding of the origin of the mechanical properties of bone.

**Acknowledgments**

This work was supported by the Director for Energy Research, Office of Basic Energy Science, in the Materials Chemistry and Biomolecular Materials Program of Ames Laboratory, operated for the U.S. Department of Energy by Iowa State University (Contract No. W-7405-Eng-82). KSR thanks Drs. Mufit Akinc and Surya Mallapragada for discussions that initiated this research.

**REFERENCES**

[1] T. Gullion and J. Schaefer, J. Magn. Reson. **81** (1), 196 (1989).

[2] L. M. Miller, V. Vairavamurthy, M. R. Chance, R. Mendelsohn, E. P. Paschalis, F. Betts, and A. L. Boskey, Biochim et Biophys Acta **1527** (1-2), 11 (2001).

[3] J. M. Griffiths and R. G. Griffin, Anal. Chim. Acta **283**, 1081 (1993).

[4] K. Schmidt-Rohr, A. Rawal, and X. W. Fang, J Chem Phys **126** (5), 054701 (2007).

[5] X.-W. Fang, J.-D. Mao, E. Levin, and K. Schmidt-Rohr, J. Phys. Chem. B (unpublished).

[6] A. E. Bennett, C. M. Rienstra, M. Auger, K. V. Lakshmi, and R. G. Griffin, J. Chem. Phys. **103** (16), 6951 (1995).

[7] U. Haeberlen and J. S. Waugh, Phys. Rev. **175**, 453 (1968); U. Haeberlen, *High Resolution NMR of Solids*. (Academic Press, San Diego, 1976).

[8] J. D. Mao and K. Schmidt-Rohr, J. Magn. Reson. **162** (1), 217 (2003).

[9] K. Schmidt-Rohr and H. W. Spiess, *Multidimensional Solid-State NMR and Polymers*. (Academic Press, London, 1994).

[10] D. L. VanderHart and G. B. McFadden, Solid State NMR **7**, 45 (1996).

[11] Q. Chen and K. Schmidt-Rohr, Solid State NMR **29**, 142 (2006).

[12] T. M. Duncan, *Principal Values of Chemical Shift Tensors*, 2nd ed. (Farragut, Chicago, 1997); K. Schmidt-Rohr and J.-D. Mao, J. Magn. Reson. **157**, 210 (2002).

[13] S. S. Hou, F. L. Beyer, and K. Schmidt-Rohr, Solid State Nuc Mag Reson **22** (2/3), 110 (2002).

[14] M. H. Levitt, Progr. NMR Spectroscopy **18**, 61 (1986).

[15] N. Sinha, K. Schmidt-Rohr, and M. Hong, J Magn Reson **168** (2), 358 (2004).

[16] M. Alexandre and P. Dubois, Mater. Sci. Eng. R **28**, 1 (2000).

[17] S. V. Dorozhkin and M. Epple, Angewandte Chemie, International Edition **41** (17), 3130 (2002); M. Mathew and S. Takagi, J. Res. Nat. Inst. Stand. Technol. **106** (6), 1035 (2001).

[18] G. Cho and J. P. Yesinowski, Chemical Physics Letters **205** (1), 1 (1993).

[19] M. M. Maricq and J. S. Waugh, J. Chem. Phys. **70** (7), 3300 (1979).

[20] G. Cho, Y. Wu, and J. L. Ackerman, Science **300** (5622), 1123 (2003); D. Pasteris Jill, B. Wopenka, J. Freeman John, K. Rogers, E. Valsami-Jones, A. M. van der Houwen Jacqueline, and J. Silva Matthew, Biomaterials **25** (2), 229 (2004); A. Rawal and K. Schmidt-Rohr, (unpublished).

[21] V. Gnutzmann and W. Vogel, J. Phys. Chem. **94**, 4991 (1990); B. D. Hall, Journal of Applied Physics **87** (4), 1666 (2000).

[22] A. Guinier, *X-Ray Diffracton in Crstals, Imperfect Crystals Amorphous Bodies*. (Dover, New York, 1994).

[23] J. Y. Rho, L. Kuhn-Spearing, and P. Zioupos, Med Eng Phys **20** (2), 92 (1998).

# CHAPTER 4

# COMPOSITION OF THE BIOAPATITE NANOCRYSTAL SURFACE IN COMPACT BONE

Aditya Rawal, Klaus Schmidt-Rohr

*In the style of a paper to be submitted to Colloids and Surfaces B: Biointerfaces*

**Abstract**

The components of the surface of the bioapatite nanocrystals in avian and bovine cortical bone, which form the inorganic component of the bone nanocomposite, were studied by $^{1}H$ -$^{31}P$ solid-state NMR. $^{1}H$ {$^{31}P$} rotational echo double resonance (REDOR) and heteronuclear correlation spectroscopy (HetCor) at 30 kHz MAS were used. The contact of the surface components with the core of the bioapatite crystals and collagen was proven by $^{31}P$ and $^{1}H$ spin diffusion, respectively, thereby establishing them at the interface between the hydrated organic collagen and the crystalline apatite. It was observed that a significant portion of the surface phosphates were protonated, while others were strongly hydrogen-bonded to water. The fractions of these components were determined by selecting the different protonated sites by $^{1}H\{^{31}P\}$ REDOR. Additionally, the fractions were also quantified by techniques based on $^{31}P$ chemical shift anisotropy (CSA) dephasing, which take advantage of different deviations from tetrahedral symmetry in $PO_4^{3-}$ vs. $HPO_4^{2-}$ vs. $PO_4^{3-}$–$H_2O$ groups and are combined with $^{31}P\{^{1}H\}$ recoupling. The results from the $^{1}H$ and $^{31}P$ NMR methods were found to be in excellent agreement. The data show that the avian bone had a larger surface fraction than the bovine bone (35 % vs. 28 %), and that $PO_4^{3-}$–$H_2O$ are ~ 1.5 times more abundant than $HPO_4^{2-}$.

**4.1 Introduction**

In order to understand how bone achieves its superior mechanical properties, it is important to know its structure and composition[1]. From the materials viewpoint this means that we must be able to quantify the size, the composition, spatial distribution and ordering of the bioapatite nanocrystals that make up ca. 70 % by weight in the collagen matrix of the cortical bone. Secondly, we would like to understand the bonding between the apatite and the surrounding collagen and how the collagen is "oriented" with respect to the apatite nanocrystals. The strength and toughness of bone is dictated by the interfacial bonding strength between the surface of the bioapatite nanocrystals and the collagen matrix. In this paper, we aim to characterize the surface composition, more specifically the surface phosphate environments of the bioapatite which are vital in determining the interfacial interaction between the organic and inorganic components. This is an important factor in trying to simulate similar bond strengths between the organic and inorganic phases in synthetic bone. Early work using infrared spectroscopy, to determine the constituents of the apatite suffered from the problem that the bone had to be treated by heat or chemical methods to remove the organic components whose spectra overlapped with the bioapatite, but which would often result in loss of certain constituents of the bone apatite[2]. It would be reasonable to assume that these methods altered the surface structure and composition. That the process of deproteinating the bone erodes the bioapatite crystals can be clearly seen in work done by Tong et al.[3] where efforts to obtain isolated crystallites for study by atomic force microscopy resulted in the crystallites being greatly reduced in size. Therefore it is required that the preparation methods used to investigate the surface of bone apatite are benign and ensure least alteration of the bioapatite surface structure.

Work by Posner [4] on apatite surfaces has shown that the surface of the bioapatite in bone has unique characteristics, such as a large surface area of ca. 200 $m^2/g$ and a strong

affinity to water. While significant work has been done to investigate the composition of bone mineral, [5-7] to our knowledge there is no systematic characterization of the composition of bioapatite surface in its native state.

Solid state NMR is a powerful tool for studying complex biological structures such as bone, where it combines excellent selectivity for different chemical species along with good sensitivity especially in the case of $^{31}P$ and $^{1}H$ nuclei which have a 100 % natural abundance. Because solid state NMR can selectively look at the organic phase, the inorganic phase or the interphases, we can study the bioapatite crystals in essentially their native state with only minimal mechanical alteration. In this paper, we have built upon our previous studies of the size, shape, and composition of apatite nanocrystals in bone, and elucidated the surface structure of the bioapatite using two independent approaches. The results of this study provide important input for a more accurate composition analysis of bioapatite and yield clues to the interactions of apatite with the collagen matrix.

## 4.2 Experimental

### *4.2.1 Samples.*

The mid sections of adult bovine (ca. 4 years) and avian femur bones were obtained. The outer surface was cleaned by a surgical scalpel to remove muscle tissue. The samples wee sliced into thin sections and rinsed with ethanol to remove the mass of marrow tissue. The samples were then thoroughly rinsed with a defatting solution (75-25% methanol-chloroform mixture) to remove all residual lipids. The samples were ground in liquid nitrogen and lyophilized to remove any bulk water or solvent. The ground samples were packed into 7-mm, 4-mm and 2.5-mm magic angle spinning (MAS) Kel-F rotors.

*4.2.2 NMR parameters.*

All NMR experiments were carried out on a Bruker DSX-400 spectrometer at 400 MHz for $^{1}H$ and 162 MHz for $^{31}P$ nuclei. A Bruker 7 mm double resonance magic-angle spinning (MAS) probehead was used for 6.5 kHz MAS $^{1}H$-$^{31}P$ experiments while a 2.5-mm double resonance MAS probehead was used for 30 kHz MAS $^{1}H$-$^{31}P$ experiments. The $^{1}H$ and $^{31}P$ pulse lengths were 4 μs for the 7-mm probe and 2.5 μs for the 2.5 mm probe. In direct-polarization (DP) $^{31}P$ experiments recycle delays of 200 s and 3,000 s were used depending on the type of experiments. In $^{1}H$ and $^{1}H$-$^{31}P$ cross polarization (CP) experiments, including two dimensional (2D) heteronuclear correlation (HetCor), recycle delays of 5 s were used. The $^{1}H$-$^{31}P$ HetCor spectra were obtained without any frequency-switched Lee-Goldberg (FSLG) decoupling during $t_1$, using instead fast MAS of 30 kHz to achieve $^{1}H$ homonuclear decoupling followed by 200 μs of Hartmann-Hahn CP.

*4.2.3 $^{31}P$ spin diffusion.*

The surface phosphates of the bioapatite are selected by 0.1 ms CP and then allowed to spin diffuse to the interior phosphates on a 10 s timescale. The pulse sequence is illustrated in Figure 1 (a).

*4.2.4 $^{1}H\{^{31}P\}$REDOR NMR.*

In order to isolate the apatite protons from the collagen protons we use the rotational echo double resonance experiment (REDOR)[8] where apatite protons are revealed in the difference (ΔS) spectrum, between undephased $^{1}H$ spectrum ($S_0$) and the $^{1}H$ spectrum dephased by the $^{31}P$ nuclei of the apatite (S). To selectively look at only the apatite protons,

for example in two dimensional (2D) experiments, alternate scans are run such that during the first scan the recoupling pulses on the phosphorus channel turned off, while during the next scan recoupling pulses turned on and the receiver phase inverted. The two consecutive scans therefore subtract and this gives the ΔS spectrum which selectively exhibits the bioapatite protons. These experiments are carried out at 30 kHz MAS in order to suppress the $^{1}H$ $T_2$ relaxation and enhance the resolution of the proton spectrum. The REDOR component of the pulse sequences is shown in Figure 1 (b) and (c)

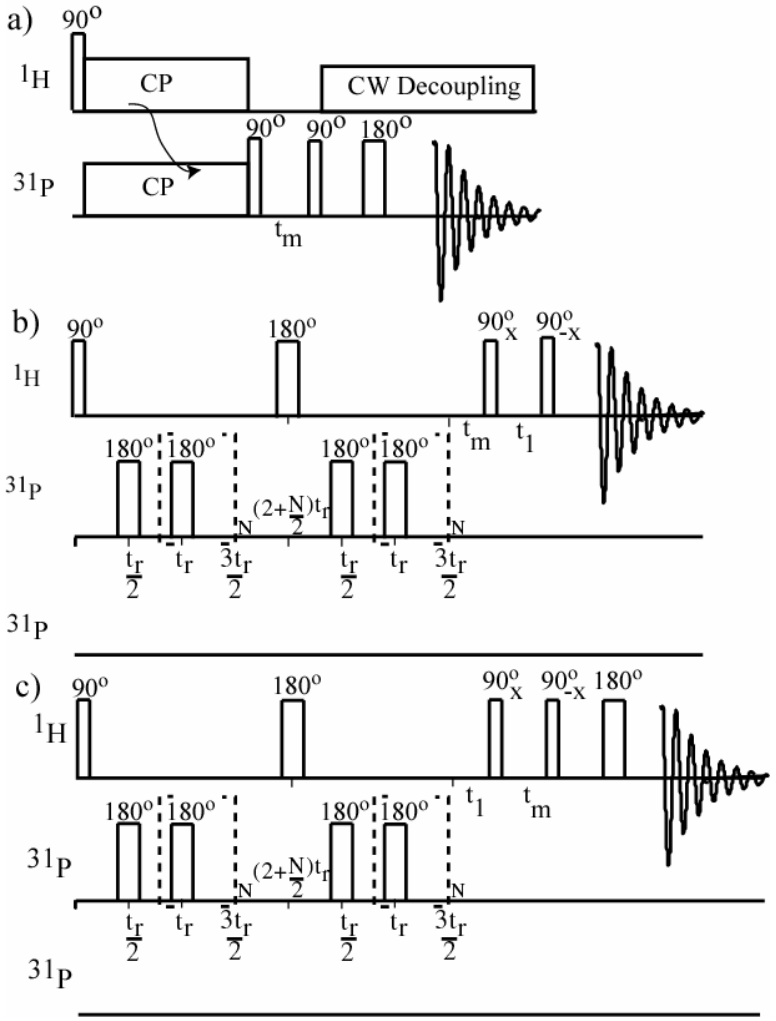


Figure 1. Pulse sequences for $^{1}H$-$^{31}P$ NMR experiments. (a) $^{31}P$ spin diffusion after $^{1}H$-$^{31}P$ cross polarization; (b) $^{1}H$ 2D double quantum filter after $^{1}H\{^{31}P\}$ REDOR difference; (c) $^{1}H$ 2D exchange after $^{1}H\{^{31}P\}$ REDOR difference.

*4.2.5 $^{1}H$-$^{31}P$ HetCor.*

Using $^{1}H$-$^{31}P$ HetCor experiments at 30 kHz MAS with short (200 μs) CP is another way to isolate the apatite protons. By applying a τ–π–τ echo sequence on the protons before cross polarization to the phosphorus, we can measure the $T_2$ relaxation of the apatite protons.

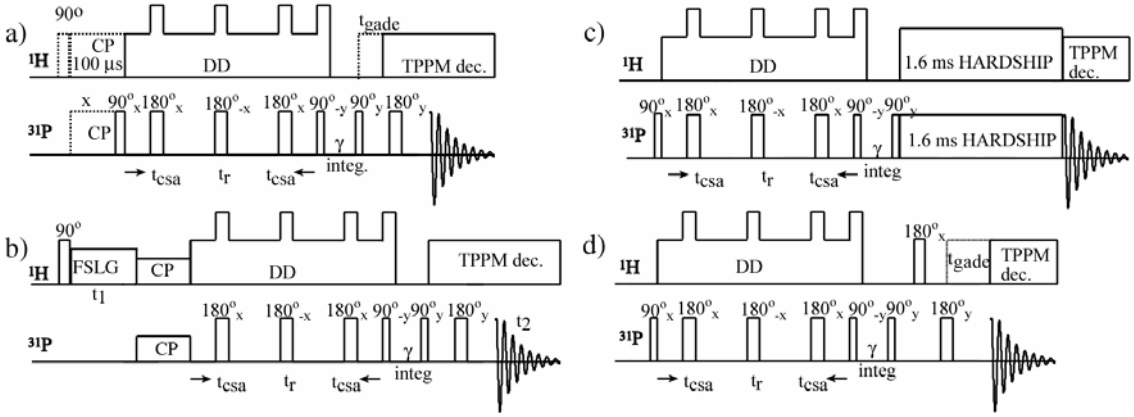


**Figure 2.** Pulse sequences for selective observation of $^{31}P$ CSA dephasing of different phosphate components. The CSA dephasing is caused by the 5 pulse scheme common to all the pulse sequences. (a) Selecting all the phosphates or the $HPO_4^{2-}$ only. (b) 2D HetCor to select the $PO_4^{3-}$–$H_2O$ phosphates. (c) HARDSHIP to select only the interior phosphates. (d) $^{1}H$-$^{31}P$ recoupling with gated decoupling to spectrally "strip away" the layers of surface phosphates.

*4.2.6 $^{1}H$ 2D double quantum NMR.*

During this experiment, we first select the apatite protons by 233 μs $^{1}H\{^{31}P\}$ REDOR and then have a double quantum excitation and reconversion period of $t_r/2$ = 16 μs each during which double quantum coherences between spatially close protons are excited. At 30 kHz MAS where the $^{1}H$-$^{1}H$ dipolar couplings are reduced, for the short DQ excitation times only protons that are very close are selected. The pulse sequence is illustrated in Figure 1 (b). The $t_1$ evolution time can be incremented in steps of $t_r/2$, with the receiver phase inverted, without intensity being dispersed into sidebands in the $\omega_1$ dimension. The $\omega_1$ dimension is

the double-quantum dimension, $\omega_2$ the single-quantum dimension.

*4.2.7 $^1H$ 2D exchange.*

This experiment enables us to see the spatial proximities of the various apatite protons within themselves and with the surrounding collagen protons. The apatite protons are selected by means of a soft and hard REDOR filter (266 μs and 733 μs respectively). The selected proton magnetization is then allowed to spin diffuse that enables them "see" neighboring protons, thereby identifying the environment of the bioapatite protons. The pulse sequence is illustrated in Figure 1 (c).

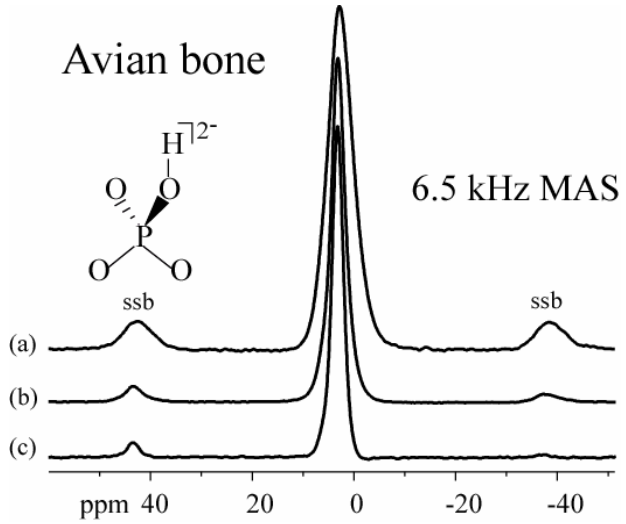


**Figure 3.** $^{31}P$ NMR spectra of avian bone. (a) The protonated phosphate species selected by 0.1 ms CP. (b) All the phosphates in the bioapatite selected by direct polarization. (c) Interior $PO_4^{3-}$ species selected by a 1.6 ms HARDSHIP filter. "ssb"= spinning sidebands

*4.2.8 HARDSHIP NMR.*

To select the phosphorus at the interior of the apatite crystal the $^{31}P$ nuclei at the surface by the protons must be dephased, without dephasing the interior $^{31}P$ nuclei by the dispersed protons in the apatite. This is achieved by HeteronucleAr Recoupling with Dephasing by Strong Homonuclear Interactions of Protons (HARDSHIP)[9] . In this method REDOR heteronuclear recoupling periods of ~0.15 ms alternate with periods of homonuclear dephasing flanked by canceling $90^0$ pulses. At the end of two rotation periods the heteronuclear evolution of the weakly coupled protons in the apatite interior is refocused, while the strongly coupled protons at the surface recouple their heteronuclear interaction thereby dephasing the surface phosphorus nuclei. For this experiment the 0.18 ppm resonance of the $^{1}H$ in the apatite was set on resonance. The HARDSHIP experiment was run at 6.5 kHz MAS.

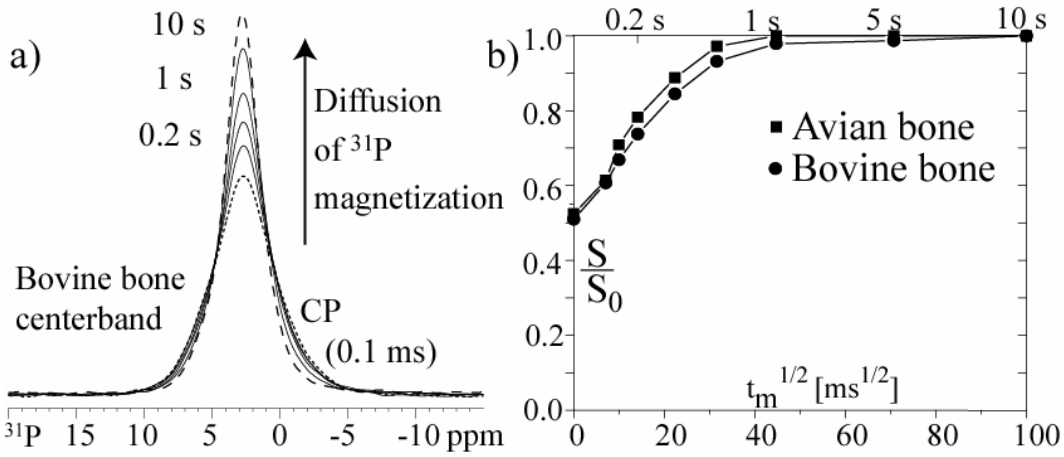


**Figure 4.** $^{31}P$ spin diffusion from protonated disordered (surface) to ordered (interior) phosphates in the bioapatite of bovine bone. (a) The $^{31}P$ lineshape changes a function of the spin diffusion from broad to narrow. (b) $^{31}P$ Spin diffusion build-up curves plotted for avian and bovine bone. Equilibration between the surface phosphates and the interior occurs within 1 s.

*4.2.9 $^{31}P$ CSA dephasing.*

Based on the symmetry of their local environments, phosphate groups have different chemical shift anisotropy (CSA). Under a five pulse scheme[10,11] depicted in Figure 2 that recouples the CSA, the phosphate groups in the apatite show a CSA dephasing behavior that is characteristic of their local environment. Direct polarization selects all the phosphates while a short 0.1 ms CP followed by an inverse 0.04 ms gated dephasing filter selects the $HPO_4^{2-}$ groups (Figure 2 a), HetCor allows us to select the $PO_4^{3-}$–$H_2O$ groups (Figure 2 b), 1.6 ms HARDSHIP selects the interior $PO_4^{3-}$ (Figure 2 c), and $^1H$-$^{31}P$ dipolar recoupling with gated dephasing from 0 to 0.3 ms selects phosphates at varying depths from the surface of the apatite crystal (Figure 2 d). The five-pulse CSA scheme is then applied to selectively look at the CSA dephasing behavior of the different phosphate species. As the total CSA dephasing behavior of the phosphates groups in the bioapatite is simply the weighted sum of the dephasing behavior of the individual phosphate groups, this method enables us to evaluate the different phosphate fractions.

**4.3 Results and Discussion**

*4.3.1 Ordered and disordered phosphate species.*

Figure 3 shows the $^{31}P$ NMR spectra of the avian bone. While the chemical shift of the peak does not change, the line width is different for the full DP, the CP and the HARDSHIP filtered DP spectra. The CP spectrum has a broader line width and larger spinning sidebands (ssb). These are primarily the protonated phosphate species $HPO_4^{2-}$ and the line shape indicates that they are in a disordered environment. The protonation breaks the symmetry of the tetrahedral phosphate resulting in a larger CSA which gives the larger ssb.

Conversely the HARDSHIP filtered spectrum, which corresponds to the interior of the apatite crystal, is narrower and with reduced spinning sidebands indicating unprotonated phosphates in a more ordered environment. Thus we see at least two distinct phosphate environments in the bioapatite.

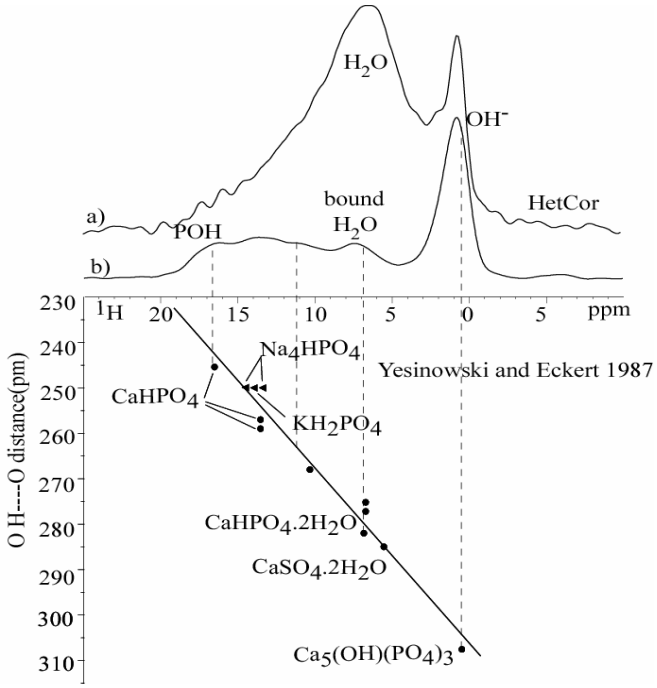


**Figure 5.** (a) $^{1}H$ cross section of 2D $^{1}H$-$^{31}P$ HetCor at 30 kHz MAS. (b) $^{1}H$ ΔS spectrum after 2.2 ms of $^{1}H\{^{31}P\}$ REDOR recoupling at 30 kHz MAS. The $HPO_4^{2-}$, $H_2O$, and $OH^-$ peaks are identified from the work on different calcium phosphates done by Yesinowski et.al.

*4.3.2 Contact of the disordered phosphates with the apatite crystal from $^{31}P$ spin diffusion.*

As shown in Figure 4 (a), the initial phosphate spectrum, which is detected after cross polarization and is mainly the $HPO_4^{2-}$, becomes narrower with increasing spin diffusion time which indicates that spin diffusion to the ordered phosphates in the interior takes place. This proves that the protonated phosphates are not a phase separated amorphous component, but constitute the disordered surface of the apatite crystals. The spin diffusion build-up curves

are plotted in Figure 4 (b) and show that the $^{31}P$ magnetization equilibrates within 1 s. The short equilibration times for spin diffusion, is consistent with the apatite crystal thickness of a few nanometers.

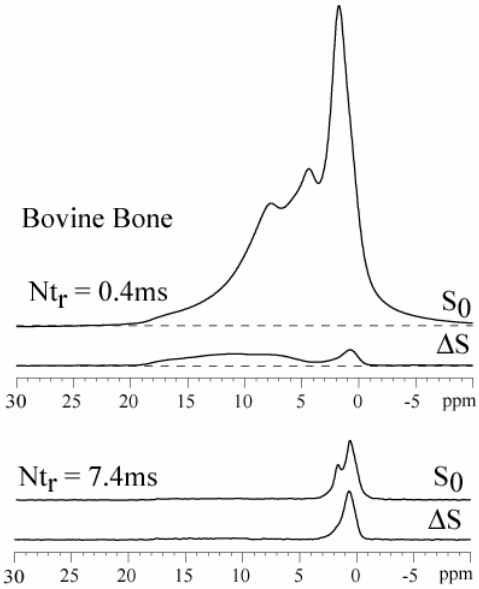


**Figure 6.** $S_0$ and ΔS $^1H$ NMR spectra of $^1H\{^{31}P\}$ REDOR of bovine bone at 30 kHz with recoupling times of 0.4 ms and 7.4 ms.

*4.3.3 Assignment of the $^1H$ spectra.*

Figure 5 (a) and (b) show the spectra of the apatite protons as revealed by $^1H$-$^{31}P$ HetCor and $^1H\{^{31}P\}$ REDOR. The spectra show a wide distribution of $^1H$ sites. The major peaks and shoulders were assigned based on the chemical shift trends compiled in by Yesinowski et al.[12] and our various 2D experiments. The 0.18 ppm peak is assigned to the hydroxyl ion of the apatite crystal. The large peak at 7 ppm seen in the HetCor (highly reduced in the REDOR spectrum due to $T_2$ relaxation) is assigned to water. The shoulder projecting out at 18 ppm is assigned to $HPO_4^{2-}$ groups. Due to the variety of the $HPO_4^{2-}$ environments these protons have a wide chemical shift distribution.

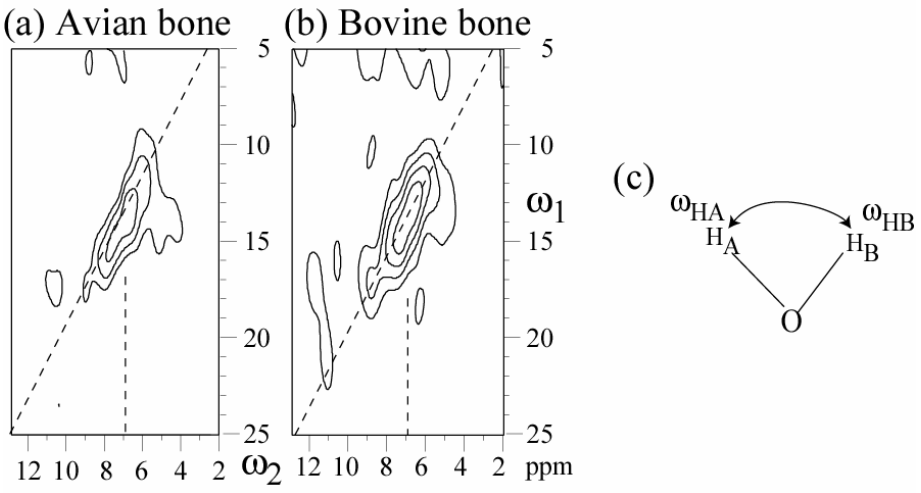


Figure 7. 2D double-single quantum $^{1}H$ spectra of protons near $^{31}P$ selected by $^{1}H\{^{31}P\}$ REDOR difference for (a) avian bone and (b) bovine bone at 30 kHz MAS. Spectra indicate a ridge along the slope 2 diagonal centered at 7 ppm. (c), a flipping water molecule, where $\omega_{HA} = \omega_{HB}$ and the dipolar coupling is unusually strong.

To confirm the assignment of the bound-water peak, a 2D double quantum experiment was performed. A 0.2 ms REDOR difference filter selects the apatite protons, followed by a 16 μs period during which double quantum coherences are allowed to evolve. Reconverting back to single quantum coherence and detecting, as seen in Figure 6, the only signal that appears is a ridge along a slope-2 diagonal centered at the 7 ppm resonance. The frequency in the DQ dimension is the sum of the frequencies of the $^{1}H$ spin pairs. As the DQ frequency is exactly twice the SQ frequency, this means that both the spins in the spin pair have the same frequency. This is a signature of a flipping $H_2O$ molecule where the chemical shifts of the two protons are averaged by the flipping motion. The $H_2O$ is frequency is shifted to a higher ppm value compared to liquid water because of hydrogen bonding to the apatitic phosphates.

*4.3.4 $^{1}H$ 2D exchange NMR to spatially locate the apatite protons.*

The previous experiments prove the presence of three types of apatitic protons namely **H**$PO_4^{2-}$, $PO_4^{3-}$–**H**$_2O$ and O**H**$^-$. $^{1}H$ spin diffusion can spatially locate these protons in the crystal interior, at the surface, or as uniformly distributed throughout the apatite crystal. The apatite protons are selected by REDOR, after which the magnetization of the apatite protons is allowed to spin diffuse to other protons. Figure 7 shows the $^{1}H$ 2D exchange spectra before and after spin diffusion. In the 266 μs REDOR selected spectrum, the exchange occurs on a timescale of 10 ms, while in the 733 μs selected spectrum it occurs on a 100 ms timescale. This is because the longer REDOR filter more strongly selects the protons in the interior of the apatite crystal. The $HPO_4^{2-}$ and the $PO_4^{3-}$–$H_2O$ protons are seen to quickly exchange with the surrounding collagen protons and with one another, while the $OH^-$ does not exchange much. This indicates that the $HPO_4^{2-}$ and the $PO_4^{3-}$–$H_2O$ protons are essentially surface species, while the $OH^-$ are largely isolated and located in the interior of the bioapatite crystals.

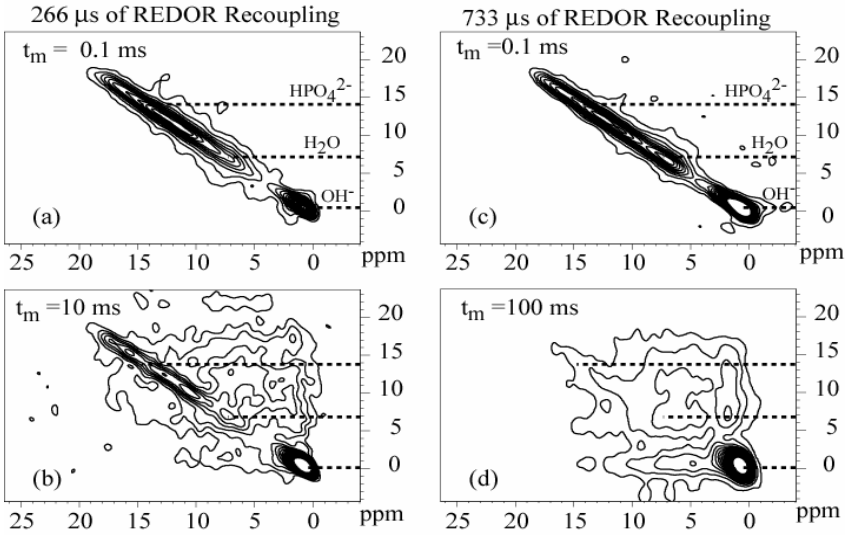


**Figure 8.** $^{1}H$ 2D exchange spectra of bovine bone at 30 kHz of protons near $^{31}P$ selected by $^{1}H\{^{31}P\}$ REDOR difference. 266 μs REDOR filter (a) without and (b) with 10 ms of spin diffusion. 733 μs REDOR filter (c) without and (d) with 10 ms of spin diffusion.

*4.3.5 $^{1}H\{^{31}P\}$ REDOR and $^{1}H$ $T_2$ of the apatite protons sites.*

To evaluate the apatite protons selected by the ΔS, the spectra must be normalized by the $S_0$ spectrum to account for the $T_2$ relaxation effect. However as seen in Figure 8, in the case of bone the $S_0$ spectrum is dominated by the collagen protons and even at longer recoupling times mobile components from the collagen persist. As a result, $\Delta S/S_0$ cannot be determined reliably. To overcome this problem, we introduce time periods before and after the REDOR time, during which only $T_2$ decay occurs. We vary these "$T_2$" periods along with the REDOR period in such a way that the total time and therefore the $T_2$ decay in all the experiment within the series is constant. Thus, using this "constant time" REDOR method we eliminate the effect of $T_2$ without determining $\Delta S/S_0$. The spectra for constant time REDOR are plotted in Figure 9 and the build-up curves for the different components are shown in Figure 10.

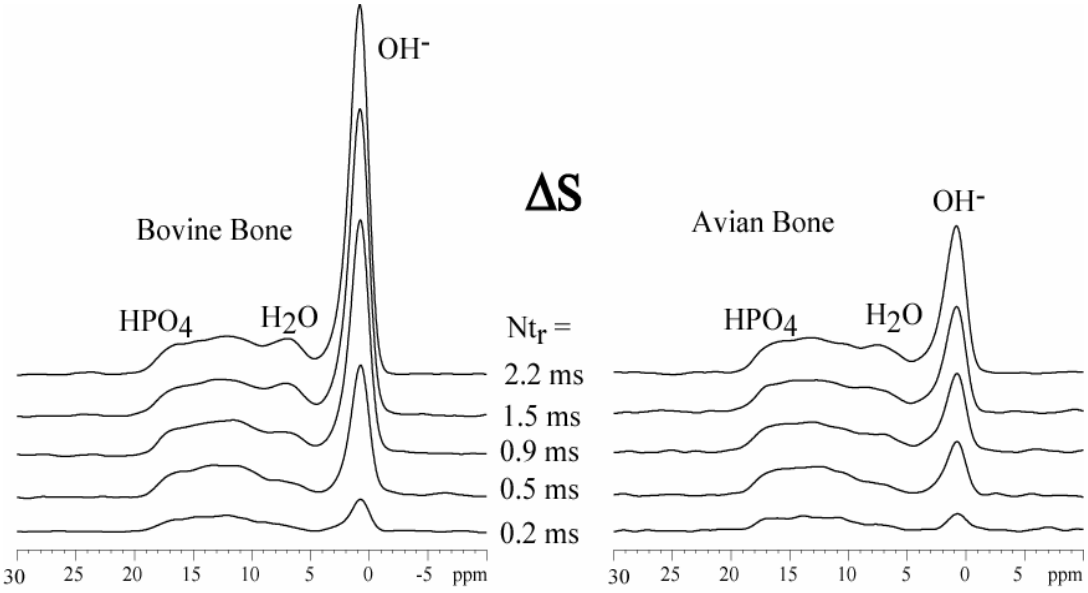


**Figure 9.** Series of $^{1}H\{^{31}P\}$ constant-time REDOR difference spectra of bovine and avian bone at 30 kHz MAS. The spectra show the build-up of the three different types of apatite protons with increasing dephasing time. All the spectra have the same $T_2$ relaxation effects.

The REDOR ΔS curve of the band at 18 ppm in Figure 9, corresponding to the $HPO_4$, has the strongest $^1H$-$^{31}P$ coupling as the $^1H$ is only two bonds away from the $^{31}P$ nucleus. The existence of a definite coupling as indicated by the presence of the REDOR rise curve for 8 ppm $H_2O$ peak confirms that this water is tightly bound to the apatite surface ($PO_4^{3-}$–$H_2O$) and is not mobile on a millisecond time scale. The REDOR curve of the $H_2O$ peak indicates a weaker coupling which is due to the longer hydrogen bond length. The $OH^-$ protons, which are at a distance of 0.4 nm from the nearest phosphorus, provide a useful reference for the $PO_4^{3-}$–$H_2O$ data.

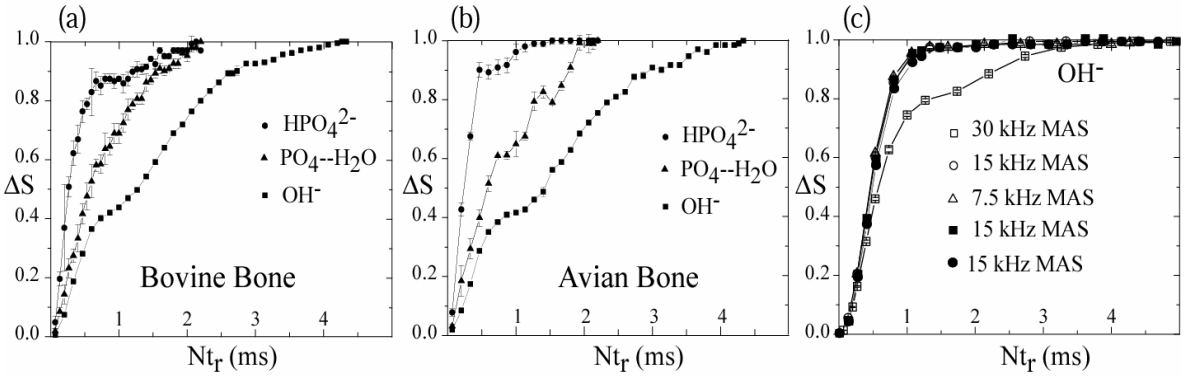


**Figure 10.** Constant-time $^1H\{^{31}P\}$ REDOR build-up curves at 30 kHz for (a) bovine bone, (b) avian bone and (c) NIST HAp. In (a) and (b) circles represent $HPO_4^{2-}$, triangle represent $PO_4^{3-}$–$H_2O$ and squares represent $OH^-$. (c) $OH^-$ REDOR build-up curves of NIST HAp at different spinning speeds (open circles, squares, and triangles), and of avian bone (filled squares) and bovine bone (filled circles) at 15 kHz MAS. All the build-up curves for REDOR at 15 kHz and 7.5 kHz MAS coincide.

To evaluate the relative fractions of the $HPO_4^{2-}$, $PO_4^{3-}$–$H_2O$ and $OH^-$ protons from a REDOR ΔS spectrum, we must integrate the corresponding peaks and then correct the integral for the $T_2$ relaxation effect and the REDOR dephasing, which is obtained from Figure 10. As shown before we cannot avail of the $S_0$ spectrum to determine the $T_2$ behavior, therefore we use a variable time REDOR method where the REDOR time is flanked with two equal $T_2$ decay times. This $T_2$ decay time is varied for a given REDOR time. Thus we get the

$T_2$ behavior around each REDOR point. Scaling out the REDOR effect we get a smooth $T_2$ decay curve as shown in figure 11. However it is not possible to determine the initial decay behavior by this method, because for very short REDOR recoupling times the ΔS spectrum has very low intensity. To determine the initial $T_2$ behavior, we use $^{1}H$-$^{31}P$ HetCor to selectively observe the apatite protons and apply echo periods to measure the $T_2$ decay.

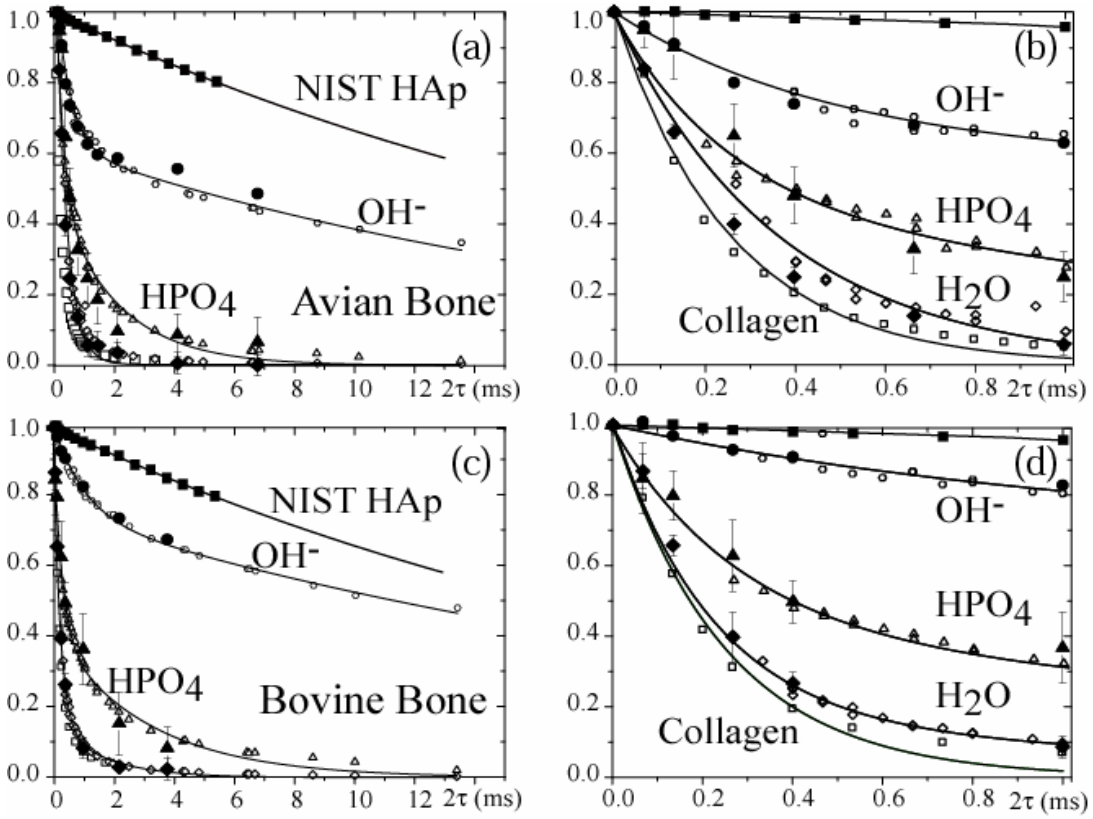


**Figure 11.** $T_2$ decay for various $^{1}H$ components measured in variable-time REDOR and 2D HETCOR experiments. (a) and (c) plot the $T_2$ decays of the various types of protons in avian and bovine bone at 30 kHz MAS. (b) and (c) are expanded view of the $T_2$ decay during the first millisecond. Filled squares at the top of each plot are NIST HAp $OH^-$ as a reference. The decay behavior for the apatite protons is essentially bimodal and can be fitted by a biexponential curve, with a sharp initial decay associated with the strongly coupled surface protons and a slow decay from the protons in the interior of the crystal. The collagen protons detected in unselective $S_0$ spectra are the fastest decaying (represented by open circles at the bottom of each plot) and an almost single exponential decay.

The HetCor data calibrates the initial $T_2$ decay and is plotted with the variable-time REDOR $T_2$-curves in Figure 11. $T_2$ decays of collagen and NIST hydroxyapatite (HAp: $Ca_{10}(PO_4)_6(OH)_2$), which are obtained by simple $^1H$ echo experiment, are also plotted in Figure 9. The NIST HAp which has very isolated $OH^-$ groups, has the longest $^1H$ $T_2$ relaxation time, while the collagen with its high density of protons has the shortest relaxation times. The collagen decay curves, obtained by a simple $T_{2,H}$ experiment are fit quite well by a single exponential decay curve while all the apatite proton species have a bimodal decay behavior with an initial sharp decay that corresponds to the surface groups and a long "tail" that corresponds to hydrogen atoms successively deeper from the bioapatite surface. Among the apatite protons, the $PO_4^{3-}$–protons have the shortest $T_2$, almost coinciding with the collagen decay curve due to strong dipolar couplings with each other and the collagen protons. The $HPO_4^{2-}$ curve has a slower decay indicating that while these are surface protons they are a little further away from the collagen and water protons. Although the $OH^-$ are isolated from one another, there is a significant fraction near the surface that has a short $T_2$ due to coupling with the bound water and collagen protons.

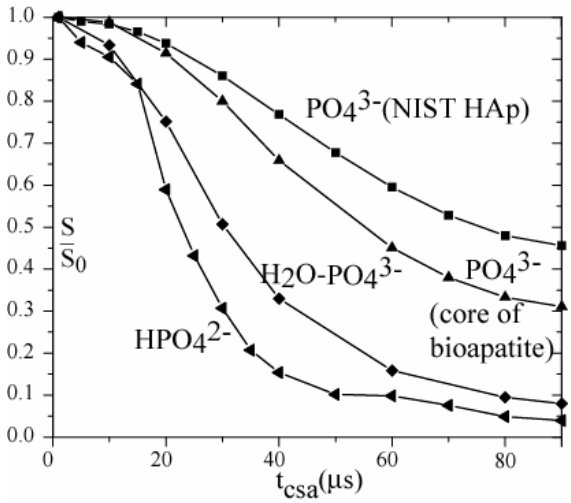


**Figure 12.** Normalized CSA dephasing curves of the different types of phosphates in the bioapatite are plotted. Filled squares represent $PO_4^{3-}$ ions in ideal hydroxyapatite; filled triangles represent $PO_4^{3-}$ groups in the core of the bioapatite; diamonds and tilted triangles represent the $PO4^{3-}$—$H_2O$ and $HPO_4^{2-}$ groups, respectively.

Correcting the peak integrals for the $T_2$ decay gives the ratios of the $HPO_4^{2-}$:$H_2O$:$OH^-$ listed in Table 1. To convert these ratios into fractions of the total phosphate i.e. $HPO_4^{2-}$: $PO_4^{3-}$–$H_2O$:$PO_4^{3-}$ we have calculated the mole fraction of the $OH^-$ by comparison with the NIST HAp[13]. The $OH^-$ peak integral is normalized by the integral of the fully relaxed phosphate peak. For NIST HAp the $OH^-$:P ratio corresponds to 100% $OH^-$ occupation. For the avian and bovine bone we get 14% and 20% $OH^-$ occupation, respectively (i.e. bovine bone has 0.066 moles of $OH^-$ per mole of phosphate ions). Knowing the $OH^-$:P ratio and ratios of the various apatite protons, we can obtain the fractions of the different phosphates as shown in Table 2.

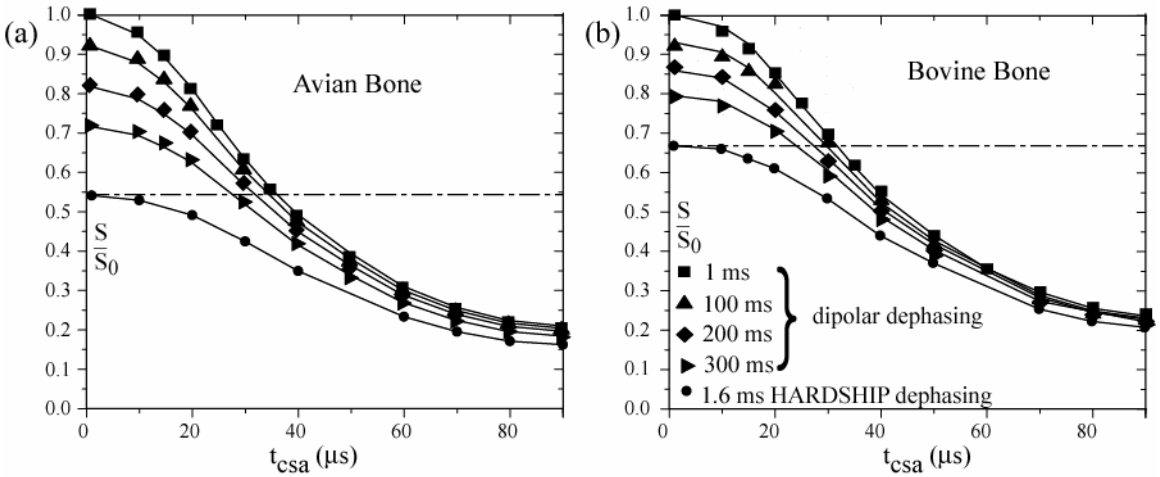


**Figure 13.** The CSA dephasing behavior of (a) avian and (b) bovine bone is plotted. The pulse sequence illustrated in figure 2 (c) and (d) were used. The filled squares represent the total CSA dephasing of all the phosphate components and are fit by a linear combination of the CSA dephasing curves of $PO_4^{3-}$, $PO_4^{3-}$—$H_2O$ and $HPO_4^{2-}$ plotted in Figure 11. The CSA dephasing behavior after 100 μs, 200 μs and 300 μs of gated recoupling and 1.6 ms of HARDSHIP recoupling, is plotted as closed triangles, diamonds, tilted triangles, and circles, respectively, with fit curves.

### *4.3.6 Evaluating the phosphate fractions by $^{31}P$ detected NMR.*

In addition to using $^1H$-detected NMR to evaluate the different phosphate fractions,

we have also determined the phosphate fractions via $^{31}P$ detected NMR. The CSA dephasing curves of the interior $PO_4^{3-}$, the $HPO_4^{2-}$, and the $PO_4^{3-}$–$H_2O$ are plotted in Figure 12. The CSA dephasing of $PO_4^{3-}$ of NIST hydroxyapatite (Hap) is also plotted for reference. From the dephasing behavior we can see that the $HPO_4^{2-}$ has the fastest CSA dephasing and therefore the largest CSA followed by the water bound $PO_4^{3-}$. The unbound $PO_4^{3-}$ in the apatite interior has the smallest CSA of the bioapatite phosphate species, which is however larger than that of the NIST HAp. This indicates a somewhat more distorted environment for the apatite $PO_4^{3-}$ groups as compared to the ideal NIST HAp.

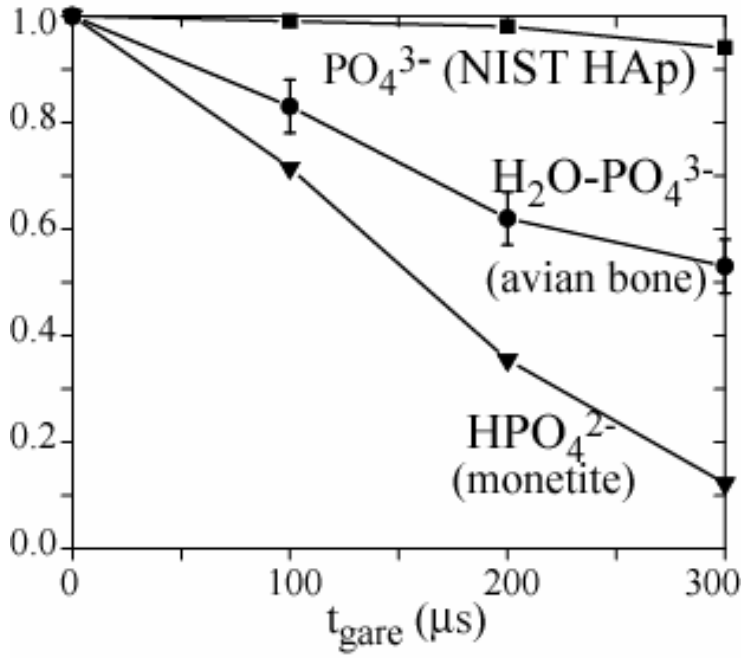


**Figure 14.** Dephasing of different phosphate species under $^1H$ recoupling with gated decoupling. Squares represent ideal $PO_4^{3-}$, circles represent $PO_4^{3-}$-$H_2O$ and triangles represent $HPO_4^{2-}$ species.

Knowing the CSA dephasing of the individual phosphate components of the apatite, we measure the total CSA dephasing curve of the bioapatite by direct polarization of the $^{31}P$ to select all the phosphate groups, followed by CSA dephasing and as shown in Figure 12. This CSA dephasing is then fitted by the fractional sum of the component $HPO_4^{2-}$, $PO_4^{3-}$–

$H_2O$ and $PO_4^{3-}$ CSA dephasing curves.

| Species | Avian Bone | Bovine Bone |
|---|---|---|
| $OH^-$ | 1 | 1 |
| $PO_4^{3-}$–$H_2O$ | 9.5 ± 2 | 2.3 ± 0.8 |
| $HPO_4^{2-}$ | 2 ± 0.5 | 0.8 ± 0.5 |
| Collagen | 90 | 159 |

**Table 1.** Relative amounts of $^1H$ in different protonated species

Although the dephasing curves in Figure 12 have different time constants, they still overlap heavily. In order to constrain the fit better, we combined CSA dephasing with gated decoupling and $^1H$-$^{31}P$ recoupling. Figure 13 shows the CSA dephasing behavior measured after applying 100 μs, 200 μs and 300 μs of $^1H$ recoupling with gated decoupling, and 1.6 ms of HARDSHIP. The application of varying periods of this gated decoupling/recoupling successively dephases the $HPO_4^{2-}$ and $PO_4^{3-}$–$H_2O$ phosphates. To fit these, curves we additionally need to determine the dipolar dephasing of the individual components. For $PO_4^{3-}$ and $HPO_4^{2-}$ we used NIST HAp and monetite ($CaHPO_4$) as model compounds. To measure the dipolar dephasing of the $PO_4^{3-}$–$H_2O$ group, it is selectively observed by HetCor, followed by the dipolar dephasing. This $^1H$-$^{31}P$ dipolar dephasing of the various components is plotted in Figure 14. The CSA dephasing behavior in Figure 13 is fit by the sum of the CSA dephasing curves of the three different phosphate groups weighted by their fractions and an additional dipolar dephasing factor obtained from the plots in Figure 14. The resulting fractions determined for the three phosphate components are tabulated in Table 2. The fitted curves in Figure 13 reveal the comparative fraction of the surface vs. the interior for the

bovine and avian bone apatite. We define the core of the apatite as the remnant after 1.6 ms of HARDSHIP dephasing. Thus the bovine bone has a thicker core and consequently a smaller surface fraction than the avian bone as, 46 % or the avian apatite is dephased by the HARDSHIP filter compared to only 34 % of the bovine apatite.

| Species | Avian Bone | | | | Bovine Bone | | | |
|---|---|---|---|---|---|---|---|---|
| Recoupling time | 0.1 ms | 0.2 ms | 0.3 ms | 1.6 ms HARDSHIP | 0.1 μs | 0.2 μs | 0.3 μs | 1.6 ms HARDSHIP |
| $PO_4^{3-}$ | 63% | 61% | 58% | 54 % | 71% | 71% | 69% | 66 % |
| $PO_4^{3-}$--$H_2O$ | 18% | 15% | 11% | 0 % | 14% | 11% | 9% | 0 % |
| $HPO_4^{2-}$ | 10% | 5% | 2% | 0 % | 8% | 4% | 1% | 0 % |

**Table 2**. Comparative fractions of different phosphate species after 0.1 ms, 0.2 ms, 0.3 ms of $^1H$ recoupling with gated decoupling, and 1.6 ms HARDSHIP.

### 4.4 Synopsis of $^1H$ and $^{31}P$ results.

Table 3 compiles the phosphate fractions and that were determined via $^1H$ and $^{31}P$ detected NMR experiments. The interior $PO_4^{3-}$ groups constitute a larger fraction of the total phosphates in bovine bone than in the avian bone. The avian bone has a larger fraction of the $PO_4^{3-}$–$H_2O$ while both types of bones have a similar fraction of and $HPO_4^{2-}$ groups. The values as determined by the two different approaches are in very good agreement with one another.

### 4.5 Conclusions and Outlook.

Solid state NMR is an excellent tool for investigating the surfaces of nanomaterials especially in biological systems where the surface is often sensitive to any harsh treatment. Using various advanced $^1H$-$^{31}P$ experiments we have shown the presence of three different

phosphate environments in the bioapatite of bone, associated with different kinds of protons: $PO_4^{3-}$ near $OH^-$, $HPO_4^{2-}$, and $PO_4^{3-}$–$H_2O$. We have shown that the surface consists of phosphates that are protonated or hydrogen bound to water. The hydrogen bonded water was observed selectively and shown to be strongly immobilized on the apatite surface. We showed that as much as 35 % of the phosphate constitutes the surface in avian bone while it is about 28 % for the bovine bone. This highlights the effects of nanocrystallinity on apatite in bone. This leads us to a more complete understanding of the bioapatite which is seen a more complex than previously thought. Combining this analysis of various types phosphates in conjunction with the quantification of other components of the bioapatite, such as the cations, carbonate species etc., we can achieve a full understanding of the composition of bioapatite in bone.

| Species | Avian Bone | | Bovine Bone | |
|---|---|---|---|---|
| Method | $^1$H NMR | $^{31}$P NMR | $^1$H NMR | $^{31}$P NMR |
| Interior $PO_4^{3-}$ | 67±5 % | 65±1 % | 76±4 % | 72±1 % |
| $PO_4^{3-}$--$H_2O$ | 23±5 % | 21±3 % | 17±2 % | 16±2 % |
| $HPO_4^{2-}$ | 10±3 % | 14±3 % | 7±2 % | 12±2 % |

**Table 3.** Fractions of different phosphate species in the avian and bovine bioapatite as determined by $^1$H and $^{31}$P quantification methods.

**Acknowledgments.**

Work at the Ames Laboratory was supported by the Department of Energy-Basic Energy Sciences (Materials Chemistry and Biomolecular Materials Program) under Contract No. DE-AC02-07CH11358.

**References**


1. Currey, J. The Mechanical Adaptations of Bone; Princeton University Press: Princeton, NJ, 1984.
2. Termine, J. D.; Eanes, E. D.; Greenfield, D. J.; Nylen, M. U.; Harper, R. A. *Calc Tiss Res* 1973, 12, 73-90.
3. Tong, W.; Glimcher, M. J.; Katz, J. L.; Kuhn, L.; Eppell, S. J. *Calci. Tiss. Int.* 2003, 72, 592-598.
4. Posner, A. S. *J Biomed Mater Res* 1985, 19, 241-250.
5. Hendricks, S. B.; Hill, W. L. *Science* 1942, 96, 255-257.
6. Betts, F.; Blumenthal, N. C.; Posner, A. S. *J Crystal Growth* 1981, 53, 63-73.
7. Armstrong, W. D.; Singer, L. *Clin Orthop Relat Res* 1965, 38, 179-190.
8. Gullion, T.; Schaefer, J. *J. Magn. Reson.* 1989, 81, 196-200.
9. Schmidt-Rohr, K.; Rawal, A.; Fang, X. W. *J Chem Phys* 2007, 126, 054701-054716.
10. Blanco, F. J.; Tycko, R. *J. Magn. Reson.* 2001, 149, 131-138.
11. Mao, J. D.; Schmidt-Rohr, K. *Solid State Nucl. Magn.* 2004, 26, 36-45.
12. Yesinowski, J. P.; Eckert, H. *JACS* 1987, 109, 6274-6282.
13. Rawal, A.; Schmidt-Rohr, K. *The Composition of Nanocrystalline Bioapatite in Bone* To be submitted.

# CHAPTER 5
# THE COMPOSITION OF NANOCRYSTALLINE BIOAPATITE IN BONE

Aditya Rawal, Klaus Schmidt-Rohr

*In the style of an article to be submitted to Science*

**One-sentence summary:** A comprehensive compositional analysis of the nanocrystalline bioapatite in bone has been achieved by solid-state NMR, resolving controversies and probing the depth of various ions from the organic-inorganic interface.

**Abstract**

Bone is a fascinating biological nanocomposite of calcium phosphate platelets imbedded in a hydrated collagen matrix. The nanocrystalline calcium phosphate is often referred to as hydroxyapatite, but hydroxide has been undetectable in vibrational spectra. Selective $^{1}H\{^{31}P\}$ nuclear magnetic resonance (NMR) enables quantification of the 5- to 8-fold reduced hydroxide concentration and explains the invisibility of $OH^-$ in unselective spectra. Carbonate, which is not a component of ideal hydroxyapatite, is conclusively proven to be incorporated in the bioapatite nanocrystals of native bone. A carbonate ion substitutes for about one out of every eight phosphates. $^{13}C\{^{1}H\}$ and $^{31}P\{^{1}H\}$ NMR experiments show that carbonate is neither a surface deposit nor a central nucleation layer, but has a slightly reduced concentration in the crystallite center. Strongly bound water is proven for the first time and is distinguished from monohydrogen phosphate at the nanocrystal surface. By combining NMR with energy dispersive analysis, a comprehensive view of bone apatite composition is obtained.

## 5.1 Introduction

The load-bearing material in bone is a nanocomposite of ~ 3-nm thick apatite (calcium phosphate) platelets imbedded in a collagen matrix, with a volume ratio typically near 45:50 and the remaining 3-10% accounted for by water. The origin of nanocrystallinity and the composition of the bone apatite, which are of significant interest in the design of bone-mimetic materials, is still contentious. While it shows the wide-angle X-ray diffraction pattern of hydroxyapatite, $Ca_{10}(PO_4)_{10}(OH)_2$, spectroscopic analyses have detected no[1,2] or reduced (21%)[3] hydroxide ($OH^-$) concentrations. Carbonate is detected easily in chemically or thermally treated anorganic bone[4], but reliable quantification in native bone has been challenging due to the collagen background, with reported values ranging between 3.5 and 5 wt%. Methods to rigorously prove to what extent carbonate is indeed located in the apatite and not a separate phase [5] have been lacking, and quantification by double difference[6] has large error margins. For hydrogen phosphate, $HPO_4^{2-}$, another component absent from ideal hydroxyapatite, concentrations between 5 % and 25 % of all phosphates have been reported[7].

We resolve these issues conclusively by advanced solid-state NMR, which allows us not only to quantify many species in the apatite but also to prove the proximity of carbonate to collagen and $OH^-$ protons. Our recently developed HeteronucleAr Recoupling with Dephasing by Strong Homonuclear Interactions of Protons (HARDSHIP) NMR method[8] furthermore enables us to determine whether carbonate is concentrated in a central nucleation layer[9] or a surface deposit[10] and compare its distribution to that of hydroxide. In addition, we prove the presence of strongly phosphate-bound water and quantify $HPO_4^{2-}$, which is found mostly near the apatite surface. Combining quantitative NMR of $PO_4^{3-}$, $OH^-$, $CO_3^{2-}$, $HPO_4^{2-}$, and bound $H_2O$ with information on cation concentrations from energy-dispersive analysis, we are able to provide a comprehensive analysis of the average composition of bone apatite.

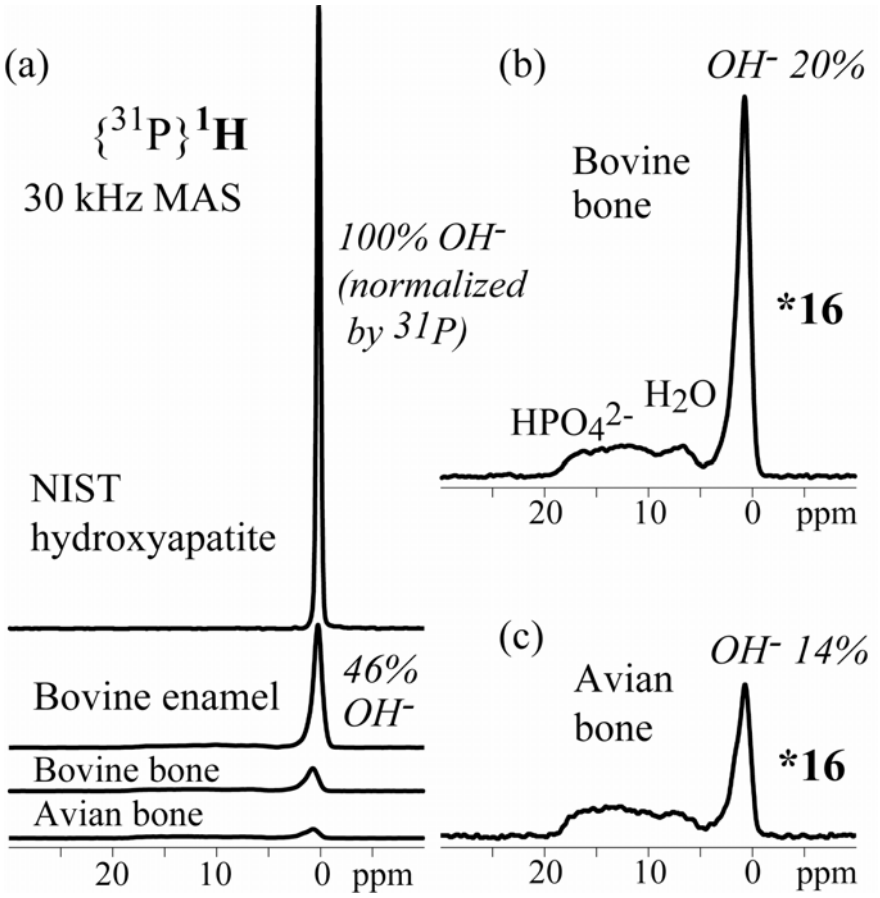


**Figure 1.** $^{1}H\{^{31}P\}$NMR spectra for quantifying the $OH^-$ concentration in native bone. (a) Spectra of $OH^-$ in NIST HAp (the same material as in the Raman study of ref.[1]), bovine enamel, avian bone, and bovine bone (top to bottom), selected based on their proximity to $^{31}P$ and long $T_{2,H}$. Spectra after 16-fold vertical scaling of (b) bovine bone, (c) avian bone.

## 5.2 Results and Discussion

### *5.2.1 Hydroxide concentration.*

There is consensus that bone apatite is depleted in $OH^-$ groups, but their concentration has been a matter of debate. Recent NMR experiments have yielded a value of 21 ± 1% of

the $OH^-$ concentration in regular hydroxyapatite[3], while the Raman spectrum of mouse bone did not show the sharp $OH^-$ vibration peak observed in NIST hydroxyapatite[1]. We can resolve this apparent contradiction by comparing selective NMR spectra of $OH^-$ protons in standard HAp, bovine enamel, bovine bone, and avian bone with their actual relative intensities, see Figure 1a. The $OH^-$ signals were selected from the background of collagen protons based on their 0.4-nm proximity to $^{31}P$ and their large $^1H$-$^1H$ internuclear distances, using $^{31}P\{^1H\}$ REDOR difference NMR spectroscopy at 30-kHz MAS. The distinctive 0.35-ppm chemical shift further helps in the identification and quantification of the hydroxide ions. For a meaningful quantification, we have referenced the hydroxide amount to the amount of phosphate in the same samples by quantitative $^{31}P$ NMR spectroscopy. We have also corrected for the $T_{2,H}$ decay, measured in $^{31}P\{^1H\}$ HetCor experiments, and for incomplete heteronuclear dephasing (a common factor for all samples) during the REDOR experiment.

The vastly different intensities of the spectra in Figure 1a show that detection of hydroxide in bone is much more challenging than in standard hydroxyapatite. It is clear that the corresponding miniscule Raman signals of bone $OH^-$ are invisible due to background from hydroxyproline, while advanced NMR has the required selectivity and sensitivity for their detection. The height of the bone $OH^-$ signals in NMR and Raman spectroscopy is reduced by three factors: (i) 2.5-fold dilution of apatite in bone collagen; (ii) peak broadening due to imperfect ordering; and (iii) 5- to 8-fold reduced $OH^-$ concentration in bone apatite. Figures 1b, c show the spectra of bovine and avian bone after 16-fold vertical scaling; their signal-to-noise ratios are excellent.

*5.2.2 Bound water and $HPO_4^{2-}$.*

Figures 1b, c show additional signals of protons near phosphorus, with $^1H$ chemical shifts ranging from 18 to 5 ppm. These can be assigned to $HPO_4^{2-}$ and $PO_4^{3-}$ near $H_2O$. The signals can be observed at close to their full intensity, without $T_{2,H}$ dephasing, in $^1H\{^{31}P\}$ HetCor spectra. These experiments provide the $^1H$ spectrum of protons near $^{31}P$, with weighting in favor of the nearest species. The $^1H$ projection shows the $OH^-$ peak at 0.35 ppm, most clearly after $T_{2,H}$ filtering, Figure 2c,d, with higher intensity in bovine than in avian bone, as expected.

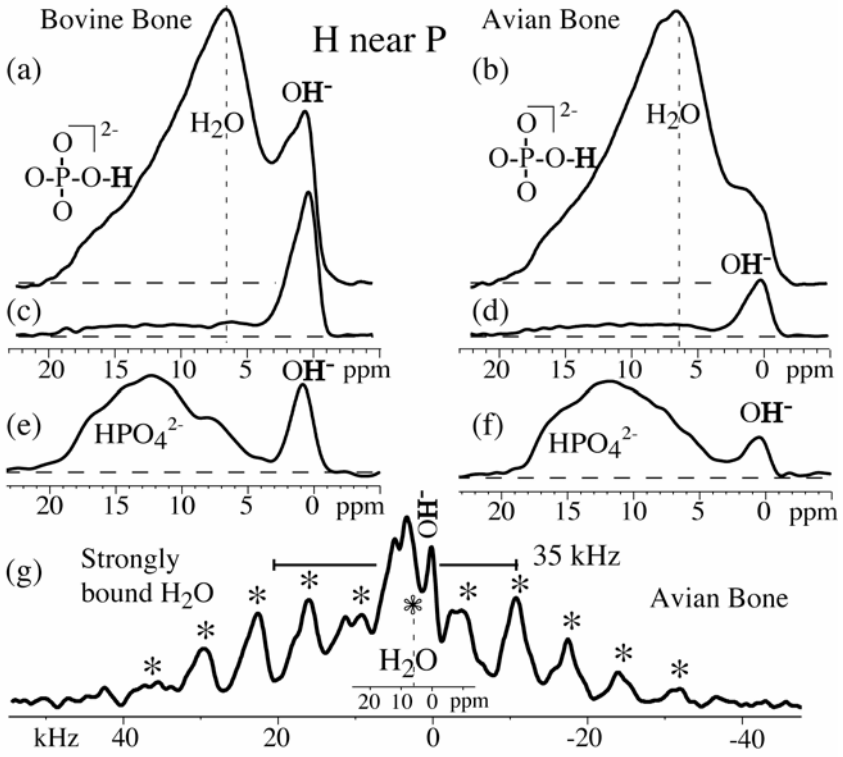


**Figure 2.** $^1H$-$^{31}P$ NMR spectroscopic characterization of protons near phosphate for avian (left column) and bovine bone (right column) by various $^1H$-$^{31}P$ double-resonance NMR experiments. (a, b) Projections of the $^1H$-$^{31}P$ HetCor spectra on the $^1H$ axis. (c, d) Same as (a, b) but after a $T_{2,H}$ filter that selects signals of protons dispersed in the apatite. (e, f) Spectra highlighting monohydrogen phosphate and hydroxide, obtained by 30-kHz $^1H\{^{31}P\}$ REDOR difference with a 0.2 ms $^1H$-$^{31}P$ recoupling period. (g) Sideband pattern of strongly bound water after 1-ms $T_{1\rho}$ and inverse $T_{2,H}$ filter, for avian bone. Sidebands and the centerband, which are spaced by the spinning frequency of 6.5 kHz, are marked by *. The same sideband pattern is observed for bovine bone (not shown).

The spectra in Figure 2a,b are dominated by a broad band around 7 ppm. This signal can be assigned to strongly bound $H_2O$ based on the wide range of spinning sidebands in its wideline spectrum, Figure 2e. The sidebands with an envelope exhibiting two maxima reminiscent of a Pake powder pattern[11] and a dipolar coupling constant of ~ 35 kHz are characteristic of relatively isolated H-H spin pairs with an internuclear distance of ~0.17 nm distance, as in $H_2O$. No significant motional averaging of the H-H dipolar coupling is observed, proving the strong binding of both $H_2O$ protons to specific H-bond acceptors. It is possible that these $H_2O$ molecules undergo $180^o$-flips, which interchange the O-H bonds but just inverts the H-H vector and thus leaves the geminal H-H coupling invariant.

Hydrogen phosphate, $HPO_4^{2-}$, account for the signals between 10 and 18 ppm. These protons show fast $^1H$-$^{31}P$ cross polarization and REDOR dephasing, but only weak dipolar sidebands in Figure 2e, confirming that they are at a two-bond distance from P and relatively isolated from other protons. The presence of two types of protons near phosphate, namely $PO_4…H_2O$ and $HPO_4$, was not previously recognized, for instance in a study claiming to have proven a water layer at the apatite surface.[12] Further confusion was generated in that study when these surface-bound protons were conflated with a third type of protons near the nanocrystals, a layer of long-$T_{2,H}$, mobile water that is not directly bound to the nanocrystals since it gives no signal in $^1H$-$^{31}P$ wideline-separation (WISE) NMR without spin diffusion.

*5.2.3 Carbonate in native bone.*

Based on vibrational spectroscopy of chemically or thermally treated anorganic bone, or of enamel, it has been concluded that apatite in bone is carbonated, but this has been difficult to prove rigorously for native bone. Quantitative $^{13}C\{^1H\}$ NMR spectroscopy of carbonate, after sufficiently long recycle delays (2,000 s) and selective dephasing of the collagen signals, can achieve the task of detecting and quantifying carbonate even in the

presence of collagen. Figure 2a shows the total $^{13}C$ NMR spectrum of native avian bone, which is dominated by collagen signals. After short $^{13}C\{^{1}H\}$ HARDSHIP dephasing, the collagen bands are suppressed and the peak of carbonate with its characteristic chemical shift between 165 and 170 ppm is selected, see Figure 2b. In contrast to other dephasing methods such as REDOR, HARDSHIP avoids dephasing of carbonate by $OH^-$ protons in the apatite. The observed carbonate chemical shift of 169 ppm is indicative of type B carbonated apatite, where carbonate replaces phosphate rather than hydroxide;[13] this is consistent with vibrational spectroscopy of chemically or thermally treated anorganic bone, though IR studies of enamel have suggested a ~1:1 ratio of type A and B.

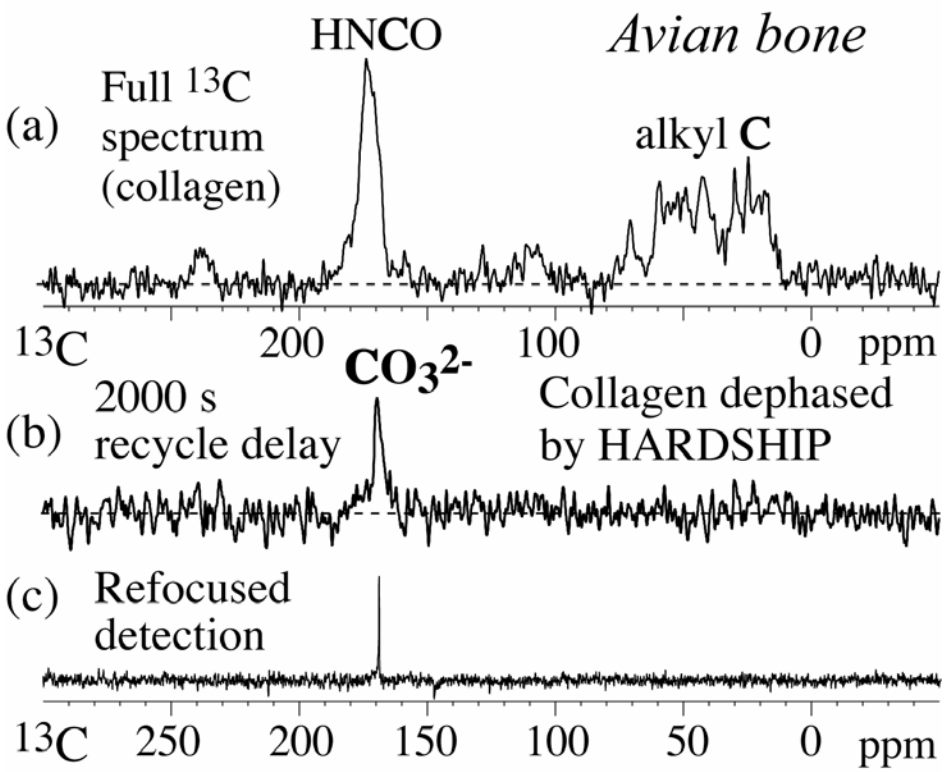


**Figure 3.** Quantitative $^{13}C$ NMR spectra for quantifying the carbonate concentration in native avian bone. (a) Quantitative direct-polarization $^{13}C$ spectrum (b) Selective spectrum of carbonate after short 0.3-ms HARDSHIP dephasing of $^{13}C$ near $^{1}H$, with a recycle delay of 2,000 s. (c) Same as b) but with refocused detection of the carbonate signal, which provides ~8-fold signal enhancement. The corresponding spectra of bovine bone are similar.

Figure 2c demonstrates carbonate signal enhancement by refocused detection,[14] which takes advantage of the long (> ADU 20 ms) transverse relaxation time of carbonate. Integration shows that the carbonate accounts for 5 % of all carbon and replaces one out of eight phosphates. The quantification relative to phosphate requires knowledge of the apatite : collagen ratio in the sample, which we have determined by thermogravimetric analysis and confirmed by calibrated quantitative $^{31}$P and $^{1}$H NMR spectroscopy. The carbonate weight fraction of avian-bone apatite is 5.5 ± 3 wt%, while it is 7.8 wt% in bovine-bone apatite. These values are higher than previously estimated using more indirect wet-chemistry and double-difference vibrational spectroscopy methods.

*5.2.4 Proof of carbonate in bone apatite.*

The mere detection of carbonate does not prove its incorporation into the apatite. Skinner warned that "Biological apatitic materials contain bio-molecules and probably carbonate, if not $CaCO_3$, associated with apatitic minerals".[5] However, advanced NMR can provide this proof even in native bone, based on dipolar dephasing of carbonate by protons of collagen and hydroxide, with refocused detection for signal enhancement. Figure 4a shows that $^{31}$P{$^{1}$H} and $^{13}$C{$^{1}$H} REDOR dephasing curves of carbonate and phosphate, respectively, track very closely, after correction for the 1.6-times smaller gyromagnetic ratio of $^{13}$C vs. $^{31}$P, down to a residual intensity of 5%. This proves that >95% of carbonate is not precipitated as large crystals of proton-free minerals such as $CaCO_3$ and suggests that they are part of the apatite nanocrystals. Proof that carbonate is incorporated into the apatite crystal lattice is provided by HARDSHIP NMR without and with $OH^-$ dephasing, see Figure 4b. When dephasing by $OH^-$ protons is switched on, by inverting the phase of every other 90$^o$ pulse in the HARDSHIP sequence, carbonate is dephased more strongly, just like

phosphate, see Figure 4c. This proves that carbonate is within 0.6 nm from the residual hydroxide in bone apatite.

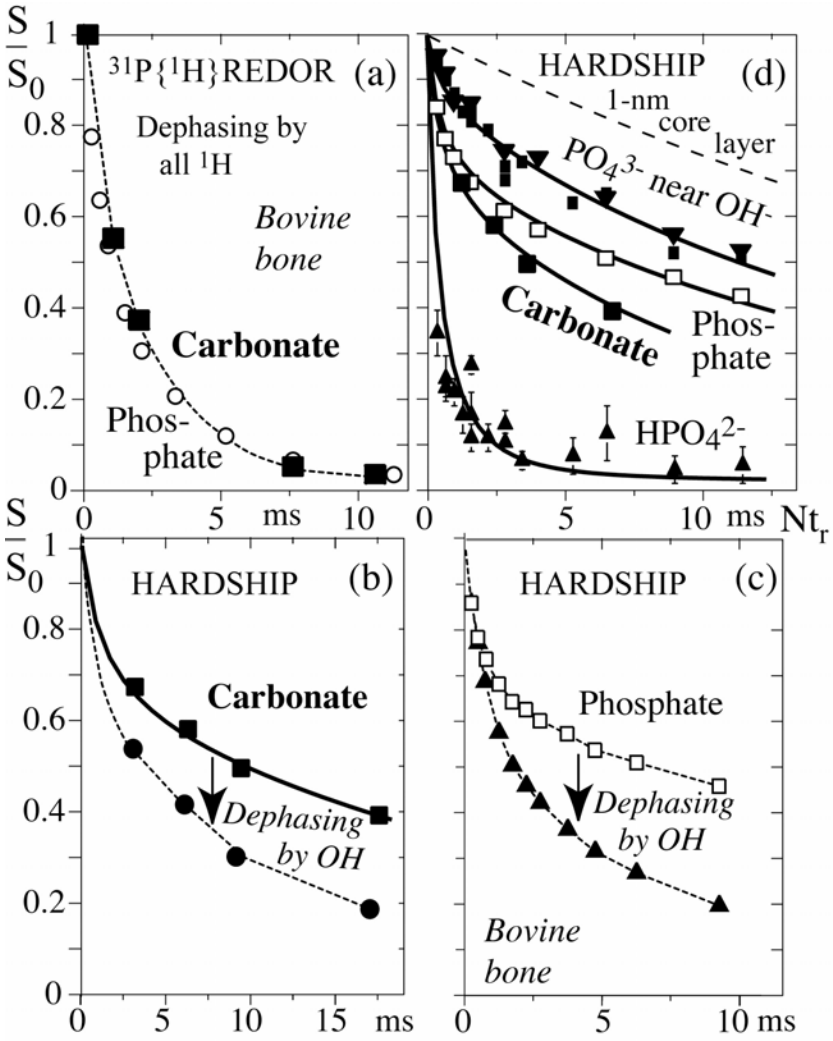


**Figure 4. NMR data proving that all carbonate is part of the apatite nanocrystals, and probing the distance of various anions from the organic-inorganic interface in bovine bone**. (a) $^{13}C\{^1H\}$ (filled triangles) and $^{31}P\{^1H\}$ (open circles) dephasing by all protons, using REDOR. (b) $^{13}C\{^1H\}$ HARDSHIP dephasing without (squares) and with (circles) dephasing by $OH^-$. (c) $^{13}C\{^1H\}$ HARDSHIP dephasing without (squares) and with (circles) dephasing by $OH^-$. In a), the time axis of the $^{13}C$ data was scaled by $\gamma_P/\gamma_C$, in b) by $(\gamma_P/\gamma_C)^2$ as required by REDOR and HARDSHIP theories, respectively. (d) Heteronuclear dephasing by surface and collagen protons, using $^{31}P\{^1H\}$ and $^{13}C\{^1H\}$ HARDSHIP NMR. $PO_4^{3-}$ near $OH^-$: Small squares and inverted triangles are from dephasing of the OH- peak in 2D HetCor spectra and $T_{2,H}$-filtered 1D experiments, respectively. Dashed line: simulation of the dephasing of a central layer of 1-nm thickness. Spinning frequency: 6.5 kHz.

*5.2.5 Depth from the interface.*

The HARDSHIP data of Figure 4b do not just prove that carbonate is incorporated in the bone apatite, but also provide information on its distance from the organic-inorganic interface. The comparison with the phosphate dephasing in Figure 4d, again after correction for the 1.6-times smaller gyromagnetic ratio of $^{13}C$ vs. $^{31}P$, shows that carbonate is not a surface deposit[10], which would be dephased very quickly, like the $HPO_4^{2-}$ ions in Figure 4d. Neither is it concentrated in a central layer,[9] where it would be so far from the collagen protons that it hardly dephases on the 10-ms time scale (dashed line in Figure 4d). Carbonate is seen to dephase slightly faster than phosphate, which indicates that it is somewhat depleted near the crystal core.

The phosphate dephasing was simulated for assuming a wide platelet of 2.2 nm P-to-P thickness, with a 0.36-nm phosphate layer spacing. The actual platelet thickness would be $2 \cdot 0.3$ nm larger than the P-to-P thickness, i.e. ~2.8 nm, since P is surrounded by oxygen and therefore never directly at the surface. A proton number density of $1/(0.29\ nm)^3$ in the collagen matrix was used in the simulation, and $T_{2,H}^* = 0.4$ ms relaxation of the $OH^-$ protons was taken into account; 13-kHz MAS HARDSHIP data with much slower $OH^-$ relaxation of $T_{2,H} \sim 6$ ms were fitted simultaneously. The model of platelets of a single thickness is only an approximation; any model with the same surface-to-volume ratio will give similar HARDSHIP dephasing. Small-angle X-ray scattering shows strong evidence of a distribution of nanoparticle thicknesses,[15] while wide-angle X-ray diffraction disproves wide platelets. The carbonate dephasing curve was fit by assuming no carbonate in the central phosphate layer, only 20% in the two layers flanking the central one, and only 40% in the surface layer.

The HARDSHIP dephasing of $PO_4^{3-}$ near hydroxide, selectively observed at 0.35 ppm in the $^1H$ dimension of $^1H$-$^{31}P$ HetCor spectra, is shown as the top curve in Figure 4d. It tracks that of all the phosphate, except that it lacks the fast initial decay of 60% of the sites near the organic-inorganic interface, according to the simulated curve. The phosphates near the surface are mostly protonated $HPO_4$ and therefore resonate at > 9 ppm rather than at 0.35 ppm in the $^1H$ dimension. Homonuclear dephasing of directly detected $OH^-$ protons by collagen protons (not shown) gives no indications of surface depletion.

(a)

| Method | Composition ratios | NIST HAp | Bovine bone | Avian bone |
|---|---|---|---|---|
| EDA | Ca:P | 1.67 | 1.4(9±1) | 1.4(2±4) |
| NMR | $OH^-$:P | 0.33 | 0.06(3±6) | 0.03(8±5) |
| NMR | $HPO_4^{2-}$:P | 0.0 | 0.1(0±4) | 0.1(4±4) |
| NMR | $CO_3^{2-}$:P | 0.0 | 0.1(6±4) | 0.1(4±4) |
| EDA | Mg:Ca | 0.0 | 0.02(9±6) | 0.03(9±8) |
| EDA/NMR | Na:Ca | 0.0 | 0.0(4±1) | 0.0(2±1) |

(b)

| | | | |
|---|---|---|---|
| Ideal hydroxyapatite: | $(Ca^{2+})_{10}$ | $(PO_4^{3-})_6$ | $(OH^-)_2$ |
| CDHAp (x = 1): | $(Ca^{2+})_9$ | $(PO_4^{3-})_5 (HPO_4^{2-})$ | $(OH^-)$ |
| Bovine bone: $(Ca^{2+})_8(Mg^{2+})_{0.32}(Na^+)_{0.4}$ | $(PO_4^{3-})_{4.74}(HPO_4^{2-})_{0.53}(CO_3^{2-})_{0.73}$ | $(OH^-)_{0.3}$ $(H_2O)_{0.8}$ | |
| Avian bone: $(Ca^{2+})_{7.9}(Mg^{2+})_{0.37}(Na^+)_{0.25}$ | $(PO_4^{3-})_{4.57}(HPO_4^{2-})_{0.81}(CO_3^{2-})_{0.62}$ | $(OH^-)_{0.22}$ $(H_2O)_{1.1}$ | |

**Table 1.** Composition of bovine and avian bone, compared with NIST hydroxyapatite, obtained from NMR and EDA. (a) Molar ratios of elements or ions. (b) Charge-balanced compositions of apatite in the three samples.

*5.2.6 Quantitative composition.*

Based on the quantitative $^{31}P$, $^{1}H$, and $^{13}C$ NMR spectra, combined with data from energy-dispersive analysis, and the proof that all the carbonate is in fact incorporated into the apatite nanocrystals, we can calculate the average composition of the bone apatite in a given sample. Table I(a) gives the composition data from NMR and EDA. In part (b), the corresponding compositions of bovine and avian bones, adjusted within their error margins to ensure charge balance, are compared with those of ideal hydroxyapatite. $^{19}F$ NMR showed no indication of significant fluoride incorporation in these bones. The data provide quantitative proof that the chemical complexity of apatite in bone is much greater than that of standard hydroxyapatite. Depletion of calcium and hydroxide accompanies enrichment in carbonate and hydrogen phosphate; the latter is a direct consequence of the large fraction of surface sites in nanocrystalline apatite.

It has been suggested that bone apatite is calcium deficient hydroxyapatite (CDHAp): $Ca_{10-x}(HPO_4)_x(PO_4)_{6-x}(OH)_{2-x}$ with $0 < x < 1$.[16] However, even at $x = 1$, the hydrogen phosphate concentration would not exceed the $OH^-$ concentration, in contrast to our experimental findings. Correspondingly, the $OH^-$ concentrations found here and by Ackermann et al.[3] are smaller than the allowed range of CDHA. Furthermore, HARDSHIP and spin diffusion experiments (not shown here) demonstrate that the $HPO_4$ groups mostly cover the apatite surfaces.

It is interesting that the compositions of the avian and bovine bone nanocomposite are so similar, given that the evolutionary lines of birds and mammals diverged more than 150 million years ago. It seems reasonable to attribute these highly conserved features to important functional advantages.

## 5.3 Methods

### *5.3.1 Samples.*

Samples of the midsection of the femur bone were excised from a mature chicken and a four-year old cow. They were cleaned of all surface tissue and shaken with a methanol chloroform de-fatting solution to remove any trace of lipids. The bones were filtered, crushed under liquid nitrogen to sub-millimeter size and then dried at $-40^0$ C in a lyophilizer for several days to dry the bone and remove all traces of solvent. The samples were packed in 2.5 mm, 4 mm and 7mm rotors for NMR study. For the energy dispersive analysis, the crushed bone was embedded in resin and then polished to a smooth surface.

### *5.3.2 NMR parameters.*

The NMR experiments were performed using a Bruker DSX400 spectrometer at 400 MHz for $^1$H and 162 MHz for $^{31}$P. A Bruker 2.5-mm double-resonance magic-angle spinning (MAS) probehead was used for 30-kHz MAS $^1$H{$^{31}$P} REDOR NMR experiments that record the difference spectrum of experiments without and with $^{31}$P 180$^o$ recoupling pulses of 7 μs duration. A Bruker 7-mm double-resonance probehead was employed for $^1$H-$^{31}$P, $^{31}$P{$^1$H}, and $^{13}$C{$^1$H} experiments at 6.5-kHz MAS, with 90$^o$ pulse lengths of 4 μs. In $^1$H and $^1$H-$^{31}$P cross polarization (CP) experiments, including heteronuclear correlation (HetCor), the recycle delays were 3 s. All $^{31}$P and $^{13}$C spectra were acquired with $^1$H dipolar decoupling. Refocused detection using a train of 180$^o$ pulses[14] was used for enhancement of carbonate signals.

Quantitative $^{31}P$ spectra were obtained with 3000 s recycle delays and 2 scans. Quantitative $^{13}C$ spectra of collagen in bone were recorded with 2000 s recycle delays. The $^{1}H$-$^{31}P$ HetCor spectra were obtained with homonuclear frequency-switched Lee-Goldburg (FSLG) decoupling applied during $t_1$ evolution, followed by 0.2 ms of Lee-Goldburg cross polarization; spectra were recorded without and with $T_{2,H}$ filtering of $2t_r$ duration. $^{1}H$-$^{31}P$ wideline-separation (WISE) spectra of bound water were measured at 6.5 kHz MAS with 0.5 ms of Hartmann-Hahn CP. The hypercomplex (cosine and sine) data mode was used, with a 9.62 μs dwell time in the indirect dimension. An inverse $T_{2,H}$ filter of $2t_r$ duration was applied to remove the strong $OH^-$ peak, a 1-ms $T_{1\rho}$ filter to eliminate any signal of mobile $H_2O$.

The depth of specific anions from the organic-inorganic interface was probed using the strongly distant-dependent dipolar couplings between the abundant protons in collagen matrix and $^{31}P$ or $^{13}C$ nuclei in the apatite. This approach requires a pulse sequence that ensures heteronuclear dephasing only by the collagen and apatite surface protons, but not by the $OH^-$ protons in the apatite. This is achieved by HeteronucleAr Recoupling with Dephasing by Strong Homonuclear Interactions of Protons (HARDSHIP)[8], which distinguishes between the collagen and apatite-dispersed protons based on their different transverse ($T_{2,H}$) relaxation times. The HARDSHIP pulse sequence alternates REDOR heteronuclear dipolar recoupling [17] by 180° pulses on $^{1}H$ for 0.15 ms with 0.15-ms periods of homonuclear dipolar $T_{2,H}$-dephasing that are flanked by canceling 90° $^{1}H$ pulses. The heteronuclear evolution of the long-$T_{2,H}$ $OH^-$ protons is refocused after two recoupling periods. The rate of heteronuclear dephasing by the strongly coupled, short-$T_{2,H}$ protons in the collagen depends simply on the heteronuclear second moment, not on the homonuclear interactions[8]. For HARDSHIP dephasing of total $^{31}P$ and carbonate, quantitative signals were generated by direct polarization after long recycle delays of 200 s and 1000 s,

respectively. In order to measure dephasing of $HPO_4$ and of phosphate near $OH^-$ selectively, we have inserted HARDSHIP dephasing into $^1H$-$^{31}P$ HetCor experiments and monitored the dephasing of the $HPO_4$ and $OH^-$ signals, identified by their $^1H$ chemical shift. In some experiments, the coupling to $OH^-$ protons was selectively "switched on" by inverting the phase of every other $90^o$ pulse on $^1H$, so that these combine to $180^o$ pulses as in REDOR. All HARDSHIP experiments shown were run at 6.5 kHz MAS.

**Acknowledgments**

Work at the Ames Laboratory was supported by the Department of Energy-Basic Energy Sciences (Materials Chemistry and Biomolecular Materials Program) under Contract No. DE-AC02-07CH11358.

**References**

1. Wopenka, B.; Pasteris, J. D. *Materials Science & Engineering, C: Biomimetic and Supramolecular Systems* 2005, C25, 131-143.
2. Rey, C.; Miquel, J. L.; Facchini, L.; Legrand, A. P.; Glimcher, M. J. *Bone* 1995, 16, 583-586.
3. Cho, G.; Wu, Y.; Ackerman, J. L. *Science* 2003, 300, 1123-1127.
4. Termine, J. D.; Eanes, E. D.; Greenfield, D. J.; Nylen, M. U.; Harper, R. A. *Calc Tiss Res* 1973, 12, 73-90.
5. Catherine, H.; Skinner, W. In Origin, Evolution, and Modern Aspects of Biomineralization in Plants and Animals, 1990, p 251-264.
6. Ou-Yang, H.; Paschalis, E. P.; Mayo, W. E.; Boskey, A. L.; Mendelsohn, R. *J Bone Miner Res*, 16, 893-900.

7. Roufosse, A. H.; Aue, W. P.; Roberts, J. E.; Glimcher, M. J.; Griffin, R. G. *Biochemistry* 1984, 23, 6115-6120.

8. Schmidt-Rohr, K.; Rawal, A.; Fang, X. W. *J Chem Phys* 2007, 126, 054701-054716.

9. Marshall, A. F.; Lawless, K. R. *J Dent Res* 1981, 60, 1773-1782. .

10. Hendricks, S. B.; Hill, W. L. *PNAS* 1950, 36, 731-737.

11. Pake, G. E. *Journal of Chemical Physics* 1948, 16, 327-336.

12. Wilson, E. E.; Awonusi, A.; Morris, M. D.; Kohn, D. H.; Tecklenburg, M. M. J.; Beck, L. W. *J Bone Min Res* 2005, 20, 625-634.

13. Beshah, K.; Rey, C.; Glimcher, M. J.; Schimizu, M.; Griffin, R. G. *J Solid State Chem* 1990, 84, 71-81.

14. Hou, S. S.; Beyer, F. L.; Schmidt-Rohr, K. *Solid State Nuc Mag Reson* 2002, 22, 110-127.

15. Fratzl, P.; Schreiber, S.; Klaushofer, K. *Connect Tissue Res* 1996, 34, 247-254.

16. Kolodziejski, W. *Top Curr Chem* 2005, 246, 235-270.

17. Gullion, T.; Schaefer, J. *J. Magn. Reson.* 1989, 81, 196-200.

# CHAPTER 6

# H-REDOR AND NANOMETER-SCALE INHOMOGENEITY OF NANOCRYSTALLINE BIOAPATITE IN BONE

A. Rawal, K. Schmidt-Rohr

*In the style of a paper to be submitted to Bone*

**Abstract**

A solid-state NMR method, X{$^1$H} H-REDOR, for relatively selective recoupling of dispersed protons in inorganic particles in nanocomposites is described. It is closely related to the X{$^1$H}HARDSHIP pulse sequence, but its results are complementary. The ratio of H-REDOR / HARDSHIP intensities represents the dephasing by the isolated interior protons in the inorganic fraction. Additional dephasing in H-REDOR compared to HARDSHIP is the telltale sign that certain species, such as a 50% fraction of Na, are incorporated into the bioapatite. Applications to nanocrystalline bioapatite in various bone samples are shown where a significant fraction of phosphates are not dephased by the $OH^-$ protons, indicating hydroxide-free regions. These are only a few nanometers wide, as proved by $^{31}$P spin diffusion to the more hydroxide-rich regions.

## 6.1 Introduction

For NMR studies of organic-inorganic nanocomposites, the X{$^1$H} HARDSHIP method[1] has provided a new approach to relatively quantitative thickness measurements of the nanoparticles. It yields dephasing of X-nuclei, such as $^{31}$P, $^{29}$Si, $^{13}$C, $^{29}$Al, in the inorganic nanoparticles selectively by the short-$T_{2H}$ protons of the organic phase, without significant interference by long-$T_{2H}$ protons within the inorganic particles, see Figure 1a. The dephasing rate is proportional to the second moment of the X-$^1$H dipolar couplings,

which is strongly dependent on the depth of the X-nucleus from the organic-inorganic interface.[1]

In this paper, we present H-REDOR, a pulse sequence derived from HARDSHIP that switches on the couplings to the long-$T_{2H}$ protons selectively, as indicated in Figure 1b. The ratio of H-REDOR/HARDSHIP intensities yields the dephasing only by the interior long-$T_{2H}$ protons, if the dispersed protons are distributed homogeneously in the nanoparticles. It is thus complementary to HARDSHIP, which provides dephasing only by the short-$T_{2H}$ protons. We show applications for determining the hydroxide concentration in bioapatite of bone. Additional dephasing of H-REDOR over HARDSHIP provides strong evidence for the incorporation of species such as $^{23}$Na into bone apatite.

Further, the long-time plateau in H-REDOR/HARDSHIP curves of bone is shown to be due to an inhomogeneous distribution of $OH^-$, on a nanometer length scale amenable to equilibration by 5-second $^{31}$P spin diffusion. This is achieved by recording the H-REDOR/HARDSHIP ratio after an H-REDOR filter and a $^{31}$P spin-diffusion period. The inhomogeneity is confirmed by complementary H-REDOR/HARDSHIP dephasing after $T_{2H}$-filtered CP from $OH^-$, which selects the $OH^-$-rich regions.

## 6.2 Experimental

### *6.2.1 Sample preparation*

The midsection of femur bone from a four year old cow, a three month old chicken, and 6 week old balb-C mice, and the thorny bone from *O. niloticus* (a fresh water fish) were obtained and cleaned of all muscular and connective tissue and the marrow removed. A sharp

razor was used to cut away the surface layer of the femur as it is poorly mineralized and porous, thus ensuring that sample is composed only of compact (cortical) bone. The enamel was extracted from the molars of a slaughtered cow by carefully grinding away the dentine until only the thin outer layer of enamel remained. It was then further ground on the surface to clean it of residual organic matter. The bones and enamel were then cryo-milled in a *SPEX 6750* Freezer Mill. The powder was washed in a 3:1 mixture of methanol and chloroform to remove any lipids. It was freeze dried and then packed into 7 mm and 4mm kel-F NMR rotors.

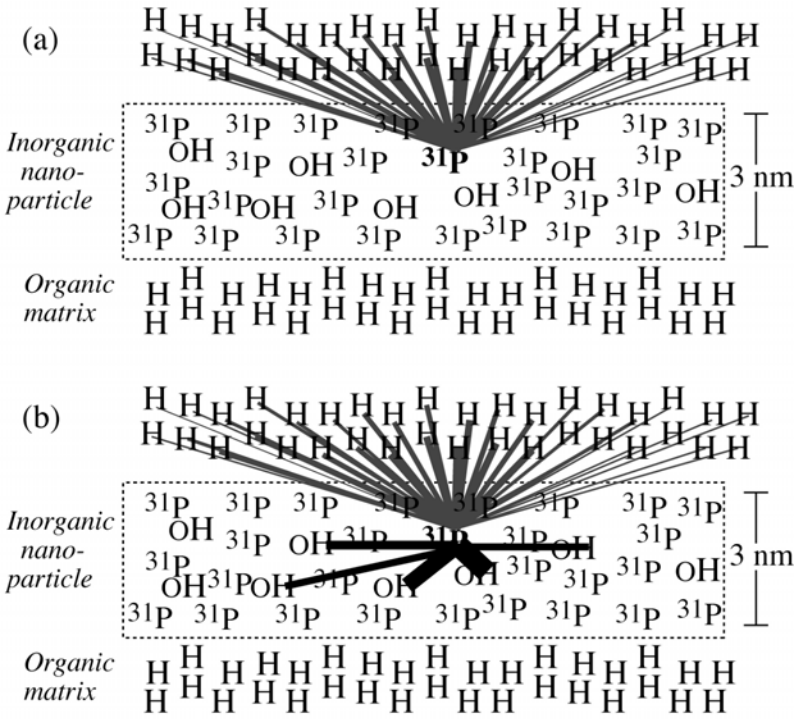


**Figure 1.** Schematic of active $^{1}H$-$^{31}P$ dipolar couplings in bioapatite, containing hydroxide ions and surrounded by a collagen matrix rich in $^{1}H$, using (a) $^{31}P\{^{1}H\}$ HARDSHIP, (b) $^{31}P\{^{1}H\}$ H-REDOR. For clarity, the couplings to the protons in the lower collagen layer have been omitted.

*6.2.2 NMR parameters and methods.*

The NMR experiments were performed using a Bruker DSX400 spectrometer at 400

MHz for $^{1}H$ and 162 MHz for $^{31}P$. The experiments were run in a Bruker 4-mm triple resonance magic-angle spinning (MAS) or a 7 mms double resonance probe when better sensitivity was needed. The $^{1}H$ and $^{31}P$ and $^{23}Na$ 90$^{o}$ pulse lengths were ca. 4 μs.

The HARDSHIP and H-REDOR experiments were carried out at primarly at 8 kHz MAS (magic angle spinning) in 4 mm rotors. The HARDHIP pulse sequences for intermediate and faster spinning are discussed elsewhere.[1] $^{23}Na\{^{1}H\}$ REDOR was run at 6.5 kHz MAS in a 7 mm rotor. For direct polarization, recycle delays of 100 s for $^{31}P$ and 2 s for $^{23}Na$, and 4 s for $^{1}H$-$^{31}P$ cross polarization, were used to excite the observed nuclei. In selective dephasing experiments, the $OH^{-}$ deficient regions In the bone apatite were selected by a 22 ms H-REDOR filter after direct polarization. The $OH^{-}$ regions were selected by employing a 300 s $T_{2,H}$ filter before 1ms of Hartmann-Hahn cross polarization. In all experiments the $^{1}H$ frequency was placed on resonance to the $OH^{-}$ peak at 0.18 ppm. Composite $^{1}H$ 180$^{o}$ recoupling pulses were used in conjunction with EXORCYCLE to minimize the effects of pulse length imperfections.[2] After an $^{31}P\{^{1}H\}$H-REDOR filter of 22.3 ms duration, $^{31}P\{^{1}H\}$H-REDOR and HARDSHIP data were recorded. In a complementary experiment, after a $T_{2,H}$ filter of 2 $\tau$ = 0.3 ms duration selecting $OH^{-}$ proton magnetization and cross polarization, H-REDOR and HARDSHIP data were recorded. The [$OH^{-}$] determination by $^{1}H\{^{31}P\}$ and $^{31}P$ NMR has been described in Chapter 5.

## 6.3 Theoretical Background.

### *6.3.1 H-REDOR pulse sequence.*

The H-REDOR sequence is very similar to the HARDSHIP pulse sequence, differing only by the phase of every second 90$^{o}$ pulse. However, this completely changes the effect of

the pulse sequence on the long-$T_{2H}$ protons. The two 90° pulses, rather than canceling as in HARDSHIP, now effectively combine into a 180° pulse. Thus, instead of refocusing the dephasing by the long-$T_{2H}$ protons, the H-REDOR sequence effectively applies a 180° pulse every half rotation period and thus recouples their dipolar interactions maximally, exactly like a REDOR sequence. By contrast, the H-REDOR dephasing by the short-$T_{2H}$ protons is the same as in HARDSHIP, since their transverse coherence is dephased by the strong homonuclear coherence, so the flip-back pulse is without effect.

In sum, this means that the dephasing by the long-$T_{2H}$ protons is switched on selectively by H-REDOR compared to HARDSHIP. The pulse sequence thus combines HARDSHIP and REDOR features, and therefore we have termed it H-REDOR.

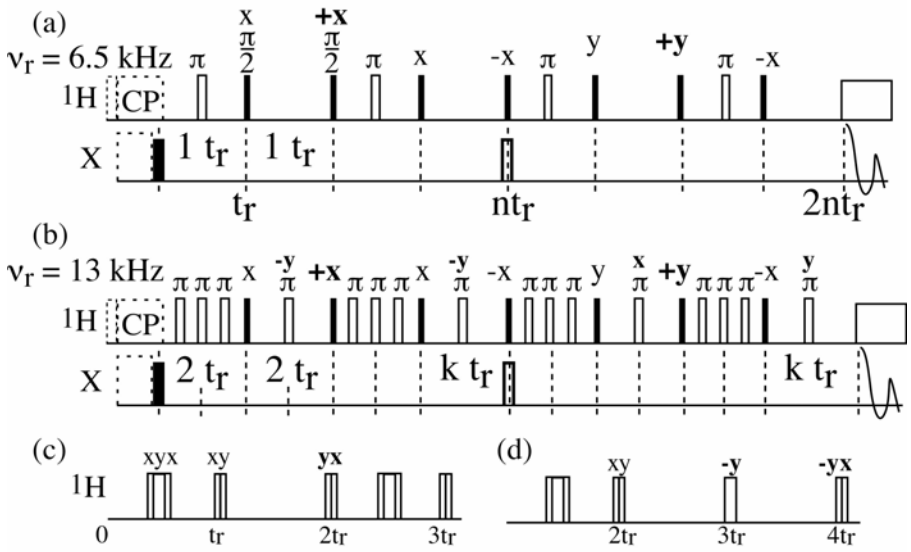


**Figure 2.** X{$^1$H} H-REDOR pulse sequences for (a) intermediate spinning frequencies (b) faster spinning. (c) Typical phases of the composite pulses used in (a). (d) Typical phases of the composite pulses used in (b).

*6.3.2 Dephasing by randomly placed $^1$H.*

The REDOR dephasing around each proton can be approximated as that of a

spherical hole in the X-nucleus distribution that expands with time $Nt_r$. An estimate of the hole volume has been derived Chen et al.[3] based on the radius of 50% dephasing, $r_{0.5}$, which fulfills

$$\frac{\delta_{XH,1A}.A^3.\, Nt_r}{r^3_{0.5}} = 0.8 \qquad (1)$$

with the dipolar coupling constant for a 1-Å internuclear distance,

$$2\pi\delta_{XH,1A} = + \frac{\mu_0}{4\pi}\eta\ \frac{\gamma_h\,\gamma_X}{A^3} \qquad (2)$$

On this basis, we obtained

$$V_{hole} = 4/3\ \pi\ .\ r^3_{0.5} = 4/3.\ \pi.(\delta_{XH,1A}.A^3 / 0.8)\ .\ Nt_r$$
$$= 5.2\ .\ \delta_{XH,1A}\ Nt_r.A^3 \qquad (3)$$

with $\delta_{PH,1A}$ = 48 kHz for X = $^{31}$P. According to eq. (3), the volume of the hole, or the total dephased magnetization, increases linearly with the dephasing time $Nt_r$.

The $N_{dH}$ dephasor protons in the sample of volume $V_{tot}$ have a number density of $n_{dH} = N_{dH}/V_{tot}$ (with units of $1/Å^3$), which proportionally increases the dephasing. At short times, overlap of the holes of total volume $V_{holes} = N_{dH}\ V_{hole}$ is minimal and the magnetization dephases as

$$R(Nt_r) = 1 - V_{holes}/V_{tot} = 1 - V_{hole}(Nt_r)\cdot n_{dH}$$
$$= 1 - 5.2\ \delta_{XH,1A}\ Nt_r\ Å^3\ n_{dH} \qquad (4)$$

where we have used eq.(3) in the last step. Thus, the initial slope of the dephasing curve is proportional to the number of dispersed protons,

$$- dR/dt|_0 = 5.2\ \delta_{XH,1A}\ n_{dH}\ Å^3 \qquad (5)$$

For X = $^{31}$P,

$$- dR/dt|_0 = 251\ \text{kHz}\ Å^3\ n_{dH}$$
$$= 0.25\ \text{nm}^3/\text{ms}\ n_{dH} \qquad (6)$$

In ideal HAp, the $OH^-$ density is $n_{OH} = 2/(0.53\ \text{nm}^3) = 3.77/\text{nm}^3$,[4] predicting a dephasing rate of 0.95/ms, which is easily detectable. We can also solve eq.(6) for the proton density:

$$n_{dH} = 4.0\ \text{kHz}\ (- dR/dt|_0)/\text{nm}^3 \qquad (7)$$

The increasing overlap of the holes at longer times for randomly distributed $^1$H dephasors is the same as in Poisson's "waves on a pond" problem, and gives exponential dephasing

$$R(Nt_r) = \exp(-V_{hole}(Nt_r) \cdot n_H)$$
$$= \exp(-5.2\ \delta_{XH,1A}\ Nt_r\ Å^3\ n_{dH}) = \exp(-WNt_r) \qquad (8)$$

with

$$W = - dR/dt|_0 = 5.2\ \delta_{XH,1A}\ n_{dH}\ Å^3. \qquad (9)$$

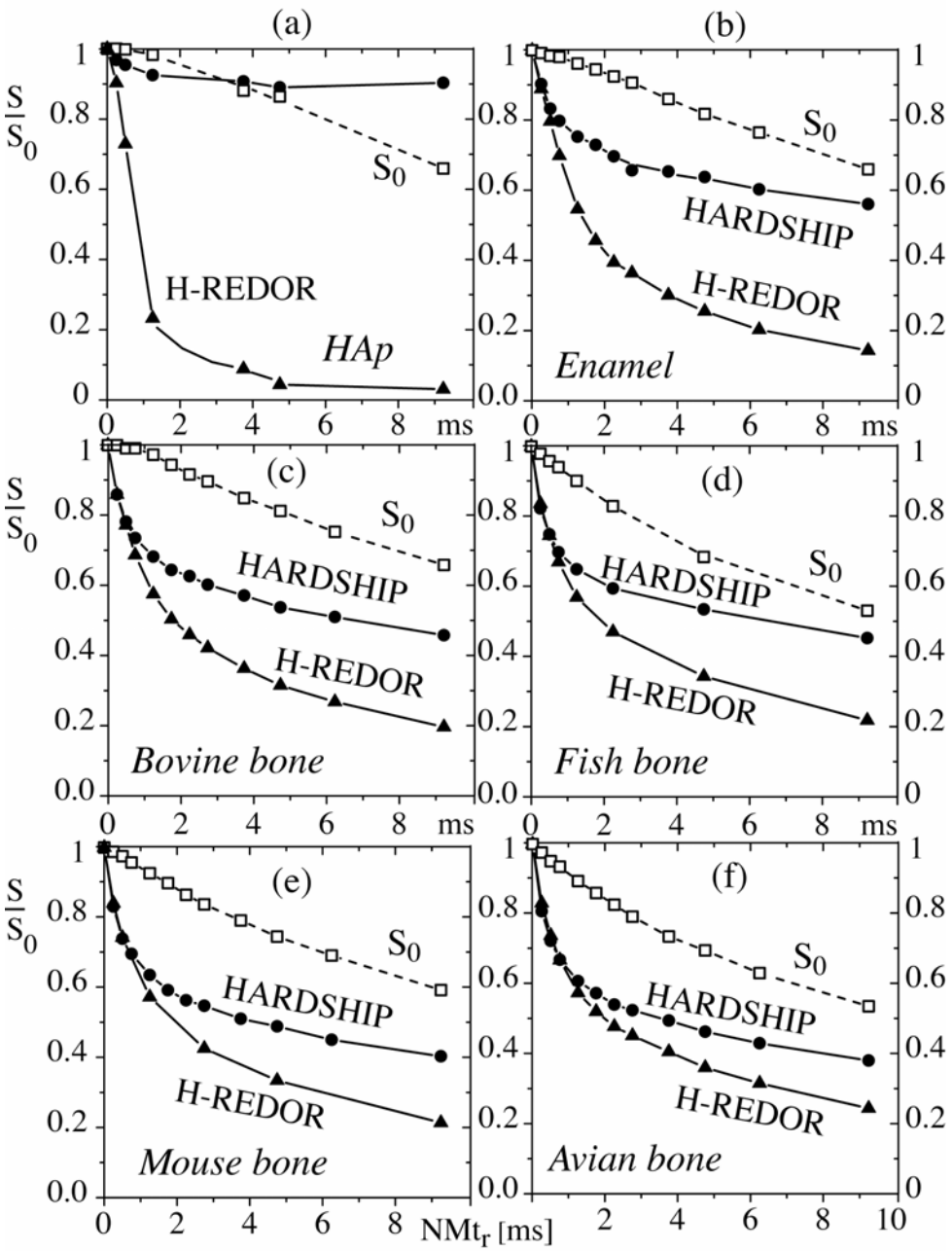


**Figure 3**. $^{31}P\{^{1}H\}$HARDSHIP and $^{31}P\{^{1}H\}$H-REDOR of (a) hydroxyapatite (HAp), (b) bovine enamel, (c) bovine bone, (d) fish bone, (e) mouse bone, and (f) avian bone.

## 6.4 Results and Discussion

### *6.4.1 $^{31}P\{^{1}H\}$H-REDOR and HARDSHIP of bioapatite.*

Figure 3 shows the HARDSHIP and HREDOR curves for five different samples containing bioapatite, plus hydroxyapatite. In all cases, the HREDOR curves show stronger dephasing than HARDSHIP. The additional dephasing confirms that the H-REDOR sequence selectively switches on dephasing by the dispersed protons. The additional dephasing varies significantly between samples, suggesting a different density of dephasing OH- protons. This interpretation is confirmed in the following.

### *6.4.2 H-REDOR/HARDSHIP rate vs. [OH$^-$].*

Figure 4a shows the H-REDOR/HARDSHIP ratios calculated from the data for the six samples shown in Figure 3. The ratio of H-REDOR/HARDSHIP intensities divides out the dephasing by the matrix protons, if the dispersed protons are distributed homogeneously in the nanoparticles. In other words, it represents the REDOR dephasing of the phosphate that has not been significantly dephased by HARDSHIP. The curves in Figure 4a have been fit by exponential decays with a constant offset

$$R(t) = (1-C)\exp(-WNt_r) + C \qquad (10)$$

The observed initial $^{31}P$ dephasing rates in HAp, enamel, and four types of bone are plotted as a function of $OH^-$ concentration (lower x-axis) or OH number density $n_{OH^-}$ (upper x-axis) in Figure 4(b). According to eq.(5), they should be proportional, and indeed a good

correlation is observed. The slope of the best-fit line is 0.225 $nm^3$/ms, in good agreement with the value of 0.25 $nm^3$/ms predicted in eq.(6). The quantitative agreement with theoretical predictions confirms that the dephasing by these long-$T_{2H}$ protons in the HARDSHIP data is quite insignificant.

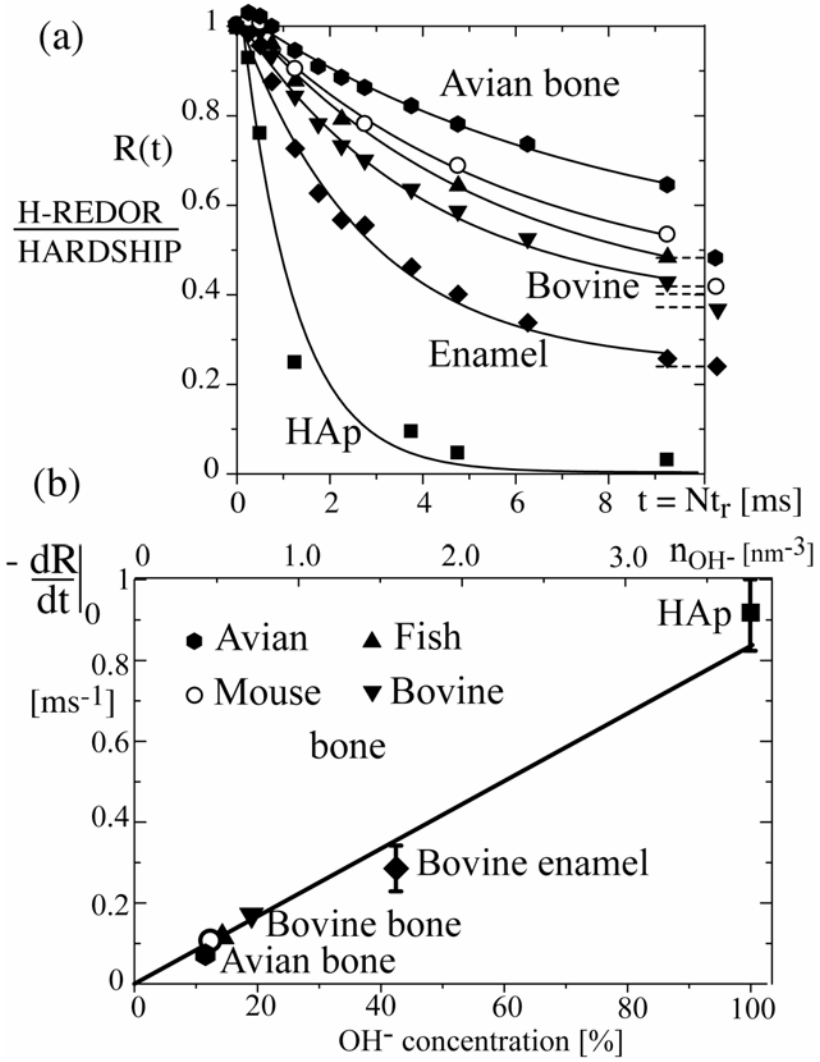


**Figure 4.** (a) H-REDOR/HARDSHIP ratio, giving the dephasing by the isolated interior OH- protons of the bioapatite. Apparent final values are indicated on the right by dashed horizontal lines. (b) Initial rates of the dephasing curves in a) vs. $OH^-$ concentration (lower x-axis) from $^1H\{^{31}P\}$ NMR normalized by quantitative $^{31}P$ NMR. The $OH^-$ density $n_{OH^-}$ is shown on the upper x-axis.

Given this calibration curve, H-REDOR/HARDSHIP measurements can be used for quantifying [$OH^-$] at moderate spinning frequencies and in the presence of highly mobile aliphatic molecules that mask the $OH^-$ proton resonance. Indeed, such background peaks prevented a direct observation of the OH- peak in $^1H$ NMR of fishbone.

*6.4.3 $OH^-$-rich vs. $OH^-$-poor regions in bone apatite.*

As discussed in the theoretical-background section, the dephasing by randomly placed $OH^-$ protons should be exponential, without an offset C. The constant C in the observed dephasing by the OH protons indicates that some phosphates in the bone samples are far from the nearest OH- dephasors. In other words, there appears to be an inhomogeneity in the distribution of $OH^-$ ions (or conversely their vacancies).

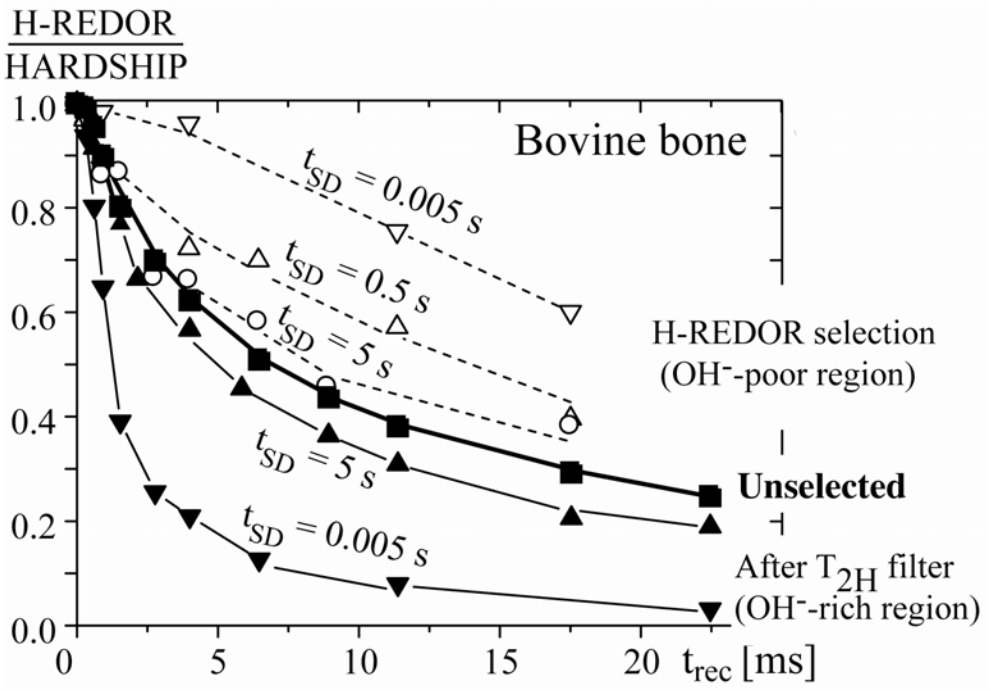


**Figure 5.** H-REDOR/HARDSHIP dephasing after $^{31}P$ spin diffusion following H-REDOR filtering, which selects $OH^-$-poor regions (top curves), and after $T_{2,H}$-filtered CP from OH- to $^{31}P$, which selects $OH^-$-rich environments (bottom curves). The H-REDOR/HARDSHIP curve obtained without any selection is also shown.

The diameter of a typical $OH^-$-rich region must be is >1.2 nm, given that after $Nt_r$ = 10 ms of $^{31}P\{^1H\}$REDOR, the magnetization of $^{31}P$ within a $(1.2\ nm)^3$ volume (1.5-nm diameter sphere) around each $OH^-$ group has been dephased. For comparison, the density of $OH^-$ groups in ideal HAp is $n_{OH} = 2/(0.53\ nm^3) = 3.77/nm^3 = 1/(0.64\ nm)^3$, and in bovine bone it is $n_{OH} = 0.75/nm^3 = 1/(1.1\ nm)^3$ on average.

Both the dephasing rate W decreases and the constant C increases as the $OH^-$ concentration decreases. Given that $W \sim n_{OH}$, see eq.(9), this means that the $OH^-$ concentration even in the $OH^-$-rich regions is still strongly decreased compared to ideal HAp. For instance, it is 30% in bovine bone, and 15% in avian bone. The increase in the constant C indicates that the fraction of hydroxide-free regions increases.

*6.4.4 Size of $OH^-$-rich regions.*

Is this inhomogeneity due to different compositions of different nanocrystals, or does it occur within each nanocrystals? This question can be addressed by $^{31}P$ spin diffusion after selection of the $^{31}P$ magnetization from the $OH^-$ depleted regions by H-REDOR dephasing. The $OH^-$ concentration in the regions reached by $^{31}P$ spin diffusion is assessed by H-REDOR/HARDSHIP measurements. Without spin diffusion, the further decay is very slow, top curve in Figure 5, as expected given the small slope of the H-REDOR decay at the end of the filter period. Within 5 s of $^{31}P$ spin diffusion, the curve without selection is almost recovered. This shows that the $^{31}P$ magnetization has reached the $OH^-$-depleted regions and thus proves that the inhomogeneities occur on a scale of a few nanometers, not in different crystals.

The model predicts $OH^-$-rich regions. This prediction can be confirmed by experiments selecting phosphates near the $OH^-$ proton by cross polarization. To remove cross polarization from the collagen protons, the $OH^-$ magnetization was selected by a $T_{2H}$-filter. The bottom curve in Figure 5 shows the expected fast decay of the H-REDOR/HARDSHIP ratio. After 5 s of $^{31}P$ spin diffusion, the unselective curve is approached, but not completely matched.

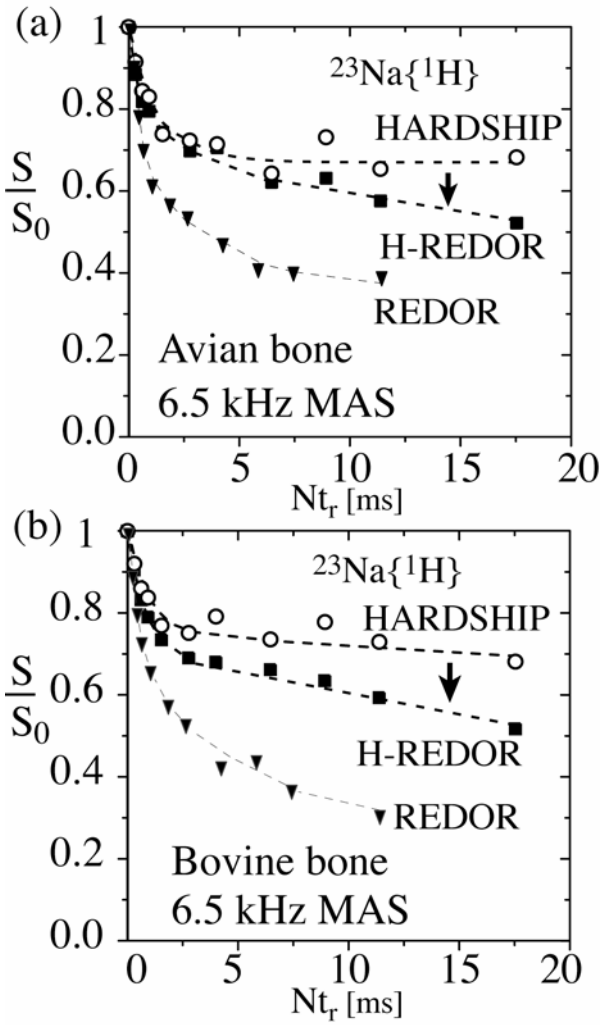


**Figure 6.** $^{23}Na\{^1H\}$REDOR (filled triangles), $^{23}Na\{^1H\}$HARDSHIP (open circles), and $^{23}Na\{^1H\}$H-REDOR (filled squares) dephasing in (a) avian and (b) bovine bone, at 6.5 kHz MAS. The additional dephasing by the $OH^-$-protons is indicated by arrows. Dashed lines are guides to the eyes.

Is the depleted region localized in the core of each nanocrystals, or are there lateral

fluctuations in OH- concentration ? This question could be answered by H-REDOR measurements after HARDSHIP dephasing of the $^{31}P$ in the surface layers.

*6.4.5 Na in bone apatite.*

Figure 6(a) shows $^{23}Na\{^{1}H\}$REDOR, HARDSHIP, and H-REDOR data for bovine bone, Figure 6(b) the same for bovine bone. Partial REDOR dephasing is observed, indicating that some sodium is in nanoparticles, while another fraction is in larger particles and not near any protons. The additional dephasing in H-REDOR compared to HARDSHIP provides strong evidence for the sodium being incorporated into the bioapatite nanocrystals.

**6.5 Conclusions**

The $X\{^{1}H\}$H-REDOR sequence, in conjunction with the closely related $X\{^{1}H\}$HARDSHIP method, provides information on long-$T_{2H}$ protons dispersed in nanoparticles. It is thus complementary to HARDSHIP itself, where the dephasing is only due to the short-$T_{2H}$ protons of the organic matrix. We have confirmed that the initial dephasing rate in H-REDOR/HARDSHIP ratios is proportional to the concentration of the long-$T_{2H}$ protons, in quantitative agreement with theoretical predictions, and that the dispersed-proton concentration can be determined conveniently from this dephasing rate. Plateaus in the H-REDOR/HARDSHIP ratio curves in five samples of bioapatite indicated the presence of hydroxide-poor regions. This was confirmed by complimentary experiments with cross-polarization from $OH^-$. The size of these inhomogeneities was shown to be within the reach of 5-s $^{31}P$ spin diffusion, i.e. a few nanometers. Further, by comparing $X\{^{1}H\}$H-REDOR and $X\{^{1}H\}$HARDSHIP curves, we can determine whether the X-nucleus is incorporated into the proton-containing nanoparticles. This was demonstrated for $X=^{23}Na$, which was found to be partially incorporated into bone apatite.

## References


1 K. Schmidt-Rohr, A. Rawal, and X. W. Fang, J Chem Phys **126** (5), 054701 (2007).

2 N. Sinha, K. Schmidt-Rohr, and M. Hong, J Magn Reson **168** (2), 358 (2004).

3 Q. Chen and K. Schmidt-Rohr, Solid State NMR **29**, 142 (2006).

4 M. Mathew and S. Takagi, J. Res. Natl. Inst. Stand. Technol. **106** (6), 1035 (2001).

# CHAPTER 7.
# ASSIGNMENT OF ORGANIC MOITIES AT THE INTERFACE WITH APATITE NANOCRYSTALS IN BONE

A. Rawal, K. Schmidt-Rohr

*In the style of a paper to be submitted Calcified Tissue International*

**Abstract**

The organic moieties at the organic-inorganic (collagen-apatite) interface in bone, identified by $^{13}C\{^{31}P\}$ REDOR NMR, have been analyzed by spectral editing and two-dimensional NMR experiments. The previously suggested assignment to sugar rings has been disproved, while the data support assignment to hydroxyproline with unusual hydrogen bonding and to glutamate residues.

## 7.1 Introduction

The nanocomposite in bone is a remarkable structure composed of ~ 45 % by volume of an inorganic mineral phase (bioapatite) and ~ 55 % by volume of the fibrous protein type I collagen. Together they form a material that is uniquely suited to form a load bearing structure for vertebrates. The strength of a composite material is determined not only by the mechanical properties of its components but also by the nature and strength of interaction between the components. This interaction, which occurs at the interface of the component phases, must be optimized or the resulting composite material might be too brittle or not have the required stiffness[1]. The organic-inorganic interface plays a crucial role for the excellent mechanical properties of bone and for the biomineralization process. For gaining a better understanding of that interface, it is important to identify the specific organic moieties near the apatite surface and to understand how the collagen interacts with the apatite.

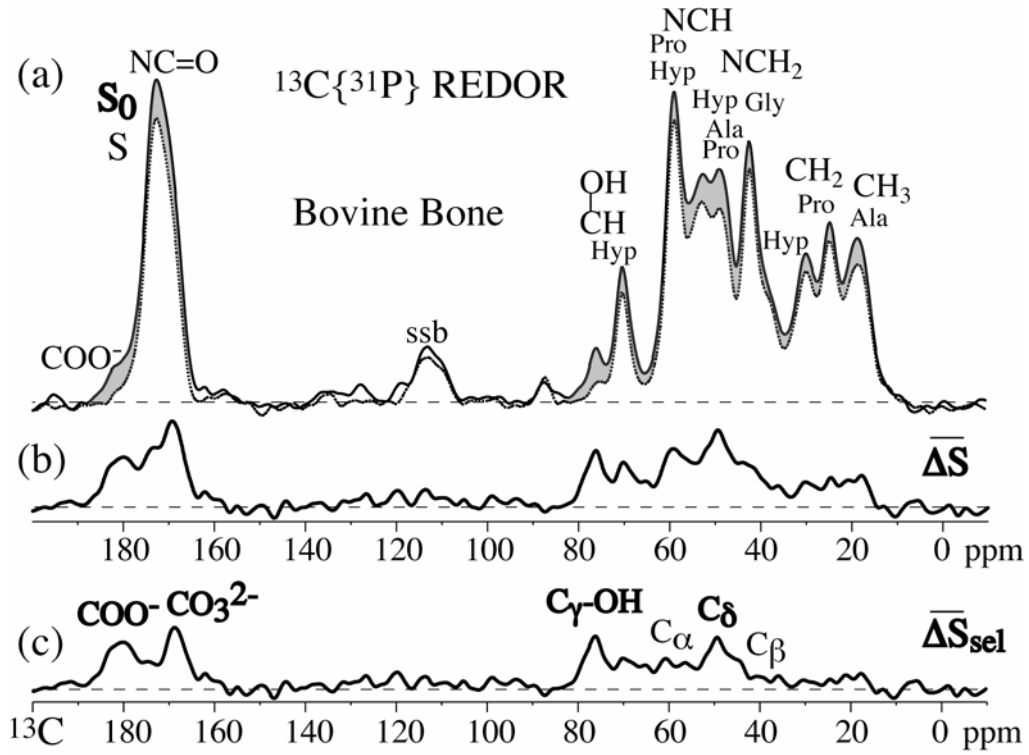


**Figure 1.** $^{13}C\{^{31}P\}$ REDOR spectra of bovine bone. (a) Full spectrum ("$S_0$") and spectrum with recoupled dipolar dephasing ("S") with the shaded areas indicating the dephasing. (b) Total regular-difference ($\Delta S$) (summed for spectra with, $Nt_r$ = 3 ms, 4.66 ms, 6 ms and 7.66 ms)and (c) total scaled-difference spectrum. The spectrum S was scaled up by 1.1 to match the 42-ppm peak of Gly in $S_0$ and thus remove the long-range dephasing of all collagen residues. Total measuring time: 19 days.

The $^{13}C$ NMR signals of the organic groups at the organic-inorganic interface in bone can be identified by $^{13}C\{^{31}P\}$ REDOR, as first shown by Jaeger et al.[2] Figure 1a shows full ($S_0$) and dephased (S) $^{13}C\{^{31}P\}$ REDOR spectra of bovine bone; their difference, the signal of $^{13}C$ dephased by $^{31}P$, is displayed in Figure 1b. The most pronounced dephasing is observed for signals at 75 and 182 ppm. While it is clear that they are associated with OCH and COO groups, respectively, the further chemical environment is contentious. Recently, it was proposed that the 75 ppm and 182 ppm signals should be assigned to sugars[3] (see Figure 2a). On this basis, a completely new model of the organic-inorganic interface in bone was proposed, with a layer of glycosoaminoglycans (GAG) between the apatite nanocrystals and the collagen matrix[3].

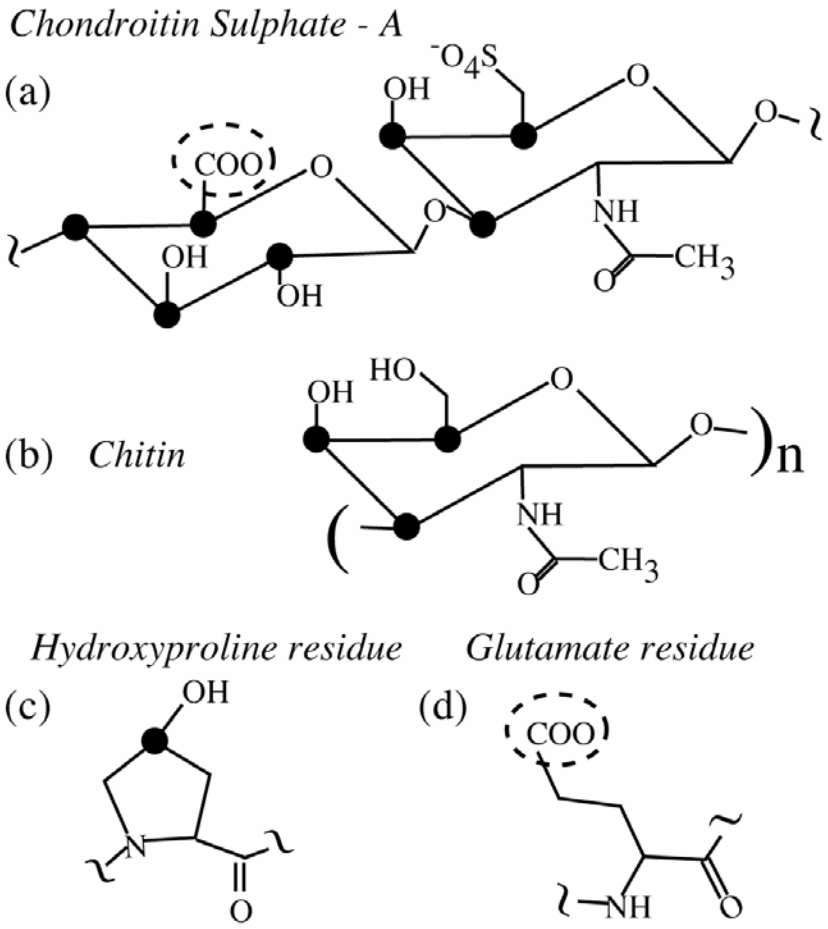


**Figure 2.** Structures of (a) acidic GAG sugar (chondroitin Sulphate), (b) Chitin, (c) Hydroxyproline residue, (d) Glutamate residue

In this Note, we present evidence against assignment of the 75- and 182-ppm signals to sugar rings and for their assignment to hydroxyproline and glutamate residues, respectively, of the collagen matrix (see Figure 2b). We also present a more comprehensive assignment of the solid state NMR spectrum of collagen in mineralized bone tissue, where as in previous in previous work[4] only the major residues, viz. glycine, proline , hydroxyproline and alanine were assigned.

## 7.2 Experimental

### *7.2.1 Samples*.

The midsection of bovine femur bone from a four year old cow was obtained and cleaned of all muscular and connective tissue and the marrow removed. A sharp razor was used to cut away the surface layer of the femur as it is poorly mineralized and porous, thus ensuring that sample is composed only of compact (cortical) bone. The bone was then cryo-milled in a *Specman Norris 3700* cryogenic grinder. The powder was washed in a 3:1 mixture of methanol and chloroform to remove any lipids. IT was freeze dried and then packed into 7 mm and 4mm kel-F NMR rotors.

### *7.2.2 NMR parameters and methods.*

The NMR experiments were performed using a Bruker DSX400 spectrometer at 400 MHz for $^{1}H$ and 162 MHz for $^{31}P$. A Bruker 4-mm triple resonance magic-angle spinning (MAS) probehead was used for 6-kHz MAS $^{1}H$-$^{31}P$-$^{13}C$ NMR experiments, while 6.5-kHz MAS $^{1}H$-$^{13}C$ NMR experiments were performed with in a 7 mm Bruker double-resonance probehead for enhanced sensitivity. The $^{1}H$ and $^{31}P$ 90$^{o}$ pulse lengths were ca. 4 μs. The collagen spectra were obtained by cross-polarizing (CP) the $^{13}C$ from the $^{1}H$ and detection was done after applying the total suppression of sidebands[5] (TOSS) scheme. Spectral editing was done by applying the CH selection[6], $CH_2$ selection[7] and gated decoupling schemes, to identify the various types of organic moieties present and to assign them to the various amino acid residues. The spinning frequency was 5.8 kHz MAS for these experiments. Heteronuclear correlation spectroscopy at 6.5 kHz MAS was used to obtain $^{1}H$-$^{13}C$ correlation spectra. Frequency switched Lee Goldberg (FSLG) scheme was applied to

remove the $^{1}H$-$^{1}H$ homonuclear couplings during the $t_1$ evolution period. 66 $t_1$ increments were carried out at intervals of 24 μs to collect the 2D dataset. The $^{13}C\{^{31}P\}$ REDOR experiments were carried out at 6 kHz MAS with recoupling times upto 7.6 ms. The EXORCYCLE[8] and composite 180$^{o}$ degree pulses were used to achieve optimal dephasing.

## 7.3 Results and Discussion

### *7.3.1 Evidence against sugar.* \

It has been proposed that the features of the $^{13}C$ spectrum of bone between 72 and 110 ppm resemble those of sugar rings. However, closer inspection makes this claim highly questionable. In sugars, the OCO (anomeric carbon) signal somewhere between 92 and 110 ppm represents 1/4 of the OCH signal intensity. Figure 3b-d shows several examples from natural organic matter. In bone collagen, no peak of such intensity is observed in this spectral region. In addition, there are four OCH sites in a sugar ring, which give rise to several resonances or a broader band between 72 and 84 ppm. By contrast, bone shows only a single sharp peak. Furthermore, if we look at the structure of chondroitin sulfate-A, which is the most relevant GAG in connective tissues, the ratio of carbonyl CO to OCH carbon is 1:7. However, the intensities of the peaks observed at 180 ppm and 75 ppm are nearly equal.

$^{1}H$-$^{13}C$ HetCor spectra of bone, see Figure 4, provide further evidence against assignment of the 75 and 182 ppm signals to sugar. The $^{1}H$-$^{13}C$ HetCor spectrum of sugars would be distinctive in exhibiting only OCH proton bands around 4 ppm. By contrast, the 182-ppm carbon band correlates with nonpolar alkyl protons around 2.5 ppm, exactly as expected for glutamate. On a slightly longer time scale of 0.2 ms, the 75-ppm carbons correlate readily with nonpolar alkyl and NH protons. This is unlikely to be attributable to

spin diffusion. Within this spin diffusion time, the magnetization has not equilibrated between different amino acids residues, as shown by the different $^{1}H$ signal profile of the alanine resonance near 20 ppm in the $^{13}C$ dimension.

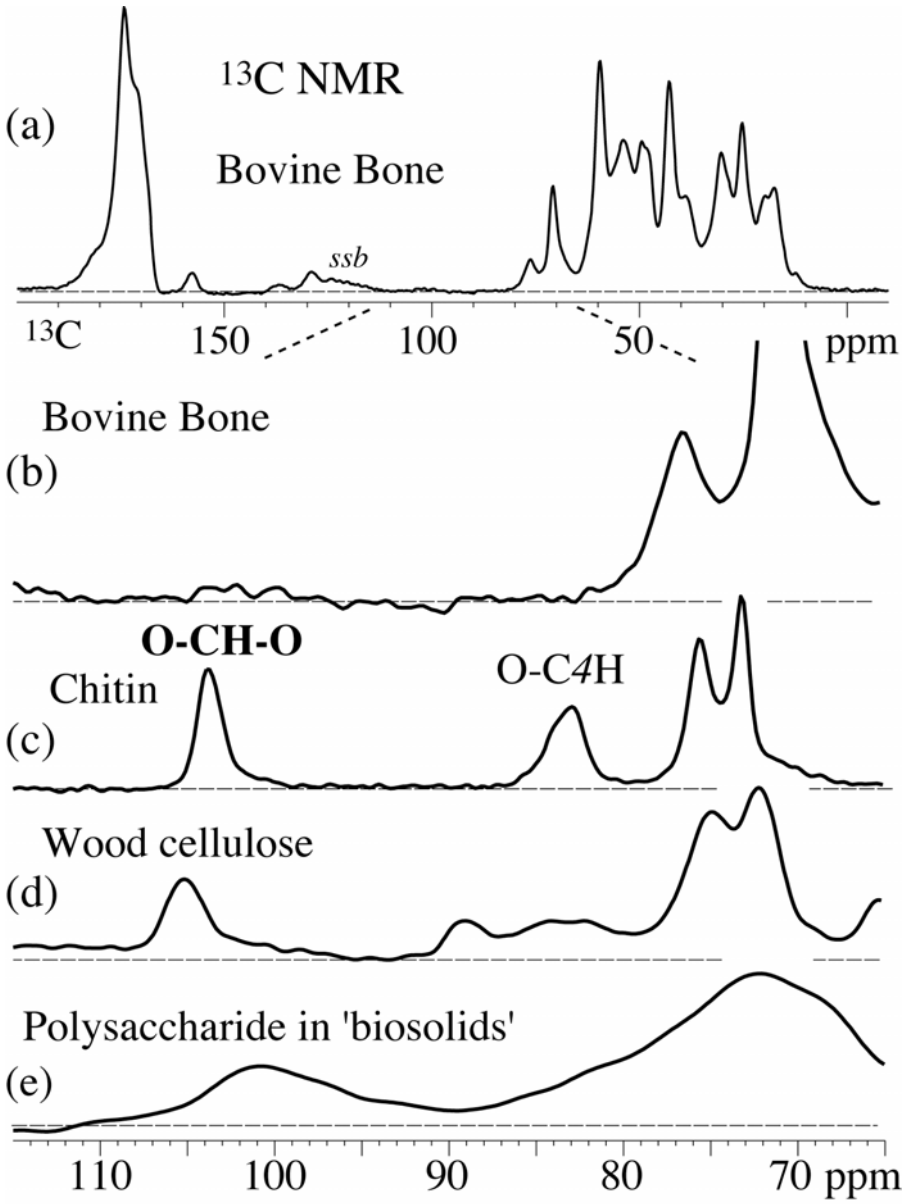


**Figure 3.** (a)1D $^{13}C$ CP TOSS NMR spectrum of bovine bone at 6.5 kHz MAS. (b) 65 – 115 ppm region from (a). (c-e) Same spectral region as in (b) for (c) Chitin, (d) cellulose in wood, (e) the hydrophilic high molecular weight fraction of biosolids in sludge

*7.3.2 Evidence for hydroxyproline.*

Our spectra show strong evidence for an assignment of the 75-ppm peak to Cγ of Hyp in an unusual conformation or hydrogen-bonding environment. This site is a CH-OH moiety, and the spectral editing, Figures 5b and c, confirms that the signal at 75 ppm is due to an OCH, but not an $OCH_2$ group.

The slow C-H dephasing of the 75-ppm signal in the gated-decoupling experiment, Figure 5a, is noteworthy. It shows that this segment undergoes fast anisotropic large-amplitude motions. In solution, the Hyp ring can undergo motions of $30^o$ amplitude, and ring motions of smaller amplitude are also known to occur in the solid state.

The $^{13}C\{^{31}P\}$ REDOR scaled-difference spectrum of the surface sites, Figure 1d, shows significant intensity below 60 ppm, with a distinctive peak near 53 ppm. This signal cannot be assigned to sugars, which do not show resonances in this spectral range. Instead, it is consistent with Cδ of Hyp, if we allow for a 4-ppm conformational shift analogous to that from 70 to 75 ppm for Cγ. A $CH_2$ band of matching intensity is observed in the $CH_2$-only spectrum near 53 ppm. Note that if Cγ is within 0.5 nm from the apatite surface, Cδ must be within 0.65 nm from the surface, too, given their 0.15 nm bond distance. In fact, the weak Cβ signal can only be explained by assuming that the Cδ sites is closest to the apatite.

*7.3.3 Glutamate.*

It has been suggested that the shoulder at 180 ppm in the $^{13}C$ spectrum is either from a sugar or a non-collagenous protein. However, the collagen sequences clearly show that the glutamate residues along with the aspartate residues comprise 6 % and 10 % of the residues

for avian and bovine type I collagen, respectively, as listed in Table 1 (for avian bone). The integral of the COO resonance which is seen as the shoulder at 180 ppm in the $^{13}C$ spectrum is approximately 10 % of the NCO resonance at 170 ppm, which corresponds to its mole % in collagen. Therefore one cannot assign this shoulder to any molecule other than the collagen in bone.

| Residue | Symbol | Mole % | Residue | Symbol | Mole % |
|---|---|---|---|---|---|
| Glycine | G | 34 | Serine | S | 3 |
| Hydroxyproline | O | 12 | Aspartate | D | 3 |
| Proline | P | 11 | Glutamine | Q | 3 |
| Alanine | A | 10 | Leusine | L | 2 |
| Arginine | R | 5 | Valine | V | 2 |
| Glutamate | E | 5 | Threonine | T | 2 |
| Lysine | K | 3 | Phenylalanine | F | 1 |

**Table 1.** Amino acid residues in collagen, their symbols and their mole % listed in decreasing order of occurrence. The hydroxyproline residues are 12 % while aspartate and glutamate residue combined form 6 % of the total.

### 7.4 Conclusion

From the spectral editing HETCOR and REDOR experiments, we can confirm that the organic moieties that are closest to the apatite surface are indeed from the collagen and not from other components as has been suggested. There is special interaction of the hydroxyproline and glutamate residues with the apatite surface. Indeed as these residues have the longest sidechains, they would be the ones able to make the closest approach to the apatite surface. The proposed changes in the H-Bonding or conformation of the

hydroxyproline that lead to the 5 ppm shift from the standard resonance position will be investigated in future work.

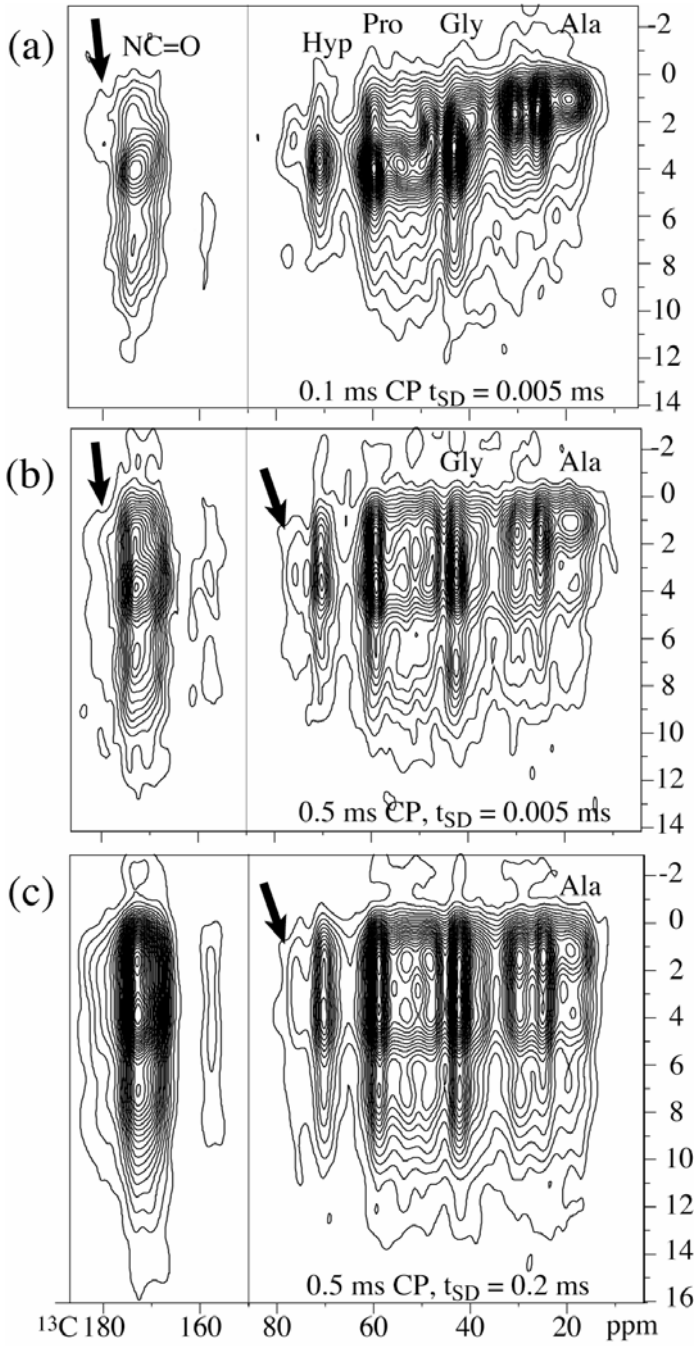


**Figure 4.** Contour plots of $^{1}$H-$^{13}$C HetCor spectra for (a) short LGCP contact time of 100 μs. (b) LGCP contact time of 500 μs with $t_{sd,eff}$ of 0.005 ms and (c) LGCP contact time of 500 μs with $t_{sd,eff}$ of 0.2 ms values. The relevant cross peaks of the 182- and 75-ppm bands are labeled by arrows.

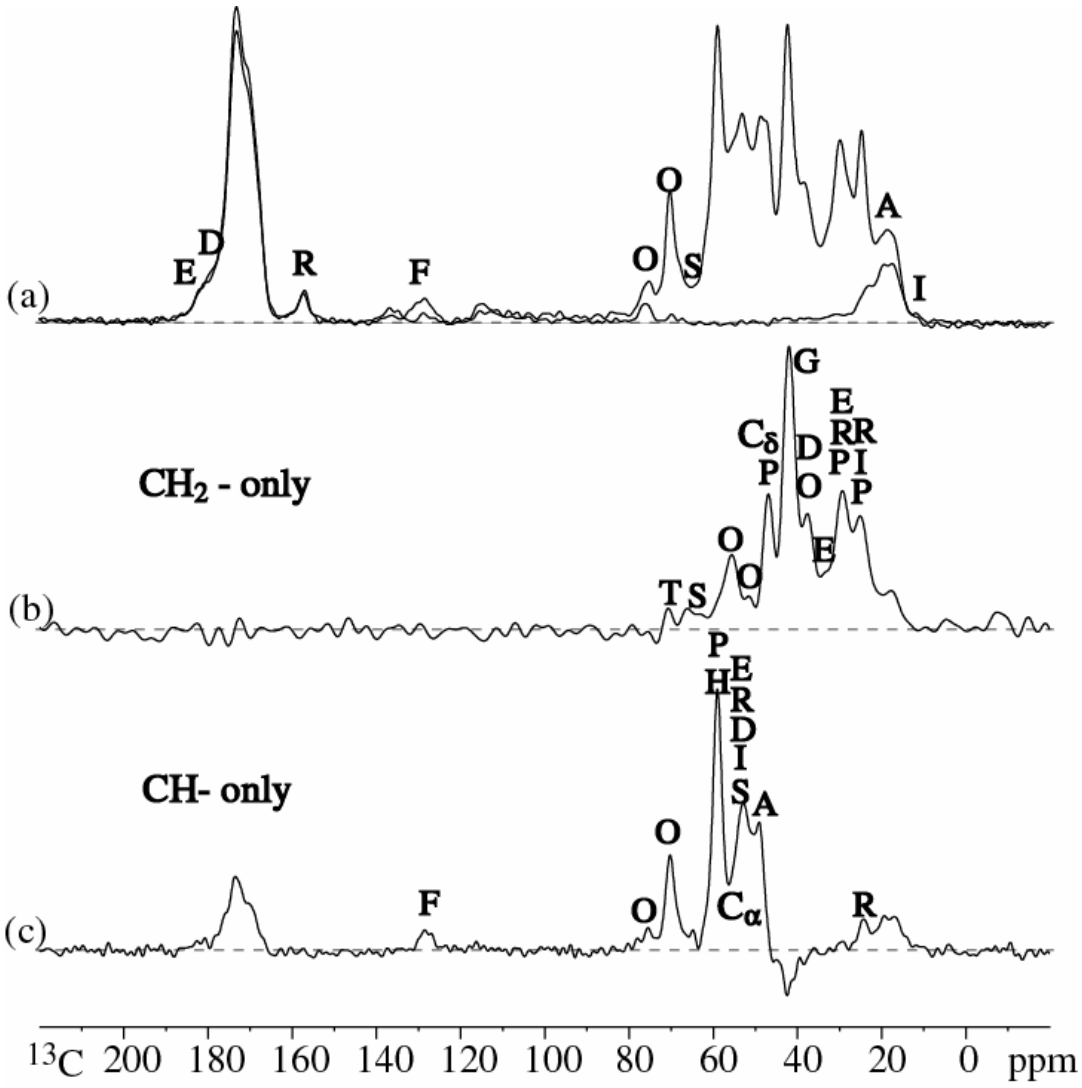


**Figure 5.** $^{1}H$-$^{13}C$ NMR spectra at 5.8 kHz MAS. (a) Full CP spectrum and spectrum after 40-μs gated decoupling, selecting nonprotonated C and C in mobile segments such as rotating $CH_3$ groups. (b) $CH_2$-only spectrum obtained by three-spin coherence selection. (c) CH-only spectrum selected by dipolar DEPT (without subtraction of non protonated carbon signal). The amino acid residues are indicated by their one letter symbols (refere Table 1). Note: O is the one letter code for hydroxyproline.

**Acknowledgments**

Work at the Ames Laboratory was supported by the Department of Energy-Basic

Energy Sciences (Materials Chemistry and Biomolecular Materials Program) under Contract No. DE-AC02-07CH11358.

**References**

(1) Lopattananon, N.; Kettle, A. P.; Tripathi, D.; Beck, A. J.; Duval, E.; France, R. M.; Short, R. D.; Jones, F. R. Composites Part A 1998, 30A, 49-57.

(2) Jaeger, C.; Groom, N. S.; Bowe, E. A.; Horner, A.; Davies, M. E.; Murray, R. C.; Duer, M. J. Chem Mater 2005, 17, 3059-3061.

(3) Wise, E. R.; Duer, M. J.; Reid, D. G.; Maltsev, S.; Jaeger, C.; Davies, E.; Loveridge, N.; Murray, R. C. 49th Rocky Mountain Conference on Analytical Chemistry, 2007.

(4) Fujisawa, R.; Kuboki, Y. Biochem Biophys Res Commun 1990, 167, 761-766.

(5) Dixon, W. T.; Schaefer, J.; Sefcik, M. D.; Stejskal, E. O.; McKay, R. A. J Magn Reson 1982, 49, 341-345.

(6) Schmidt-Rohr, K.; Mao, J. D. J Am Chem Soc 2002, 124, 13938-13948.

(7) Mao, J. D.; Schmidt-Rohr, K. J Magn Reson 2005, 176, 1-6.

(8) Sinha, N.; Schmidt-Rohr, K.; Hong, M. J Magn Reson 2004, 168, 358-365.

# CHAPTER 8.
# WATER LAYERS AT THE APATITE-COLLAGEN INTERFACE IN BONE ELUCIDATED BY NMR

A. Rawal, K. Schmidt-Rohr

*In the style of a paper to be submitted to Colloids and Surfaces B: Biointerfaces,*

**Abstract**

The interface between collagen and bioapatite in native compact bone has been characterized by a variety of solid state nuclear magnetic resonance (NMR) experiments. Two major forms of water are detected at the interface: Strongly bound molecules, and a layer of viscous water exhibiting dipolar spinning sidebands and a narrow line with short $T_{1\rho}$ relaxation time of spin-locked magnetization, respectively. $^{1}H$-$^{31}P$ wideline separation (WISE) NMR experiments show that the rigid water is strongly bound to the apatite phosphate. Its faster $^{1}H$ spin diffusion to collagen proves its location at the organic–inorganic interface. $^{1}H$ spin diffusion from the mobile water to the apatite protons is faster than spin diffusion to the collagen protons, seen by $^{1}H$-$^{31}P$ WISE and $^{1}H$-$^{13}C$ WISE, respectively, which indicates that the mobile water is also located at the interface. The rotational correlation time of the mobile water estimated from its $T_{1\rho}$ indicates that it is $10^{6}$ times more viscous than liquid water. The mobile water accounts for 15 % of all $^{1}H$, which indicates that the mobile water layer is one molecule thick. $^{13}C\{^{31}P\}$ rotational echo double resonance (REDOR) experiments show that $COO^{-}$ of the glutamate and hydroxyproline $C_{\gamma}$-OH are at a distance of ~ 0.5 nm from the apatite surface phosphorus, consistent with an intervening water layer. On the basis of these data, a model of the collagen-bioapatite interface is presented, where the viscous mobile water acts as “glue” between collagen and the apatite nanocrystals.

**8.1 Introduction.**

Bone is a nanocomposite material, combining the rigidity of an inorganic bioapatitic phase with the toughness of collagen, a fibrous protein. While the mechanical and material properties of bone have been studied for a long time[1-4], the interface between the apatite and collagen is not well understood. The nature of the interface is crucial in determining the interaction between the components of the composite and its overall performance[5]. In this regard, there are two issues that need clarification. The first is the role of water in the bone composite. Curry[1] has presented bone as a ternary system of collagen-apatite-water and it is well known that the impact strength of the dehydrated bone is greatly reduced[6]**.** This has been attributed to the reduced toughness of dehydrated collagen, where in addition to absorbed water, the hydrogen bonding network that is formed between the water and the collagen is important in the self assembly of the collagen triple helix[7,8] and also potentially of the collagen fibril.

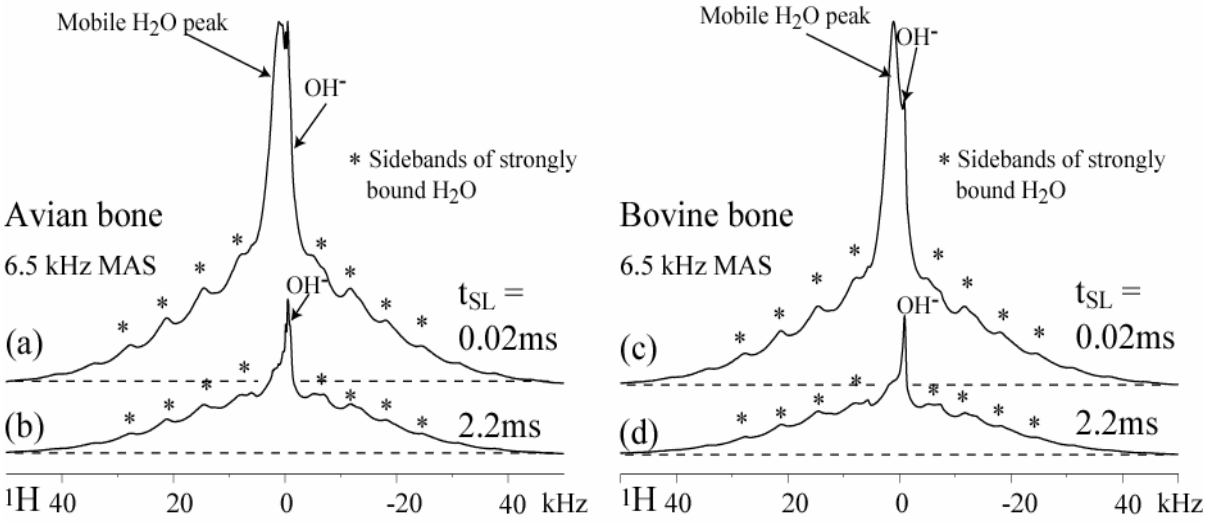


**Figure 1.** $^{1}$H NMR spectra of avian and bovine cortical femur bone at 6.5 kHz MAS. (a) and (c) are the $^{1}$H spectra detected after a $^{1}$H spinlock of 0.02 ms while (b) and (d) were detected after a $t_{SL}$ of 2.2 ms. The spin lock field of the $T_{1\rho,H}$ filter was 62.5 kHz.

However, indications of another water species, which is not bulk water and does not form part of the collagen triple helical structure, have been seen in bone[9-12]. Wilson *et al.*[9] using $^{1}H$-$^{31}P$ NMR and Lee-Goldberg cross polarization dynamics, proposed that there is an "ordered" water layer surrounding the bioapatite and a bulk water layer in bone. On heating, the bulk water is removed and only the ordered water remains with further heating permanently disrupting the ordered water layer. In later work[10], they proposed that the ordered water was in fact part of the bioapatite apatite crystal and located in the vacancies and defects of the bioapatite, because it was not removable from their deproteinated bone samples even at 200 $^{o}$C. However, one must note that LGCP dynamics may not be a reliable method to quantify the water if relaxation during CP ($T_{1\rho}$) is short. Furthermore, very dry deproteinated apatite has a very strong affinity towards water[13] and will readily adsorb it from the atmosphere. Indeed, we have noted that even dried hydroxyapatite samples, which have a much smaller surface area than bioapatite, will adsorb water in a relatively short time. Turov *et al.*[12] have also looked at hydrated rat-tail vertebrae, and proposed that regular water resonating at 5 ppm was located into pores, cavities and pockets of bone tissue, while non-freezable water resonating at 1.3 ppm is located in a hydrophobic environment. Sukhodub *et al.*[11] investigated the bone water with piezogravimetry and IR spectroscopy and proposed that there are two water compartments in collagen, one surrounding the collagen and the other in the gap region of the collagen fibril. Comparing collagen fibrils to mineralized bone they concluded that as the gap region in bone is occupied by the bioapatite crystal, the second compartment is not available and the only water is the one surrounding collagen. However, it is an incorrect but unfortunately prevalent assumption that the bioapatite crystals are located only in the gap regions of the collagen fibril. This is inconsistent with SAXS data and it has been shown via NMR that the apatite is close to most collagen residues[14].

Another issue regarding the interface in bone is the nature and distance of organic

moieties from the bioapatite surface. Langmuir-Blodget film experiments[15] suggest that the $COO^-$ of the glutamate residue nucleates the bioapatite by binding the $Ca^{2+}$ ions in the solution.

Therefore, in this paper, we have investigated cortical bone that has been minimally treated and is devoid only of bulk water, to elucidate the nature of the remaining water and the structure of apatite-collagen interface. This is an important step in understanding what makes bone such a successful material and has implications in developing 21$^{st}$ –century structural materials[16] as well as materials for biomedical application such as bone grafting.

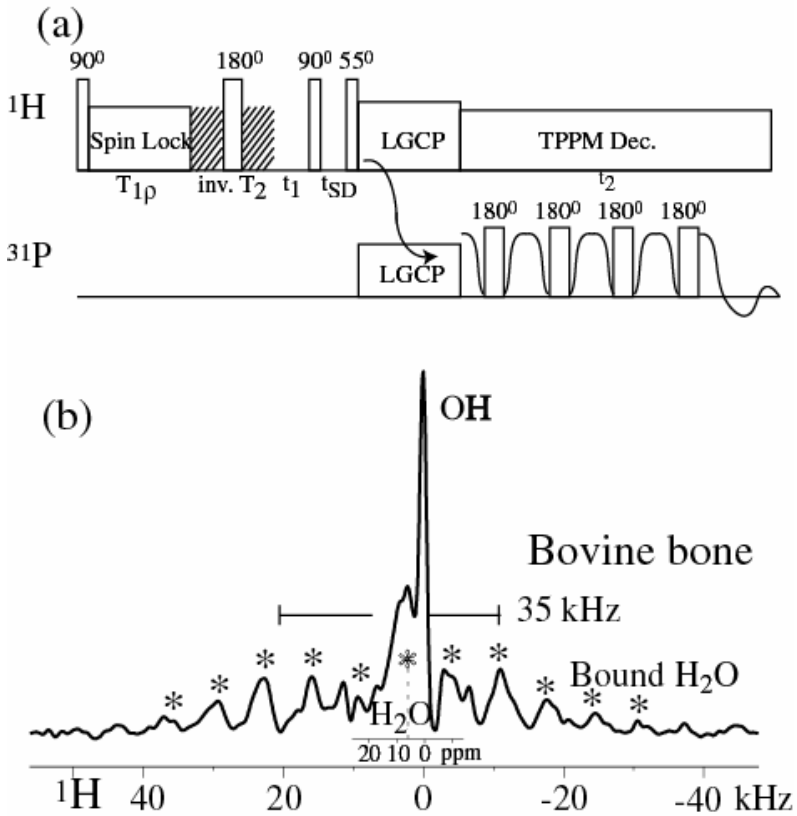


**Figure 2.** (a) Pulse sequence for a $^1H$-$^{31}P$ LGCP WISE experiment with a $^1H$-$T_{1\rho}$ filter to suppress mobile protons, and inverse $T_2$ filter to suppress long $T_2$ protons. A spin diffusion time $t_m$ is incorporated to detect the proximity of protons from the organic phase. A train of refocusing 180$^o$ pulses on the $^{31}P$ channel is used to enhance sensitivity. (b) $^1H$ cross section of the $^1H$-$^{31}P$ LGCP WISE spectrum of bovine bone at 6.5 kHz MAS, 1 ms $T_{1\rho}$ filter, 0.3 ms inverse $^1H$-$T_2$ filter and 0.4 ms LGCP.

## 8.2 Experimental

### *8.2.1 Samples.*

The midsections of femur bone from a four-year-old cow and three-month- old chicken were obtained and cleaned of all muscular and connective tissue, and of the marrow. A sharp razor was used to cut away the surface layer of the femur as it is poorly mineralized and porous, thus ensuring that the sample is composed only of compact (cortical) bone. The bone was then cryo-milled in a *SPEX 6750 Freezer Mill* cryogenic grinder. The powder was washed in a 3:1 mixture of methanol and chloroform to remove any lipids. It was freeze dried and then packed into 7 mm and 4mm Kel-F NMR rotors.

### *8.2.2 NMR parameters and methods.*

The NMR experiments were performed using a Bruker DSX-400 spectrometer at 400 MHz for $^{1}H$ and 162 MHz for $^{31}P$. The experiments were run in a Bruker 4-mm triple resonance magic-angle spinning (MAS) or a 7 mm double resonance probe when better sensitivity was needed. The $^{1}H$ and $^{31}P$ and $^{13}C$ $90^{o}$ pulse lengths were ca. 4 μs.

Two-dimensional $^{1}H$-$^{31}P$ WISE and $^{1}H$-$^{13}C$ WISE[17] experiments were performed with 0.4 ms of Lee Goldberg cross polarization (LGCP) to transfer magnetization only from those $^{1}H$ nuclei that are close to the $^{13}P$/$^{13}C$ nuclei. To generate the 2D data set, 200 increments of 9.6 μs in were used to. A 1 ms $T_{1r}$ filter was used to suppress the mobile protons, while a 0.3 ms inverse $T_{2,H}$ filter was used to suppress signal from protons with a long $T_2$ (especially the $OH^-$ of the bioapatite), to selectively see the rigid water. No filtration was used during WISE experiments with spin diffusion. The 2D $^{1}H$-$^{31}P$ Heteronuclear correlation (HetCor) spectra

were run at 6.5 kHz MAS with Frequency switch Lee Goldberg (FSLG) scheme applied to remove the $^{1}H$-$^{1}H$ homonuclear couplings during the $^{1}H$ $t_1$ evolution period. LGCP with a 0.2 ms contact time and 72 $t_1$ increments of 26 μs were used to obtain the 2D HetCor dataset. The $^{13}C\{^{31}P\}$ REDOR[18] experiments were carried out at 6 kHz MAS with recoupling times up to 7.6 ms. The EXORCYCLE along with composite 180° degree pulses was used to minimize pulse length errors and achieve maximal dephasing[19].

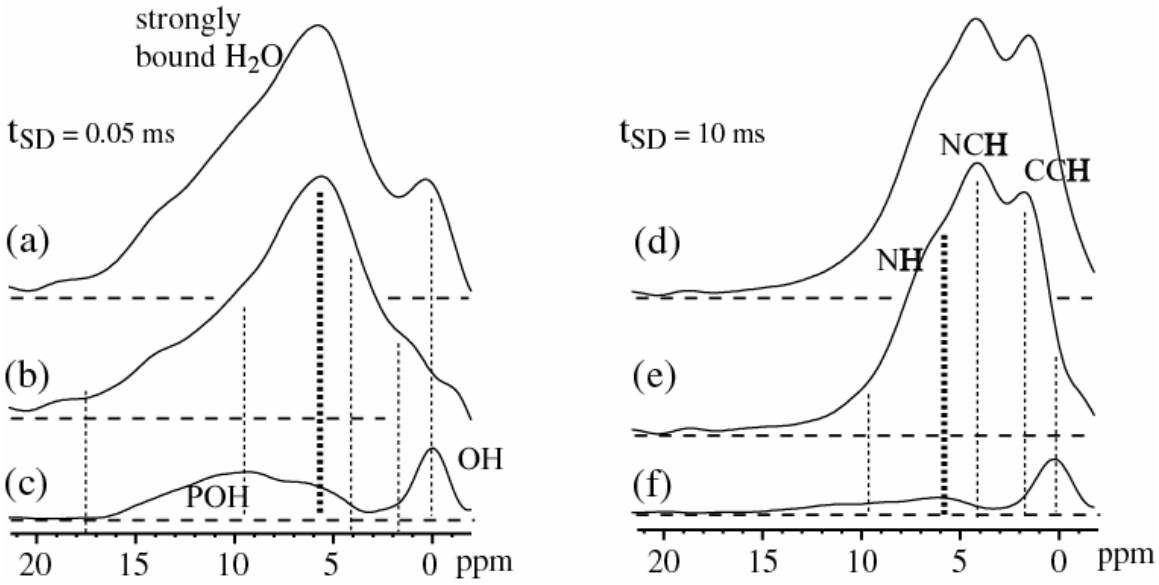


**Figure 3.** $^{1}H$ slices of $^{1}H$-$^{31}P$ HetCor spectra of avian bone at 6.5 kHz MAS. A 0.5-ms $T_{1\rho}$ filter was used to suppress the mobile protons. $^{1}H$ spectra of (a) all the protons near the apatite; (b) the protons at the interface; (c) the apatite protons with long $T_2$. Spectra (d), (e) and (f) correspond to (a), (b) and (c) but are detected after a spin diffusion time of 10 ms.

## 8.3 Results and discussion.

### *8.3.1 Mobile and rigid water.*

In Figure 1 (a) and (c), $^{1}H$ spectra of bovine and avian bone show a strong motionally narrowed line centered at 5 ppm, which is suppressed by a $T_{1\rho}$ filter, as seen in Figure 1 (b)

and (d). This indicates that this component has dynamics on the 10μs timescale, and is not associated with a hydrogen bond to collagen, as it is absent in the $^{1}H$-$^{13}C$ WISE spectra without spin diffusion (Figure 4 (b)). We therefore assign this peak to hydrogen of mobile water, especially since bone does contain 5-15 wt% of $H_2O$ in the native hydrated state.

Figures 1 (b) and (d) show indications of a component with strong dipolar sidebands indicative of strongly dipolar coupled protons such as in a rigid $H_2O$ molecule or isolated $CH_2$ group. This component can be observed selectively in a $T_{1\rho,H}$ and inverse-$T_{2,H}$-filtered $^{1}H$-$^{31}P$ WISE spectrum.as shown in Figure 2. Figure 2 (a) shows the pulse sequence for this experiment, and the $^{1}H$ cross-section is plotted in Figure 2 (b). The spectrum shows that the component with the strong dipolar spinning sidebands is also centered at ca. 7 ppm and closely associated with the phosphate species in the bioapatite. We therefore assign this component to a rigid water species, which is hydrogen-bonded to the phosphate. Note that this is not the rigid water postulated to be part of the collagen triple helical structure[7,8]. This is seen by the absence of this component in a similar $^{1}H$-$^{13}C$ WISE experiment (lowermost spectra in the series of Figure 4 (b)). Additionally the rigid bound water hypothesis in proved by a 2D double quantum filtered experiment published elsewhere[20].

Figure 3 shows $^{1}H$ slices of 2D $^{1}H$-$^{31}P$ HetCor spectra in avian bone. Figure 3 (a) shows the spectrum of the protons associated with the phosphate of the bioapatite. Note that the mobile-water signal has been suppressed by a $T_{1\rho}$ filter. Figure 3 (c) exhibits the bands of protons with a long $T_2$, which are subsurface or interior protons of the bioapatite. These are primarily the $OH^-$ and some POH in addition to a small amount of $H_2O$ protons. Figure 3 (b) which is the difference between the spectra in Figure 3 (a) and 3 (c), shows spectrum of the protons at the surface of the bioapatite, which have short $T_2$'s due to strong couplings with the organic protons. The largest band in this spectrum is primarily from the rigid water peak.

Note that the dipolar sidebands are absent due the homonuclear dipolar decoupling. Figure 3 (d-f) show the proton spectrum after 10 ms of $^{1}H$ spin diffusion. Figure 3 (e) exhibits peaks that correspond to CCH, NCH and NH protons of the collagen, indicating spin diffusion contact between the rigid water and the collagen protons. Similarly, comparing Figure 3 (b) to 3 (f), we can see that the POH proton magnetization has spin diffused, indicating that most of these protons are also close to the surface of the bioapatite. However a significant, fraction of the $OH^-$ protons remain, along with a small fraction of the $H_2O$ and POH protons. This indicates that most of the $OH^-$ along with a small fraction of the rigid $H_2O$ is isolated in the bioapatite.

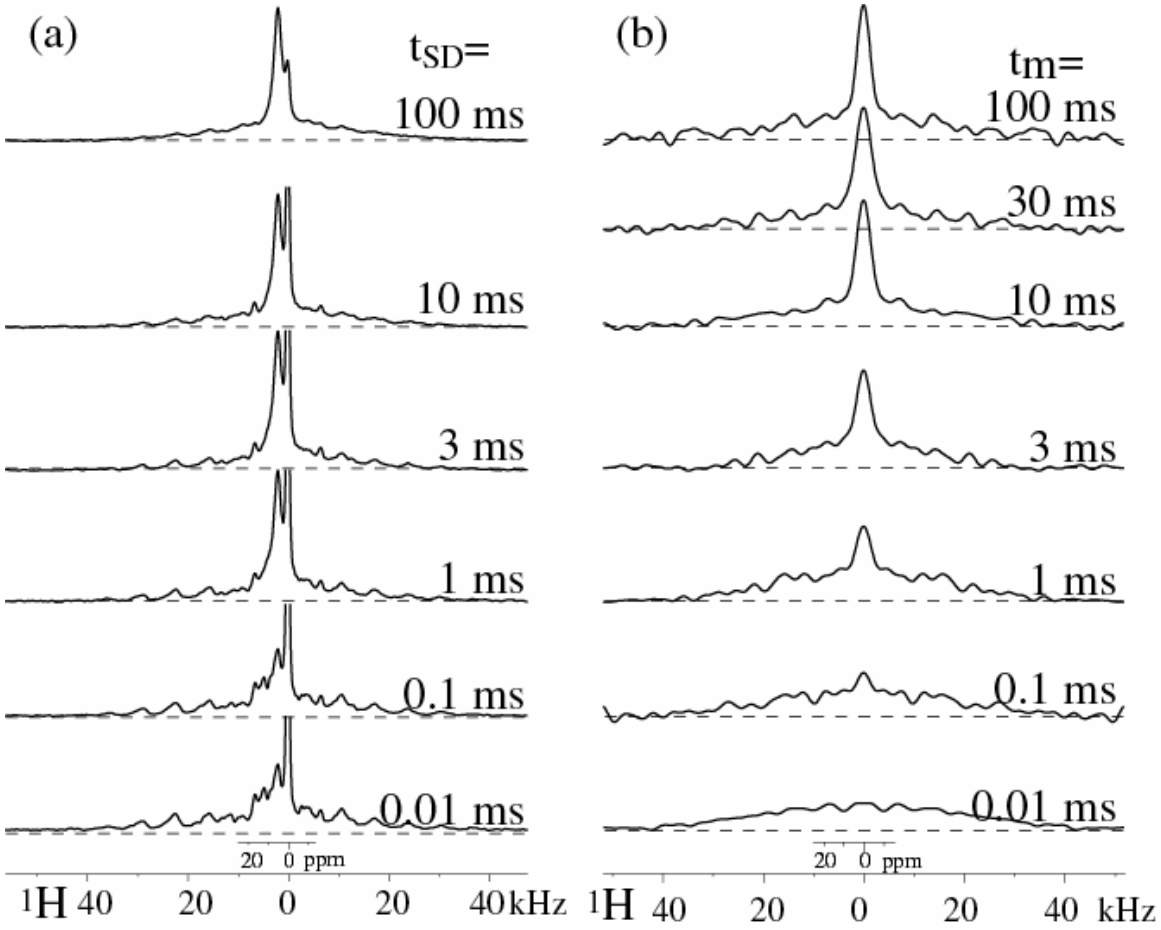


**Figure 4.** Spectra of bovine bone at 6.5 kHz MAS. (a) $^{1}H$ cross sections from $^{1}H$-$^{31}P$ LGCP WISE for varying $t_{SD.}$ (b) $^{1}H$ cross sections from $^{1}H$-$^{13}C$ LGCP WISE taken at 41.5 ppm in the $^{13}C$ dimension for varying $t_{SD.}$

*8.3.2 Location and nature of the mobile water.*

Figure 4 (a) and (b) show the $^{1}H$ cross-sections of $^{1}H$-$^{31}P$ and $^{1}H$-$^{13}C$ WISE spectra respectively. We can thus compare the spin diffusion rate of the mobile water to the apatite and collagen. The mobile-water peak is absent at short spin diffusion times in both Figures 4 (a) and (b), but builds up intensity with longer spin diffusion time with complete equilibration by 100 ms.

The spin diffusion behavior of the various protons is plotted in Figure 5. Spin diffusion from the $OH^-$ and POH and rigid $H_2O$ protons is plotted in Figure 5(a). The slow rate of spin diffusion of the $OH^-$ protons as compared to the POH and the rigid $H_2O$ prove that the $H_2O$ and POH are primarily interfacial, species unlike the $OH^-$. The residual intensity of the POH protons also indicates that some of these may be isolated, subsurface species within the bioapatite.

*8.3.3 Quantification of the mobile layer.*

The spin diffusion behavior of the mobile water to the collagen and the bioapatite along with the spin diffusion of the rigid water to the collagen is plotted in Figure 5 (b). It shows that the spin diffusion of the mobile water is faster to the apatite protons that to the collagen protons. This indicates that the mobile water is in more intimate contact with the thin layer of apatite surface protons than with the collagen molecules, proving that it is not water within collagen, but a water layer between apatite and collagen. The fractional area of the mobile water peak, obtained as a difference between the spectra in Figure 1 (c) and Figure 1 (d), is $f_{H,\,mH2O} = 0.15$. Based on the known volume fractions and densities of the three main components of bone, this gives us an estimate of the volume fraction of the

interfacial mobile water layer. Via the average thickness of the apatite nanocrystals of 2.8 ± 0.4 nm[14] obtained by NMR and quantitative WAXD analysis, we can estimate the thickness of the water layer.

From $^{1}$H NMR, we get

$$A_{H,\,mH2O}/(A_{H,\,colla} + A_{H,\,mH2O} + A_{H,\,rH2O}) = f_{H,\,mH2O} = 0.15 \qquad (1)$$

where $A_{H,\ldots}$ are the $^{1}$H signal areas of the different components.

$^{1}$H nuclei account for 2/18 of the mass of $H_2O$, and for 7% of the mass of collagen. The (relative) mass of the mobile water and collagen can thus be calculated from the $^{1}$H area fractions as

$$2/18\ m_{mH2O} = c\ A_{H,\,mH2O} \qquad (2)$$

$$0.07\ m_{Colla} = c\ A_{H,\,Colla} \qquad (3)$$

where c is a constant. Substituting (2) and (3) in (1) and using $A_{H,\,rH2O}/A_{H,\,mH2O} \approx 1$, we get

$$(2/18\ m_{mH2O}) / (0.07\ m_{Colla} + 2/18\ m_{mH2O} \bullet 2) = 0.15 \qquad (4)$$

Taking the inverse, we can easily calculate the collagen : water mass ratio.

$$0.07\ m_{colla}/ (1/9 \bullet m_{mH2O}) + 1 \bullet 2 = 1/0.15$$

$$\Rightarrow m_{Colla}/ m_{mH2O} = (1/0.15 - 1 \bullet 2) \bullet (1/9)/ 0.007 = 7.4/1$$

$$\Rightarrow m_{Colla}/ m_{H2O} = 3.7/1 \qquad (5)$$

The relative volume can then be calculated via the density ratio:

$$V_{Colla} / V_{H2O} = (m_{Colla} / \rho_{colla}) / (m_{H2O} / \rho_{H2O})$$
$$= (m_{Colla} / m_{H2O}) \times (\rho_{H2O} / \rho_{colla}) = (3.7/1) \times (1/1.43) = 2.6 \quad (6)$$

Then, the water volume fraction $v_{H2O} = V_{H2O}/V_{tot}$ is determined from

$$1/v_{H2O} = (V_{H2O} + V_{Colla} + V_{apa}) / V_{H2O}$$
$$= 1 + V_{Colla} / V_{H2O} (1 + V_{apa} / V_{Colla})$$
$$= 1 + V_{Colla} / V_{H2O} (1 + (m_{apa} / m_{Colla}) \times (\rho_{Colla} / \rho_{apa}) ) \quad (7)$$

The mass ratio in the last expression can be determined from the apatite mass fraction, which is 67% according to thermogravimetric analysis:

$$1/0.67 = m_{tot}/m_{apa} = (m_{apa}+m_{Colla}+m_{H2O})/m_{apa}$$
$$= 1 + m_{Colla}/m_{apa} (1 + m_{H2O}/m_{colla}) \quad (8a)$$

$$\Rightarrow \; m_{Colla}/m_{apa} = (1/0.67 - 1)/(1 + m_{H2O}/m_{colla}) = 0.49 / 1.27 = 0.39 \quad (8b)$$

Thus, eq.(7) gives

$$1/v_{H2O} = 1 + 2.6 (1 + 1/0.39 \times 1.34/3.1 ) = 6.5$$
$$\Rightarrow v_{H2O} = 1/6.5 = 0.154 \quad (9)$$
$$\Rightarrow v_{mH2O} = v_{rH2O} = 0.077$$

The volume and weight fractions of the four components are tabulated in Table 1.

Thus, given the bioapatite volume fraction of 45%, and 2.8-nm thick bioapatite the

average period of the bone nanocomposite is

2.8 nm / 0.45 = 6.2 nm.

Therefore for a repeat unit of 6.2 nm the thickness of each of the two water layers (one on either side of a bioapatite crystal) would be

6.2 nm x 0.154 / 2 = 0.48 nm.

This thickness corresponds to two layers of $H_2O$ molecules, one strongly bound, and one mobile.

| Component | Volume % | Weight Fraction |
|---|---|---|
| Collagen | 40 ± 5 | 26 ± 5 |
| Bioapatite | 45 ± 5 | 67 ± 5 |
| Mobile $H_2O$ | 7.5 ± 3 | 3.5 ± 3 |
| Rigid $H_2O$ | 7.5 ± 3 | 3.5 ± 3 |

**Table 1.** The volume and weight fractions of the different components present in the bone nanocomposite.

*8.3.4 Distance between the collagen and bioapatite.*

In $^{13}C\{^{31}P\}$ REDOR experiments, where the collagen $^{13}C$ is dephased by the distance dependent couplings with phosphate $^{31}P$ from the bioapatite[21], one can quantify the distance of the collagen residues from the bioapatite surface. The specific residues that are maximally dephased have been identified elsewhere[22], and their dephasing is plotted in Figure 6, along

with simulated curves based on a multispin model of the apatite-collagen structure. The dephasing behavior shows that the carboxylate ($COO^-$) of the glutamate residue is the closest to the apatite surface, at a distance of 0.45 nm from the phosphorus layer closest to the interface. The hydroxyproline $C_\gamma$ is at a distance of 0.5 nm while the backbone carbonyls (CO) are at an average distance of 0.9 nm. If the $COO^-$ group was directly coordinated with $Ca^{2+}$ at the apatite surface, the $^{13}C$-$^{31}P$ distance would be much shorter. The observed relatively long distance indicates that even the glutamate does not directly bond with the apatite $Ca^{2+}$ ions as has been suggested.

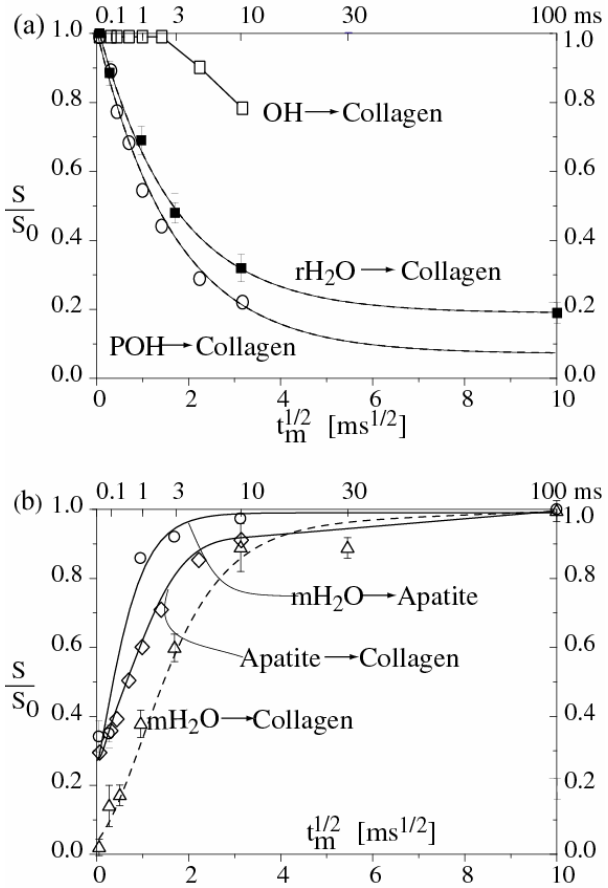


**Figure 5.** Proton spin diffusion curves of cortical bone. (a) Spin diffusion from $OH^-$ (open squares) and POH (open circles) to the organic protons, measured by $^1H$-$^{31}P$ HetCor and from the rigid water to the organic protons (filled squares) as detected by $^1H$-$^{31}P$ WISE. (b) Spin diffusion build-up curves of collagen protons to the apatite protons (open diamonds) detected by $^1H$-$^{31}P$ HetCor. Spin diffusion of mobile water to the apatite protons (open circles) and to the collagen protons (open triangles) detected by $^1H$-$^{31}P$ WISE and $^1H$-$^{13}C$ WISE, respectively. All experiments were run at 6.5 kHz MAS. The lines are guides to the eye.

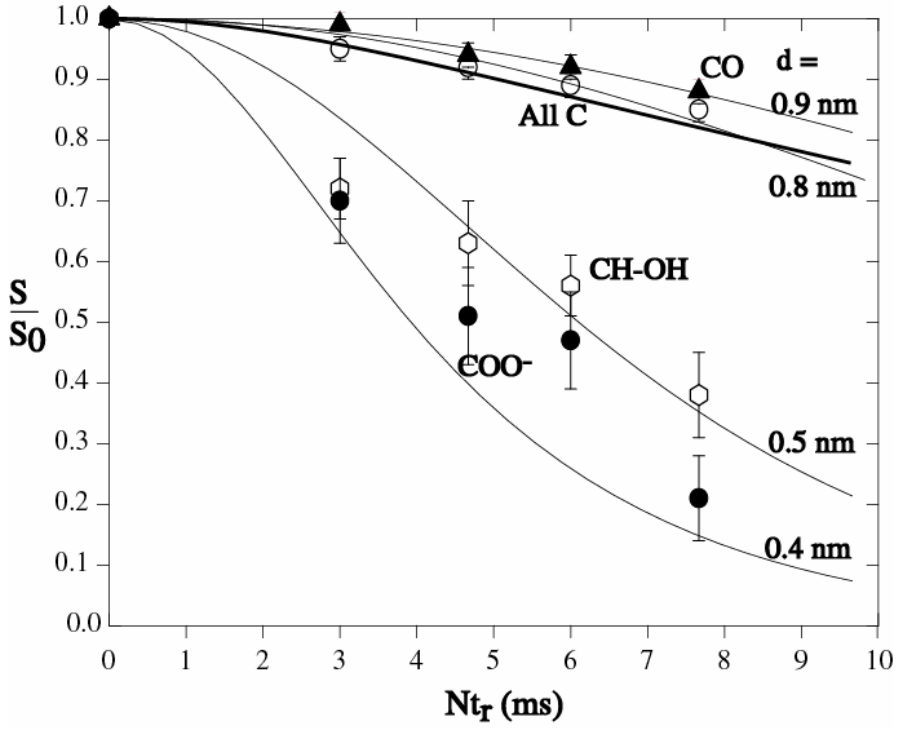


**Figure 6.** $^{13}C\{^{31}P\}$ REDOR of bone. Experimental dephasing $S/S_0$ is plotted along with fit curves for different distances between the phosphate layer closest to the interface and the $^{13}C$ of interest. Date points are plotted for the glutamate carboxylate (filled circles), the $C_\gamma$ of the hydroxyproline residue (open hexagons), the collagen carbonyl (filled triangles) and the average of all the carbons (open circles).

*8.3.5 Viscosity of the interfacial water layer.*

The mobile water layer has a $T_{1\rho}$ relaxation time of 1 ms. This corresponds to a rotational correlation time $\tau_C$ of ~ 1 μs, which is $10^6$ times the $\tau_C$ of bulk water. Assuming that the viscosity η is directly proportional to the $\tau_C$, we conclude that the mobile water layer is approximately six orders of magnitude more viscous than bulk water.

*8.3.6 Structural model of the collagen-bioapatite interface.*

We have shown that most of the surface phosphorus in the bioapatite is protonated. In

addition there are bound rigid water molecules distributed on the surface. Thus the distance between the surface of the bioapatite and the glutamate and hydroxyproline residues is less than $^{13}C$-$^{31}P$ distance determined by $^{13}C\{^{31}P\}$ REDOR. Based on average projected bond lengths of about 0.1 nm, the $COO^-$ is at a distance of approximately 0.2 nm (assuming that the P-O-H bond angle is not $180^o$). This is slightly less than the thickness of the interfacial water layer. Based on these results we present a model for the structure of the interface as shown in Figure 7. A bioapatite crystallite with a cross section of 10 nm x 2.8 nm is covered by a 0.3 nm thick layer of mobile water, surrounded by the collagen molecules which are represented as cylinders. The inset shows an enlarged view of the interface, showing the protonated surface phosphates, the strongly-bound water, and the layer of the mobile viscous water. The side-chains of the glutamate and hydroxyproline are shown extending into the water layer. Scale bars with increments of 1 Å are provided at the left of the inset box. A schematic diagram is placed to the right to indicate the repeat unit of the nanocomposite structure.

We postulate that the mobile water plays an important part in imparting (the) bone with its characteristic toughness. The water layer can be considered as “viscous glue” that holds the components of the nanocomposite together, provide a mechanism of dissipating the stresses at the surface and by virtue of its flexible H-bonding, reduce the requirement of matched lock-and-key binding sites for collagen sidegroups on the apatite surface.

**8.4 Conclusion.**

We have identified a monolayer of mobile water at the surface of the bioapatite in cortical bone and presented a model for the interfacial structure and the repeat unit of the nanocomposite. These findings suggest that subtler interactions govern the mechanical behavior of bone than has been previously considered[1]. The viscous mobile water might also

be instrumental in limiting the reduction in impact strength which would normally be caused due to particle aggregation in heavily loaded composites. Our hypothesis regarding the role of water may represent a significant step forward in the understanding of the properties of biomaterials and serve as a guide for the design of new, stronger composite materials.

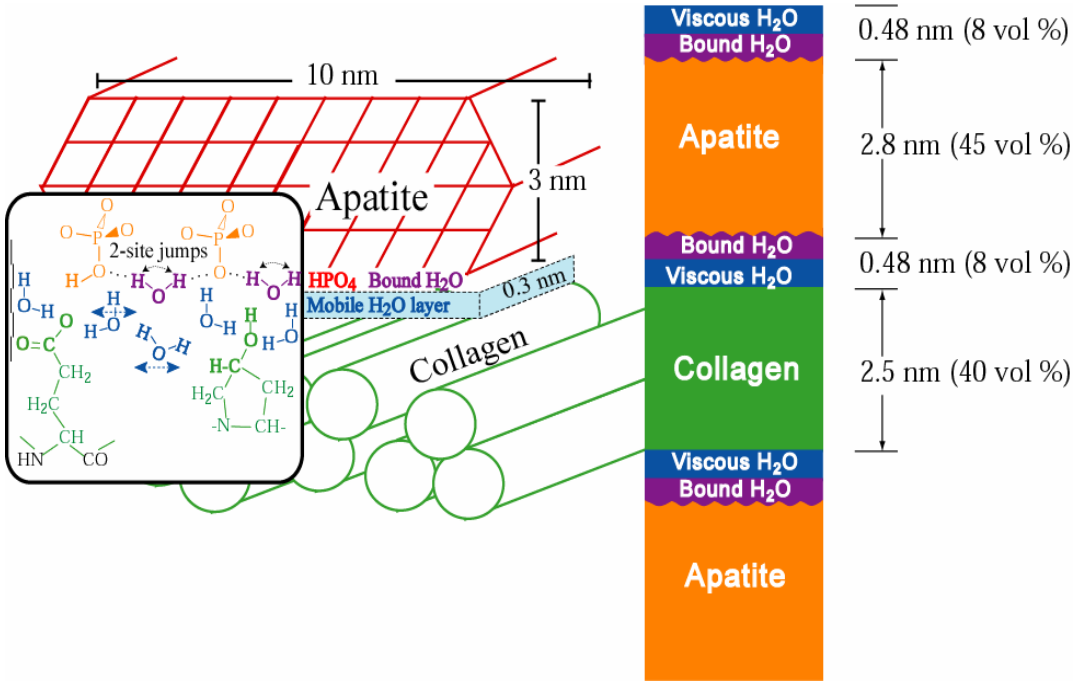


**Figure 7.** Model of the apatite-collagen interface, with a close-up of the interface in the inset shown to the left and a schematic of the repeat unit of the bone nanocomposite on the right. .

**Acknowledgments.**

Work at the Ames Laboratory was supported by the Department of Energy-Basic Energy Sciences (Materials Chemistry and Biomolecular Materials Program) under Contract No. DE-AC02-07CH11358.

**References**


1. Currey, J. The Mechanical Adaptations of Bone; Princeton University Press: Princeton, NJ, 1984.
2. Rho, J. Y.; Kuhn-Spearing, L.; Zioupos, P. *Med Eng Phys* 1998, 20, 92-102.
3. Bembey, A. K.; Bushby, A. J.; Boyde, A.; Ferguson, V. L.; Oyen, M. L. *J Mater Res* 2006, 21, 1962-1968.
4. Fratzl, P.; Gupta, H. S.; Paschalis, E. P.; Roschger, P. *Journal of Materials Chemistry* 2004, 14, 2115-2123.
5. Lopattananon, N.; Kettle, A. P.; Tripathi, D.; Beck, A. J.; Duval, E.; France, R. M.; Short, R. D.; Jones, F. R. *Composites Part A* 1998, 30A, 49-57.
6. Wang, X.; Puram, S. *Ann Biomed Eng* 2004, 32, 123-135. .
7. Ramachandran, G. N.; Chandrasekharan, R. *Biopolymers* 1968, 6, 1649-1658.
8. Bella, J.; Brodsky, B.; Berman, H. M. *Structure* 1995, 3, 893-906.
9. Wilson, E. E.; Awonusi, A.; Morris, M. D.; Kohn, D. H.; Tecklenburg, M. M. J.; Beck, L. W. *J Bone Min Res* 2005, 20, 625-634.
10. Wilson, E. E.; Awonusi, A.; Morris, M. D.; Kohn, D. H.; Tecklenburg, M. M. J.; Beck, L. W. *Biophys J* 2006, 90, 3722-3731.
11. Sukhodub, L. F.; Moseke, C.; Sukhodub, L. B.; Sulkio-Cleff, B.; Maleev, V. Y.; Semenov, M. A.; Bereznyak, E. G.; Bolbukh, T. V. *J Mol Struct* 2004, 704, 53-58.
12. Turov, V. V.; Gun'ko, V. M.; Zarko, V. I.; Leboda, R.; Jablonski, M.; Gorzelak, M.; Jagiello-Wojtowicz, E. *Colloids and Surfaces, B: Biointerfaces* 2006, 48, 167-175.

13. Posner, A. S. *J Biomed Mater Res* 1985, 19, 241-250.

14. Schmidt-Rohr, K.; Rawal, A.; Fang, X. W. *J Chem Phys* 2007, 126, 054701-054716.

15. Sato, K.; Kumagai, Y.; Tanaka, J. *J Biomed Mater Res* 2000, 50, 16-20.

16. Enlow, D.; Rawal, A.; Kanapathipillai, M.; Schmidt-Rohr, K.; Mallapragada, S.; Lo, C. T.; Thiyagarajan, P.; Akinc, M. *Journal of Materials Chemistry* 2007, 17, 1570-1578.

17. Schmidt-Rohr, K.; Clauss, J.; Spiess, H. W. *Macromolecules* 1992, 25, 3273-3277.

18. Gullion, T.; Schaefer, J. *J. Magn. Reson.* 1989, 81, 196-200.

19. Sinha, N.; Schmidt-Rohr, K.; Hong, M. *J Magn Reson* 2004, 168, 358-365.

20. Rawal, A.; Schmidt-Rohr, K. *Composition of the bioapatite nanocrystal surface in compact bone* To be submitted.

21. Jaeger, C.; Groom, N. S.; Bowe, E. A.; Horner, A.; Davies, M. E.; Murray, R. C.; Duer, M. J. *Chem. Mater*. 2005, 17, 3059-3061.

22. Rawal, A.; Schmidt-Rohr, K. *Assignment of organic moieties at the interface with apatite nanocrystals in bone* To be submitted.

# CHAPTER 9.
# SYNTHESIS AND CHARACTERIZATION OF SELF-ASSEMBLED BLOCK COPOLYMER TEMPLATED CALCIUM PHOSPHATE NANOCOMPOSITE GELS

*A paper published in Journal of Materials Chemistry (2007), 17(16), 1570-1578*

D. Enlow, A. Rawal, M. Kanapathipillai, K. Schmidt-Rohr, S. Mallapragada, C.-T. Lo, P. Thiyagarajan, and M. Akinc

**Abstract**

Self-assembled macroscale calcium phosphate-copolymer nanocomposite gels were prepared using a bottom-up approach from aqueous solutions. Amphiphilic block copolymer micelles in aqueous solutions were used as templates for growth of calcium phosphate nanocrystals and then allowed to self-assemble in solution to form thermoreversible nanocomposite gels. NMR and XRD showed that calcium phosphate precipitation in a Pluronic® F127 copolymer gel resulted in a disordered brushite phase while the calcium phosphate-poly(2-diethylaminoethyl methacrylate) (PDEAEM) modified Pluronic® F127 pentablock copolymer nanocomposite contained the same brushite phase along with a calcium dihydrogen phosphate second phase. TEM, SAXS, and NMR experiments confirmed that the calcium phosphate precipitated on and interacted with the polymer micelles forming an organized network of ~20 nm diameter nanospheres. The resulting polymer-calcium phosphate nanocomposite gels contained between 6.5 and 15 weight percent calcium phosphate, which could be controlled by manipulating the pH of the constituent solutions.

## 9.1 Introduction

In natural bone, nanoscale collagen fibrils act as templates for the growth of the

calcium phosphate inorganic phase, thereby forming a hierarchically ordered structure with unique properties. In this study, we investigate the formation of bioinspired calcium phosphate nanocomposites on nanostructured self-assembling polymeric micelle templates in solution, which can self-assemble further to form macroscale gels.

Because of their excellent bone biocompatibility, calcium phosphate based materials and coatings have been studied as potential implant materials. For example, brushite based materials have been developed as bone cements [1], and biomimetic apatite coatings on titanium have been studied for bone implants [2,3]. Because calcium and phosphate are natural components in bone, many of these materials have improved bone bonding properties.

In an effort to mimic Nature, Muller et al. investigated biomimetic apatite formation on chemically modified cellulose templates [4]. After treating highly oriented trimethylsilylether-cellulose (TMS-cellulose) fibers with a supersaturated $Ca(OH)_2$ solution, and exposing to simulated body fluid, Muller et al. observed directed calcium phosphate precipitation on the surfaces of the cellulose fibers. Starting with an initial cellulose fiber diameter of about 20 μm, these coated fibers reached a final diameter of over 90 μm. After analyzing the electron diffraction patterns in transmission electron microscopy (TEM), it was found that the calcium phosphate precipitated as both octacalcium phosphate and carbonated hydroxyapatite ($CO_3$-HAp). This was supported by the strong calcium and phosphorus signals and the Ca/P ratio was found to be 1.35 with energy dispersive spectroscopy (EDS). As a mechanism, it was proposed that the chemically treated active surfaces attracted ions from solution, which initiated precipitation. However, the large initial diameter of the fibers acting as templates did not allow for control of the composite nanostructure.

Similarly, Song et al. developed a procedure using poly(2-hydroxyethyl methacrylate) (pHEMA) hydrogel scaffolds [5]. Like the cellulose in the previous study, Song et al. were able to precipitate calcium phosphate onto the surface of hydrogel strips. In this case, urea was used to slowly raise the solution pH and induce precipitation of calcium phosphate on the carboxylate-rich pHEMA surfaces. The result was a poorly crystalline ~5 μm thick coating of hydroxyapatite over the surface of the hydrogel strip.

On a smaller length scale, Rusu et al. used chitosan as a natural biopolymer matrix for their hydroxyapatite nanoparticle composites [6]. By mixing calcium chloride and sodium dihydrogen phosphate with a solution of chitosan in water, they were able to show self-assembly and size control as the hydroxyapatite crystallites formed inside the chitosan matrix. Using this process at 22 $^{o}$C, the initial product was nearly all brushite. This was converted to hydroxyapatite by raising the pH of the sample to the upper end of hydroxyapatite stability, making brushite a far less stable phase. They held the sample at this high pH and checked the phase with powder X-Ray Diffraction (XRD) at time intervals from 4 to 24 hours. Hydroxyapatite peaks began to appear immediately after the pH was raised above 11 and hydroxyapatite was the dominant phase after 24 hours. Using XRD line broadening and TEM analysis, a bimodal crystallite size distribution was observed with 15-20 nm primary crystallites and larger “cluster-like” domains of 200-400 nm.

While all of these studies produced biomimetic polymer-ceramic composites, the polymer-ceramic interaction was limited mostly to the surface of the bulk polymer or the polymer micelles. With a similar process using copolymer micelles that self-assemble to form a gel, our approach involves precipitating calcium phosphate onto the copolymer micelles and have them self-assemble to form a network of agglomerated polymer-inorganic nanospheres, a model for a bottom-up approach to the design of nanocomposites.

The Pluronic® F127 block copolymer, poly(ethylene oxide)-b-poly(propylene oxide)-b-poly(ethylene oxide) (PEO-PPO-PEO) and the poly(2-diethylaminoethyl methacrylate, PDEAEM) modified Pluronic® F127 pentablock copolymer (PDEAEM-b-PEO-b-PPO-b-PEO-b-PDEAEM) developed by Determan et al. [7] self-assemble into micelles at low temperature and concentration in aqueous solutions. These micelles entangle to form viscous gels at higher temperatures or concentrations, typically above 25°C [8]. The temperature dependent phase transformation of the copolymers allows mixing the solutions of copolymer and inorganic constituents followed by formation of homogeneous mixture of the micelle spheres and calcium phosphate by manipulating the temperature and/or pH of the solution. While previous studies were limited to calcium phosphate-polymer interaction on the surface of a bulk polymer, or agglomerates of nanocomposites at the sub-micro scale from solution, these polymers make it possible to precipitate calcium phosphate in the interstitial spaces between and on the surfaces of the concentrated spherical micelles within a macro-scale copolymer gel formed completely by self-assembly. The Pluronic® F127 is uncharged and the pentablock copolymers are charged at low pH, so the effect of surface charge on the formation of the inorganic phase was also investigated.

**9.2 Materials and Methods**

Unless otherwise noted, all chemicals in this study were obtained from Fisher Scientific and are of laboratory grade and purity. Precipitation of calcium phosphate into the copolymer gel matrix was achieved using aqueous solutions of ammonium dihydrogen phosphate ($NH_4H_2PO_4$), phosphoric acid ($H_3PO_4$), calcium nitrate ($Ca(NO_3)_2$), and the Pluronic® or PDEAEM pentablock copolymers. A saturated solution of calcium phosphate with a Ca:P ratio of 1.67 as in stoichiometric hydroxyapatite was prepared by mixing 120 mL of a 0.5M solution of ammonium $NH_4H_2PO_4$ with 200 mL of a 0.5M $Ca(NO_3)_2$ solution. This solution was stirred for 30 minutes until a white precipitate formed. The mixture was

then centrifuged and the clear supernatant was drawn off as the saturated calcium phosphate solution. This supernatant solution had a pH of 3.0.

A more concentrated solution was prepared by mixing 4.0M solutions of $H_3PO_4$ and $Ca(NO_3)_2$. NaOH was added until the solution reached a pH of 1.0 and a cloudy precipitate formed. Like the dilute solution described above, the supernatant was saved as the saturated calcium phosphate solution at pH=1.0.

Commercially available Pluronic® F127 (BASF Corporation, Florham Park, New Jersey) ($M_n$=12,600, 70% PEO) and the modified $PDEAEM_{35}$-F127-$PDEAEM_{35}$ pentablock copolymer developed by Determan et al. [7] were used as the polymer matrix phase. Gel samples were prepared by dissolving 3 g of the copolymer directly into the calcium phosphate solutions. Control samples of the copolymer dissolved in deionized water were also prepared. These mixtures were placed in a refrigerator at 3°C and stirred daily until the copolymer was completely dissolved. It took usually about 3 to 4 days to get a homogeneous solution. After dissolving, the samples were warmed to room temperature (22°C) and aged for 24 hours. During this time, as predicted by the temperature/concentration phase diagram the calcium phosphate-copolymer solution thickened into a viscous nanocomposite gel.

In order to analyze the growth of the ceramic coatings on the micelles, a less concentrated 0.5 wt% polymer solution (below the critical gel concentration) was also tested. To prepare this sample, 10 mL of the pH 3.0 calcium phosphate solution was mixed with an equal amount of 1.0 wt% pentablock copolymer solution yielding a solution of 0.5 wt% pentablock copolymer, and half of the saturated calcium phosphate ion concentrations. This solution was placed in a 25° C temperature controlled water bath, and allowed to age. Samples were taken after 30 min, 1 h, 24 h, and after two weeks for TEM observation.

Micrographs of the 24 h and the two-week samples were indistinguishable, implying that the system reaches apparent equilibrium within the first 24 hours.

### 9.3 Characterization Methods

Transmission electron microscopy (TEM) was used to directly visualize the nanostructure of the gels. Because it was important to retain and analyze the solution structure of the copolymer micelle or gel, cryogenic TEM was necessary. To prepare the TEM samples of the copolymer solutions, 50 µL of the aqueous sample was placed onto a formvar coated copper grid for 1 min allowing contents to settle. Most of the supernatant was wicked away and 1% phosphotungstic acid (pH 6.2) was applied for 30 s as a negative contrast stain. The grid was wicked and allowed to dry. Images were captured on a JEOL 1200EX II scanning transmission electron microscope (Japan Electron Optic Laboratories, Peabody, MA) using a Megaview III digital camera and SIS Pro. software (Soft Imaging Systems Inc., LLC, Lakewood, CO).

Gel samples were prepared as described above, placed onto a bulls-eye stub, and frozen at -100°C in the chamber of a Reichert Ultracut S ultramicrotome with FCS cryo unit (Mager Scientific Inc., Dexter, MI). Sections were made using a Diatome cryo-diamond knife (35°-dry Electron Microscopy Sciences, Ft. Washington, PA) at 100 nm and collected onto 300 mesh copper grids and placed into a grid transfer unit stored in liquid nitrogen until transferred to the TEM chamber. TEM samples were loaded into a liquid nitrogen cooled Gatan cold stage (Model 626DH, Gatan Inc. Pleasanton, CA) and imaged at 100 kV in a Phillips CM 30 TEM (Phillips Corporation, Schaumburg, IL). Qualitative chemical analysis was done with a ThermoNoran EDS unit calibrated to its internal standards (Thermo Electron Corporation, Waltham, MA).

Small angle X-ray scattering (SAXS) experiments were performed on the Pluronic® F127 and pentablock copolymer gels with and without the inorganic phase using the instrument at the 12-ID beam line at the Advanced Photon Source in Argonne National Laboratory to elucidate the gel nanostructure. A 15x15 cm detector was used to measure the scattered intensity and the transmitted intensity was measured using a photodiode. Samples were held in liquid DSC pans, 2 m from the detector. The beam energy used for the analysis is 12 keV ($\lambda$ = 1.035 Å) and the data were collected at 1 s exposures. The collected 2D data was corrected, azimuthally averaged, and placed on an absolute scale.

Crystalline phases were identified by X-ray diffraction, using a theta-theta X-ray diffractometer (Scintag, XGEN-400, Cupertino, CA). Wet gel samples were placed in an amorphous polymer sample holder and analyzed immediately to minimize drying. The Cu Kα x-ray source was set to 45 kV and 40 mA, and the samples were scanned at a rate of $1^{o}$/min over a 2θ range of $10^{o}$ – $70^{o}$. Phase analysis was done using the ICDD database and the Scintag DMSNT search / match software.

Thermogravimetric analysis (TGA) was performed with a Perkin Elmer thermogravimetric analyzer (Perkin Elmer, TGA 7, Downers Grove, IL) to obtain the fraction of the inorganic phase. Approximately 40 mg of the gel sample was placed in a platinum pan and the experiments were performed in a flowing air environment. The program was set to heat up to $100^{o}$C and hold at this temperature for 10 min, then heat from $100^{o}$C to $150^{o}$C at a rate of 3 $^{o}$C/min, and finally, heat from $150^{o}$C to $800^{o}$C at a rate of $10^{o}$C/min.

Solid-state NMR can provide useful information about the composition of the calcium phosphate and about the proximity of organic and inorganic components, i.e. about

the size of the nanostructures formed. The presence of water in solid-state NMR samples is undesirable since ionic currents lead to dissipation of radio-frequency power and can cause broadening of the probe-head tuning curve as well as sample heating. To prevent this, the samples were first dried by rotary evaporation and then lyophilized. For magic-angle-spinning NMR experiments, the samples were packed into 2.5-mm zirconia rotors with Kel-F caps. As desired, the probe head-tuning curve showed no significant broadening and the $^{1}H$ NMR spectrum was free of signals of loosely bound water.

All NMR experiments were carried out on a Bruker spectrometer (Bruker-Biospin DSX400, Rheinstetten, Germany) at 400 MHz for $^{1}H$ and 162 MHz for $^{31}P$ nuclei. A Bruker 2.5 mm double resonance magic-angle spinning (MAS) probehead, which enables short $^{1}H$ and $^{31}P$ pulses lengths of 2.5 μs duration for a $90^{o}$ flip angle, was used for 6.5 kHz MAS $^{1}H$-$^{31}P$ experiments. In direct-polarization (DP) $^{31}P$ experiments, recycle delays of 400 s and 1000 s were used. In $^{1}H$ and $^{1}H$-$^{31}P$ cross-polarization (CP) experiments, including two-dimensional (2D) $^{1}H$-$^{31}P$ wideline separation (WISE), recycle delays of 2 s were used before 400 μs of Hartmann-Hahn cross-polarization (CP). The $t_1$ increment was 20 μs. Due to the presence of sharp peaks in the $^{1}H$ spectrum, both cosine- and sine-modulated data were acquired to give the full frequency information in the $^{1}H$ dimension.

Direct polarization (DP) and cross polarization (CP) $^{31}P$ NMR spectra were acquired with $^{1}H$ decoupling at 6.5 kHz MAS. The DP spectrum is quantitative if the recycle delay is sufficiently long. In order to ensure this, the DP experiments were run with increasing recycle delays until there was no further increase in signal intensity. $^{1}H$-$^{31}P$ CP experiments indicate the protonation state of the phosphate group, most pronouncedly after a short (< 500 μs) cross-polarization time. The comparison with the DP spectrum indicates whether there are non-protonated phosphates present, which cross polarize slowly or not at all. No Hahn

spin echoes were used before detection because the transverse relaxation time of $^{31}P$ in one sample (Pluronic®-based composite) was extremely short, possibly due to unfavorable proton dynamics in the phosphate.

All $^{1}H$ NMR spectra were recorded at 6.5 kHz MAS using probe-head background suppression [9]. The line-width of the proton spectrum indicates the $^{1}H$-$^{1}H$ dipolar coupling, which increases with the proton density and decreases with the mobility of the segment. In rigid organic solids, the dipolar line width is ~ 40 kHz.

Supramolecular proximities and domain sizes can be probed in NMR using $^{1}H$ proton spin diffusion, during a "mixing" time $t_m$ on the ms to 0.5-s time scale. During the evolution period of a two-dimensional experiment, the magnetization of protons in one phase (A) is modulated by its characteristic chemical-shift frequency $\omega_A$. If during $t_m$ the magnetization diffuses to protons in a different phase (B), it will be detected with frequency $\omega_B$; thus, domain proximity on the spin diffusion length scale (0.5 – 30 nm, depending on $t_m$) results in an ($\omega_A$, $\omega_B$) cross peak in the two-dimensional spectrum. For small domain sizes, the equilibration is a fast process, while it is relatively slow for large domains. In the present case, phosphate protons are only a small percentage of the protons in the sample and therefore difficult to detect. Hence, we detect them indirectly, with excellent selectivity, in terms of $^{31}P$ spins to which these protons cross-polarize.

The experiment with $^{1}H$ evolution flanked by excitation and z-storage $90^{o}$ pulses, spin diffusion time $t_m$, read-out pulse, cross polarization to $^{31}P$, and $^{31}P$ detection effectively is a 2D WISE experiment [10]. At short $t_m$, the slice along the $^{1}H$ dimension will reflect only the phosphate protons near the detected $^{31}P$ spins; at longer $t_m$ times, if there is spin diffusion contact between the phosphate protons and the protons from the surrounding polymer matrix,

the $^{1}H$ line shape will change to that of the polymer protons. This approach was previously demonstrated in polymer-clay nanocomposites using $^{1}H$-$^{29}Si$ WISE NMR by Hou et al. [11].

## 9.3 Results and Discussion

### *9.3.1 Supramolecular structure*.

Transmission electron microscopy of the pentablock copolymer micelles in deionized water in dilute aqueous solutions is consistent with cryo-TEM analysis done by Determan et al. [7], who observed 60-90 nm diameter spheres in a 3 wt% pentablock micelle solution. A TEM micrograph of the polymer micelles is shown in Figure 1a. The micrographs of the pH 3.0 micelle samples prepared in inorganic solutions and aged for different time periods are presented in Figure 1b-e. They clearly show the growth of the calcium phosphate coating (dark regions) around some, but not all the micelles, with time. The two 24 h aged micrographs, Figures 1d, and 1e, are from different areas of the same sample. These images show single coated micelles as well as agglomerates of many. The pentablock gels prepared with the pH 1.0 calcium phosphate solution (Figure 1f), clearly indicated aggregates of spheres. The cryo-frozen gel appeared as a concentrated matrix of ~60 nm diameter spheres. Similar results were obtained with the Pluronic® solutions and gels While there was no obvious visible second phase in the gel micrograph (Figure 1f), EDS analysis showed strong calcium and phosphorous signals. These could be attributed to the amorphous calcium and phosphate ions in solution, or the precipitation of an inorganic calcium phosphate phase in the gel. XRD, NMR and SAXS studies were conducted to investigate the structure of the inorganic phase as well as the composite gel.

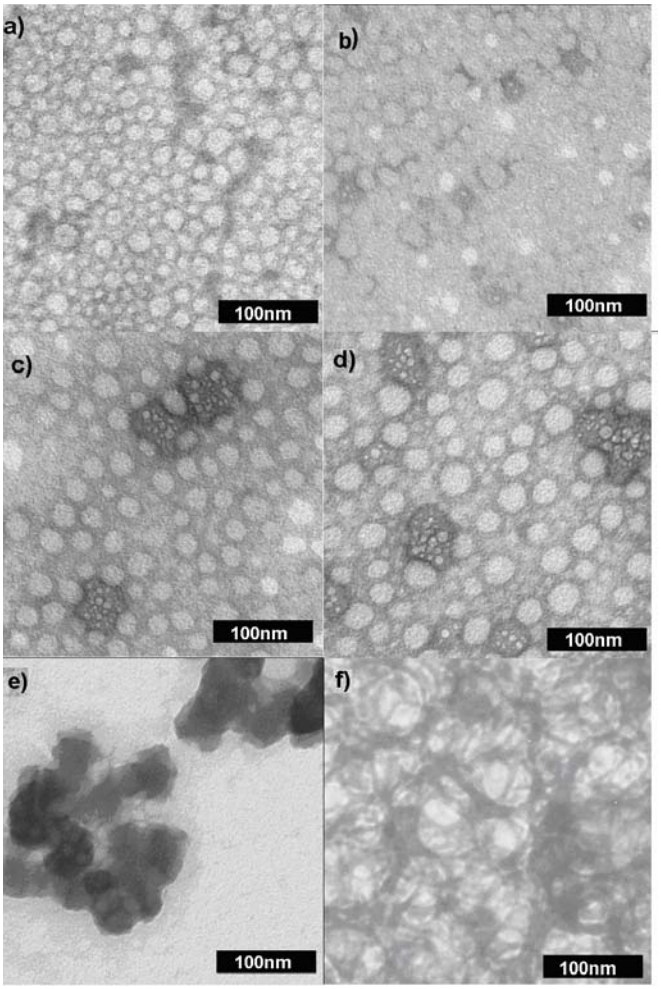


**Figure 1:** Transmission electron micrographs of a) 0.5 wt% pentablock copolymer micelles in deionized water, b) 0.5 wt% pentablock copolymer micelles in pH 3.0 calcium phosphate – aged 30 min, c) 0.5 wt% pentablock copolymer micelles in pH 3.0 calcium phosphate – aged 1 hour, and d, and e) different regions of 0.5 wt% pentablock copolymer micelles in pH 3.0 calcium phosphate – aged 24 hours;. f) 30 wt% pentablock copolymer-pH 1.0 calcium phosphate gel.
*Figure courtesy of Drew Enlow*

SAXS analysis was performed to investigate the ordered superstructure of the polymer-based nanocomposites. As shown in Figure 2, the self assembled Pluronic® copolymer gel with and without the calcium phosphate nanocomposites both at the pH 1.0 and pH 3.0 has distinct diffraction peaks with $Q/Q^*$ ($Q^*$ is the first order peak position) of $\sqrt{3}:\sqrt{4}:\sqrt{8}:\sqrt{11}:\sqrt{12}$, indicating that the system exhibits a face-centered cubic (FCC)

structure. The Pluronic® with calcium phosphate at pH 1.0 has additional higher order peaks, which implies that the system is better ordered. In addition, the Pluronic® gel with and without inorganic phase at pH 3.0 showed a similar inter-particle distance, D where

$$D = \sqrt{3} d_{111} \text{ and } \qquad d_{111} = \frac{2\pi}{Q^*}$$

At pH 1.0, however, D increases from 15.5 nm to 17.1 nm with the addition of calcium phosphate. This may be attributed to the different level of calcium phosphate precipitation over polymer micelles at different pH values. At pH 3.0, the precipitation rate of calcium phosphate is slow, the weight fraction of the inorganic phase is lower, as seen from TGA experiments (below) and only few micelles were coated with calcium phosphate, as seen in the TEM images. Due to the large number of micelles without inorganic coatings, the micelles coated with the calcium phosphate do not contribute much to the scattering. Hence, the D value remains similar in both Pluronic® gels with and without the inorganic phase at pH 3.0. At pH 1.0, the higher ionic concentration expedites the precipitation of calcium phosphate, and more micelles are coated with the inorganic phase. Thus, the micelle size increases due to the inorganic phase precipitation on the Pluronic®, causing an increase in D. This result is in agreement with the TEM data.

As for the pentablock copolymer gel nanocomposites in Figure 3, few SAXS peaks are observed. Besides, the peaks are much broader than those for the Pluronic® gels, which means that the system is relatively poorly ordered. However, comparing the SAXS patterns of the Pluronic® and pentablock gels, the trends of the profiles are fairly consistent. Therefore, the morphology of pentablock gels with and without calcium phosphate may also exhibit FCC structure, and any broad peak has contributions from several peaks. For the pentablock copolymer gel with calcium phosphate at pH 3.0, no distinct higher order peaks

were observed. This is presumably due to the formation of larger calcium phosphate particles in the interstitial spaces that disrupt the ordered pentablock copolymer packing structure. Compared to the D of the pure pentablock copolymer gel, there is a dramatic increase in D when the pentablock copolymer gels are coated with calcium phosphate at pH 1.0. This is consistent with the results seen with the Pluronic® gels with calcium phosphate at pH 1.0.

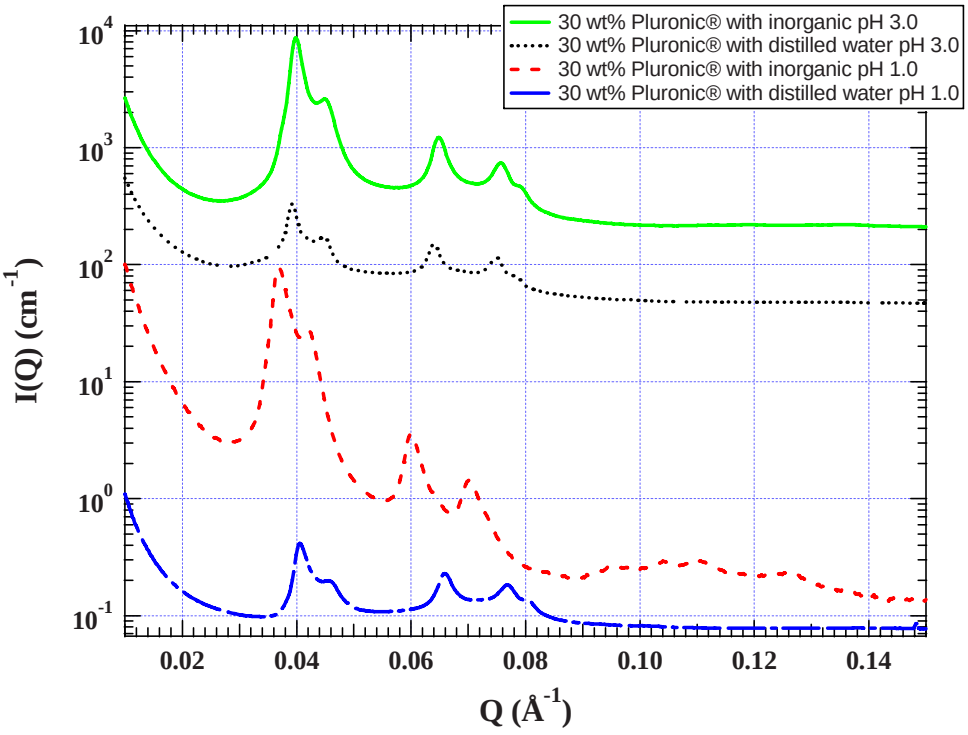


**Figure 2:** SAXS of Pluronic® F127 gels with and without calcium phosphate. Scattering patterns have been shifted vertically for clarity.
*Figure courtesy of Umai Kanapathipillai*

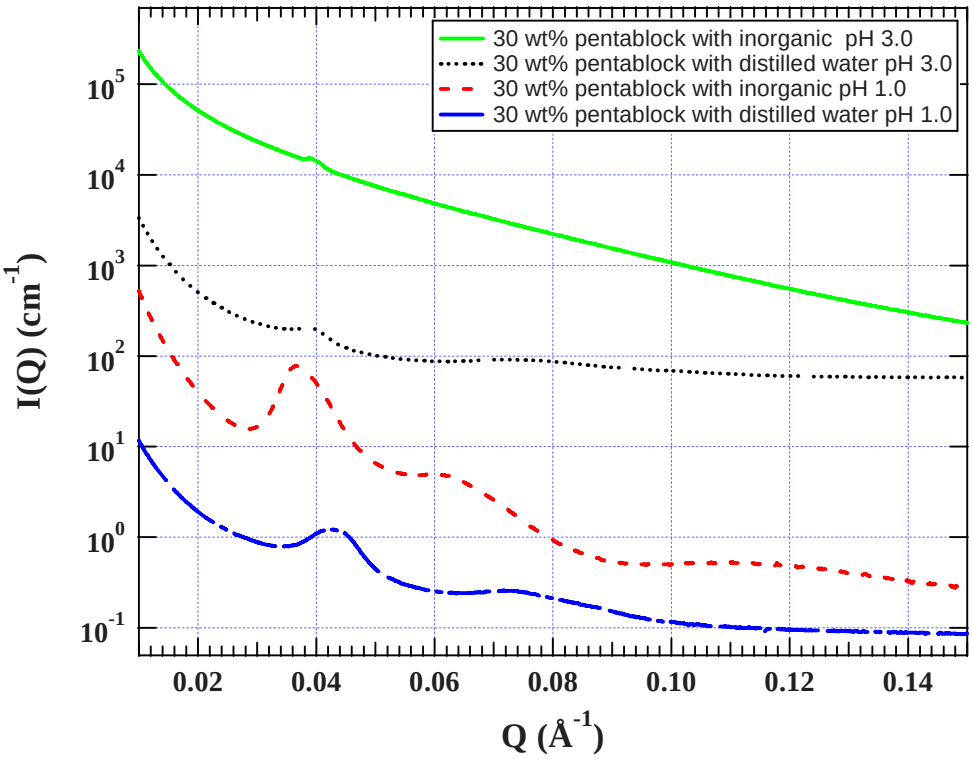


**Figure 3:** SAXS of pentablock copolymer gels with and without calcium phosphate. Scattering patterns have been shifted vertically for clarity.
*Figure courtesy of Umai Kanapathipillai*

*9.3.2 Structure of the calcium phosphates.*

The initial precipitate formed upon mixing of the 0.5 M $Ca(NO_3)_2$ and $NH_4H_2PO_4$ aqueous solutions contained a mixture of synthetic brushite ($CaHPO_4 \cdot 2H_2O$) and monetite ($CaHPO_4$). XRD of the precipitate formed in the gel samples show a different inorganic phase. When precipitated on the copolymer gel template, natural brushite, a mineral normally only found in caves [12] was observed. One of the most common cave minerals, natural brushite forms in guano deposits at low pH and high phosphate rich solutions. Apparently, the copolymer gel template nicely mimicks the biological process observed in

nature. Figure 4 presents X-ray diffraction patterns of both the Pluronic® F127 and pentablock gels dissolved in deionized water and in the pH 3.0 calcium phosphate solution, as well as the characteristic peaks of natural brushite (ICDD card # 11-0293). Figures 4a and 4b do not show any sharp peaks, but only amorphous reflections of the non-crystalline polymers. The pH 3.0 gel samples in Figures 4c and 4d, however, show all five of natural Brushite's most intense peaks, compared with Figure 4e.

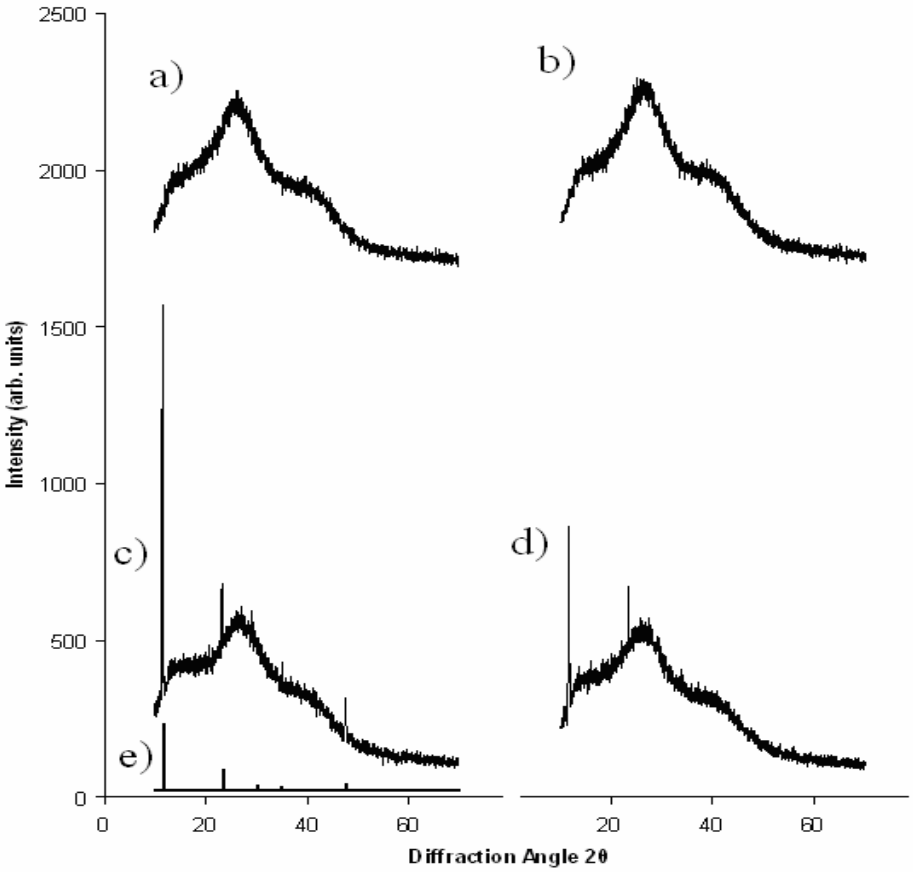


**Figure 4:** Wide-angle X-ray diffraction patterns of a) 30 wt% pentablock in deionized water, b) 30 wt% Pluronic® F127 in deionized water, c) 30 wt% pentablock in pH 3.0 calcium phosphate solution, d) 30 wt% Pluronic® F127 in pH 3.0 calcium phosphate solution, and e) characteristic natural brushite peaks.
*Figure courtesy of Drew Enlow*

Like the precipitate separated upon initial mixing of the calcium phosphate solutions, X-ray analysis of the higher ionic concentration pH 1.0 pentablock gel samples showed the synthetic brushite phase (Figure 5a). Because the solution was much more concentrated, there was more of a driving force for precipitation on the polymer. This led to less controlled precipitation and formation of the inorganic phase. After drying for 24 hours in a desiccator, a second phase, identified as calcium dihydrogen phosphate(Figure 5b). As the water evaporated from the sample, ions in solution were forced to precipitate. Because of the overwhelming driving force, ions precipitated heterogeneously as a second phase. Interestingly, this second phase was not present in the dried pH 1.0 Pluronic® F127 gel. The X-ray pattern of the dried Pluronic® F127 gel composite, Figure 5c, showed broader Bragg reflections, which is an indication of smaller crystal size. Evaluating the $2\theta = 23^{o}$ peak using the Scherrer equation, we obtain calcium phosphate crystal sizes of ~ 15 and >30 nm for the dried Pluronic® F127 gel and pentablock copolymer samples, respectively.

It was possible to control the amount of precipitation by adjusting the pH of the initial calcium phosphate solution as revealed by the TGA of the pH 3.0 and pH 1.0 samples illustrates this as shown in Figure 6. After evaporating all the water out of the gel, a baseline weight was found for each sample. Because of the chemically bound water from the brushite phase, water was not totally evaporated until the system reached 200 $^{o}$C. At 400 $^{o}$C, the polymer is burned off completely, leaving calcium phosphate residue corresponding to 6.5% of the solid phase (after removal of water by ~250 $^{o}$C) in the pH 3.0 gel. As predicted by the pH solubility diagrams [13], the inorganic weight % in the pH 1.0 gel sample was much higher at 15.0 % (again, based on the mass of the dried gel at ~250 $^{o}$C) . Using this data, it was also possible to calculate the initial concentrations of the calcium phosphate solutions. Assuming all of the left-over precipitate is the dehydrated monetite phase, it was determined that the initial calcium and phosphate concentrations were 0.5 M in the pH 1.0 and 0.2 M in the pH

3.0 calcium phosphate solutions. Considering the 40 mg size of the samples, these experimentally calculated concentrations are consistent with the pH - concentration diagram of the calcium phosphate system [13].

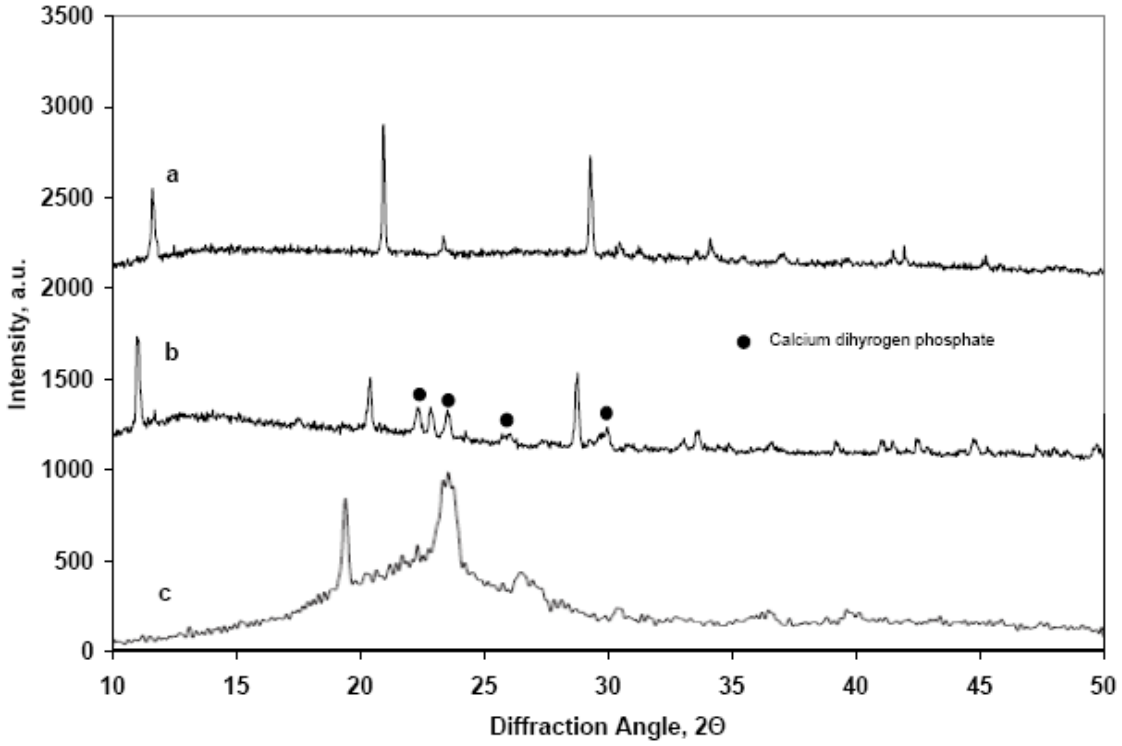


**Figure 5:** X-ray diffraction patterns of a) 30 wt% pentablock gel in pH 1.0 calcium phosphate solution, b) same sample after 24 h drying in a desiccator, and c) dried Pluronic® F127 copolymer gel in pH 1.0 calcium phosphate solution. Figure courtesy of Drew Enlow

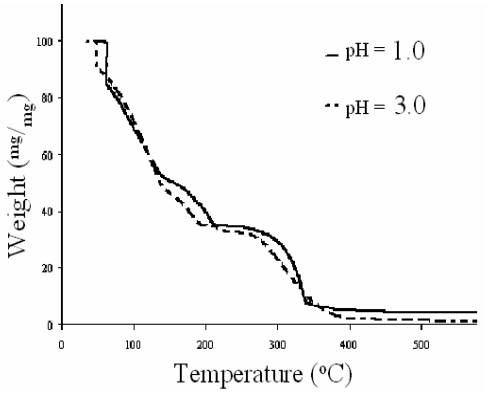


**Figure 6:** Thermogravimetric analysis of pH 1.0 and 3.0 for 30 wt% pentablock copolymer-calcium phosphate gel. Figure courtesy of Drew Enlow

The composition of the phosphate can also be assessed by $^{31}P$ NMR. The $^{31}P$ NMR spectra of the dried Pluronic® F127 - and pentablock – phosphate composites are shown in Figure 7. Comparing the $^{1}H$-$^{31}P$ cross-polarization to the direct-polarization spectra, we see in both instances that the same peaks are present in both spectra, and with almost equal intensities for the Pluronic® F127- phosphate composite. This indicates that all the phosphates exist as protonated species. For the Pluronic® F127 phosphate, the resonance is indicative of monohydrogen phosphate ($CaHPO_4$) as found in brushite / monetite, while the pentablock phosphate contains a significant contribution (ca. 1/3 of all phosphate) from calcium dihydrogen phosphate ($Ca(H_2PO_4)_2$). For reference, the spectrum of pure $Ca(H_2PO_4)_2$ is shown in Figure 7e,f; it exhibits two signals due to chemically inequivalent $H_2PO_4^-$ ions in the crystal structure. The Pluronic® F127-phosphate has a broader line shape as compared to the pentablock-phosphate, which suggests that the former exists in a more disordered environment. The spectra in Figure 7a-d have been scaled to equal peak height, but the true integrals of the spectra in Figure 7a and 7c indicate ca. five times more phosphate in the pentablock composite as compared to the Pluronic® F127 composite, given the almost equal fill factor in both sample rotors.

Furthermore, the $Ca(H_2PO_4)_2$ has a roughly twice longer $^{31}P$ longitudinal ($T_1$) relaxation time as compared to the $CaHPO_4$, which indicates that there is no efficient $^{31}P$ spin diffusion between the two phosphates on the 1-s time scale. This in turn means that the two phases are not in contact with domains on the 2-nm scale.

The $^{1}H$ proton spectra of the Pluronic® F127 composite are shown in Figure 8. The sharp resonances from the Pluronic® protons dominate the spectrum in the pentablock composite as well. Normally, in organic solid the proton resonances are very broad due to the strong multi-spin $^{1}H$-$^{1}H$ dipolar couplings. However, fast segmental motion far above the

glass transition average out the dipolar interactions in the Pluronic® F127 copolymer, resulting in the sharp lines seen in Figure 8. The proton spectrum of the Pluronic® F127 composite shows a broad component (Figure 8 c, d), which may be due to the reduced mobility of the Pluronic® F127 segments near the brushite particles.

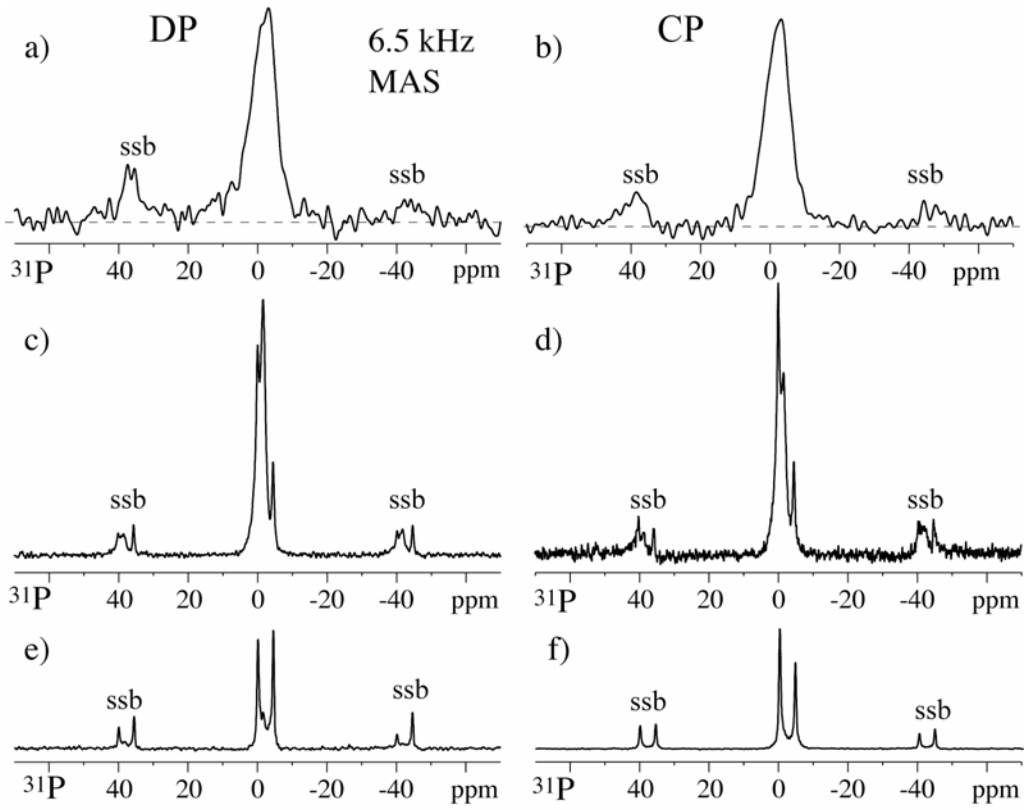


**Figure 7:** $^{31}$P NMR spectra of the dried (a, b) Pluronic® F127-phosphate composite (pH 1), (c, d) pentablock-phosphate composite (pH 1), and (e, f) calcium dihydrogen phosphate. The spectra were acquired with 6.5-kHz magic-angle spinning. Spinning sidebands are labeled "ssb". Direct-polarization (DP) spectra with (a) 400-s, (c) 1000 s, and (e) 100 s recycle delays are compared with 0.4-ms cross-polarization (CP) spectra in (b) , (d), and (f).

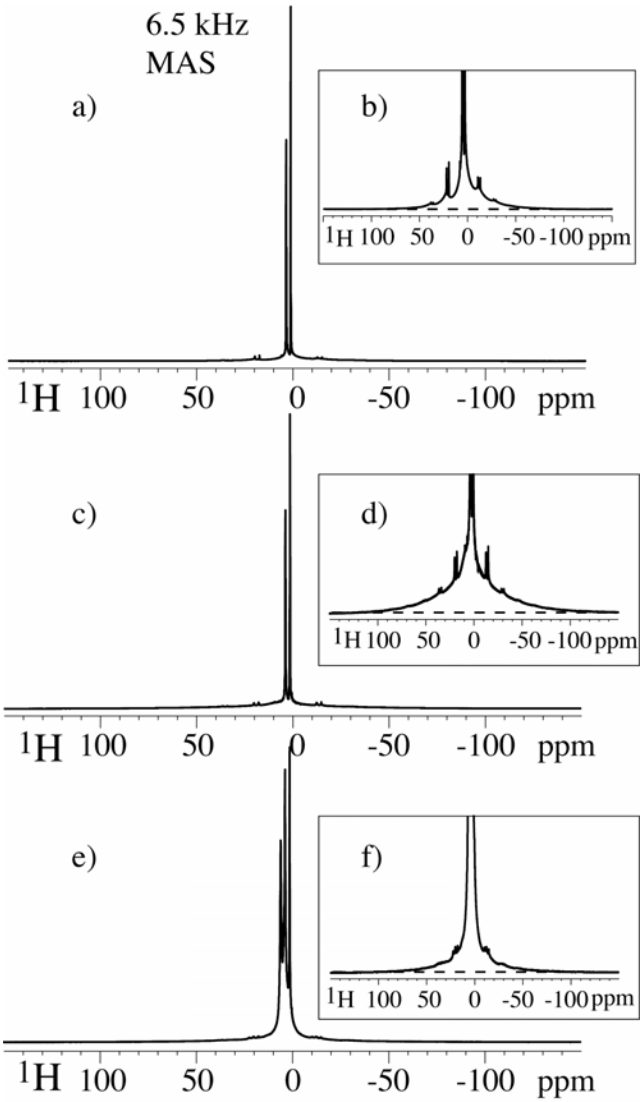


**Figure 8:** $^{1}$H NMR spectra of (a, b) the pure Pluronic® F127, (c, d) the Pluronic® F127 -phosphate composite, and (e, f) the pentablock-phosphate composite at 6.5 kHz MAS. The insets (b), (d), and (f) focus in on the base of their respective spectra, revealing a broadened base of the pluronic®-phosphate composite.

**Phosphate-polymer proximity.** $^{1}$H-$^{31}$P WISE with $^{1}$H spin diffusion proved useful for characterizing the proximity of the inorganic components to the organic matrix. As seen in the WISE spectra of Figure 9, for the Pluronic® F127 composite, $^{1}$H spin diffusion from

the Pluronic® F127 to the brushite protons occurs within 50 ms of spin diffusion time, as proved by the characteristic sharp doublet of the Pluronic® F127 protons clearly visible after 50 ms of spin diffusion. Given a spin diffusion coefficient of < 0.5 $nm^2/ms$ in protonated phosphates, this indicates domain sizes of less than 20 nm. This is completely consistent with the small crystallite size indicated by XRD peak broadening for the identical material, see Figure 5c above.

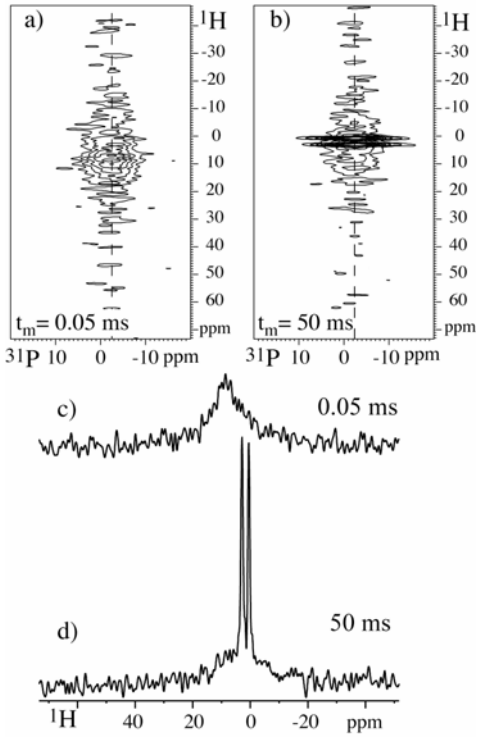


**Figure 9**: $^1H\{^{31}P\}$ 2D WISE with $^1H$ spin diffusion, at 6.5 kHz MAS, of the dried Pluronic® F127–phosphate composite. (a) and (b) are 2D contour plots of spectra recorded after 0.05 and 50 ms of spin diffusion, respectively. Figures (c) and (d) are slices along the $^1H$ dimension extracted at -1.6 ppm in the $^{31}P$ dimension from the spectra in (a) and (b), respectively.

In contrast, there is hardly any evidence of spin diffusion contact in the case of the pentablock composite, see Figure 10. After 50 ms of spin diffusion, little line-shape change is observed, see Figure 10 b, e. The characteristic doublet of the Pluronic® F127 block is absent. Only a minor signal in the 1 – 8 ppm range might be attributed to the polymer

protons. This indicates large particles > 20 nm in diameter, where most of the protons are far away from the pentablock copolymer matrix. No signs of spin diffusion, only signal reductions by $^{1}H$ $T_1$ relaxation, are observed after 500 ms, see Figure 10 c, f.

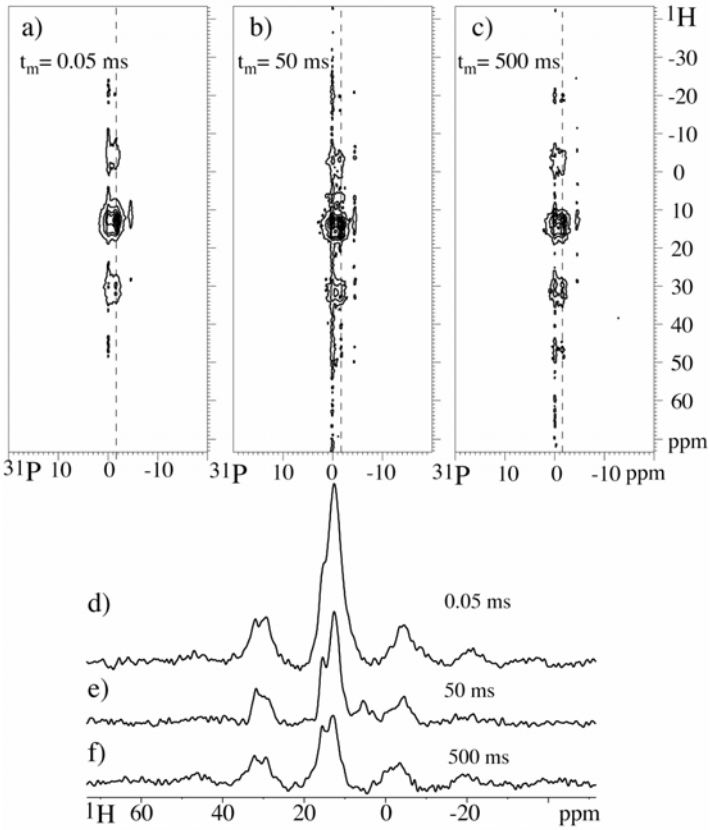


**Figure 10:** $^{1}H$ {$^{31}P$} 2D WISE with $^{1}H$ spin diffusion, at 6.5 kHz MAS, of the dried pentablock–phosphate composite (pH 1.0, 30 wt% copolymer, calcium phosphate). (a), (b) and (c), are 2D contour plots of spectra recorded after 50 μs, 50 ms and 500 ms of spin diffusion respectively. Figures (d), (e) and (f) are slices extracted along the $^{1}H$ dimension from (a), (b), and (c), respectively, indicated by the dashed lines corresponding to 1.6 ppm in the $^{31}P$ dimension. The bands flanking the main peak on either side, labeled ssb, are spinning sidebands, mostly due to the large chemical-shift anisotropy of -OH protons.

Based on the observations presented above, we propose that calcium phosphate nucleation occurs on the pentablock copolymer micelle surface, aided by the cationic characteristics of the PDEAEM end groups. This is clearly seen in the TEM images of the copolymer solutions at lower concentrations. As micelles, these hydrophilic end groups align themselves into a continuous cationic spherical surface. This attracts the ions in solution and

provides sites for nucleation. A similar mechanism provides nucleation sites in the Pluronic® F127 gel. Pluronic® F127 micelles have polar OH end groups that when assembled as a surface can provide slightly negatively charged sites for nucleation. Because of the high concentration of polymer in the gel samples, at temperatures above 5°C, the micelles with the inorganic coatings agglomerate into nano-composite networks with ordered structures.

**9.4 Conclusions**

In this work, we have successfully demonstrated the formation of macroscale polymer-inorganic nanocomposite solids with ordered micro- and nanostructures completely by self-assembly in solution. By changing the ionic character of copolymer micelles in solution, we can vary the formation and composition of the inorganic phase on copolymer micelles in aqueous solutions. Appropriate copolymer design and synthesis and the use of gel forming self assembling copolymers, makes possible the formation of macro-sized ordered networks of spherical nanocomposites for a bottom-up approach to materials design, while most previous work has focused on mineralizing the surface of bulk polymers [4,5] or forming sub-micron aggregates of organic-inorganic nanocomposites [6,14], The nanocomposites formed were characterized by electron microscopy, X-ray scattering, and advanced solid-state NMR. XRD and $^{31}$P 1-D NMR identified the phosphate in the Pluronic® F127 composite as a disordered brushite type species, while the inorganic calcium phosphate phase in the pentablock composite is relatively more ordered and contains ~25% of crystalline calcium dihydrogen phosphate that forms during drying. TGA and NMR showed that there is a higher mineral content in the pentablock composite as compared to the Pluronic® F127 composite. Analysis of peak broadening in XRD and $^{1}$H-$^{31}$P WISE experiments with $^{1}$H spin diffusion consistently showed that the brushite particles in the Pluronic® matrix are ~ 15 nm in diameter, while the brushite and calcium dihydrogen phosphate particles in the pentablock system are larger (>30 nm). Ability to form nanocrystalline calcium phosphate phase from

aqueous solutions onto self-assembling copolymer micelles and gels is a first step in mimicking mineralization of collagen in bone formation. It is believed that insight into the nucleation and growth of calcium phosphate on polymer surfaces will lead to a better understanding of bone formation, and design of better bone implants.

**Acknowledgments**

Ames Laboratory is operated for the U.S. Department of Energy by Iowa State University under contract No. W-7405-ENG-82. This research was supported by the Department of Energy. This work benefited from the use of BESSRC-CAT at APS, and the IPNS, funded by the U.S. DOE, BES, under contract No. W-31-109-ENG-38 to the University of Chicago. The authors also wish to thank E. White, Y.E. Kalay, Y. Yusufoglu, X. Wei, M. Determan, M. Kramer, and O. Ugurlu for their contributions to this work.

**References**

1. Malsy, A.; Bohner, M. *European Cells and Materials* 2005, 10, 28.
2. Jonasova, L.; Muller, F. A.; Helebrant, A.; Strnad, J.; Greil, P. *Biomaterials* 2002, 23, 3095-3101.
3. Jonasova, L.; Muller, F. A.; Helebrant, A.; Strnad, J.; Greil, P. *Biomaterials* 2004, 25, 1187-1194.
4. Muller, F. A.; Jonasova, L.; Cromme, P.; Zollfrank, C.; Greil, P. The Annual Meeting of the International Society for Ceramics in Medicine, Nov 6-9 2003, Porto, Portugal, 2004, pp 1111-1114.
5. Landis, W. J.; Hodgens, K. J.; Arena, J.; Song, M. J.; McEwen, B. F. *Microsc Res Tech* 1996, 33, 192-202. .

6. Rusu, V. M.; Ng, C.-H.; Wilke, M.; Tiersch, B.; Fratzl, P.; Peter, M. G. *Biomaterials* 2005, 26, 5414-5426.

7. Determan, M. D.; Cox, J. P.; Seifert, S.; Thiyagarajan, P.; Mallapragada, S. K. *Polymer* 2005, 46, 6933-6946.

8. Determan, M. D.; Cox, J. P.; Mallapragada, S. K. *J. Biomed. Mater. Res.* in press.

9. Danilchenko, S. N.; Moseke, C.; Sukhodub, L. F.; Sulkio-Cleff, B. *Crystal Research and Technology* 2004, 39, 71-77.

10. Schmidt-Rohr, K.; Clauss, J.; Spiess, H. W. *Macromolecules* 1992, 25, 3273-3277.

11. Hou, S. S.; Beyer, F. L.; Schmidt-Rohr, K. *Solid State Nuc Mag Reson* 2002, 22, 110-127.

12. Murray, J. W.; Dietrich, R. V. *American Mineralogist* 1956, 41, 616-626.

13. Oonishi, H.; Oomamiuda, K., Eds. Degradation/resorption in bioactive ceramics in orthopaedics; Chapman and Hall: London, 1998.

14. Wang, Y.; Yang, C.; Chen, X.; Zhao, N. *Advanced Engineering Materials* 2006, 8, 97-100.

# CHAPTER 10.
# THE DISPERSION OF SILICATE IN TRICALCIUM PHOSPHATE ELUCIDATED BY SOLID-STATE NMR

A. Rawal, X. Wei, M. Akinc, K. Schmidt-Rohr

Submitted to *Chemistry of Maerials.*

**Abstract**

The dispersion of silicate in tricalcium phosphate, a resorbable bioceramics for bone replacement, has been investigated by various solid-state nuclear magnetic resonance (NMR) methods. In samples prepared with 5 and 10 mol% of both $^{29}SiO_2$ and ZnO, three types of silicate have been detected: (i) $SiO_4^{4-}$ ($Q_0$ sites) with long longitudinal ($T_{1,Si}$) relaxation times (~10,000 s), which substitute for ~1% of $PO_4^{3-}$; (ii) silicate nanoinclusions containing $Q_2$, $Q_1$, and $Q_0$ sites with $T_{1,Si}$ ~ 100 s, which account for most of the silicon; and (iii) crystalline $Q_4$ ($SiO_2$) with long $T_{1,Si}$. Sensitivity was enhanced >100-fold by $^{29}Si$ enrichment and refocused detection. The inclusions in both samples have a diameter of ~7 nm, as proved by $^{29}Si\{^{31}P\}$ REDOR dephasing on a 30-ms time scale, which was simulated using a multispin approach specifically suited for nanoparticles. $^{29}Si$ CODEX NMR with 30-s $^{29}Si$ spin diffusion confirms that an inclusion contains >10 Si (consistent with the REDOR result of >100 Si per inclusion). Overlapping signals of silicate $Q_2$, $Q_1$, and $Q_0$ sites were spectrally edited based on their J-couplings, using double-quantum filtering. The large inhomogeneous broadening of the $Q_2$, $Q_1$ and $Q_0$ $^{29}Si$ subspectra indicates that the nanoinclusions are amorphous.

## 10.1 **Introduction**

Among the calcium phosphate ceramics, tricalcium phosphate ($Ca_3(PO_4)_2$, TCP) has been investigated particularly extensively as one of the most promising resorbable bioceramics for bone replacement.[1-3] Due to its high solubility, it is expected to degrade in

the host and be gradually replaced by the regenerating bone, meanwhile serving as a seed of the new bone and a supplier of Ca and $PO_4$ ions. TCP was reported to be more bioresorbable than hydroxyapatite, which usually shows minimal resorption. However, higher solubility of TCP results in a reduction of the bone-implant strength. Thus, the suitability of TCP for use in vivo is critically dependent on how the dissolution behavior might be controlled by chemical modification.

In our previous research, silicon and zinc were added as stabilizers to modify the dissolution behavior of TCP; these elements are osteoconductive and could stimulate osteogenesis for new bone growth.[4] The previous XRD results showed that TCP doped with 10 mol% Si and Zn at high temperature crystallizes in the low-temperature β-phase. No major secondary or amorphous phase was observed in the diffraction pattern, which indicates that Zn and Si are incorporated into the TCP structure after high temperature sintering. The dissolution study also confirmed that the Zn- or Si-doped TCP is stabilized in simulated body fluid compared with pure TCP.[5] When the doping level is reduced to 5 mol%, some α-TCP signals are observed. Doping only with Si produces α-TCP. [6-8]

The stabilization mechanism was explored from the crystallographic point of view. In the β-TCP unit cell, the Ca(4) and Ca(5) sites are distinct from the other three sites and suitable for smaller cations such as Zn, but are highly constrained for $Ca^{2+}$ ions. Ca(4) is on the 3-fold axis and has an unusual coordination to the O(9), O(9'), O(9'') face of the $P(1)O_4$ group. It has a coordination number of only three, in a flattened tetrahedral configuration, which results in a compressed Ca site. The Ca(4)···O(9) bonds are 3.041(1) Å, longer than the normal Ca···O bond of 2.4 Å. The Ca(5) sites are surrounded by oxygens in a six-fold distorted octahedral coordination, and all six Ca···O distances are relatively short, in the range 2.238-2.287Å.[9,10] Thus, substitution of smaller $Zn^{2+}$ for $Ca^{2+}$ results in a more stable

TCP structure by reducing the strain in the structure. Given the similar tetrahedral structure of $PO_4^{3-}$ and $SiO_4^{4-}$, P in the TCP structure may be replaced by Si, and substitution of Ca by the smaller Zn also leaves more open space for larger Si substituting in P sites. Our previous Rietveld analysis for lattice parameters and unit-cell volume show an effect of Zn and Si on the crystal structure.[11,12] However, Si may also exist as a secondary phase, which is too small in amount or amorphous to be detected by XRD. Due to limitations in XRD resulting from the similar electron density of Si and P, the details of Si incorporation into TCP is still unclear. Theoretical investigations have been carried out regarding the stability of α– and β–TCP and the fate of silicate ions in a TCP matrix,[13,14] but their predictions of $Q_0$ sites and $Si_2O_7$ ($Q_1$-$Q_1$) dimers have not been confirmed by experiment.

In this paper, solid-state $^{29}$Si and $^{29}$Si {$^{31}$P} nuclear magnetic resonance (NMR) is applied to analyze the Si environment in Si,Zn-doped TCP, in order to help understand the stabilization mechanism by Si. Modern solid-state NMR provides various methods for characterizing the local structure even of highly complex or disordered solids. $^{29}$Si NMR is an excellent means for elucidating structure and chemistry in silicates, which form a rich and varied class of materials including glasses[15,16] and zeolites[17-19]. The local bonding geometry is reflected in isotropic and anisotropic $^{29}$Si chemical shifts, [15,16] while the number of spins in a cluster can be counted using stimulated-echo experiments, such as CODEX,[4] with $^{29}$Si spin diffusion. The present samples were isotopically labeled by $^{29}$Si, which greatly enhances sensitivity. In combination with refocused detection,[20,21] a more than 100-fold sensitivity enhancement is achieved. By contrast, earlier routine NMR studies of Si-doped TCP did not yield $^{29}$Si NMR signal.[22] The uniform $^{29}$Si labeling also produces homonuclear J-couplings useful for distinguishing different $Q_n$ silicates sites in $^{29}$Si-$^{29}$Si J-modulation or double-quantum experiments and makes $^{29}$Si spin diffusion within silicon-rich phases efficient, which enables identification of silicate-rich domains.

The proximity of $^{31}P$ and $^{29}Si$, a crucial observable in Si-doped TCP, can be measured in terms of the strongly distance dependent dipolar couplings between these nuclear spins. In $^{29}Si\{^{31}P\}$ rotational echo double resonance (REDOR)[23] experiments, the dephasing rate of the $^{29}Si$ magnetization reflects the recoupled $^{29}Si$-$^{31}P$ dipolar interactions. We present quantitative simulations of REDOR data for nanometer-scale inclusions and demonstrate that even though $^{29}Si$-$^{31}P$ spin pair dephasing is insignificant for internuclear distances > 1 nm, almost complete dephasing can be observed even for nanoparticles of 7-nm diameter.

## 10.2 Experimental

### *10.2.1 Sample Preparation.*

Commercial reagent-grade $CaCO_3$, $NH_4H_2PO_4$, and ZnO (all from Fisher Scientific, Hampton, NH) were used as received. In order to increase the signal of the 10- to 20-fold diluted silicon species in the NMR experiments, 99% isotopically enriched $^{29}SiO_2$ (Cambridge Isotope Laboratories, Andover, MA) was used instead of regular unlabeled $SiO_2$. Since the natural abundance of the NMR-active $^{29}Si$ isotope of only 4.4%, the isotopic labeling achieves a 23-fold sensitivity gain, reducing the experiment time by a factor of 500. In addition, it results in J-couplings between any two silicon sites connected by oxygen. TCP was synthesized by reacting the appropriate chemical mixture according to the following equation:

$$3CaCO_3 + 2NH_4H_2PO_4 \rightarrow Ca_3(PO_4)_2 + 3CO_2 + 2NH_3 + 3H_2O$$

NMR samples were prepared with 5 mol% and with 10 mol% addition of ZnO and $^{29}SiO_2$. Here, 10 mol% means that the Zn and Si substitutions were 10 mol% of Ca and P

(i.e., $\frac{Si}{(Si+P)} = \frac{Zn}{(Zn+Ca)} = 0.1$). The molar ratios of (Zn+Ca):(Si+P) were kept constant at 1.5 as in stoichiometric TCP. The mixture was milled in anhydrous ethanol for 4 hours by using alumina milling media. The slurry was vacuum filtered and dried. Thereafter, the powder was sintered at 1300$^{o}$C for 10 hours in air followed by quenching in dry air. The WAXD patterns were similar to those of the corresponding materials in ref.[12]. They show β-TCP peaks, with additional α-TCP signals for the 5%-doped sample.

*10.2.2 NMR parameters.*

Solid-state NMR experiments were run on a Bruker DSX-400 spectrometer at 162 MHz for $^{31}$P and 79 MHz for $^{29}$Si. Taking advantage of the very long $^{29}$Si transverse relaxation time ($T_2$) in the system, multiple-echo (CPMG) detection was used for signal enhancement.[20,21] In this scheme, a train of rotation synchronized refocusing 180$^{o}$ pulses are applied on the detection channel ($^{29}$Si) during acquisition, with detection turned off whenever the refocusing pulse is applied. After Fourier transformation, this produces spikelets whose frequency spacing is the inverse of the time domain spacing of the refocusing pulses. While multiple-echo detection provides a large S/N enhancement, it comes at the cost of loss of some chemical shift resolution, to an extent which depends on the spacing of the refocusing pulses. The refocusing pulses were timed differently depending upon the experimental requirements of signal enhancement or spectral resolution. In order to prevent sample heating by the long (1.7 s to 6 s) train of refocusing pulses, the duty cycle of the refocusing pulses was kept under 2 % and usually ca. 0.5%, and the 180$^{0}$ pulses were usually set to a “soft” pulse length of 21 μs, which did not decrease their effectiveness.

Magic-angle spinning (MAS) and static $^{29}$Si NMR experiments were run in a Bruker double resonance probe head in single-resonance mode. Most single resonance MAS

experiments were run at 5 kHz MAS. A variety of recycle delays, up to 90,000 s, were used, with the refocusing pulses spaced at 4.2 ms for an acquisition time $t_{aq}$ = 1.7 s. For selective detection of long-$T_1$ species, recycle delays of 20,000 s and $T_1$- filtering times of 1,000 s were used. The refocusing pulses were spaced at longer intervals of 40 ms, in order to define the lineshape more accurately, with $t_{aq}$ = 5.9 s. Spectral editing was achieved mostly by $T_2$/J-modulation and by double-quantum filtering (DQF). The $T_2$/J-modulation was achieved by a simple Hahn echo with echo times $2\tau$ between 80 and 136 ms. while the DQF used a refocused INADEQUATE pulse sequence. Recycle delays of 1,000 s were used for the $T_2$/J-modulation experiments to observe $Q_0$ sites, while 400 s were sufficient for the DQF experiments because of the shorter $T_1$ of the $Q_1$ and $Q_2$ sites. The static homonuclear dephasing experiments were carried out with 5-s recycle delays for the $^{29}SiO_2$ precursor material, while 400-s and 1,000-s recycle delays were used for the labeled and unlabelled Si,Zn-doped TCP samples, respectively. The $Q_0$ sites of the 5% $^{29}$Si,Zn-doped TCP were selected by a 20,000-s recycle delay followed by a 1000-s $T_1$ filter. The refocusing pulses were spaced at 1-ms intervals, with an acquisition time of 80 ms. The CODEX experiments were carried out at 3-kHz MAS with a CODEX recoupling time of one rotation period. The refocusing pulse spacing was 2.7 ms, with $t_{aq}$ = 330 ms.

$^{29}$Si{$^{31}$P} REDOR NMR experiments were performed in a 4-mm XYH triple-resonance probe (Bruker Biospin) with a modified tuning insert, at 3 and 6 kHz MAS. The $^{31}$P 180$^o$ pulse length was 9.4 μs. For improved insensitivity to $B_1$ inhomogeneity, composite (90$^o$-180$^o$-90$^o$) pulses were used on $^{31}$P, while the phase of the single refocusing pulse on the observe channel was varied according to the EXORCYCLE scheme.[24] The composite $^{31}$P 180$^o$-pulses were optimized in $^1$H{$^{31}$P} REDOR experiments on NIST hydroxyapatite (HAp), $Ca_{10}(PO_4)_6(OH)_2$, with detection of the OH protons. HAp was also used as a model system of X{$^{31}$P} REDOR dephasing of ions homogeneously dispersed in a phosphate, as described in

the Supporting Information. The maximum duration of the REDOR dephasing was 80 ms. 32 scans were averaged with a recycle delay of 250 or 400 s. The experiment was first run at 6 kHz MAS and repeated six weeks later at 3 kHz MAS to ensure reproducibility, which turned out to be excellent. During detection, the signal was refocused by a 10- or 20-μs $180^o$ pulse every 1.2 ms, applied 6 kHz off resonance from the signal maximum, for $t_{aq}$ = 1.7 s. This "compressed" the signal into three peaks of ~1 Hz width.

### *10.2.3 $^{29}Si\{^{31}P\}$ REDOR simulations for silicate nanoparticles.*

While the details of REDOR curves in few-spin systems depend on the spatial arrangement of the spins, for nanoparticles the shape of the REDOR curve is dominated by the distribution of distances due to different depths from the interface. As shown in Figure 1, surface and core sites have dramatically different REDOR decay constants. The superposition of the curves corresponding to the different depths z from the silicate-phosphate interface, with shell-volume weighting p(z):

$$S(t) = \int_{d_{min}}^{r} S(z, t)\, p(z)\, dz \qquad (1)$$

produces the "pseudo-exponential" shape observed. Each S(z, t) curve is itself a orientational average (superposition) of the multi-spin REDOR curves of a $^{29}$Si at a given depth. For a multi-spin system, the initial REDOR decay depends only on the internuclear distances, while the intermediate-time behavior, which often shows low-amplitude oscillations, also reflect the angles between the internuclear vectors. The oscillations interfere away in complex multi-spin systems. Therefore, we have used Gaussian curves that match the initial behavior correctly. These Gaussians with the second moment $M_2(\theta, z)$ of the REDOR frequencies were calculated for a given depth z and angle θ between a given surface normal and the rotor axis, and also depend on the angle $\gamma_0$ of the external field $B_0$

around the rotor axis

$$S(z,t) \quad \int_0^{2\pi} \int_{-1}^{1} = \exp(-M_2(\theta,\gamma_0,z)\, t^2/2)\, d\cos\theta\, d\gamma_0 \qquad (2)$$

$M_2(\theta,\gamma_0,z)$ is the sum of the squared REDOR frequencies [23,25] of the $^{29}$Si-$^{31}$P spin pairs

$$M_2(\theta,\gamma_0,z) = (0.45)^2\, (2\pi\, \mu_0/(4\pi)\, \gamma_{Si}\, \gamma_P)^2 \times \Sigma_n \sin^2(2\beta_n) \sin^2\gamma_n\, 1/r_{SiP,n}{}^6 \qquad (3)$$

with $\beta_n$, $\gamma_n$, and $r_{SiP,n}$ depending on $\theta$ and z, and $\gamma_n$ also on $\gamma_0$. The sum is performed over the $^{31}$P spins, which are placed on a cubic lattice with spacing a. We can calculate

$$\sin^2(2\beta_n) = 4\cos^2\beta_n\, (1-\cos^2\beta_n) = 4\{(\mathbf{r}_{rot} \cdot \mathbf{r}_{SiP,n}/r_{SiP,n})^2 - (\mathbf{r}_{rot} \cdot \mathbf{r}_{SiP,n}/r_{SiP,n})^4\} \qquad (4)$$

from the dot product $\cos\beta_n$ between the rotor axis $\mathbf{r}_{rot}$ and the $^{29}$Si-$^{31}$P internuclear direction $\mathbf{r}_{SiP,n}/r_{SiP,n}$, and

$$\sin^2\gamma_n = 1- \cos^2\gamma_n = 1 - \{(\mathbf{B}_0/B_0 \cdot \mathbf{r}_{SiP,n}/r_{SiP,n} - \cos\beta_n \cos(54.7^o))/(\sin\beta_n \sin(54.7^o))\}^2 \qquad (5)$$

from the dot product between the applied magnetic field and the $^{29}$Si-$^{31}$P internuclear direction, $\mathbf{B}_0/B_0 \cdot \mathbf{r}_{SiP,n}/r_{SiP,n} = \cos(\theta_{B0,n})$, using $\cos(\theta_{B0,n}) = \cos\beta_n \cos(54.7^o) + \sin\beta_n \sin(54.7^o) \cos\gamma_n$ with $\cos\beta_n = \mathbf{r}_{rot} \cdot \mathbf{r}_{SiP,n}/r_{SiP,n}$ and $\sin\beta_n = (1- \cos^2\beta_n)^{1/2}$. The Gaussian dephasing curves (not the second moments) for different relative orientations $\theta$ of crystallite surface normal and rotor axis, and of the $B_0$ field around the rotor axis ($\gamma_0$), are averaged for a given depth z from the interface to produce S(z,t), see eq.(2).

How can heteronuclear dipolar couplings, which have a "reach" of < 0.8 nm for $^{31}$P-$^{29}$Si spin pairs, probe particles up to 10 nm in diameter? Two reasons can be given: (i) The

dephasing of a given $^{29}$Si spin by multiple $^{31}$P spins (typically $N_P = 20$) in the TCP matrix is $N_P^{1/2}$ times faster than in a $^{29}$Si-$^{31}$P spin pair. (ii) In a 10-nm diameter sphere, the ~1.6-nm thick outer shell that can be dephased significantly within 80 ms (see Figure 1a) accounts for 70% of the volume, so significant dephasing (down to ~30%) will be observed.

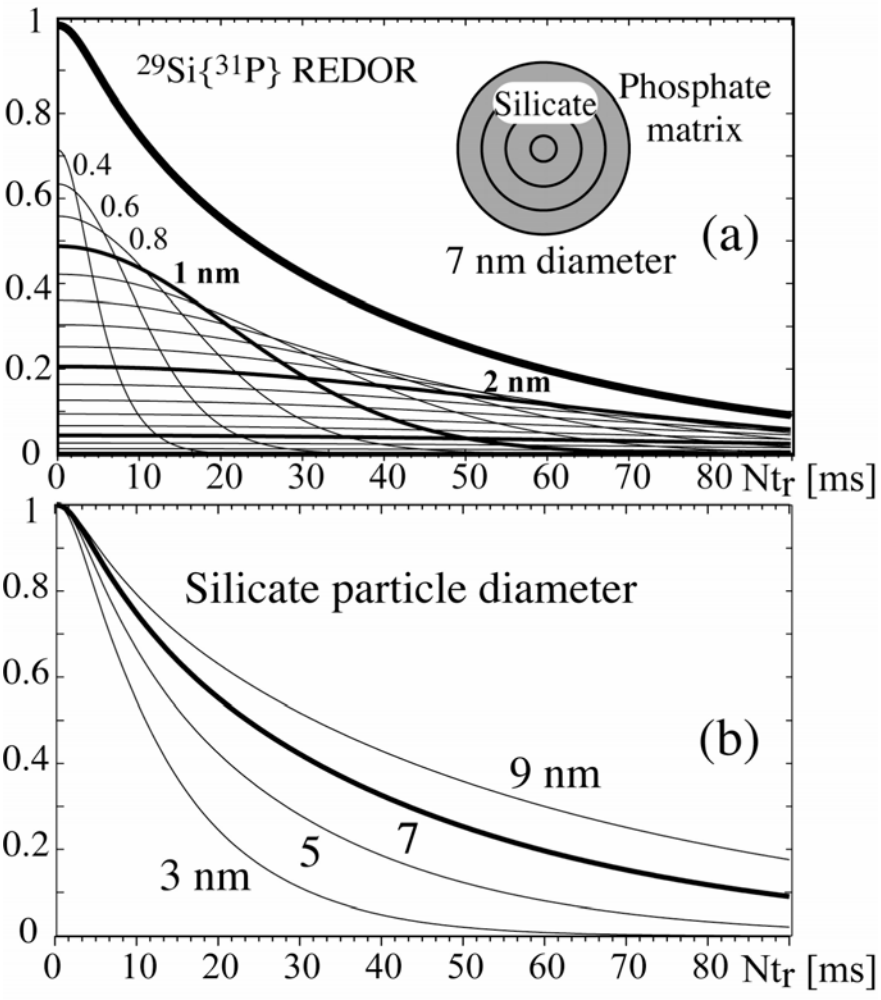


**Figure 1.** Examples of $^{29}$Si{$^{31}$P} REDOR simulations for spherical silicate particles in a phosphate matrix. (a) Dephasing of different layers, spaced by 0.2 nm. The closest approach of $^{29}$Si and $^{31}$P is 0.4 nm. The relative intensity corresponds to the number of $^{29}$Si in the various shells. Thick line: total dephasing. (b) Total dephasing for various particle diameters.

## 10.3 Results

### *10.3.1 $^{29}$Si spectra.*

Figure 2a-2d shows various one-dimensional $^{29}$Si NMR spectra of 5 and 10 mol% $^{29}$Si,Zn-doped TCP. The spectra exhibit significant inhomogeneous broadening of the peaks, which must be due to many different environments. The corresponding large $T_2/T_2$* ratio is confirmed by sharp lines in spectra obtained with refocused detection, Figure 2d,e. The chemical shifts spread from -68 to -92 ppm, covering the ranges typical of $Q_0$, $Q_1$, and $Q_2$ sites, as well as a $Q_4$ peak at -110 ppm. Given that $Q_4$ silicons are linked, via bridging oxygens, to four other silicons, they cannot be associated with the unlinked $Q_0$ sites. The different $T_{1,Si}$ indicated by the different line shapes in Figure 2a, after 1,000 s recycle delays, compared with Figure 2b, after 10,000 s, shows that the $Q_4$ clusters are not linked to the $Q_1$ and $Q_2$ sites.

The different $Q_n$ sites can be distinguished not only by their isotropic chemical shifts, but also based on two independent NMR parameters: (i) J-couplings, which increase with n, the number of bonded silicon neighbors, and (ii) chemical-shift anisotropies, which reflect the local bonding symmetry. While CSAs can be measured without isotopic enrichment, assignment based on the J-couplings requires every silicon to be $^{29}$Si, which is true in our fully $^{29}$Si-enriched samples. However, before presenting these spectral-editing data, we would like to discuss the $T_{1,Si}$ relaxation times, which reveal three main types of silicate environments.

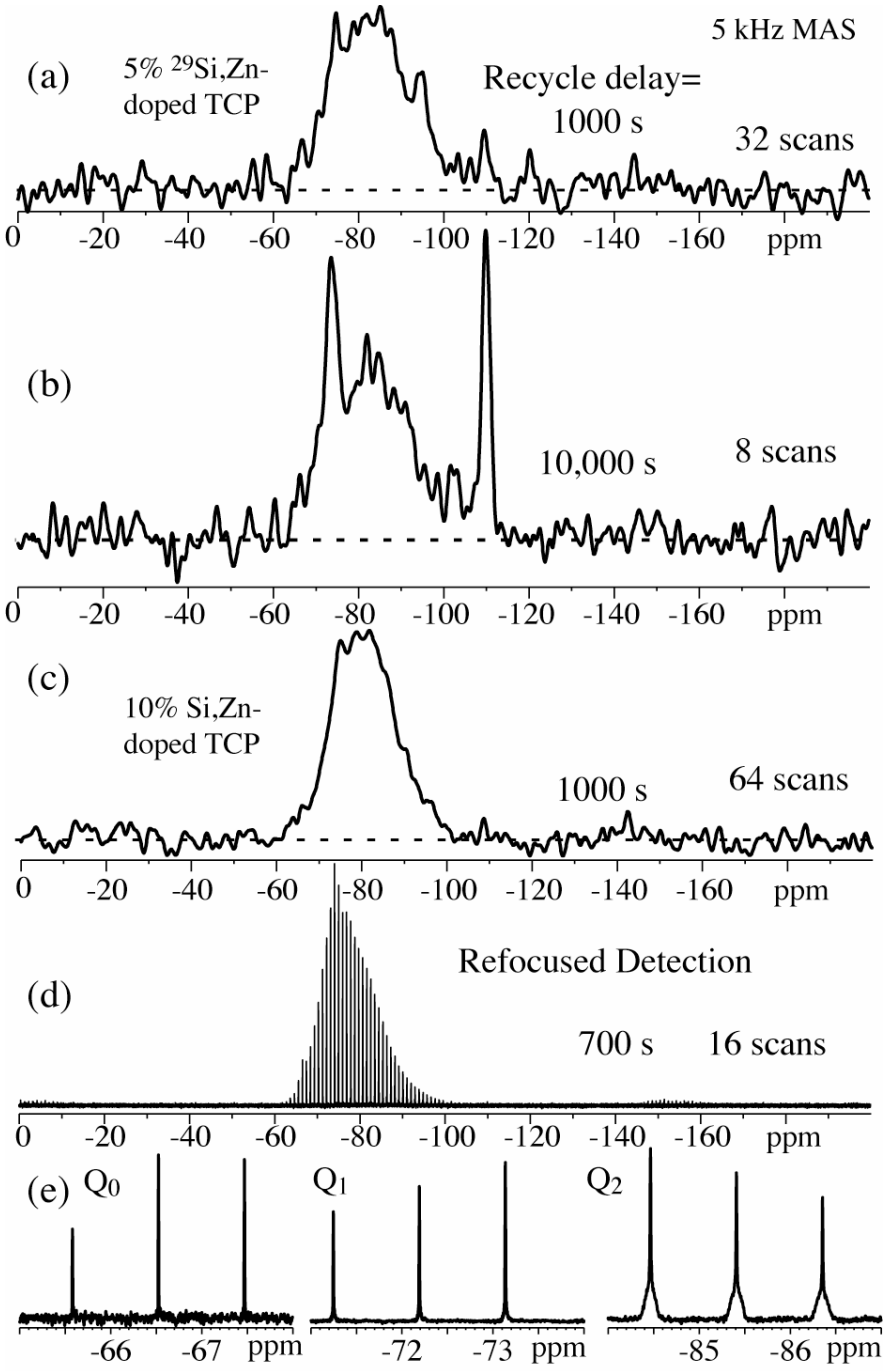


**Figure 2.** $^{29}$Si MAS NMR spectra of 5% and 10% Si,Zn-doped TCP. (a) Regular MAS spectrum of 5% Si,Zn-doped TCP with a 1,000-s recycle delay. (b) Same as (a) with 10,000-s recycle delay. (c) Regular MAS spectrum of 10% Si,Zn-doped TCP with a 1,000-s recycle delay. (d) Similar to (c), but with refocused detection for signal enhancement and with a 700-s recycle delay. (e) Expanded views of the spikelets in d) in the $Q_0$, $Q_1$, and $Q_2$ spectral ranges.

*10.3.2 $T_{1,Si}$ relaxation times.*

Figure 3 shows $^{29}$Si NMR spectra of both $^{29}$Si-doped samples, acquired with refocused detection, as a function of recycle delay, from 500 s to 90,000 s. The broad band between –70 and –100 ppm is seen to have a relatively short $T_{1,Si}$ of ~ 200 s, while the sharper signals near -70 ppm and –110 ppm exhibit ~20 times longer relaxation times. This difference is confirmed by 1,000-s $T_{1,Si}$-filtered DP spectra with 20,000 s recycle delay, Figure 4, which exhibit only the signals near -70 ppm and –110 ppm. The long $T_{1,Si}$ indicates that these silicates are not in spin-diffusion contact with the other, fast-relaxing silicates. The relatively small inhomogeneous broadening of the peaks near –70 ppm in Figure 4 suggests their origin from specific sites in a crystalline structure, indicating dispersion in TCP. The downfield chemical shift and long $T_{2,Si}$ (no observable J-coupling) of the signals near –70 ppm strongly suggest assignment to $Q_0$ sites. However, symmetric $Q_1$-$Q_1$ dimers, in which chemical equivalence makes the J-coupling undetectable, should also be considered. This will be further discussed below. The sites resonating near –110 ppm can be assigned to $Q_4$ silicates based on their chemical shift. They have six times broader spikelets than the $Q_0$ sites, see Figure 4c, due to the J-coupling to their four neighbors; their integrated area for the 5%-Si doped TCP is similar to that of the $Q_0$ sites, consistent with Figure 2b.

The first and last rows in Table 1 give the fractions of the $Q_4$ and dispersed $Q_0$ silicate, respectively, in the two samples studied. The long $T_{1,Si}$ makes a detailed characterization of these crystalline silicate sites extremely time-consuming. Nevertheless, measurements of the J-couplings, and dipolar couplings of the $Q_0$ sites will be presented below, and CSA measurements are shown in the Supporting Information.

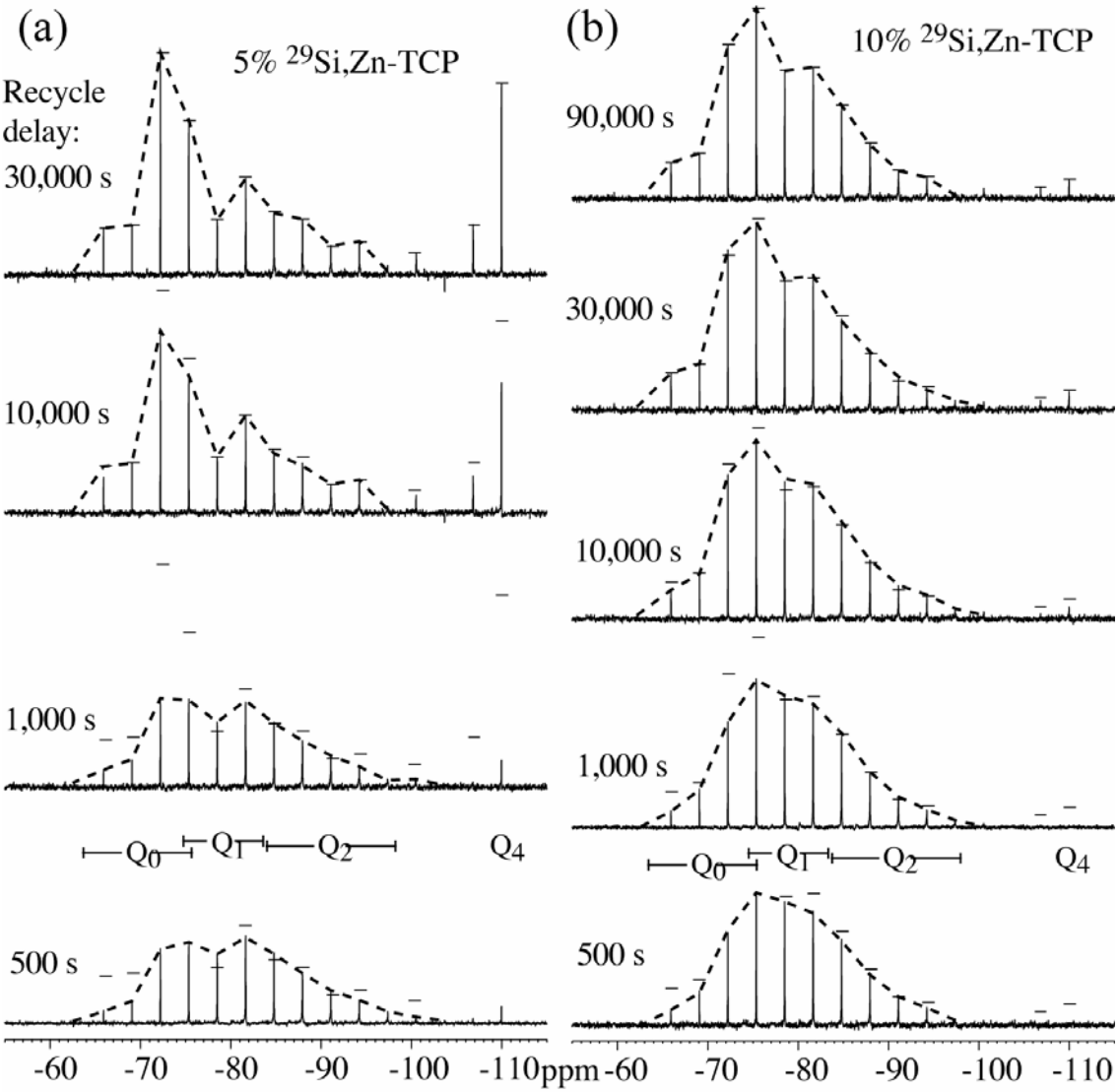


**Figure 3.** Direct-polarization $^{29}$Si MAS NMRspectra of 5% and 10% Si,Zn-doped TCP, acquired with refocused detection, as a function of increasing recycle delays of (a,b) 500 s (c, d) 1000 s (e,f) 10,000 s (g,h) 30,000 s and (i) 90,000 s. The intensities of the fully relaxed spectrum are indicated by horizontal lines in each spectrum. The ranges of $^{29}$Si chemical shifts in $Q_n$ silicate sites given in the literature are indicated above the bottom spectrum. Eight scans were averaged for most of the spectra, except for two with 500-s and 1,000-s recycle delays, where 32 scans were averaged. Due to the refocused detection, the signal is "compressed" into spikelets. Spinning frequency: 5 kHz.

*10.3.3 $Q_n$ quantification by J-couplings.*

The number of J-couplings experienced by a $^{29}$Si nucleus strongly affects its spin dynamics. This differential behavior enables us to obtain spectra predominantly of $Q_2$, $Q_2$-$Q_1$, $Q_1$-$Q_1$, and $Q_0$ sites in the $^{29}$Si-enriched samples. The J-couplings between two $^{29}$Si spins across a bonding oxygen is 3-8 Hz, requiring evolution for $\tau = 1/(2J)$ between 160 and 60 ms for maximum double-quantum signal generation. Conversely, a ~100-ms J-modulation period in a Hahn spin-echo experiment, where chemical-shift (and heteronuclear) dephasing is refocused but J-modulation continues throughout, results in dephasing first of $Q_2$ and then of $Q_1$ signals. $Q_0$ sites dephase only slowly since they experience no J-couplings and the residual homonuclear dipolar couplings are also very small. Another type of sites that would dephase slowly are symmetric $Q_1$-$Q_1$ dimers, in which the two silicons are chemically equivalent. More typically $Q_1$ sites are modulated by $\cos(\pi J 2\tau_1)$, $Q_2$ sites by $\cos^2(\pi J 2\tau_1)$. The full initial J-modulation curves are shown in Figure 6d below.

In a double-quantum (DQ) filtered spectrum, the signal is proportional to the double-quantum coherence of two coupled spins generated during the excitation period $\tau_{DQ}$. The excitation occurs due to homonuclear J-coupling, potentially aided by residual dipolar couplings. For short times, the spin-pair approximation is valid and the signal contribution from each partner in a pair is equal. For instance, a $Q_1$-$Q_2$-$Q_1$ trimer would be considered as a superposition of a $Q_1$-$Q_2$ and a $Q_2$-$Q_1$ spin pair, and the $Q_2$:$Q_1$ signal ratio would be 1:1, even though there are twice as many $Q_1$ spins. In other words, due to its two J-couplings, a $Q_2$ site exhibits a twice faster initial build-up of DQ coherence compared to the $Q_1$ sites. The differential enhancement of the $Q_2$ signals in Figure 5i,j appears to be even more pronounced, suggesting that the $Q_2$-$Q_2$ J-coupling is larger than the $Q_2$-$Q_1$ coupling, which in turn is larger than the effective $Q_1$-$Q_1$ coupling.

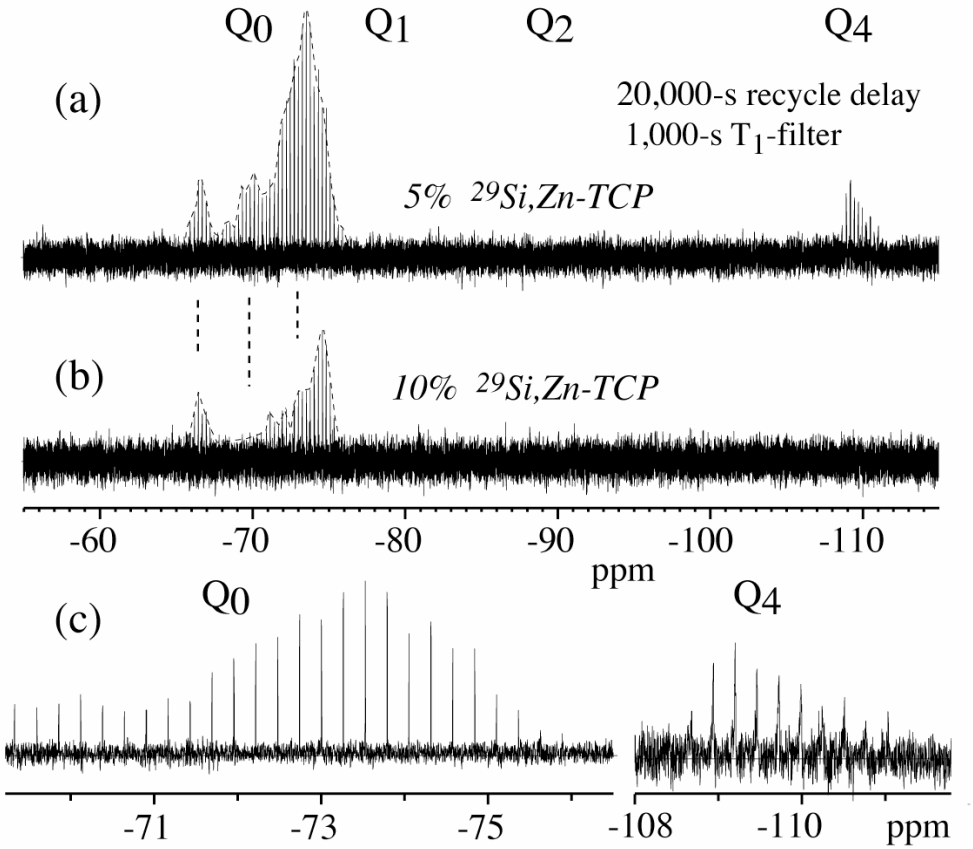


**Figure 4.** Spectra of the long-$T_{1,Si}$ component, obtained after 1000-s $T_{1,Si}$ filtering and with a 20,000-s recycle delay, acquired using refocused detection with a smaller spacing of spikelets than in Figure 3. (a) 5% $^{29}$Si,Zn-doped TCP (20 scans). (b) 10% $^{29}$Si,Zn-doped TCP (16 scans). The amount of the 10%-Si,Zn-doped sample was smaller by a factor of 0.43, according to quantitative $^{31}$P spectra of the two samples. (c) Expanded views of two spectral ranges of the spectrum in a).

At longer DQ excitation plus reconversion times of 2·120 ms, Figure 2k and 2l, the $Q_2$ signals are quickly dephased, since a $Q_2$ silicon is part of a system of three or more coupled spins, and the spins outside the DQ spin pair dephase the DQ coherence within 1/(2J). In contrast, the $Q_1$ signals grow in intensity due to the longer DQ excitation. At longer times, an even more down-field part of the spectrum grows further in intensity, see Figure 2 m and 2n. This must be assigned to $Q_1$-$Q_1$ dimers, which are ideal spin pairs unaffected by couplings to a third spin. Their relatively slow rise (no signal at -72 ppm is visible after 40 ms) supports our hypothesis that the effective J-couplings between two $Q_1$ sites (i.e. in a

dimer) are weaker than those involving $Q_2$ sites.

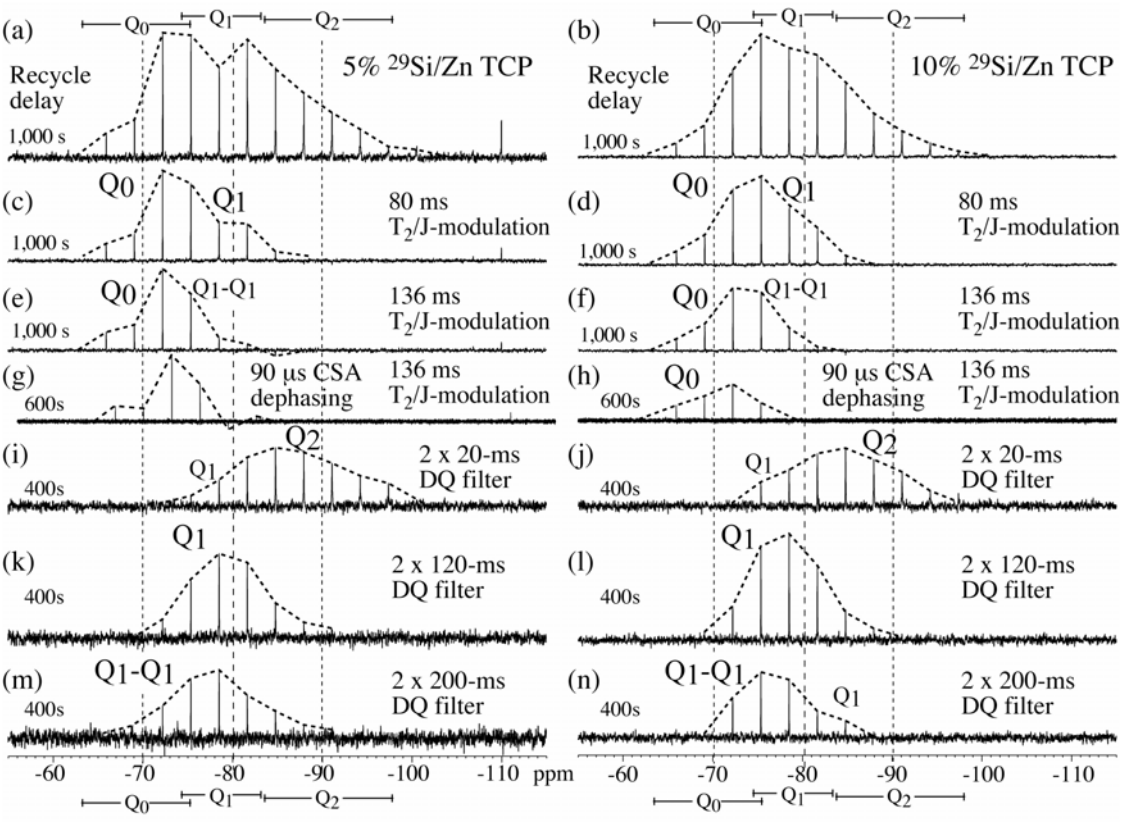


**Figure 5**. Spectral editing of silicate $Q_n$ species in $^{29}$Si NMR based on (c-g) J-couplings and (h) chemical-shift anisotropy, for the 5%- and 10% Si,Zn-doped TCP (left and right column, respectively). Spectra were obtained at 5 kHz MAS with refocused detection of ~1-s duration. Peaks are connected by a dashed line, which gives the outline of the regular spectrum. The subspectra have been scaled vertically to roughly match their contribution to the spectra in (a) and (b). Major contributions are indicated in larger, minor residual ones in smaller font. (a,b) Almost full spectra obtained with 1,000-s recycle delay; the downfield signal of $Q_0$ sites are not fully relaxed (see Figure 2). (c,d) Spectra after 80 ms of $T_2$ relaxation / J-modulation, suppressing the signal of $Q_2$ sites. (e,f) Spectra after 136 ms of $T_2$ relaxation / J-modulation, suppressing the signal of $Q_2$ and certain $Q_1$ sites. (g,h) Spectra after 136 ms of $T_2$ relaxation / J-modulation and a 90-µs CSA filter, suppressing the $Q_1$ signals more extensively. (i,j) Spectra after short DQ filter of 4*20 ms, producing a strong $Q_2$-site signal due to the two J-couplings of these sites, and a weak $Q_1$-signal contribution. (k,l) Spectra after longer DQ filter of 4*60 ms, producing a strong $Q_1$-site signal while the $Q_2$ signal is suppressed by the multiple J- and dipolar couplings of $Q_2$ sites. (m,n) Spectra after a long DQ filter of 4*100 ms, producing a strong $Q_1$-site signal that is probably dominated by $Q_1$-$Q_1$ dimers. For the spectra in (b-n), between 32 and 128 scans were averaged.

*10.3.4 Quantification of $Q_n$ species.*

By matching signals in the spectrally edited spectra of Figure 2 to the quantitative spectra after long recycle delays and recording the appropriate integrals, the fractions of silicate $Q_n$ sites can be quantified. First of all, based on the comparison of the spectra with 1,000 s and 30,000 s recycle delays in Figure 3, the fraction of dispersed long-$T_{1,Si}$ $Q_0$ sites was determined. Scaling the CSA and $T_2$/J filtered spectra (Figure 2 g,h) to match the $Q_0$ signal on the downfield side of the DP spectrum with $t_{rec}$=1,000 s gives an estimate of the fast relaxing $Q_0$ sites. Scaling the 2*20 ms DQ spectrum (Figure 2 i,j) to match the right-hand side of the DP spectrum for $t_{rec}$= 30,000 s, where there is no overlap with other signals, gives the fraction of $Q_2$ sites. Scaling the 2*120 ms DQ spectrum (Figure 2 k,l) to match the $Q_1$ sites in the DP spectrum for $t_{rec}$= 1,000 s gives a lower limit to the fraction of $Q_1$ sites. The resulting peak integrals and error margins for both samples are summarized in Table 1. The $Q_2$ fraction dominates in the 5%-doped sample; this is not fully obvious from the signal height in the refocused spectra because of the larger width of the $Q_2$ spikelets (see Figure 2f for an extreme example due to long delays between refocusing pulses), which is due to J- and residual dipolar couplings. The larger $Q_1$ fraction in the 10%-doped sample is confirmed by direct inspection of the spectra in Figures 2, 3, and 5.

*10.3.5 $^{31}$P-$^{29}$Si proximity from REDOR.*

Is all of the silicate, not just the long-$T_{1,Si}$ component resonating near -70 ppm, really dispersed in the TCP matrix? This question can be answered convincingly by $^{29}$Si{$^{31}$P} REDOR NMR, which can probe silicate inclusions between 0.4 and 10 nm in diameter, as discussed above. Figure 6 shows $^{29}$Si{$^{31}$P} REDOR data obtained on the $^{29}$Si-labeled sample. They were obtained with recycle delays of 250 s that yield strong signals of the

short-$T_{1,Si}$ component but not of the dispersed-silicon long-$T_{1,Si}$ component. When the coupling of the $^{29}$Si to the $^{31}$P spins is "switched on" by one 180$^{o}$ pulse per half rotation period, the magnetization of the $^{29}$Si spins is dephased on a time scale that is the inverse of the $^{31}$P-$^{29}$Si dipolar coupling. On the one hand, the observed dephasing of $^{29}$Si by $^{31}$P to <10% proves that more than 90% (probably all) of the silicon are in proximity of the phosphate matrix. Given that the $^{31}$P-$^{29}$Si dipolar couplings become negligible for distances >1.5 nm, the silicate must be dispersed on a nanometer scale. On the other hand, the dephasing is slower than expected for individual silicate ions dispersed in the calcium phosphate matrix. We have used $OH^-$ ions in hydroxyapatite as a reference for ions dispersed in a phosphate matrix, with a distance between $OH^-$ protons and the nearest $^{31}$P of around 0.4 nm (see also Supporting Information). Figure 6a shows that their $\gamma_H/\gamma_{Si}$-scaled dephasing by $^{31}$P is ten times faster than that of $^{29}$Si in doped TCP; it was fit by dephasing by three $^{31}$P spins at a 0.4-nm distance. This large difference in dephasing time constants can only be explained by clustering of the silicate. The quantitative REDOR fitting procedure for nanoparticles described above matches the data well, see the bold fit curve in Figure 6a, for spherical inclusions of 6.8-nm diameter. Note, however, that NMR cannot determine the shape of the inclusions reliably; various inclusion shapes with similar surface/volume ratios will produce acceptable fits.[25]

The data for the 5% and 10% $^{29}$Si,Zn-doped TCP are quite similar. The only exception is again associated with a fraction of the upfield signal from the 5%-doped sample, which is dephased quickly by $^{31}$P, see the curve of the –72-ppm peak in Figure 6b. This indicates that these ions are dispersed in the phosphate matrix. These are clearly the $Q_0$ sites identified in the J-modulation experiments. Note that the strongly differential "$T_2$" behavior (J-modulation) of the $S_0$ signals plotted in Figure 6c confirms that the three peaks, from right to left, are dominated by $Q_2$, $Q_1$, and $Q_1$+$Q_0$ sites, respectively.

In these REDOR experiments, the $^{29}Si$ isotopic labeling was necessary to increase the sensitivity, about 22-fold, but this barely compensates for the 10- or 20-fold dilution of the $SiO_2$ in the calcium phosphate matrix. Further signal enhancement by refocused detection was crucial for making the REDOR experiments feasible within an acceptable time frame, due to the large (inhomogeneous) line broadening and because the 4-mm triple-resonance probe head used for REDOR has a five times smaller sensitivity than the 7-mm double-resonance probe head used for single-resonance $^{29}Si$ NMR.

*10.3.6 Clustering of silicate: Homonuclear $T_2$.*

The $^{29}Si$ labeling enables us to confirm the clustering of silicates in inclusions. Since every silicon site contains the NMR-active nuclear magnet $^{29}Si$, close proximity of silicons can be detected in terms of homonuclear dipolar couplings. The number of nearest neighbors can be estimated based on quantitative analysis of homonuclear $T_2$ relaxation data, measured in a simple Hahn-echo experiment with multiple-echo detection for sensitivity enhancement. The $^{29}Si$ 180$^o$ pulse refocuses all heteronuclear couplings (e.g. to $^{31}P$) and chemical shifts. Without sample rotation, the dominant $T_2$ mechanism is the $^{29}Si$-$^{29}Si$ homonuclear dipolar coupling. Thus, the $T_2$ decay reflects the second moment of the $^{29}Si$-$^{29}Si$ dipolar couplings.

Figure 7 shows the dipolar $T_2$ decays of various silicate species. The curve of the $^{29}SiO_2$ precursor material traces out the relaxation behavior of silicon sites completely surrounded by homonuclear neighbors. The resulting curve, which can be fit by a Gaussian,[26] quite closely resembles the short-time behavior of the $^{29}Si$ dipolar $T_2$ curve of 10% Si,Zn-doped TCP, indicating that in the latter many $^{29}Si$ sites are indeed almost completely surrounded by other $^{29}Si$. A model system with random placement of 4.4% $^{29}Si$

is provided by unlabeled fused silica ($SiO_2$). Its slow decay matches that of the long-$T_{1,Si}$ $Q_0$ signal (filled circles), which confirms that these are dispersed $SiO_4^{4-}$ ions in the phosphate matrix. The slow dipolar dephasing proves that these are not symmetric $Q_1$-$Q_1$ dimers, as produced in a simulation of silicon in TCP,[14] While the transverse magnetization of such chemically equivalent silicon sites would commute with the $\mathbf{I}\cdot\mathbf{J}$ operator in the J-Hamiltonian and therefore show no J-modulation, it would not commute with the additional 3 $I_z$ $J_z$ term in the dipolar coupling and therefore be subject to fast homonuclear dipolar dephasing.

*10.3.7 Counting $^{29}$Si spins in clusters by CODEX NMR.*

A lower limit to the number of $^{29}$Si spins in an inclusion can be obtained by stimulated-echo measurements with spin $^{29}$Si diffusion. If during a "mixing time" $t_m$, the magnetization has diffused to a $^{29}$Si spin of different chemical shift, the contribution to the stimulated echo will be negligible if the dephasing / rephasing periods $Nt_r$ are long enough. In other words, only the magnetization that remains on the initially polarized spin contributes to the stimulated echo. If there are M spins in a cluster, at long spin-diffusion times only 1/M of the magnetization contributes to the stimulated echo.

The CODEX experiment enables stimulated-echo measurements under MAS even for chemically equivalent sites.[4] The pulse sequence of Figure 8a is modified from the standard CODEX experiment in that it contains not only recoupled anisotropic chemical shift, but also isotropic-shift evolution and reconversion periods. Thus, dephasing occurs due to a change not only in anisotropic, but also in isotropic chemical shift. Figure 8b shows a series of $^{29}$Si spectra of the 10% Si,Zn-doped TCP, obtained after CODEX with spin diffusion for times $t_m$ ranging between 1.5 and 50 s. The intensity of the $Q_1$ and $Q_2$ signals decreases by a factor of up to 10, proving that each cluster contains at least 10 distinguishable (magnetically

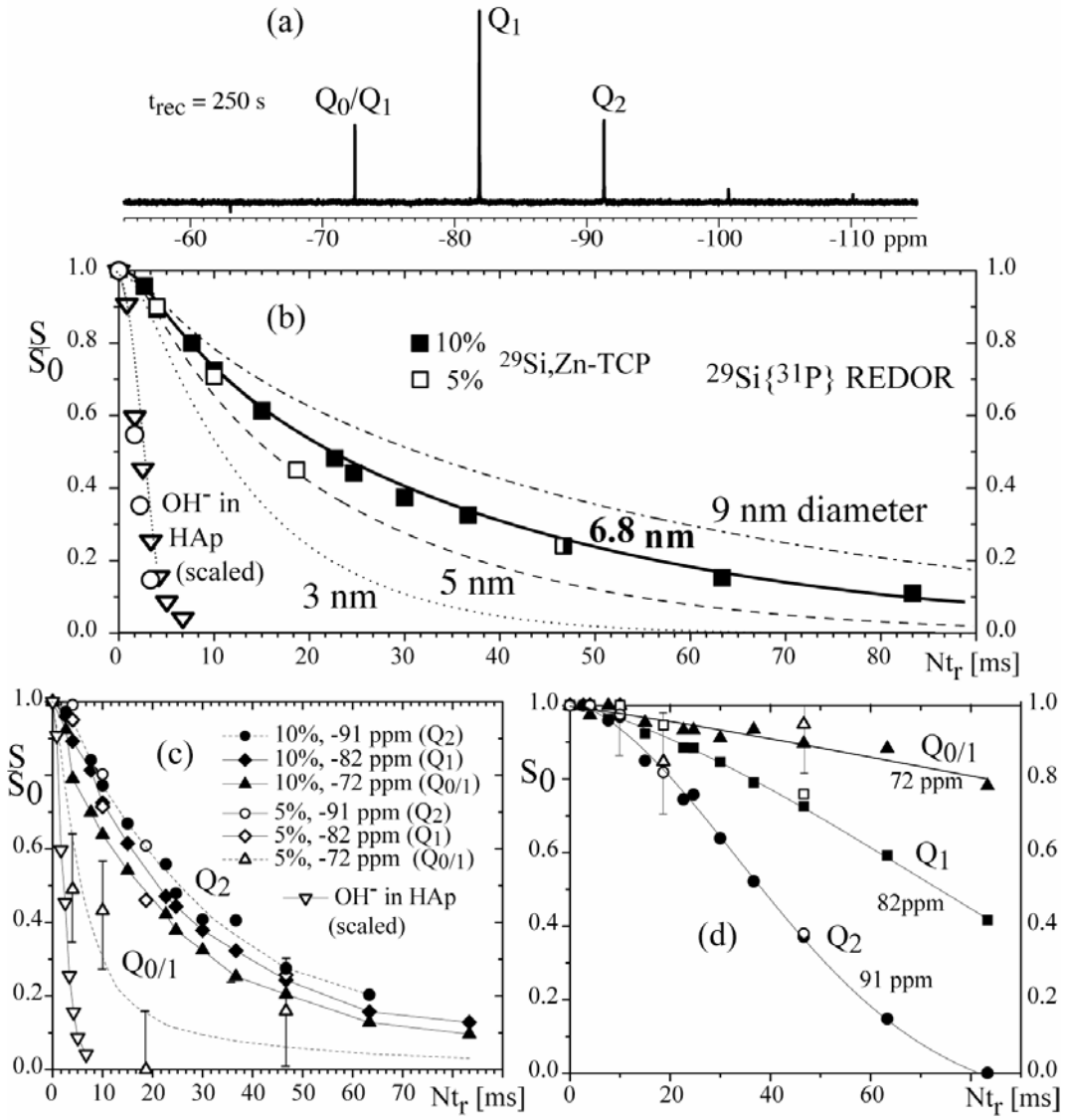


**Figure 6.** $^{29}$Si{$^{31}$P} REDOR data of 5% and 10% $^{29}$Si,Zn-doped TCP at 3 and 6 kHz MAS. (a) $^{29}$Si $S_0$ spectrum consisting of three spikelets (at -72, -82, and -91 ppm, i.e. spaced by 3 kHz/4) produced from the inhomogeneously broadened spectrum by refocused detection, which enhances the sensitivity by an order of magnitude. (b) Dephasing of the total $^{29}$Si intensity. Simulated REDOR curves for spherical silicate particles of 3 – 9 nm diameter are shown for reference. $^{1}$H{$^{31}$P} REDOR dephasing of OH protons in NIST hydroxyapatite, recorded in the same probehead with identical $^{31}$P pulses (see Supporting Information), is also shown (open squares). This shows the decay expected for isolated ions in a phosphate matrix (three $^{1}$H-$^{31}$P nearest-neighbor distances of 0.4 nm). For a meaningful comparison with the $^{29}$Si{$^{31}$P} REDOR dephasing, the $^{1}$H{$^{31}$P} dephasing time has been scaled by $\gamma_H/\gamma_{Si} = 5$, and the data were recorded at 12-kHz MAS, which results in a four-fold increase in the number of dephasing pulses compared to 3-kHz MAS. In addition, open circles mark $^{1}$H{$^{31}$P} REDOR dephasing for 10 $t_r$ with a five-fold reduction of the effective REDOR dephasing frequency by four refocusing $\pi$-pulses on $^{1}$H, recorded at 3-, 4.5-, and 6-kHz MAS. (c) Dephasing of the three sharp $^{29}$Si spikelets in (a). (d) Dephasing of $S_0$ for the three spikelets shown in (a).

inequivalent) silicon sites. The $Q_0$ signal also decreases, proving that the inclusions contain some $Q_0$ sites. The slower dephasing of the signals near –70 ppm is most likely due to contributions from some of the $SiO_4^{4-}$ ions dispersed in the TCP matrix.

### 10.4 Discussion

The spectroscopic and relaxation time analysis has revealed three distinct silicate components: (i) Long-$T_{1,Si}$ $Q_0$ silicate tetrahedra dispersed in TCP; (ii) short-$T_{1,Si}$ $Q_2$, $Q_1$, and $Q_0$ sites in clusters that form inclusions in the TCP matrix; and (iii) long-$T_{1,Si}$ $Q_4$ crystallites. Figure 9 shows a schematic of the morphology of components (i) and (ii) on the 20-nm scale. $T_{1,Si}$ and connectivity analysis shows that the $Q_4$ component (iii) is not in close contact with the other two components.

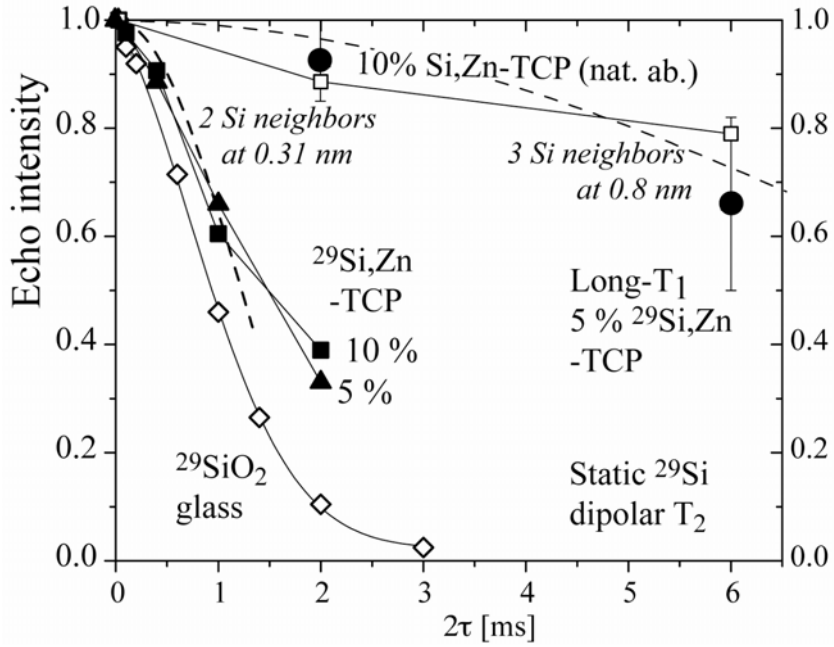


**Figure 7.** $^{29}Si$ homonuclear dipolar dephasing ($T_2$) data of 5% and 10% Si,Zn-doped TCP (filled triangles and squares, respectively), acquired without sample rotation and with refocused detection. Filled circles are data points for the long-$T_{1,Si}$ $Q_0$ component selected by a 1,000-s $T_{1,Si}$ filter after a 20,000-s recycle delay. Data for the unlabeled 10% Si,Zn-containing TCP (i.e. with 4% $^{29}Si$, open squares) and for $^{29}Si$-labeled $SiO_2$ (mostly $Q_4$ sites, open diamonds) are shown for comparison. Two dashed parabolic fit curves based on a short-time (second-moment) approximation are shown: fast dephasing by two $^{29}Si$ neighbors at 0.31 nm as typical for $Q_2$ sites in a silicate, and slow dephasing by three $^{29}Si$ neighbors at 0.8 nm.

*10.4.1 Dispersed $Q_0$ sites.*

$SiO_4^{4-}$ ions ($Q_0$ sites) dispersed in the TCP matrix have been identified by long $T_{1,Si}$ relaxation times, lack of J-modulation, a down-field chemical shift, sharp resonances, and a small chemical-shift anisotropy. Symmetric $Q_1$-$Q_1$ dimers, which would also show no J-modulation due to chemical equivalence, are excluded by the long dipolar $T_2$. Note that dispersed $Q_0$ sites that happen to be located near a silicate inclusion will have homonuclear couplings with the clustered silicate and therefore have a shortened $T_{1,Si}$. This may result in some of the dispersed $Q_0$ sites being counted incorrectly as belonging to the silicate inclusions.

The absolute concentration of dispersed silicate ions relative to phosphate ions is similar in both samples, 0.8 mol% and 1.2 mol% Si in the 5%- and 10%-doped samples, respectively. This should be compared with a value of 3.9 mol% estimated from neutron-scattering Rietveld analysis on a similar (but not identical) TCP sample with 10% Si,Zn doping. [11] We cannot exclude categorically that the true fraction of dispersed $SiO_4^{4-}$ ions is larger than estimated by NMR, if that component has an unusually long $T_{1,Si}$ relaxation time > 90,000 s. Note that in spite of similar absolute amounts of dispersed $Q_0$ sites, their sharp peaks are less visible in the spectra of the 10% $^{29}$Si,Zn-doped sample because they represent a smaller fraction of silicon.

According to neutron diffraction refinement data, the Si substitutes exclusively for P(1) at location (0,0,0) in the A column of the β-phase of TCP. [11] The fact that multiple peaks of the $Q_0$ sites are observed in NMR, see Figure 4, casts doubt on that interpretation, but more detailed investigations, for instance by $^{29}$Si-$^{31}$P NMR, would be extremely time-consuming due to the long $T_1$ relaxation times and low concentration of $Q_0$ sites.

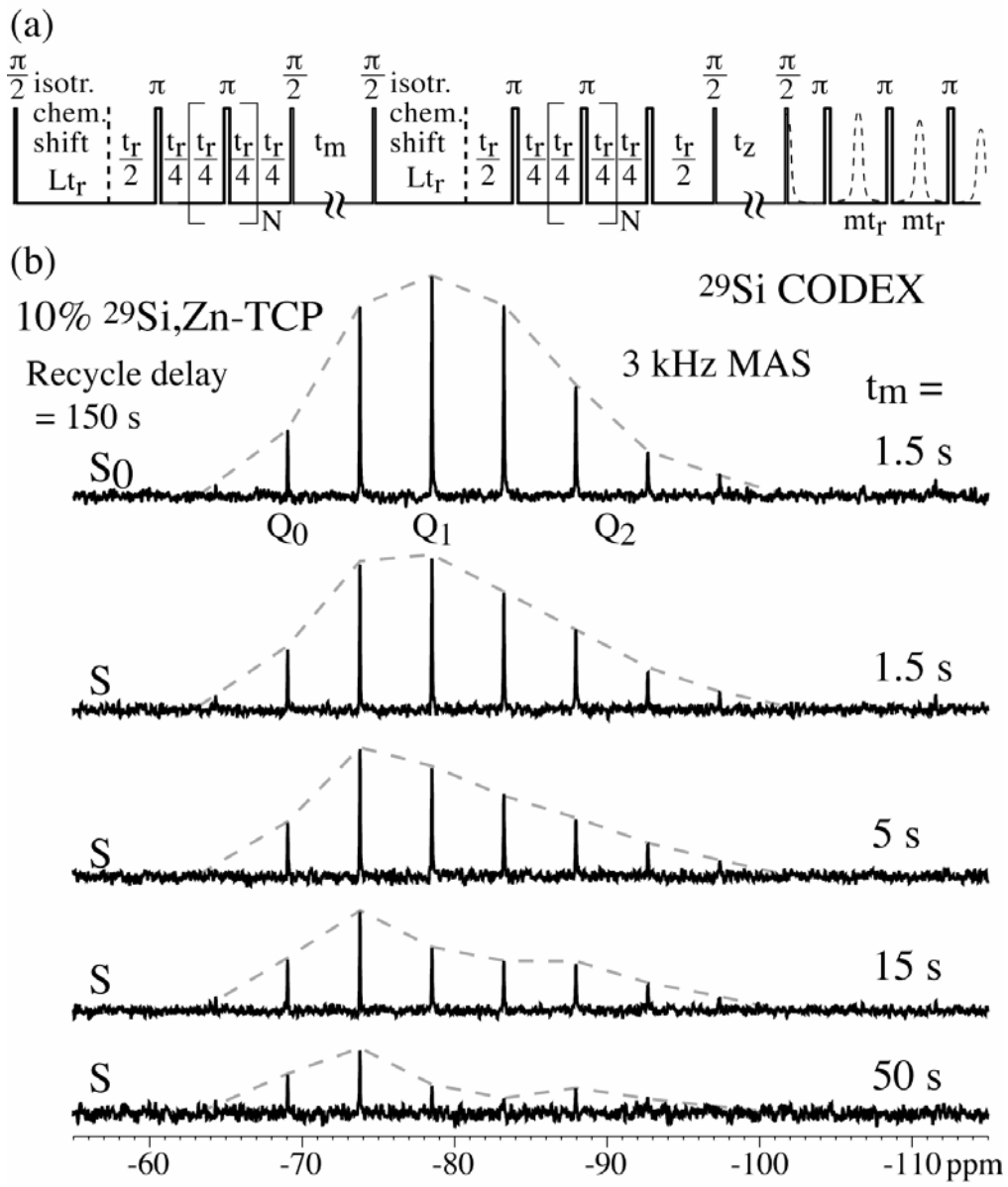


**Figure 8.** Counting silicates in clusters by CODEX $^{29}$Si NMR with $^{29}$Si spin diffusion during mixing times of up to 50 s, for 10% Si,Zn-doped TCP. (a) Pulse sequence to generate not only an anisotropic chemical-shift stimulated echo as in standard CODEX, but also an isotropic chemical-shift stimulated echo. (b) Series of spectra after CODEX with the spin-diffusion time $t_m$ given on the right. The spectra have been scaled up to eliminate the effects of $T_{1,Si}$ relaxation during the mixing time $t_m$.

*10.4.2 Silicate nano-inclusions.*

NMR and neutron scattering agree that the majority (>60%) of the silicate does not substitute for phosphate in the TCP crystal lattice. Our NMR study has identified the silicate that is "invisible" to neutron scattering as forming 7-nm diameter silicate inclusions containing a variety of $Q_2$, $Q_1$, and $Q_0$ sites. $^{29}Si\{^{31}P\}$ REDOR, $^{29}Si$ CODEX, and dipolar $^{29}Si$ $T_2$ consistently show the silicate clustering. This component exhibits a relatively short, uniform $T_{1,Si}$, which is further evidence that all these silicate sites are in spin-diffusion contact with each other, and not separated by the phosphate matrix. REDOR provides the most useful information on the composition and size of the inclusions, 6.8 ± 0.5 nm in both samples. The slow dephasing proves that this component does not contain phosphate. On the other hand, the $^{29}Si$ magnetization does dephase to less than 10% after 80 ms of $^{31}P$ recoupling, which proves that essentially all silicate is dispersed in the phosphate.

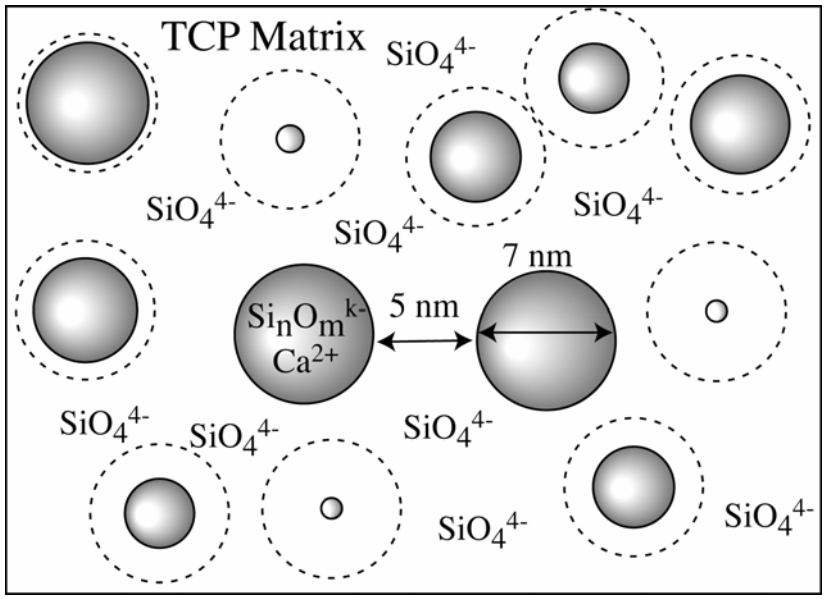


**Figure 9.** Structural model of 10% Si,Zn-doped TCP on the nanometer scale. An idealized cross section is shown. For reference, the maximum outlines of the particles are shown by dashed circles.

The three methods give consistent estimates of the cluster size. The most specific information comes from the REDOR measurements, which show that an inclusion is typically 6.8 nm in diameter and thus contains > 100 silicons. Dipolar $T_2$ only confirms that each silicon is surrounded by several other silicons. CODEX shows that at least 10 $^{29}$Si interact within a 50-s mixing time; longer mixing times could in principle reveal larger numbers but were precluded by $T_{1,Si}$ relaxation. Spherical inclusions on a similar size scale as indicated by NMR have been detected in a TEM micrograph of a related sample, 3% Si,Zn-doped TCP. [27]

The pronounced inhomogeneous broadening of the $^{29}$Si band indicates that the inclusions are most likely amorphous. This is also supported by the somewhat different proportions of $Q_2$ , $Q_1$, and $Q_0$ sites for the two samples studied (see Table 1), which would not occur for a single however complex crystalline structure. This difference is indicated directly by somewhat different intensity distributions in the spectra of the two samples, see Figure 2a vs. 2c and Figure 3a vs. 3b. Note that the $Q_2$- and $Q_1$-rich calcium silicate structure of the inclusions is completely different from the amorphous $^{29}SiO_2$ starting material, where almost all sites are $Q_4$. The inclusions are shown as spherical in the schematic of Figure 9. This is a conjecture, given that the NMR data do not provide reliable information on particle shape, but reflect mostly the surface-to-volume ratio.[25]

This study demonstrates that NMR can detect amorphous nanoinclusions that are practically invisible to scattering methods. It is conceivable that such nanoparticles also exist in other ceramics that have only been studied by scattering methods, and that they may affect mechanical properties such as hardness or toughness.

| Type of silicate site | 5% $^{29}$Si,Zn-TCP | 10% $^{29}$Si,Zn-TCP | Error margins |
|---|---|---|---|
| $Q_0$ dispersed | 16% | 12% | ± 4% |
| $Q_0$ in inclusions | 4% | 5% | ± 4% |
| $Q_1$ in inclusions | 25% | 45% | ± 5% |
| $Q_2$ in inclusions | 35% | 35% | ± 3% |
| $Q_4$ | 20% | 3% | ± 2% |

**Table 1.** Quantification of $Q_n$ silicate sites in the two Si,Zn-doped TCP samples studied, based on long-recycle-delay spectra and spectral editing.

*10.4.3 $Q_4$ silicate species.*

Signals of $Q_4$ silicates at -110 ppm are seen on both samples, but more prominently in the 5% doped sample. The significantly different mole fraction in the two samples confirms that this component is unrelated to the two others. Their long $T_1$ compared to the $Q_1$ and $Q_2$ sites further corroborates this conclusion. It also proves that these $Q_4$ components are not simply residual fused-silica starting material, which has a $T_1$ of only a few seconds. The linewidth of only ± 2 ppm, see Figure 4a and 2b, is also smaller than that of fused silica (±6 ppm). The $Q_4$ silicates could either be bonded to phosphate or other silicates. The strong loss of intensity of the $Q_4$ spikelet after a 80 ms $T_2$/J filter, see Figure 5c, and the large line-broadening due to homonuclear J-couplings, see Figure 4c, strongly suggests silicate neighbors. This is corroborated by the $^{29}$Si{$^{31}$P} REDOR dephasing of the small spikelet

mostly of the $Q_4$ sites, which is not nearly as fast as that of the dispersed $Q_0$ sites. In summary, the data suggest a crystalline $Q_4$ phase such as cristobalite.

*10.4.4 Outlook.*

The insights into the nature and relaxation times of the different components in the $^{29}$Si NMR spectrum obtained here enables $^{29}$Si NMR, even without isotopic labeling but using refocused detection, to be used to monitor the state of Si in TCP. In dissolution studies guided by NMR, processing conditions could be varied to identify, and then enhance, the component that optimizes the dissolution behavior of TCP for its application as a bone-replacement material.

**Acknowledgments**. Work at the Ames Laboratory was supported by the Department of Energy-Basic Energy Sciences (Materials Chemistry and Biomolecular Materials Program) under Contract No. DE-AC02-07CH11358.

The **Supporting Information** describes the calibration of X{$^{31}$P} REDOR by means of $^{1}$H{$^{31}$P} REDOR of hydroxyapatite, and the measurement of chemical shift anisotropy dephasing, which supports the assignment of the $Q_n$ sites.

**References**

1. LeGeros, R. Z.; LeGeros, J. P.; Daculsi, G.; Kijkowaka, R. Encyc Handbook Biomater Bioeng; Marcel Deker: New York, 1995.
2. Klein, C. P. A. T.; Driessen, A. A.; de Groot, K. Biomaterials 1984, 5, 157-160.
3. Park, J. B.; Lakes, R. S. Biomaterials: An Introduction 2nd ed.; Plenum Publishing: New York, 1992.

4. deAzevedo, E. R.; Hu, W. G.; Bonagamba, T. J.; Schmidt-Rohr, K. J Chem Phys 2000, 112, 8988-9001.
5. Wei, X.; Akinc, M. In Ceramic Engineering and Science Proceedings (the 29th International Conference on Advanced Ceramics and Composites - Advances in Bioceramics and Biocomposites); Mizuno, M., Ed.; The American Ceramic Society: Cocoa Beach, FL, 2005, p 129 - 136.
6. Reid, J. W.; Tuck, L.; Sayer, M.; Fargo, K.; Hendry, J. A. Biomaterials 2006, 27, 2916-2925.
7. Langstaff, S.; Sayer, M.; Smith, T. J. N.; Pugh, S. M.; Hesp, S. A. M.; Thompson, W. T. Biomaterials 1999, 20, 1727-1741.
8. Sayer, M.; Stratilov, A. D.; Reid, J.; Calderin, L.; Stott, M. J.; Yin, X.; MacKenzie, M.; Smith, T. J. N.; Hendry, J. A.; Langstaff, S. D. Biomaterials 2003, 24, 369-382.
9. Schroeder, L. W.; Dickens, B.; Brown, W. E. J Solid State Chem 1977, 22, 253-262.
10. Elliott, J. C. Structure and Chemistry of the Apatites and other Calcium Orthophosphates; Elsevier: London, 1994.
11. Wei, X.; Akinc, M. J Am Ceram Soc 2007, 90, 1-7.
12. Wei, X.; Akinc, M. Key Eng Mater 2005, 284-286, 83-86.
13. Yin, X.; Stott, M. J. Phys Rev B 2003, 68, 205205.
14. Yin, X.; Stott, M. J. J Chem Phys 2005, 122, 027409.
15. Zhang, P.; Dunlap, C.; Florian, P.; Grandinetti, P. J.; Farnan, I.; Stebbins, J. F. J Non-Cryst Solids 1996, 204, 294-300.
16. Zhang, P.; Grandinetti, P. J.; Stebbins, J. F. J. Phys. Chem. B 1997, 101, 4004-4008.
17. Fyfe, C. A.; Gies, H.; Feng, Y. J Am Chem Soc 1989, 111, 7702-7707.
18. Klinowski, J.; Thomas, J. M.; Fyfe, C. A.; Hartman, J. S. J Phys Chem 1981, 85, 2590-2594.
19. Fyfe, C. A.; Gies, H.; Feng, Y.; Kokotailo, G. T. Nature 1989, 341, 223-225.

20. Hou, S. S.; Beyer, F. L.; Schmidt-Rohr, K. Solid State Nucl Magn Reson 2002, 22, 110-127.

21. Trebosc, J.; Wiench, J. W.; Huh, S.; Lin, V. S. Y.; Pruski, M. J Am Chem Soc 2005, 127, 7587-7593.

22. Langstaff, S.; Sayer, M.; Smith, T. J. N.; Pugh, S. M. Biomaterials 2001, 22, 135-150.

23. Gullion, T.; Schaefer, J. J Magn Reson 1989, 81, 196-200.

24. Sinha, N.; Schmidt-Rohr, K.; Hong, M. J Magn Reson 2004, 168, 358-365.

25. Schmidt-Rohr, K.; Rawal, A.; Fang, X. W. J Chem Phys 2007, 126, 054701-054716.

26. Wu, Y.; Ackerman, J., L.; Kim, H.-M.; Rey, C.; Barroug, A.; Glimcher, M., J. J. Bone Mineral Res. 2002, 17, 472-480.

27. Wei, X. Ph.D. Thesis, Materials Science & Engineering; Iowa State University: Ames, Iowa, 2006.

**Supporting Information**

For "The Dispersion of $SiO_2$ in Tricalcium Phosphate Elucidated by Solid-State NMR"

(A. Rawal, X. Wei, M. Akinc, K. Schmidt-Rohr)

In this Supporting Information, we describe the calibration of X{$^{31}$P} REDOR by means of $^{1}$H{$^{31}$P} REDOR of hydroxyapatite, and the measurement of chemical shift anisotropy dephasing, which supports the assignment of the $Q_n$ sites. References are numbered as in the main text, with additional references listed below.

**Comparison with $^{1}$H{$^{31}$P} REDOR of hydroxyapatite.** The composite $^{31}$P 180$^{o}$-pulses were optimized in $^{31}$P-$^{1}$H REDOR experiments on NIST hydroxyapatite (HAp), $Ca_{10}(PO_4)_6(OH)_2$, with detection of the OH protons. In addition, in the experiments on the $^{29}$Si-containing TCP, we confirmed that the $^{31}$P pulses at the power level used dephased the $^{29}$Si signal maximally.

HAp was also used as a model system of $^{31}$P REDOR dephasing of ions homogeneously dispersed in a phosphate. Since $^{1}$H is a $\gamma_H/\gamma_{Si} = 5$ times stronger nuclear magnet than $^{29}$Si, for the same internuclear distance it dephases 5 times faster. Thus, to compare with the $^{31}$P-$^{29}$Si REDOR dephasing, the $^{31}$P-$^{1}$H REDOR dephasing time has been scaled by $\gamma_H/\gamma_{Si} = 5$ in our plots.

At a given MAS frequency, the slower dephasing of $^{29}$Si requires five times more recoupling pulses; if pulse imperfections are significant, this might result in reduced dephasing. We have taken two independent approaches to achieve a similar number of $^{31}$P recoupling pulses with $^{1}$H detection and $^{29}$Si detection, at the same effective dephasing time. In the first approach, the HAp data were recorded at 12-kHz MAS, which results in a four-fold increase (i.e. 80% of the desired five-fold increase) in the number of dephasing pulses

compared to 3-kHz MAS. The 3-, 6-, and 12-kHz data $^{31}$P-$^{1}$H REDOR data obtained on HAp all tracked a single universal curve, indicating good experimental conditions. In the second approach, $^{31}$P-$^{1}$H REDOR dephasing was applied for 10 $t_r$ but combined with a five-fold reduction of the effective dephasing frequency by four refocusing π-pulses on $^{1}$H, at 1 $t_r$, 3 $t_r$, 6 $t_r$, and 8 $t_r$. Then, $S/S_0$ data were recorded for HAp at 3-, 4.5-, and 6-kHz MAS. The data are shown in Figure 6b.

**Anisotropic $^{29}$Si chemical shifts.** Generally, the number n of bridging oxygens around a $Q_n$ silicon site in calcium silicates is reflected in the chemical-shift anisotropy (CSA). [15,16,28,29] A system with tetrahedral symmetry has too high a symmetry for a nonvanishing second-rank tensor like the chemical-shift anisotropy to exist. [15,16,28] Nevertheless, it was shown recently by Hansen et al.[29] that the CSAs of $Q_0$ sites in calcium silicates may be significantly nonzero, in the range of 10 – 26 ppm. For $Q_1$ sites, CSA values between 40 and 60 ppm have been reported, for $Q_2$ sites, CSAs typically between 40 and 70 ppm. [15,16 29] We can probe the CSA at any isotropic shift position using a constant-time, five-pulse CSA-dephasing or –filtering sequence [30,31] before refocused $^{29}$Si detection.

Figure S1 shows the CSA dephasing of the intensities at various frequencies of the inhomogeneously broadened MAS spectrum for the 10% $^{29}$Si,Zn-doped sample (filled symbols). The dephasing for $Q_2$ sites is somewhat faster than that of the $Q_1$ sites, but the difference is not very pronounced. The expected significantly slower dephasing is indeed seen for the long-$T_{1,Si}$ $Q_0$ sites selected by a 1,000-s $T_{1,Si}$ filter after a 20,000-s recycle delay (open symbols in Figure S1).

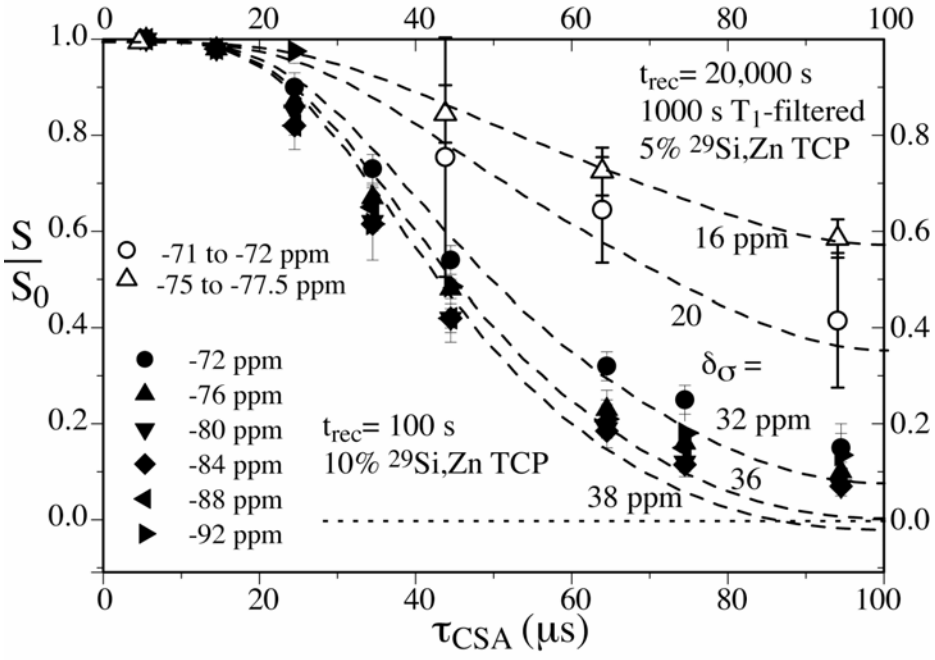


**Figure S1.** $^{29}$Si CSA dephasing of $SiO_2$ in TCP at 5 kHz MAS. Filled symbols show the $^{29}$Si intensity as a function of CSA dephasing time for the 10% $^{29}$Si,Zn-doped sample, at the main peak positions of the spectrum. Open symbols are for the long-$T_{1,Si}$ sites in the 5% doped sample. Dashed curves are fit curves for chemical-shift anisotropy parameters $\delta_\sigma$ between 16 and 38 ppm, assuming a uniaxial interaction ($\eta = 0$). The CSA recoupling was performed using a five-pulse scheme [30,31] with a 100-s recycle delay to observe dephasing behavior of only $Q_1$ and $Q_2$ species, while 20,000-s recycle delays followed by a 1000-s $T_1$ filter were used to selectively observe the CSA dephasing of the $Q_0$ sites.

## Additional References


28. Duncan, T. M. Principal Values of Chemical Shift Tensors; Farragut: Chicago, 1997.

29. Hansen, M. R.; Jakobsen, H. J.; J., S. Inorg Chem 2003, 42, 2368-2377.

30. Blanco, F. J.; Tycko, R. J Magn Reson 2001, 149, 131-138.

31. Mao, J. D.; Schmidt-Rohr, K. Solid State Nucl Magn Reson 2004, 26, 36-45.

# CHAPTER 11.
# DETECTION OF NANOMETER-SCALE MIXING IN PHOSPHATE-GLASS / POLYAMIDE-6 HYBRIDS BY $^{1}H$-$^{31}P$ NMR

*A paper published in Chemistry of Materials 18(2006)3333-3338*

A. Rawal, K. Urman, J. Otaigbe, K. Schmidt-Rohr

**Abstract**

The size of phosphate-glass (Pglass) particles dispersed in a polyamide-6 (PA6) matrix by melt blending has been characterized by $^{1}H$-$^{31}P$ solid-state nuclear magnetic resonance (NMR). $^{1}H$ spin diffusion from ~75% of the $^{1}H$ in the glass to the polyamide is observed within 50 ms, indicating proximity on a 30-nm scale. Fast dephasing of a quarter of the $^{31}P$ magnetization by dipolar couplings to polyamide protons in $^{31}P\{^{1}H\}$ HeteronucleAr Recoupling with Dephasing by Strong Homonuclear Interactions of Protons (HARDSHIP) NMR shows that ~25% of the Pglass is within 0.5 nm from the polyamide. This is confirmed by $^{1}H$-$^{31}P$ heteronuclear correlation NMR spectra with inverse $T_{2,H}$ filtering, which document relatively fast (1-ms) cross polarization from PA6 protons, identified by their upfield chemical shift and short transverse relaxation time $T_{2,H}$, to a significant fraction of $^{31}P$ in the glass. The $^{31}P$ spectrum associated with the polyamide $^{1}H$ reveals that the phosphate sites near the polyamide matrix are chemically altered, but differently than previously observed in Pglass-polyethylene hybrids, where no such contact was proven. As expected, the $^{31}P$ sites that cross polarize from the polyamide protons also exhibit pronounced dephasing in $^{31}P\{^{1}H\}$ HARDSHIP experiments. HARDSHIP experiments after cross polarization and $^{31}P$ spin diffusion experiments indicate that the ~25% of phosphate that is within 0.5 nm from the polyamide is not dispersed in the polymer but on the surface of ~10-nm-diameter Pglass particles. This study represents the first conclusive evidence of intimate mixing of the hybrid components. Further, it suggests that this is an excellent model system for exploring new

routes for driving organic polymers and inorganic glass to self-assemble into useful organic/inorganic hybrid materials.

**11.1 Introduction**

While conventional polymer blends and composites can more or less satisfy current material needs, the demand for advanced materials is still growing. In order to meet the material requirements for new applications, it is necessary to develop and evaluate novel materials like inorganic-glass/organic-polymer hybrids. Hybrid materials are broadly defined as synthetic materials containing both organic and inorganic components[1,2]. They can be further classified into homogeneous systems derived from monomers or miscible components, and phase-separated or heterogeneous systems[1,2]. Low-$T_g$ phosphate glass (Pglass)/polymer hybrids are a good example of the latter. Phosphate glasses that display excellent water resistance and chemical durability are now readily available[3,4]. An example is tin fluorophosphate glass with a $T_g$ of 125 ˚C [5-7]. Due to the low $T_g$ of the Pglass component, these hybrids can be melt-processed conventionally with Pglass loadings as high as 60% by volume or 90% by weight, thereby eliminating the intractable viscosity problem inherent in conventional high-filler composition polymer composites[8,9]. Another advantage of these hybrids, which stems from both hybrid components being fluid during processing, is the unique morphologies, such as fibrils, droplets, and co-continuous networks, that can be generated due to the molecular-level (i.e. single-phase) mixing of the components[8,10]. The final morphology can be partially controlled through careful choice of processing parameters[11]. As the morphology greatly impacts the macroscopic properties, the "tunability" of the morphology presents the opportunity to design a hybrid to meet specific materials needs. Therefore, a better knowledge of hybrid miscibility and molecular dynamics, especially at the interface, and of the thermodynamics of hybrid phase separation is clearly desirable. The Pglass/polyamide 6 (PA6) hybrid system studied here provides an

excellent opportunity to investigate new processing routes for controlling the self-assembly of organic polymers and inorganic phosphate glasses into useful materials.

It is noteworthy that existing hybrid materials are almost exclusively silica-based polymer hybrids prepared via solution or sol-gel methods[1,12,13]. To our knowledge, very few applications of these methods to inorganic phosphate-based hybrid systems have been reported in the literature[14]. As pointed out by Niida and coworkers[14], it is difficult to use the sol-gel method for the hybrid systems discussed in the present article because the samples from sol-gels are often porous and crack or severely contract to squeeze out the incorporated organics when the solvents evaporate from the gels. This article describes the characterization of a class of hybrid materials produced by a relatively new and facile (but radically different) method. These hybrids of ultra-low $T_g$ inorganic phosphate glass and a polymer matrix combine in one material the excellent gas/liquid barrier properties and flame resistance of inorganic glasses with the mechanical toughness and ease of processing of organic commodity polymers for next-generation applications where either pure glass or polymer is not useable.

While the effects of interactions and miscibility on morphology have been studied for many different polymer blends[15-17], there are relatively few investigations of the miscibility of polyamides with other polymers[18,19]. Miscibility is often enhanced in polymer blends or hybrid materials where there is a large potential for interactions between the components. Good polymer/glass adhesion is often achieved in conventional glass-filled polymer composites through coupling agents that promote interaction between the glass filler and polymer matrix[20]. In Pglass/polyamide hybrids, this may be unnecessary since it has been reported that certain Pglass compositions will bind amine groups to the glass surface[21]. This classical interaction facilitates a high degree of interaction between the PA6 and Pglass

phases, thereby encouraging both miscibility in the melt and polymer/glass adhesion in the solid state. Urman and Otaigbe examined the interaction between Pglass and PA6 using melting point depression[11]. By using the Nishi-Wang equation[22] to describe the thermodynamics of this system, we were able to calculate a $\chi$ interaction parameter of -0.067, which indicated that the components were miscible in the melt. This was the first reported evidence of miscibility of an inorganic glass and an organic polymer. The high degree of interaction also facilitated a 10-K drop in the PA6 $T_g$ (as measured by dynamic mechanical analysis) as well as a plasticizing effect on tensile mechanical properties. Since the PA6 and Pglass are only miscible in the liquid (melt) state, the phase separation of the components can generate morphologies that are very suitable for nuclear magnetic resonance (NMR) studies.

Modern solid-state NMR can provide useful information on composition and size of domains in nanoheterogeneous polymer-based materials, even in the absence of long-range order. $^{1}H$ spin diffusion between $^{1}H$ dispersed in the Pglass and polyamide $^{1}H$ can prove mixing on a 30-nm scale [23,24]. Our recently developed $^{31}P\{^{1}H\}$ HeteronucleAr Recoupling with Dephasing by Strong Homonuclear Interactions of Protons (HARDSHIP) NMR method is particularly suited for determining the size and fraction of phosphate particles that are < 15 nm in diameter [25]. In this $^{1}H$-$^{31}P$ recoupling experiment, the particle thickness is probed using the strongly distant-dependent dipolar couplings between the abundant $^{1}H$ spins in the polyamide and the $^{31}P$ nuclear magnets in the Pglass. Furthermore, if the fraction of interfacial phosphate sites is large enough, their $^{31}P$ spectrum can be read off at the polymer-proton frequency in a two-dimensional $^{31}P$-$^{1}H$ heteronuclear correlation (HetCor) experiment with $^{1}H$-$^{31}P$ cross polarization. All three experiments are demonstrated successfully on PA6 / Pglass hybrid samples containing 10% Pglass by volume, and the fraction and size of the Pglass nanoparticles is estimated.

## 11.2 Experimental

### *11.2.1 Samples.*

The low-$T_g$ Pglass used in the study has a molar composition of 50% $SnF_2$ + 20% SnO + 30% $P_2O_5$, a density of 3.75 g/cc, and a $T_g$ of 125.7˚C. The glass was synthesized in our laboratory using procedures reported elsewhere[26]. The tin fluoride and tin oxide were supplied by Cerac Inc. and the ammonium phosphate was supplied by Sigma-Aldrich. The polyamide 6 used was Capron 8270 HS supplied by Allied Signal. The hybrids were prepared using a Thermo-Haake Polydrive® Melt Mixer equipped with roller rotor blades. Prior to melt-mixing, the Polydrive® mixer was heated to 250 ˚C and allowed to equilibrate for at least 20 minutes. The PA6 was added to the Polydrive first and allowed to mix for 5 minutes in order to obtain a homogeneous melt. The Pglass was then added and the two components were allowed to mix together for 10 minutes. Hybrid samples containing 10% Pglass by volume were made for testing. The materials were collected in "chunks" from the Polydrive® mixer and subsequently ground into fine particles using an IKA® A11 basic laboratory mill for the NMR measurements.

### *11.2.2 NMR parameters.*

The NMR experiments were performed using a Bruker DSX400 spectrometer at 400 MHz for $^1H$ and 162 MHz for $^{31}P$. A Bruker 4-mm double-resonance magic-angle spinning (MAS) probehead was used for 13-kHz MAS $^1H$-$^{31}P$ NMR experiments, while 6.5-kHz MAS $^1H$-$^{31}P$ NMR experiments were performed with larger 7-mm sample rotors in a different Bruker double-resonance probehead. The $^1H$ and $^{31}P$ $90^o$ pulse lengths were 4 μs. In direct-polarization (DP) $^{31}P$ experiments, recycle delays of up to 200 s were used. In $^1H$ and $^1H$-$^{31}P$

cross polarization (CP) experiments, including two-dimensional (2D) heteronuclear correlation (HetCor), the recycle delays were 5 s. The $^{1}H$-$^{31}P$ HetCor spectra were obtained with homonuclear frequency-switched Lee-Goldburg (FSLG) decoupling applied during $t_1$ evolution, followed by 1 ms of standard Hartmann-Hahn cross polarization for optimum sensitivity. The $^{1}H$ spin diffusion data were obtained using a dedicated $^{1}H$ NMR ("CRAMPS") probehead.

### *11.2.3 $^{1}H$ spin diffusion.*

In order to detect spin diffusion from the small number of protons in the Pglass to the PA6 matrix, we have combined $T_{2,H}$ filtering with 2D exchange NMR. Before the spin diffusion time, this identifies the Pglass protons in terms of $T_{2,H}$ and their 7-ppm chemical shift. After the spin-diffusion time $t_m$, the sharp Pglass proton signal at 7 ppm is detected, and its intensity is quantified as a function of $t_m$. As $^{1}H$ magnetization diffuses into PA6, the magnetization in the Pglass, and thus the Pglass diagonal signal, is reduced. We record the intensity of the Pglass diagonal peak as a function of the spin diffusion time. The data were plotted after correction for $T_{1,H}$ relaxation during the spin-diffusion time.

After equilibration to equal magnetization per $^{1}H$, the fraction of the total $^{1}H$ magnetization remaining in the Pglass is negligible, on the order of 0.01, due to the at least ten times larger density of $^{1}H$ in the polyamide and ten times larger amount of PA6. As a result, if the Pglass $^{1}H$ diagonal signal reaches a finite constant value, this value gives an estimate of the fraction of large Pglass particles (> 30 nm).

*11.2.4 HARDSHIP NMR.*

The Pglass particle thickness is probed using the strongly distant-dependent dipolar couplings between the abundant protons in the polyamide matrix and $^{31}P$ nuclei in the Pglass. This approach requires a pulse sequence that ensures heteronuclear dephasing only by the polymer protons, but not by dispersed protons in the Pglass (which are probably due to $H_2O$). This is achieved by HeteronucleAr Recoupling with Dephasing by Strong Homonuclear Interactions of Protons (HARDSHIP) [25], which distinguishes between the polymer and Pglass-dispersed protons based on their different transverse ($T_{2,H}$) relaxation times. In short, the HARDSHIP pulse sequence alternates REDOR heteronuclear dipolar recoupling [27] for ~0.15 ms with periods of homonuclear dipolar $T_{2,H}$-dephasing that are flanked by canceling $90^o$ pulses. The heteronuclear evolution of the long-$T_{2,H}$ protons in the Pglass is refocused after two recoupling periods. We have shown that for the strongly coupled, short-$T_{2,H}$ protons in the PA6 matrix, the heteronuclear dephasing rate depends simply on the heteronuclear second moment, not on the homonuclear interactions, even though no homonuclear decoupling is applied [25]. Simulations and experiments on model systems [25] show that the majority of $^{31}P$ spins within 0.5 nm from the interface with the polymer matrix will be dephased within 5 ms.

In these experiments, the 7-ppm resonance of the $^1H$ in Pglass was set on resonance. In order to minimize the effects of $T_{2,H}$ relaxation of the protons in Pglass, most HARDSHIP experiments were run with faster (13-kHz rather than 6.5 kHz) spinning that increases the $T_{2,H}$ relaxation time due to improved homonuclear decoupling by faster MAS. Recoupling for 2 $t_r$ = 154 μs alternated with 154- and 77-μs periods of $T_{2,H}$ relaxation (pulse sequence (d) in Figure 5 of ref. [25], with k = 1).

*11.2.5 Inverse $T_{2,H}$ filtering.*

We will show below, using $^{1}H$-$^{31}P$ HetCor experiments, that cross polarization from PA6 protons to a significant fraction of $^{31}P$ is possible. The undesirable signal of $^{31}P$ cross polarized from the $^{1}H$ dispersed in the Pglass can be reduced by an "inverse $T_{2,H}$ filter", which again relies on the differences in the $T_{2,H}$ relaxation of protons in the PA6 vs. the Pglass. After a 0.3-ms $T_{2,H}$ filter, the polyamide-proton magnetization has been suppressed while the Pglass proton magnetization is only slightly reduced. Subtracting out the CP signal of these long-$T_{2,H}$ protons from the total CP signal results in the "inverse-$T_{2,H}$-filtered" CP signal that mostly shows $^{31}P$ near the PA6 protons.

Due to the relatively weak $^{1}H$-$^{31}P$ couplings in the Pglass, the rf-field match condition for cross-polarization is rather sensitive to small drifts in the amplifiers or probes. To avoid experimental artifacts, the match condition in HARDSHIP experiments with CP was carefully monitored.

**11.3 Results and Discussion**

Figure 1 shows the $^{31}P$ and $^{1}H$ NMR spectra of pure Pglass and a hybrid of 10% Pglass with PA6. A change in $^{31}P$ line shape is observed from pure glass to hybrid, but differently than previously reported for Pglass / LDPE hybrids [2]. The inhomogeneously broadened bands observed have been assigned to $Q_1$ phosphate species (dimers with one bridging oxygen) that are shifted upfield by a nonbridging fluorine [2].

A sharp $^{1}H$ signal at 7 ppm is observed in the pure Pglass, Figure 1c, probably due to absorbed water. It is also seen in the hybrid, Figure 1d,e, but is small in area compared to the PA6 proton signal. The smaller line width corresponds to a longer $T_{2,H}$ relaxation time,

which allows the sharp signal to be selected easily by a Hahn spin echo that serves as a $T_{2,H}$ filter.

*11.3.1 Dispersed Pglass fraction from $^1H$ spin diffusion.*

The distinct difference in the widths, or equivalently $1/T_{2,H}$ values, of the $^1H$ spectra of the Pglass and the PA6 matrix makes it easy to select the protons in the Pglass, whose magnetization survives for hundreds of microseconds, and observe the spin diffusion to the polyamide protons, during a time $t_m$, in terms of the changes of the detected spectrum. Small domains show fast equilibration.

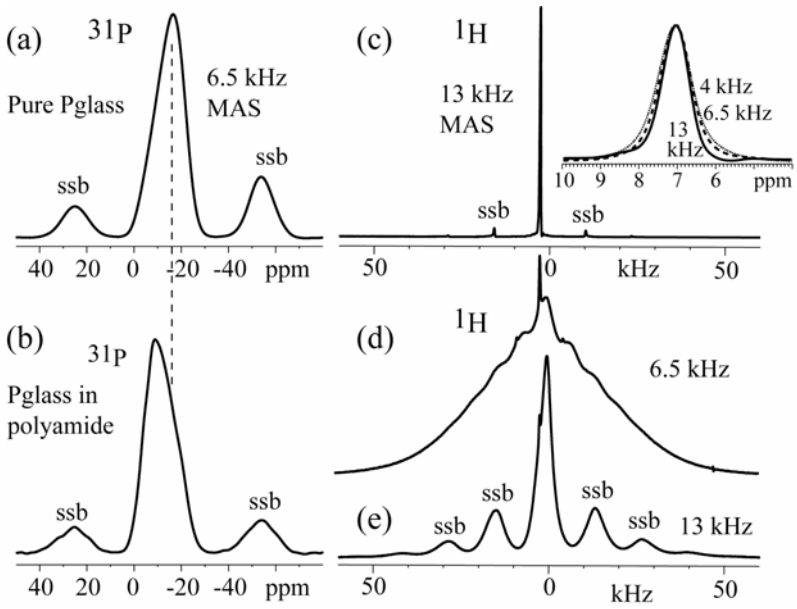


**Figure 1**. (a, b) $^{31}P$ and (c, d, e) $^1H$ NMR spectra of (a, c) pure Pglass and (b, d, e) a hybrid of 10% Pglass and 90% polyamide-6, at spinning frequencies of 6.5 or 13 kHz. The inset in (c) shows the centerband of the sharp 7-ppm signal of pure Pglass at spinning frequencies of 4 kHz, 6.5 kHz and 13 kHz. Spinning sidebands are labeled "ssb".

Figure 2 shows the $t_m^{1/2}$-dependence of the Pglass $^1H$ diagonal signal in a $T_{2,H}$-filtered 2D exchange spectrum (see description above). For large Pglass domains (> 30 nm), most of

the $T_{2,H}$-selected Pglass $^1H$ magnetization would not reach the polyamide matrix within 100 ms. Thus, their signal after the spin-diffusion time would remain essentially unchanged.

For small Pglass domains and correspondingly smaller distances between domains across the matrix, the $^1H$ magnetization of the Pglass diffuses significantly into the polyamide. If the Pglass $^1H$ diagonal signal retains a finite constant value, this value gives an estimate of the fraction of large Pglass particles (> 30 nm). The plateau observed in Figure 2 indicates that about 75% of the Pglass is close enough to the protons of the PA6 matrix to equilibrate with them, and 25% is in larger domains. Since the proton density in the Pglass is low, spin diffusion certainly occurs with an effective diffusion coefficient of < 0.8 $nm^2/ms$, the value found in rigid polymers.[29] Given the 20-ms time-scale of the spin diffusion, the data prove mixing of 75% of the Pglass with the PA6 on a <30-nm scale, conservatively estimated.

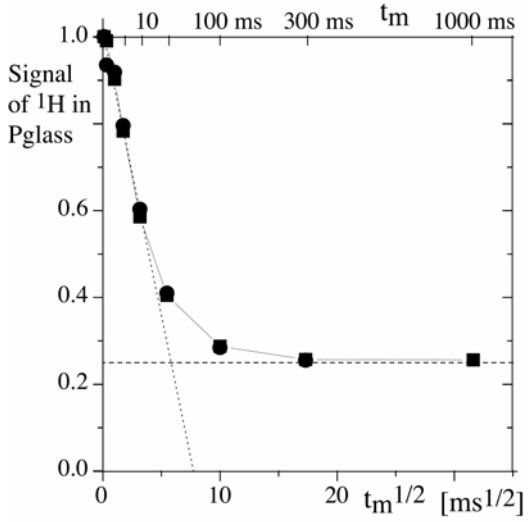


**Figure 2**. Spin diffusion from $^1H$ dispersed in the Pglass (10 vol%) to the PA6 matrix, obtained at 13-kHz MAS in a dedicated $^1H$ NMR probehead. The data were obtained with spin-diffusion times $t_m$ between 0.1 ms and 1 s from two series of $T_{2,H}$-filtered two-dimensional $^1H$ NMR exchange spectra, with two different $T_{2,H}$ filters. The intensity of the diagonal signal of the Pglass protons (7 ppm, 7 ppm), corrected for $T_{1,H}$ relaxation, is plotted as a function of the square-root of the spin diffusion time.

*9.3.2Dispersed Pglass fraction from $^{31}P\{^{1}H\}$ HARDSHIP NMR.*

The size of phosphate nanoparticles can be probed further by $^{31}P\{^{1}H\}$ HARDSHIP NMR, which measures the dephasing of $^{31}P$ in the glass by polymer $^{1}H$. [25] Figure 3a,b shows $^{31}P\{^{1}H\}$ HARDSHIP and $^{31}P\{^{1}H\}$ REDOR [27] dephasing curves for pure Pglass and for 10% Pglass in PA6, obtained at 13 kHz MAS.

As desired, little HARDSHIP dephasing is observed in the pure Pglass (diamonds in Figure 3a), while REDOR dephasing (open inverted triangles) is fast due to the $^{1}H$ dispersed in the Pglass. In the hybrid material, see Figure 3b, quantitative $^{31}P\{^{1}H\}$ HARDSHIP after a long (50 or 200 s) recycle delay and $90^{o}$-pulse excitation (squares) shows fast initial dephasing by the polyamide protons, indicative of phosphates in intimate contact with the PA6 matrix. The plateau of 75% shows that the amount of Pglass within 0.5 nm from the polyamide matrix is ~25% of the total.

We can detect more pronounced HARDSHIP dephasing if we selectively enhance the signal from phosphates at the interface with the PA6 matrix. This can be achieved partially by using a short recycle delay of 5 s, which reduces the signal of the slower-relaxing interior phosphates. Indeed, more pronounced HARDSHIP dephasing is observed (open triangles in Figure 3b).

The signal of the phosphates in close contact to the polyamide can be selected even more efficiently by cross polarization from the PA6 protons, whose magnetization can in turn be selected by the "inverse $T_{2,H}$ filter" described above. This magnetization is indeed strongly dephased by the PA6 protons in HARDSHIP experiments (Figure 3b, filled circles), to 40% within 2 ms. The 1/3 of the magnetization that dephases more slowly probably

originates from $^{1}H$ in the dispersed Pglass that have a shortened $T_{2,H}$, most likely due to proximity (within ~ 0.7 nm) to PA6 protons. A corresponding signal is observed at 7 ppm in the inverse-$T_{2,H}$-filtered $^{1}H$-$^{31}P$ HetCor spectrum presented below.

*11.3.3 Interface-interior connectivity from $^{31}P$ spin diffusion.*

In phosphates, magnetization can be transferred from $^{31}P$ to $^{31}P$ based on their magnetic couplings, over a ~2-nm distance within 5 s. Inserting a $^{31}P$ spin diffusion period ($t_m$) into the inverse-$T_{2,H}$-filtered CP-HARDSHIP experiment, immediately after CP from $^{1}H$ to $^{31}P$, enables such a transfer of the $^{31}P$ magnetization from the interfacial phosphates to the interior. The HARDSHIP dephasing is then indeed slowed down, see Figure 3c. These data were acquired in a larger rotor at a 6.5 kHz spinning frequency for increased signal and reduced effects of rf fluctuations on cross polarization.

After 5 s of $^{31}P$ spin diffusion (filled triangles), the asymptotic dephasing, due to sites in the interior that cannot be dephased on this time scale, is 2/3 of the level without surface selection (HARDSHIP after DP under the same conditions, filled squares). This shows that the phosphates at the interface are within ~2 nm from 2/3 of the other phosphates, which is consistent with the $^{1}H$ spin diffusion data.

*11.3.4 Pglass surface fraction detected in $^{1}H$-$^{31}P$ HetCor NMR.*

The close proximity of a significant phosphate fraction to the polyamide can be confirmed in $^{1}H$-$^{31}P$ HetCor experiments, where they are manifested in $^{31}P$ signals correlating with polyamide $^{1}H$ resonance(s). Figure 4b shows this signal at 2 ppm in the $^{1}H$ dimension, as well as a strong 7-ppm peak of the $^{1}H$ in the Pglass, which is also seen in the pure Pglass,

Figure 4a. The aliphatic PA6 protons are identified not only by their upfield chemical shifts (~ 2 ppm), but also by their short $T_{2,H}$, which is characteristic of organic solids. A 0.3-ms $T_{2,H}$ filter added before the $^{1}H$ evolution time dephased the 2-ppm signal, while leaving most of the 7-ppm peak unaffected, see Figure 4c. The "inverse-$T_{2,H}$-filtered" difference of the full and the $T_{2,H}$ -filtered HetCor spectrum is dominated by signals of protons with short $T_{2,H}$, i.e. of the polyamide. This spectrum, shown in Figure 4d, prominently shows the 2-ppm $^{1}H$ signal of the PA6 matrix. The residual 7-ppm peak is likely due to $^{1}H$ in the phosphate that are so close to the interface that their $T_{2,H}$ is shortened by dipolar couplings to PA6 protons.

Previously, Tischendorf et al. [2] tried to detect polymer-Pglass correlation signal in $^{1}H$-$^{31}P$ wideline separation (WISE) NMR [30], which is equivalent to HetCor without homonuclear $^{1}H$ decoupling. Without decoupling, the peak of $^{1}H$ in Pglass is ca. 2 ppm = 0.8 kHz, the band of the PA6 protons ca. 40 kHz wide. Given the approximate 1:1 integral-intensity ratio of the 7- and 2-ppm bands in the $^{1}H$ dimension of the $^{1}H$-$^{31}P$ HetCor spectrum of Figure 4b, the polyamide proton peak height in $^{1}H$-$^{31}P$ WISE spectra would be 50 times lower than the Pglass proton peak. Therefore, this signal is effectively unobservable in a WISE experiment.

### *11.3.5 $^{31}P$ spectra of the surface Pglass fraction from $^{1}H$-$^{31}P$ HetCor NMR.*

In the inverse-$T_{2,H}$-filtered HetCor spectrum, the $^{31}P$ signal correlated with the polyamide $^{1}H$ peak at 2 ppm is exclusively due to the surface sites of the Pglass particles. The $^{31}P$ spectrum of these interfacial phosphates can thus be obtained as the cross section at the 2-ppm polyamide $^{1}H$ frequency. Figure 5c shows this cross section and compares it with the cross section at the Pglass $^{1}H$-frequency of 7 ppm, Figure 5b, and the cross section from pure Pglass, Figure 5a. The cross section from the inverse-$T_{2,H}$-filtered HetCor spectrum,

Figure 5d, shows the centerband region without interference from interior phosphates, but the sidebands are noisier.

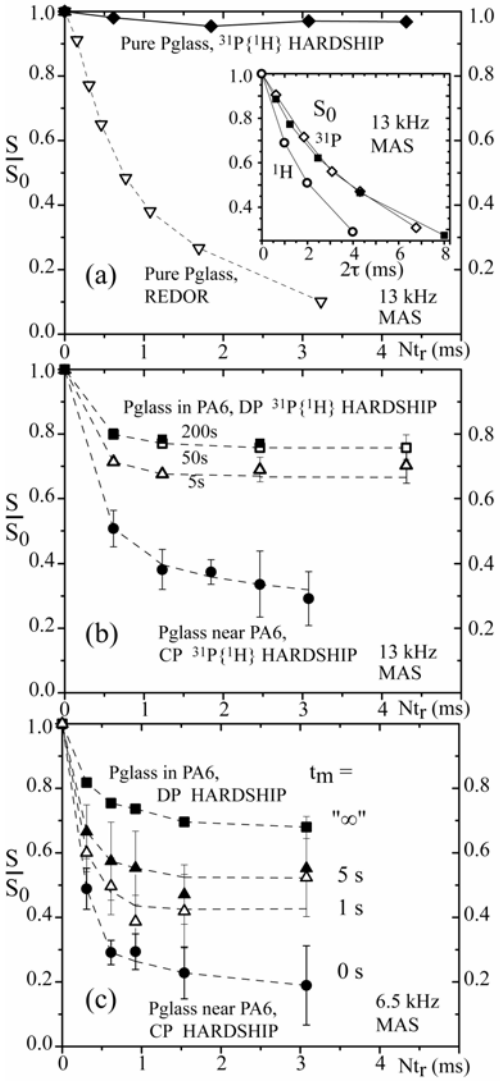


**Figure 3**. $^{31}P\{^{1}H\}$ HARDSHIP NMR data for determining the size and fraction of Pglass nanoparticles in the 10% Pglass/PA6 hybrids. (a) $^{31}P\{^{1}H\}$ HARDSHIP (diamonds) and $^{31}P\{^{1}H\}$ REDOR (open inverted triangles) data obtained for the pure glass, shown for reference. The inset shows the proton-decoupled $T_2$ decay of $^{31}P$ $S_0$ signals in pure Pglass (open diamonds) and Pglass in the hybrid (filled squares), and the $T_2$ decay of $^{1}H$ in pure Pglass as a function of spin-echo time $2\tau$ (open circles). (b) $^{31}P\{^{1}H\}$ HARDSHIP NMR data of the 10% Pglass/PA6 hybrids. Some data were obtained after 90°-pulse $^{31}P$ excitation, with recycle delays of 5 s (open triangles), 50 s (open squares), and 200 s (filled squares, quantitative), indicating that 23% of the phosphate is within 0.5 nm from the polyamide matrix. After selection of the phosphates near polyamide $^{1}H$, by 1.8-ms CP after a 0.3-ms inverse $^{1}H$ $T_2$ filter, more pronounced HARDSHIP dephasing was observed, filled circles. (c) $^{31}P\{^{1}H\}$ HARDSHIP NMR after 0.3-ms inverse $T_2$ filtering and 1.8-ms CP, which selects $^{31}P$ near the interface, and $^{31}P$ spin diffusion from the interface during $t_{sd}$ = 0.1 ms, 1 s, and 5 s. Spinning frequency: 6.5 kHz. The lines are guides to the eye.

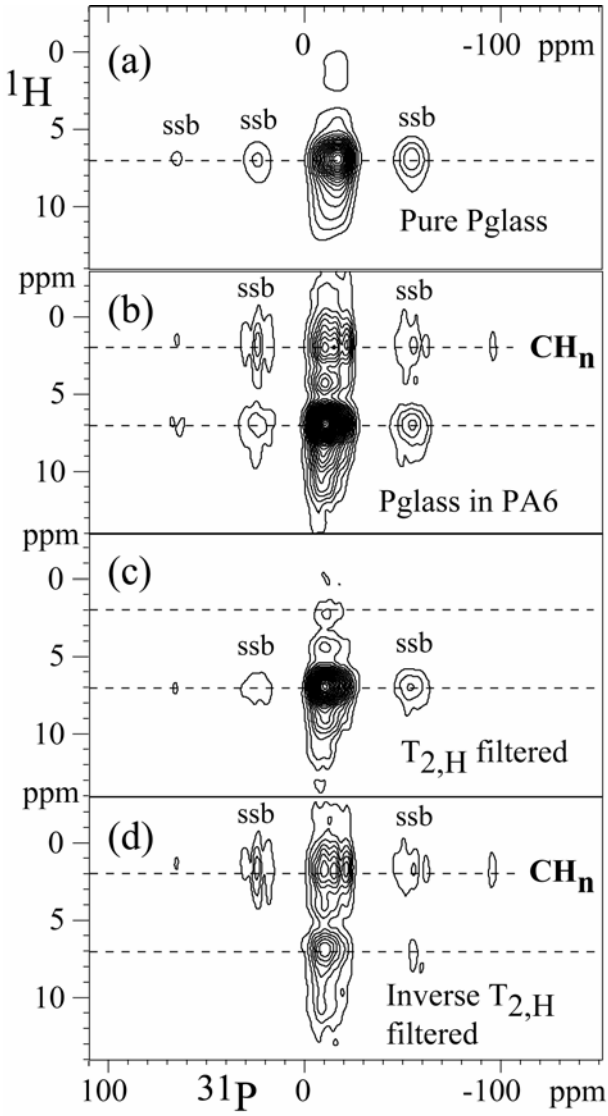


**Figure 4**. $^1$H-$^{31}$P HetCor spectra of pure Pglass and the 10% Pglass/PA6 hybrid. $^1$H homonuclear FSLG decoupling was applied during $t_1$ evolution, followed by 1 ms of Hartmann-Hahn cross polarization for optimum sensitivity. (a) Spectrum of pure Pglass. (b) Spectrum of the Pglass/PA6 composite, showing a new $^1$H signal near 2 ppm, with multiple $^{31}$P chemical shifts. (c) Same as (b) but after a 0.3-ms $^1$H $T_2$-filter. The short $^1$H $T_2$ of the 2-ppm signal confirms its assignment to the PA6 protons; hydrogen sites in the glass are so dilute that they have a much longer $T_2$. (d) Unscaled difference of (b) and (c), which retains the signals of short $T_{2,H}$ hydrogens as found in PA6. The spectra were acquired at 6.5 kHz MAS. Spinning sidebands are labeled "ssb".

While all the signals appear to fall within the range of $Q_1$ sites (phosphate dimers) [2], both the centerband and the sideband pattern of the interfacial component show pronounced differences compared to the other spectra. An upfield centerband with significant sidebands is seen. One of the downfield species has sharp sidebands of high intensity. Possibly, these are indicative of trans-amidation of polyamide nitrogen to interfacial phosphates.

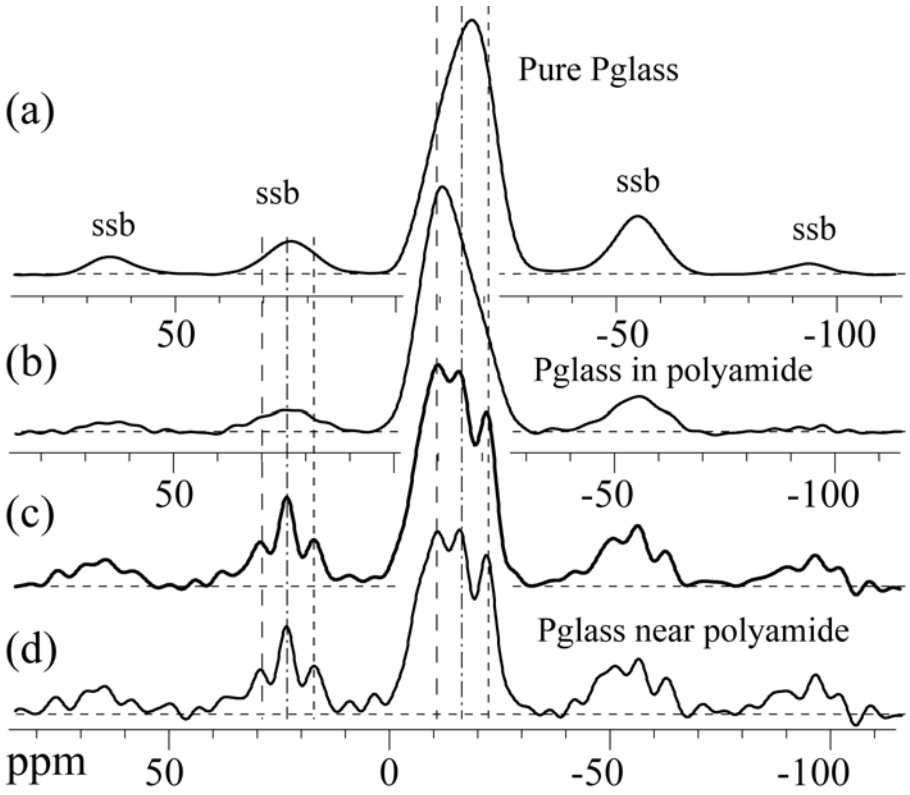


**Figure 5**. $^{31}$P NMR cross sections from the $^{1}$H-$^{31}$P HetCor spectra in Figure 4. (a) Pure Pglass, at the 7-ppm $^{1}$H peak. (b) Pglass in PA6, at 7 ppm. (c) Pglass in PA6, at the aliphatic-H 2-ppm resonance. (d) Inverse-$T_2$ filtered spectrum of Pglass in PA6, cross section at the aliphatic-H 2-ppm resonance. Spinning sidebands, labeled by "ssb", show differences in the $^{31}$P chemical-shift anisotropies of interfacial and interior sites in the Pglass.

*11.3.6 Structural model.*

The plateau in the $^{1}$H spin diffusion data of Figure 2 shows that 75% of the Pglass is dispersed on a scale < 30 nm. The HARDSHIP data of Figure 3b yield an (operationally

defined) Pglass surface fraction of 23%. The thickness of this surface layer is $d_S$ ~ 0.5 nm, since that is the "reach" of $^{31}P\{^1H\}$ HARDSHIP on the 5-ms time scale. [25] As indicated above, the $^{31}P$ spin diffusion data of Figure 3c show that at least 2/3 of this surface layer is in close contact with the Pglass interior. This means that it does not consist of small clusters of phosphate dimers dispersed in the PA6 matrix, but that most of the Pglass forms particles containing many dozens of phosphate dimers.

The volume fraction of the 0.5-nm thick surface layer of the finely dispersed Pglass, $V_S/V = 23/75 = 31\%$, enables us to estimate the minimum size of the nm-scale particles. For a spherical particle of diameter d, the surface-layer volume fraction is

$$V_S/V = 1 - (d-2d_S)^3/d^3, \qquad (1)$$

For a d = 10-nm diameter particle and a surface layer thickness of $d_S = 0.5$ nm, Eq.(1) gives $V_S/V = 0.27$, close to the 31% measured. The 10-nm diameter is also consistent with the $^{31}P$ spin diffusion results, since a 2-nm thick outer shell of a 10-nm diameter particle would contain 80% of its material, which is thus accessible to $^{31}P$ spin diffusion from the surface layer on the 5-s time scale. If the surface is rough, the particle size will be larger; however, the $^{31}P$ spin diffusion data, see Figure 3c, limit the particle diameter to < 20 nm, since otherwise the protrusions of the particle surface would be too distant from the particle interior.

**11.4 Conclusions and Outlook**

Various advanced $^1H$-$^{31}P$ NMR experiments have shown conclusive evidence of a significant fraction, ~75%, of Pglass dispersed as ~10-nm diameter particles in the polyamide

matrix of a hybrid material. We have documented $^{1}H$ spin diffusion out of the Pglass and fast dipolar dephasing of $^{31}P$ by the short-$T_{2,H}$ polyamide protons. Cross polarization from the short-$T_{2,H}$ polyamide protons to $^{31}P$ surface sites in Pglass was detected in HetCor and HARDSHIP experiments. Significant $^{31}P$ spin diffusion from the interfacial to the interior sites was observed. The bonding of the surface sites is varied and significantly changed from that of the interior. With a large organic-inorganic interfacial area established, we can now apply $^{13}C$ NMR to look for effects on the polyamide matrix, providing further insights into the structure and dynamics of the Pglass/polymer hybrid system. Further, we will use TEM to characterize the ~25% larger Pglass particles and confirm the NMR results.

**Acknowledgments**

We acknowledge the U.S. National Science Foundation for financial support of this research under award numbers CTS-0317646 and DMR-0309115, and a Hearin Foundation Fellowship (to K.U). We also thank J.U.O's former graduate students and a number of our colleagues for their collaborative and complementary efforts in this research program.

**References**

1. Loy, D. A., Hybrid Organic-Inorganic Materials. *MRS Bulletin* **2001,** *26,* 368.
2. Tischendorf, B. C.; Harris, D. J.; Otaigbe, J. U.; Alam, T. M., Investigation of Structure and Morphology Dynamics in Tin Fluorophosphate Glass-Polyethylene Hybrids Using Solid-State H, C, and P MAS NMR. *Chem. Mater.* **2002,** *14,* 341.
3. Otaigbe, J. U.; Beall, G. H., Inorganic Phosphate Glasses as Polymers. *Trends in Polymer Science* **1997,** *5,* 369.
4. Brow, R. K. In *Review: the structure of simple phosphate glasses,* Structure, Properties and Applications of Phosphate and Phosphate-Containing Glasses, University of

Missouri-Rolla, 1999; Brow, R. K., Ed. North-Holland: University of Missouri-Rolla, 1999.

5. Tick, P. A., Water durable glasses with ultra low melting temperatures. *Physics and Chemistry of Glasses* **1984,** *25*, 149.
6. Xu, X. J.; Day, D. E., Properties and structure of Sn-P-O-F glasses. *Physics and Chemistry of Glasses* **1990,** *31*, 183.
7. Xu, X. J.; Day, D. E.; Brow, R. K.; Callahan, P. M., Structure of tin fluorophosphate glasses containing PbO or B2O3. *Physics and Chemistry of Glasses* **1995,** *36*, 264.
8. Otaigbe, J. U.; Quinn, C. J.; Beall, G. H., Processability and properties of novel glass-polymer melt blends. *Polymer Composites* **1998,** *19*, 18.
9. Young, R. T.; McLeod, M. A.; Baird, D. G., Extensional processing behavior of thermoplastics reinforced with a melt processable glass. *Polymer Composites* **2000,** *21*, 900.
10. Adalja, S. B.; Otaigbe, J. U., Melt Rheology of Tin Phosphate Glasses. *Applied Rheology* **2001,** *11*, 10.
11. Urman, K.; Otaigbe, J. U., Morphology, Crystallization Kinetics, and Dynamic Mechanical Analysis or Phosphate Glass-Polyamide 12 Hybrid Materials. *SPE ANTEC Tech. Papers* **2004,** *62*, 2063.
12. Arkles, B., Commercial Applications of Sol-Gel-Derived Hybrid Materials. *MRS Bulletin* **2001,** 26, 402.
13. Brinker, C. J.; Scherer, G. W., *Sol-Gel Science, The Physics and Chemistry of Sol-Gel Processing*. Academic Press: San Diego, 1990.

14. Niida, H.; Takahashi, M.; Uchino, T.; Yoko, T., Preparation and structure of organic-inorganic hybrid precursors for new type low-melting glasses. *Journal of Non-Crystalline Solids* **2002,** *306*, 292.

15. Cheng, S.-K.; Wang, C.-C.; Chen, C.-Y., Study on the Phase Behavior of EVA/PS Blends During in situ Polymerization. *Polymer Engineering and Science* **2003,** *43*, 1221.

16. Veenstra, H.; J.J. van Lent, B.; van Dam, J.; Posthuma de Boer, A., Co-continuous morphologies in polymer blends with SEBS block copolymers. *Polymer* **1999,** *40*, 6661.

17. Bourry, D.; Favis, B. D., Cocontinuity and Phase Inversion in HDPE/PS Blends: Influence of Interfacial Modification and Elasticity. *Journal of Polymer Science: Part B: Polymer Physics* **1998,** 36, 1889.

18. Zheng, S.; Huang, J.; Liu, W.; Yang, X.; Guo, Q., Miscibility and Phase Behaviour in Blends of Poly(Vinyl Alcohol) and a Copolyamide. *European Polymer Journal* **1996,** *32*, 757.

19. Deimede, V. A.; Fragou, K. V.; Koulouri, E. G.; Kallitsis, J. K.; Voyiatzis, G. A., Miscibility behavior of polyamide 11/sulfonated polysufone blends using thermal and spectroscopic techniques. *Polymer* **2000,** *41*, 9095.

20. Laura, D. M.; Keskkula, H.; Barlow, J. W.; Paul, D. R., Effect of glass fiber surface chemistry on the mechanical properties of glass fiber reinforced, rubber-toughened nylon 6. *Polymer* **2002,** *43*, 4673.

21. Hersh, L. S.; Onyiriuka, E. C.; Hertl, W., Amine-reactive surface chemistry of zinc phosphate glasses. *Journal of Materials Research* **1995,** *10*, 2120.

22. Urman, K.; Otaigbe, J. U., Novel Phosphate Glass/Polyamide 6 Hybrids: Miscibility, Crystallization Kinetics, and Mechanical Properties. *Journal of Polymer Science, Part B: Polymer Physics* **2006,** *44*, 441.

23. Nishi, T.; Wang, T. T., Melting Point Depression and Kinetic Effects of Cooling on Crystallization in Poly(vinylidene fluoride)-Poly(methyl methacrylate) Mixtures. *Macromolecules* **1975,** *8*, 909.

24. Hou, S. S.; Beyer, F. L.; Schmidt-Rohr, K., High-Sensitivity Multinuclear NMR Spectroscopy of a Smectite Clay and of Clay-Intercalated Polymer. *Solid-State NMR* **2002,** *22*, 110.

25. Hou, S. S.; Bonagamba, T. J.; Beyer, F. L.; Madison, P. H.; Schmidt-Rohr, K., Clay Intercalation of Poly(styrene-ethylene oxide) Block Copolymers Studied by Two-Dimensional Solid-State NMR. *Macromolecules* **2003,** *36*, 2769.

26. Schmidt-Rohr, K.; Rawal, A.; Fang, X.-W., Determining Nanocrystal Thickness in Organic-Inorganic Nanocomposites by NMR Using Heteronuclear Recoupling with Dephasing by Strong Homonuclear Interactions of Protons. *J. Chem. Phys.*, accepted for publication.

27. Adalja, B. S.; Otaigbe, J. U.; Thalacker, J., Glass-Polymer Melt Hybrids. I: Viscoelastic Properties of Novel Affordable Organic-Inorganic Polymer Hybrids. *Polymer Engineering and Science* **2001,** *41*, 1055.

28. Gullion, T.; Schaefer, J., Rotational-echo double-resonance NMR. *Journal of Magnetic Resonance* **1989,** *81*, 196.

29. Clauss, J.; Schmidt-Rohr, K.; Spiess, H. W., Determination of domain sizes in heterogeneous polymers by solid-state NMR *Acta Polymerica* **1993**, *44*, 1.

30. Schmidt-Rohr, K.; Clauss, J.; Spiess, H. W., Correlation of Structure, Mobility, and Morphological Information in Heterogeneous Polymer Materials by Two-Dimensional Wideline-Separation NMR Spectroscopy. *Macromolecules* **1992,** *25*, 3273.

# CHAPTER 12.
# PROMOTION OF THE γ-PHASE OF POLYAMIDE 6 IN ITS NANOCOMPOSITE WITH PHOSPHATE GLASS

Submitted as a *Note* to *Journal of Polymer Science, Polymer Physics Edition.*

A. Rawal, K. Urman, D. Iverson, J. U. Otaigbe, K. Schmidt-Rohr

**Abstract**

The effect of tin fluorophosphate-glass (Pglass) nanoparticles on the polyamide-6 (PA6) matrix in Pglass/PA6 hybrids has been investigated by $^{13}C$ solid-state nuclear magnetic resonance (NMR). The crystallinity determined by direct-polarization $^{13}C$ NMR combined with longitudinal relaxation-time ($T_{1C}$) filtering varied only slightly between 25 and 35% in all samples studied. $T_{1C}$-filtered $^{13}C$ spectra with cross polarization clearly showed resonances of both the α- and γ-crystalline phases of PA6, typically at ratios near 50:50, while the similarly processed neat polymer contained only the α-phase. This suggests that the Pglass promotes the growth of the γ-crystalline phase.

**Short Synopsis**

The crystallinity and crystal modifications of polyamide-6 (PA6) in hybrid materials with tin fluorophosphate-glass have been determined by $^{13}C$ solid-state NMR. The crystallinity varied only slightly between 25 and 35%. Both the α- and γ-crystalline phases of PA6 were present in the hybrids, typically at ratios near 50:50, while the similarly processed neat polymer contained only the α-phase. This suggests that the Pglass promotes the growth of the γ-crystalline phase.

## 12.1 Introduction

The hybrid materials formed by melt-blending of polyamide-6 with low-Tg tin-

fluorophosphate glass ("Pglass") exhibit favorable processing and mechanical properties as well as chemical resistance.[1,2] Our previous NMR investigation of a hybrid containing 10 wt% Pglass showed intimate contact of 75% of the Pglass with the polymer matrix on the 10-nm scale, thus proving the formation of a nanocomposite.[3] In this Note, we report the effect of the Pglass on the crystallinity and crystalline structure of the PA6 in the hybrid material, probed by $^{13}C$ NMR spectroscopy. PA6 has two stable crystalline phases,[4-6] labeled α- and γ-phase, and a metastable β-phase that is thought to be an intermediate structure between the α- and γ-crystals.[6] The α-phase is thermodynamically most stable and obtained by slow cooling from melt or annealing in superheated water.[7] The crystals of the γ-phase can be obtained by iodine treatment of the α-phase and by high-speed melt spinning.[5] The γ-phase has also been observed in PA6-clay nanocomposites,[8] where it appears to be nucleated near the silicate surfaces.[9] The effect of the crystal modification on the mechanical properties of the polyamide is significant, as seen by the very different tensile stress-strain curves for the two phases.[10] While the α-phase imparts improved stiffness and barrier properties, the β and γ-phases provide much better ductility and draw ratios, which are desirable for fiber and film applications. [10] In $^{13}C$ NMR, the α- and γ-phases exhibit distinct peak patterns, in particular well-resolved signals at 43.2 and 39.8 ppm, respectively.[8] Using quantitative $^{13}C$ NMR with direct polarization, we quantify the mass fractions of the crystalline phases in three hybrids and in a neat polyamide-6 reference material subjected to the same processing steps.

## 12.2 Experimental Section

### *11.2.1 Samples.*

The low-$T_g$ Pglass was synthesized according to procedures reported elsewhere[2,11]. It has a molar composition of 50% $SnF_2$ + 20% SnO + 30% $P_2O_5$, a density of 3.75 g/cm$^3$, and

a $T_g$ of approximately 126 $^oC$. The tin fluoride and tin oxide were supplied by Cerac Inc., and the ammonium phosphate was purchased from Sigma-Aldrich. The polyamide-6 used was Capron 8270 HS supplied by Allied Signal. The hybrids were prepared using a Thermo-Haake Polydrive Melt Mixer equipped with roller rotor blades. Prior to melt-mixing, the Polydrive mixer was heated to 250 $^oC$ and allowed to equilibrate for at least 20 min. The PA6 was added to the Polydrive first and allowed to mix for 5 min in order to obtain a homogenous melt. The Pglass was then added, and the two components were allowed to mix together for 10 mins. Hybrid samples containing 0%, 5%, and 30% Pglass by volume were made for testing in 2006. A sample containing 10% Pglass, previously studied by $^{31}P$-$^1H$ NMR, had been prepared in 2004. The materials were collected in chunks and ground into fine particles using an IKA A11 basic laboratory mill for the NMR measurements.

*12.2.2 NMR parameters.*

Solid-state NMR experiments were performed using a Bruker DSX400 spectrometer at 400 MHz for $^1H$ and 100 MHz for $^{13}C$. A Bruker 7-mm double-resonance magic-angle spinning (MAS) probehead was used with a spinning frequency of 6.5 kHz. $^{13}C$ and $^1H$ 90$^o$ pulse lengths of 4 μs were employed. The $^{13}C$ nuclei of the PA6 were excited either by cross or by direct polarization (CP or DP, respectively). In the CP experiments, polarization is transferred from $^1H$ to $^{13}C$ before detection, which results in strong signals but with reduced intensity of mobile segments, e.g. in the amorphous regions. The recycle delay in the CP experiments was 2 s, the cross-polarization time 0.4 ms. In the DP experiments, the $^{13}C$ were directly polarized by a 90$^o$ pulse after recycle delays of ca. 2000 s. CP/$T_1$ measurements [12] were applied to ensure that 2000 s is long enough for complete equilibration of the $^{13}C$ magnetization so that the DP $^{13}C$ NMR spectra are quantitative. $T_{1C}$ filter times of 5 s were used to suppress the signal from the amorphous fraction of the PA6. The full DP spectra were

recorded using the same pulse sequence with a negligible 0.001-s $T_{1C}$ filter time. Shorter recycle delays of 2 s were used to selectively observe the signals from the amorphous phase, which have a shorter $T_{1C}$ due to their fast segmental mobility. In the CP and the DP experiments with short recycle delay, the total suppression of sidebands (TOSS)[13] scheme was used before detection to remove spinning sidebands of the NC=O signal, which is centered at 175.3 ppm. Chemical shifts were referenced to TMS, using the COO resonance of α-glycine at 176.5 ppm as a secondary external reference. Two-pulse phase modulation (TPPM) decoupling was applied during detection.

**12.3 Results and Discussion**

Figure 1 shows the $^{13}C$ NMR spectra of neat PA6 as-received and of neat PA6 that has been run through exactly the same processing steps as the Pglass/PA6 hybrid materials. The only significant difference between the spectra is an increased amorphous fraction after processing. The $T_{1C}$-filtered CP/TOSS spectra, which selectively show signals of the crystalline PA6 due to the short $T_{1C}$ of the noncrystalline polymer, are essentially the same in both neat PA6 samples. They exhibit only peaks corresponding to the crystalline α-phase; the observed peak positions agree with the literature values within 0.2 ppm. The DP spectra with the short recycle delay, which select the amorphous component, exhibit only minor differences for the two neat PA6 samples.

By contrast, the $T_{1C}$-filtered spectra of three Pglass/PA6 hybrids, shown in Figure 2, exhibit additional peaks from a crystalline phase other than the α-phase. In order to show these peaks more clearly, the signals of the pure α-phase as measured in the neat PA6 (see Figure 1g) were subtracted out. With the scaling factor adjusted such that the α-phase peaks at 43.2 and 26.3 ppm vanish, all three samples show the same residual peak pattern, see Figures 2d, h, and l. Comparing with previous work,[8,14] these peaks are found to correspond

exactly to the γ-phase. As shown earlier,[3] there is a large-area interface between between the Pglass phase and the PA6 matrix. The spectra of Figures 1 and 2 strongly suggest that the presence of the Pglass promotes growth of the γ-phase crystallites of PA6. It is worthy to note that in clay-PA6 nanocomposites, VanderHart et al. similarly showed by NMR that the γ-phase is promoted by 5 wt% clay.[8,9] Note, however, that the Pglass in our system is a liquid at the nylon crystallization temperature and therefore does not present a solid surface for nucleation, unlike the clay silicate.

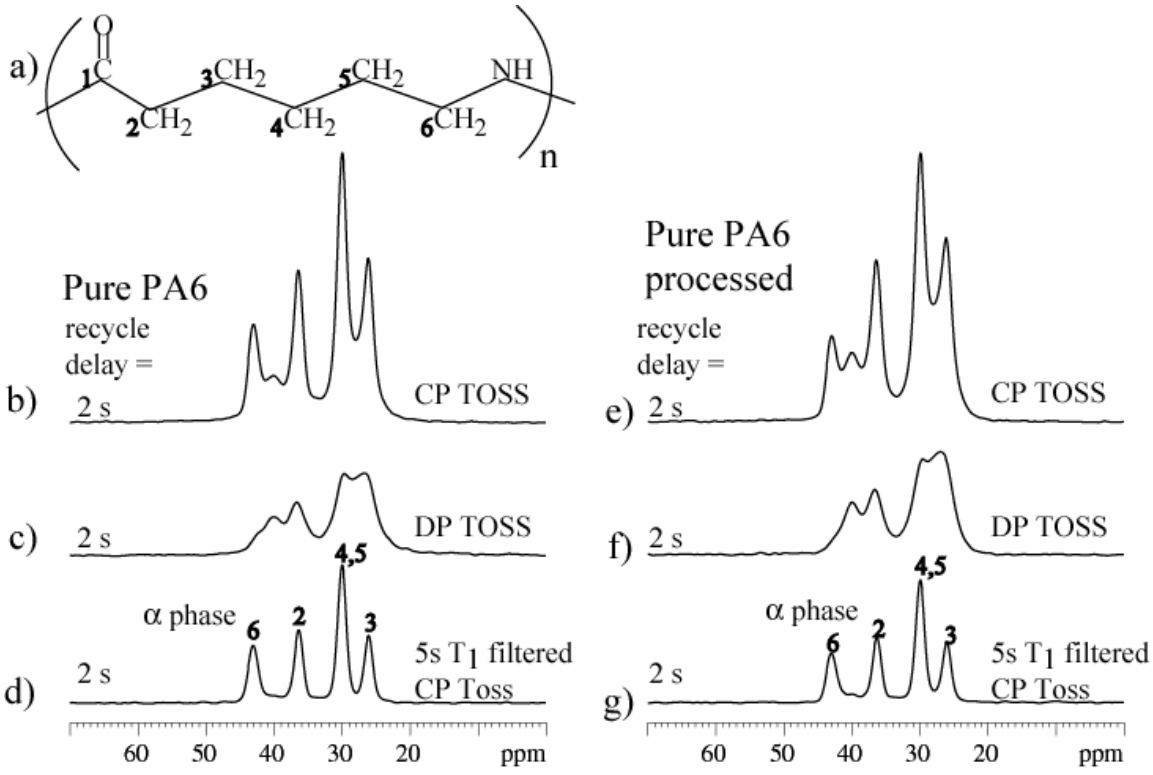


**Figure 1.** a) Chemical structure of PA6. b) - g) CP/MAS $^{13}C$ NMR spectra of neat PA6 samples. The plots show the spectral range from 70 ppm to 0 ppm, which contain the methylene peaks of interest. The NC=O carbon resonance at 175.3 ppm is not shown here. a) and e) are the CP/TOSS spectra of the processed and unprocessed PA6. c) and f) are the short-recycle-delay DP/TOSS spectra, which are selective towards the amorphous phase. d) and g) are the $T_{1C}$-filtered CP/TOSS spectra, which are selective towards the crystalline phase. The peaks have been assigned to the carbons using the numbering scheme shown in a). The spectra show little effect of processing on neat PA6.

The relative amounts of the γ- and α-phases can be evaluated by comparing the integrated intensities of the $T_{1C}$-filtered CP/TOSS spectra of the hybrid materials, before and after subtraction of the α-phase signal. While the 5 % and 30 % Pglass containing hybrids have a γ- : α-phase ratios of 58:42 and 47:53 (±4), the ratio in the 10 % Pglass hybrid is only 12:88. This discrepancy may have arisen because the 10% Pglass hybrid was made several years earlier than the three other samples.

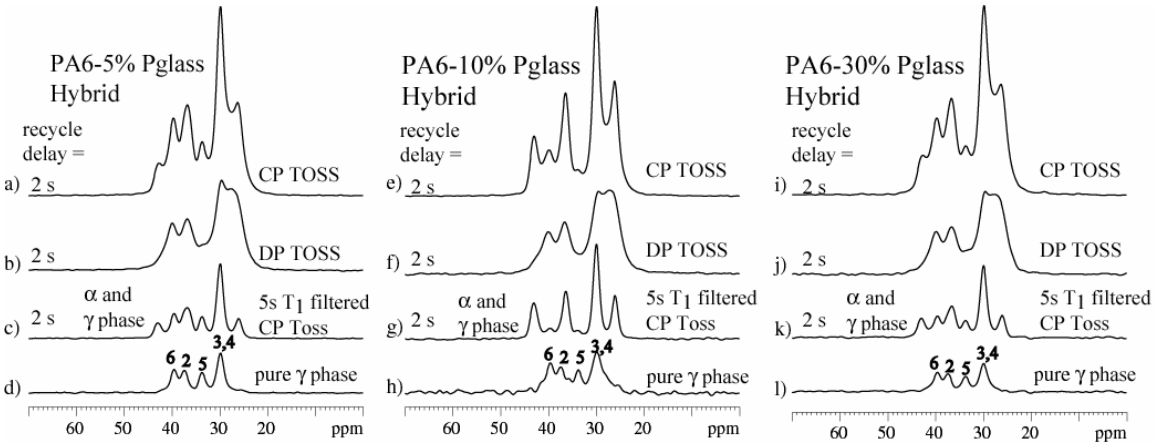


**Figure 2**. $^{13}C$ NMR spectra of PA6/Pglass hybrids with 5 %, 10 % and 30 % loading of the Pglass are shown. The DP/TOSS spectra obtained after a short, 2-s recycle delay show the spectrum of the amorphous components. The $T_{1C}$-filtered CP/TOSS spectra c), g) and k) exhibit only peaks from the crystalline phases. The signals from the γ-phase are isolated in d), h) and l) by subtracting out the α-phase using the scaled $T_{1C}$-filtered CP/TOSS spectrum of the pure polyamide. The spectrum in h) has been scaled up by a factor of 4 because the 10 % Pglass/PA6 hybrid has a lower fraction of the γ-phase than the other two compositions.

Figure 3 shows the quantative, directly polarized $^{13}C$ NMR spectra of the neat PA6 and the three Pglass/PA6 hybrids. The ratio of the spectral areas with and without $T_{1C}$ filtering gives the weight-based crystallinity. While the crystallinity in the neat PA6 is 30 ± 2 %, the 5 % and 30 % Pglass hybrids have reduced crystallinities of 26 and 27 ± 2 %, respectively. The 10 % Pglass has a higher crystallinity of 37 ± 2 %. The presence of the γ-phase and the increased amorphous content may explain the enhanced ductility observed

previously in these hybrids[1], although this may be concomitant with a plasticizing effect from the Pglass as previously reported[2]. This study points to a new facile route to tuning the morphology and properties of PA6 by adding small amounts of Pglass, and it may stimulate a better understanding of the structure/property relationships of this interesting nanostructured hybrid system with enhanced benefits.

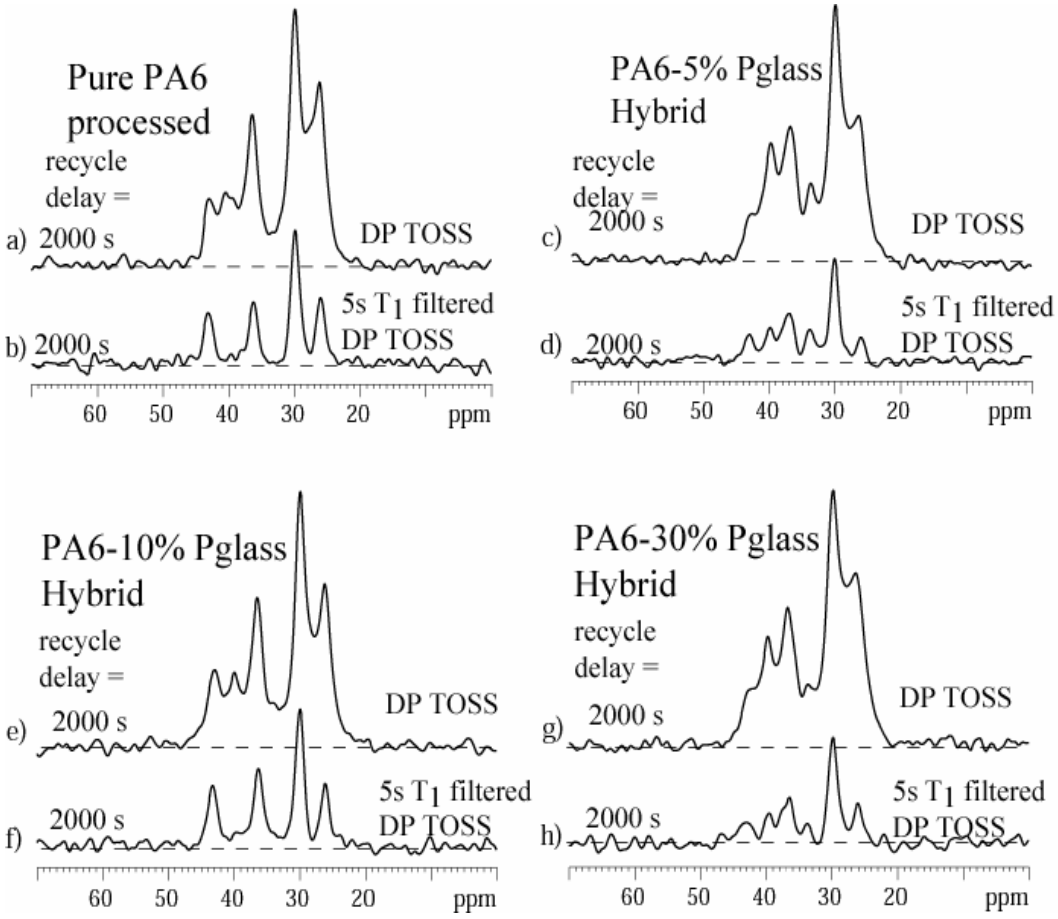


**Figure 3.** a), c), e), and g): Quantitative $^{13}C$ NMR spectra of the processed neat PA6 and the PA6/Pglass hybrids, obtained using the DP/echo sequence with a 2,000-s recycle delay. b), d), f), and h): Corresponding spectra of the crystalline phases, selected by the application of a 5-s $T_{1C}$ filter before detection. The ratio of the integrated intensities gives the crystallinity.

## 12.4 Conclusion

We have shown that the addition of an inorganic Phosphate glass even at relatively low concentrations has a significant effect on the crystallization behavior of PA6, producing a remarkably large fraction of γ-phase crystals. This is consistent with our previous finding of intimate mixing of the hybrid components on a 10-nm scale.

## Acknowledgements

We acknowledge the U.S. National Science Foundation for financial support of this research under award numbers CTS-0317646 and DMR-0309115, and a Hearin Foundation Fellowship (to K.U).

## References

1. Urman, K.; Otaigbe, J. U. Journal of Polymer Science, Part B: Polymer Physics 2005, 44, 441-450.
2. Urman, K.; Otaigbe, J. U. Prog Polym Sci 2007, in press.
3. Rawal, A.; Urman, K.; Otaigbe, J. U.; Schmidt-Rohr, K. Chem Mater 2006, 18, 6333-6338.
4. Holmes, D. R.; Bunn, C. W.; Smith, D. J. J Polym Sci 1955, 17, 159-177.
5. Arimoto, H.; Ishibashi, M.; Hirai, M.; Chatani, Y. J Polym Sci, Part A: General Papers 1965, 3, 317-326.
6. Penel-Pierron, L.; Depecker, C.; Seguela, R.; Lefebvre, J. M. Journal of Polymer Science, Part B: Polymer Physics 2001, 39, 484-495.
7. Persyn, O.; Miri, V.; Lefebvre, J. M.; Depecker, C.; Gors, C.; Stroeks, A. Polym Eng Sci 2004, 44, 261-271.
8. VanderHart, D. L.; Asano, A.; Gilman, J. W. Chem. Mater. 2001, 13, 3781-3795.
9. VanderHart, D. L.; Asano, A.; Gilman, J. W. Chem. Mater. 2001, 13, 3796-3809.

10. Seguela, R. J Macromol Sci-Poly R 2005, C45, 263-287.

11. Adalja, S. B.; Otaigbe, J. U.; Thalacker, J. Polym Eng Sci 2001, 41, 1055-1067.

12. Torchia, D. A. J. Magn. Reson. 1978, 30, 613-616.

13. Dixon, W. T.; Schaefer, J.; Sefcik, M. D.; Stejskal, E. O.; McKay, R. A. J Magn Reson 1982, 49, 341-345.

14. Hatfield, G. R.; Glans, J. H.; Hammond, W. B. Macromolecules 1990, 23, 1654-1658.

# CHAPTER 13.
# GENERAL CONCLUSIONS

In this thesis, the capabilities of solid-state NMR for characterizing many aspects of nanocomposites are demonstrated. The natural nanocomposite in bone; a synthetic biomimetic nanocomposite; the dispersion of silicate in a TCP matrix; and polyamide-phosphate glass based hybrid materials have been studied by a variety of solid state NMR methods. The various components or moieties in these materials have been characterized, thicknesses of particles dynamics elucidated, interfacial compositions determined, and structural models proposed.

An understanding of the size of the bioapatite nanocrystals in bovine and avian cortical bone has been gained by combining $^{31}P\{^{1}H\}$ HARDSHIP along with WAXD results. It shows that the apatite particles are “boards” 3-4 nm thick , and ca. 8 nm by 14 nm in the other two dimensions. Based on these measurements a more accurate model of the nanocomposite in bone has been presented.

The surface moieties of the bioapatite nanocrystals in bovine and avian bone have been identified and quantified by $^{31}P$ CSA and $^{1}H\{^{31}P\}$ recoupling experiments. It shows that the surface consists primarily of protonated $HPO_4^{2-}$ groups and $H_2O$-$PO_4^{3-}$ species. Controlled dephasing of the surface phosphates has revealed that the bioapatite nanoparticles of the avian bone have a larger surface fraction than those of bovine bone, which is consistent with the smaller size of the nanocrystals in the avian bone. The concentrations of the $OH^-$ in the bioapatite were determined accurately and it was shown that there is a nanometer scale heterogeneity in their distribution within the bioapatite crystal. Significantly the carbonate signal was selectively observed and specifically located within the $OH^-$ bearing

apatite, for the first time in unaltered bone. Its quantification indicates that 5-8 % of the bone apatite is carbonate. Based on quantitative solid state NMR measurements, a comprehensive charge balanced composition of the bioapatite has been determined. A species of mobile $H_2O$ has been identified in the nanocomposite by $^1H$ $T_{1\rho}$ measurements and located at bioapatite-collagen interface by $^{31}P$ and $^{13}C$ detected $^1H$ spin diffusion where it forms a layer 1-2 molecule thick. This mobile $H_2O$ has a correlation time of microseconds which implies very high viscosity (~ $10^6$ greater than bulk water) and is postulated to act as a viscous glue that contributes to the high impact strength of bone.

CH and $CH_2$ selection along with gated decoupling of the $^{13}C$ spectra of bone, in conjunction with $^1H$-$^{13}C$ HetCor have enabled a more complete spectral assignment of the residues of mineralized collagen. A peak at 75 ppm has been identified to belong to the $C_\gamma$ of hydroxyproline in a unique hydrogen bonding environment. It was shown that this peak and the shoulder at 180 ppm ($COO^-$ of glutamate/aspartate) do indeed belong to collagen residues and not to sugar-based macromolecules (glycosamines), as has been proposed. Furthermore, the $^{13}C\{^{31}P\}$ REDOR shows that the collagen –bioapatite interaction is through the sidechains of the hydroxyproline and glutamate residues, which come within 0.2-0.3 nm of the apatite surface and is mediated by the viscous $H_2O$ layer. Combining these results, a structure of the bioapatite-collagen interface is proposed.

In addition to investigating the structure and composition of the nanocomposite in bone, solid state NMR has been utilized as an efficient guide to the synthesis of biomimetic block-copolymer–phosphate based nanocomposite materials. $^{31}P$ NMR identified the presence and type of phosphate precipitated in the system, while $^1H$-$^{31}P$ WISE NMR with $^1H$ spin diffusion was used as a convenient method to monitor the formation of a nanocomposite.

Further, Si/Zn-doped tricalcium phosphate (TCP), a promising bone-replacement material, was investigated. $^{29}$Si and $^{29}$Si{$^{31}$P} NMR revealed that while some of the silicon atoms replaced the phosphorous to form isolated $Q_0$ species, the predominant fraction clustered into nano-domains dispersed within the TCP matrix, as revealed by $^{29}$Si{$^{31}$P} REDOR measurements. Form the broad distribution of the $^{29}$Si chemical shifts, the clusters appear to be amorphous or glassy with $Q_1$, $Q_2$ and $Q_4$ species present. Spectral filtering methods based on J-coupling and double quantum selection enabled the quantification of the various overlapping silicate species. Use of CPMG refocused detection along with $^{29}$Si isotopic labeling enabled high sensitivity measurements to be performed in spite of the low silicon concentration.

The length scale of the dispersion of inorganic phosphate glass is a central question in recently developed polyamide6-phosphate glass composites. $^{31}$P{$^{1}$H} HARDSHIP revealed that ca. 75 % of the phosphate glass was in contact with the polyamide matrix, implying formation of a nanocomposite. $^{1}$H-$^{31}$P HetCor experiments revealed correlations between the phosphate and the amide protons, which indicates potential modification to the phosphate surface by the polyamide during the processing step. The $^{13}$C NMR of these materials revealed the presence of the crystalline γ-phase of the polyamide, which is absent in similarly processed polyamide without the phosphate glass.